Development of Metal Cluster Catalysts for Conversion of Middle Distillates Fractions in Synthetic Fuels

by

Geoffrey A. Ozin

(Principal Investigator)

and

J.P. Godber, D.M. Haddleton, H.X. Huber, A.F. Kuperman, R.A. Prokopowicz

Lash Miller Chemical Laboratories
University of Toronto

MICROMEDIA

Work on this project was conducted under the auspices of
Canada Centre for Mineral and Energy Technology
Energy Mines and Resources, Canada

DSS File Number	: 41ST. 23440-5-9074
DSS Contract Serial Number	: OST85-00183
CANMET Scientific Authority	: Dr. M.F. Wilson

Date: October 1989

241 pp

This report shall be cited as Contract Report No. OST85-00183

ABSTRACT

Liquid phase (rotary reactor) and cocondensation phase (rotary and static) metal vapor syntheses have been used to produce subnanometre particles of Fe, Ru and Fe/Ru, as well as Ni, Pt and Ni/Pt on SiO_2 and Al_2O_3, through the intermediacy of labile bis-toluene and tris-ethylene metal(0) precursors. These novel materials demonstrate unusual catalytic functions in the conversion of hydrocarbons and have many remarkable properties which have been examined using such techniques as: Conventional Transmission Electron Microscopy (CTEM), high resolution (1.0 x 1.0 nm) Scanning Transmission Electron Microscopy coupled with Energy Dispersive X-ray elemental Analysis (STEM/EDAX), X-ray Photoelectron Spectroscopy (XPS), Electron Paramagnetic and Ferromagnetic Resonance Spectroscopies (EPR/FMR), Fourier Transform Infrared Spectroscopy (FTIR), Diffuse Reflectance (UV-visible) Spectroscopy, Extended X-ray Absorption Finestructure Spectroscopy (EXAFS), and Chemisorption. Intimate details of the spatial and electronic structures of these materials have been determined, and evidence indicating that truly bimetallic particles are produced has been found. The catalytic results for the bimetallic ssamples, which show behaviour quite different from either of the two constituent metals, are explained by a computer model of the structure of the supported particles. Also, the application of EXAFS has verified the major assumptions used in the modelling, while providing an even greater understanding of the structural details of the supported metal particles.

RESUME

Des synthèses de vapeurs métalliques en phase liquide (réacteur rotatif) et en phase de cocondensation (réacteur rotatif et statique) ont été utilisées pour produire des particules subnanométriques de Fe, Ru et Fe/Ru ainsi que de Ni, Pt et Ni/Pt sur SiO_2 et Al_2O_3, par l'intermédiaire des précurseurs labiles bis-toluène-métal(0) et tris-éthylène-métal(0). Ces nouveaux matériaux remplissent des fonctions catalytiques inhabituelles dans la conversion des hydrocarbures et présentent de nombreuses propriétés remarquables qu'on a étudiées à l'aide de différentes techniques, par exemple: microscopie électronique à transmission classique (CTEM), microscopie électronique à balayage et transmission à haute résolution (1,0 x 1,0 nm) couplée à l'analyse élémentaire X en dispersion d'énergie (STEM/EDAX), spectroscopie des photoélectrons X (XPS), spectroscopies de résonance ferromagnétique et paramagnétique électronique (EPR/FMR), spectroscopie à l'infrarouge avec transformation de Fourier (FTIR), spectroscopie de réflectance diffuse (UV-visible), spectroscopie de structure fine d'absorption X étendue (EXAFS) et chimisorption. On a déterminé des détails fins des structures spatiales et électroniques de ces matériaux et on a prouvé que des particules réellement *bimétalliques* étaient produites. Les résultats relatifs à la nature catalytique des échantillons bimétalliques dont lecomportement est tout à fait différent de celui des deux métaux constituants, sont expliqués au moyen d'un modèle informatisé de la structure des particules supportées. De plus, l'application de la technique EXAFS a permis de confirmer les hypothèses principales utilisées dans la modélisation tout en permettant une meilleure compréhension des détails structuraux des particules métalliques supportées.

ACKNOWLEDGEMENTS

The Authors of this report wish to acknowledge the financial and technical support provided by the Canada Centre for Mineral and Energy Technology, Department of Energy Mines and Resources, during the past four years. In particular, thanks are due to **Dr. M. F. Wilson** at EMR for his assistance and technical input into the investigation.

The helpful administrative assistance provided by **Drs. S. Whittington** and **M.J. Dignam**, Chairmen of the Department of Chemistry at the University of Toronto, **Carol Gillen**, Director of the Office of Research Administration (University of Toronto), and **Chris Takenaka**, Contracts Officer are recognized.

Technical collaboration involving various experimental studies and analyses has been provided by: **Dr. Pierre Gallezot**, Centre National de la Recherche Scientifique, Villeurbanne, France, who coordinated much of the work with Electron Microscopy, and as well associate researchers **Christiane Leclercq** and **Christian Richard** at CNRS; **Dr. Stuart McIntyre**, and **Margaret Hyland**, Surface Science Facility at the University of Western Ontario, who carried out experiments using X-ray Photoelectron spectroscopy; **Dr. Albert Vannice**, Department of Chemical Engineering, at Pennsylvania State University, who performed chemisorption and calorimetric studies; **Dr. J. Lee** and **Battista Calvieri**, Medical Sciences Department, University of Toronto, who organized and assisted in carrying out the original group of electron microscopy experiments; **Dr. Ron Hancock**, Supervisor of the Slowpoke Reactor Facility at the University of Toronto, in whose laboratories, the Neutron Activation Elemental Analyses were performed; and Messrs. **Newton Milne** and **Juan Labastida-Bardales**, Department of Chemical Engineering at the University of Waterloo, who supervised and assisted with Elemental Analyses by Plasma Emission Spectroscopy.

TABLE OF CONTENTS

CHAPTER I Introduction 16

CHAPTER II Synthesis of MVS Materials 21

2.1 Experimental Details 21
2.1.1 Preparation of Reagents for MVS Reactions 21
2.1.2 The Metal Vapour Synthesis Reaction 22
2.1.3 Support Impregnation Procedure 27
2.2 List of All Samples Produced 29
2.3 Bulk Elemental Analyses 29

CHAPTER III Electron Microscopy Results 37

3.1 CTEM Study of Particle Size Distributions 37
3.1.2 Analysis of CTEM Data 38
3.1.3 Results of the CTEM Study of Surface Hydroxyl Effect 42
3.1.4 CTEM Study of Support Choice, Treatments and Bimetallic Incorporation 53
3.1.5 CTEM Study of MVS Materials Produced in the Static Reactor 55
3.2 STEM-EDAX Investigation of Iron/Ruthenium Bimetallics 60
3.3 STEM-EDAX Study of the Nickel/Platinum System 62

CHAPTER IV Characterization by X-ray Photoelectron Spectroscopy 67

4.1 General Theory 67
4.2 Experimental Details 69
4.3 Results and Discussion of XPS Investigations 70
4.3.1 Charging Problems, Referencing and Curve Fitting 71

4.3.2 Examination of Unimetallic Iron, Ruthenium and Bimetallic Materials..... 71
4.3.3 Examination of the Unimetallic Nickel, Platinum and Bimetallic Materials..... 78
4.4 Summary of the XPS Study..... 81

CHAPTER V Magnetic Resonance Characterization Studies..... 84

5.1 General Theory..... 84
5.1.1 Analytical Capabilities of Magnetic Resonance Spectroscopy..... 84
5.1.2 Magnetic Resonance Spectroscopy Theory..... 86
5.1.3 Contrast and Comparison of EPR and FMR Resonances..... 87
5.2 Special Magnetic Properties of Nickel..... 90
5.3 Experimental Details..... 92
5.3.1 Procedure and Spectrometer Details..... 92
5.3.2 Experiments Conducted..... 92
5.4 Results of the EPR/FMR Investigation..... 93
5.4.1 Supported Nickel Sample on High Temperature Pretreated Support..... 93
5.4.2 Supported Nickel Sample on Low Temperature Pretreated Support..... 95
5.5 Discussion of Magnetic Resonance Spectroscopy Results..... 96
5.5.1 High Temperature Support Pretreated Material..... 97
5.5.2 Low Temperature Support Pretreated Material..... 101
5.6 Summary of the EPR/FMR Study..... 101

CHAPTER VI Chemisorption Studies..... 105

6.1 Mid-Infrared Examination of CO Chemisorption on Pt/SiO_2..... 105
6.1.1 Theory of Coverage Dependent Behaviour..... 106
6.1.1.1 Local Field Effects..... 106
6.1.1.2 Dipolar and Vibrational Coupling Effects..... 109
6.1.1.3 Through-Space Electrodynamical Dipolar Coupling..... 111
6.1.1.4 Through-Metal Vibrational Coupling..... 111
6.1.2 Results of IR Examination of Adsorbed CO..... 113
6.1.3 Discussion of IR Results for CO Adsorption..... 121
6.2 Adsorption Enthalpy Studies on Supported Platinum Materials..... 128
6.2.1 Experimental Details..... 128
6.2.2 Chemisorption and Calorimetric Results..... 130

6.2.3 Discussion of Results....130

CHAPTER VII Catalysis on the Iron, Ruthenium and Iron/Ruthenium Bimetallic MVS Materials....141

7.1 Introduction and Literature Review....141
7.1.1 Catalysis on Similar Bimetallic Materials....141
7.1.2 Particle Size Effects....142
7.1.3 Preparation of Catalysts....143
7.2 General Catalysis Results....144
7.2.1 Control Experiment....145
7.2.2 MVS Generated Ruthenium Catalyst....150
7.2.3 MVS Generated Iron Catalyst....153
7.2.4 MVS Generated 3:1 Ru/Fe Bimetallic Catalyst....153
7.2.5 MVS Generated 2:3 Ru/Fe Bimetallic Catalyst....156
7.2.6 Control Experiment for Support Activity....159
7.3 Additional Studies on Heavily Loaded Iron Catalysts....159
7.3.1 MVS Generated Fe Catalyst on Silica/Alumina Support....169
7.3.2 MVS Generated Fe Catalyst on Alumina....173
7.4 Mechanistic Interpretation of Results....174
7.4.1 Dehydrogenation Submechanism....175
7.4.2 Hydrogenolysis Submechanism....178
7.5 Summary....180

CHAPTER VIII Catalysis on the Nickel, Platinum and Nickel/Platinum Bimetallic MVS Materials....181

8.1 Unimetallic Platinum Samples....181
8.1.1 Platinum on Silica Materials....181
8.1.2 European Standard Platinum Catalyst....184
8.1.3 Platinum on Alumina Materials....185
8.1.4 Summary of Platinum Results....186
8.2 Unimetallic Nickel Samples....186
8.2.1 Nickel on Silica Materials....186

8.2.2 Nickel on Alumina Materials....189
8.3 Bimetallic Nickel/Platinum Materials....190
8.3.1 General Results....190
8.3.2 Selectivity as a Function of Atomic Composition....191
8.4 Static MVS Generated Platinum Materials....193
8.5 Bimetallic Surface Model....198
8.5.1 Neighbour Independent Occupation Model....199
8.5.2 Variable Short Range Order Model....204
8.5.3 Fully Segregated Particle Model....206

CHAPTER IX Examination of MVS Materials by Extended X-ray Absorption Fine Structure Spectroscopy....209

9.1 Introduction and Analytical Capabilities....209
9.2 Theory of EXAFS....210
9.2.1 Isolation of the EXAFS Signal from X-ray Absorption Data....211
9.2.2 Theoretical Scattering Function for K and L_I Edges....212
9.2.3 Theoretical Scattering Function for L_{II} and L_{III} Edges....213
9.2.4 Application of the Theoretical Equations in Curve Fitting Data....214
9.3 Experimental Details....215
9.3.1 Sample Preparation and Data Collection....215
9.3.2 Calculations....218
9.4 EXAFS Results....218
9.4.1 Pt L_{III} Edge EXAFS for Unimetallic Pt and Bimetallic Ni/Pt Samples....218
9.4.2 Ni K Edge EXAFS for Unimetallic Ni and Bimetallic Ni/Pt Samples....221
9.5 Discussion of EXAFS Results....224
9.5.1 Examination of the Platinum L_{III} Edge....224
9.5.2 Examination of the Nickel K Edge....225
9.6 Summary of the EXAFS Study....227

CHAPTER X Conclusions and Recommendations....229

10.1 Conclusions....229
10.2 Recommendations....231

REFERENCES.....233

SUMMARY.....240

APPENDIX A.....242

APPENDIX B.....274

LIST OF TABLES

2-1 List of All MVS Materials and Characterization Tests Made

2-2 Bulk Elemental Analysis Results

3-1 Particle Size Distributions of Silica-Supported Nickel and Platinum Clusters

3-2 EDAX Analysis for Supported Iron/Ruthenium Particles from Various Precursors

3-3 EDAX Analysis Results for Bimetallic Ni/Pt Particles Produced by MVS

4-1 Measured XPS Binding Energies for Fe/Ru MVS Materials on Alumina

4-2 Measured XPS Binding Energies for Ni/Pt MVS Samples

4-3 Standard Reduction Potentials for Fe, Ru, Ni and Pt in Aqueous Media

6-1 Force Constants for Carbonyl Stretch-Stretch Coupling in Several Compounds

6-2 Results of Adsorption Measurements made Prior to Calorimetric Studies

6-3 Heats of Chemisorption of Hydrogen on Pt/SiO_2 MVS Samples

6-4a Heats of Chemisorption of Oxygen on Pt/SiO_2 MVS Samples

6-4b Reaction Enthalpies for Subsequent Hydrogen Titrations

6-5 Heats of Chemisorption of Carbon Monoxide on Pt/SiO_2 MVS Samples

7-1 List of Preliminary Experiments Performed on Fe, Ru and Fe/Ru Bimetallic MVS Materials

7-2 Catalytic Characteristics of MVS-Generated Supported Iron Samples

9-1 Structural Parameters of MVS Materials Determined by EXAFS Analysis

LIST OF FIGURES

1-1 Design of the Static Reactor used for Metal Vapour Synthesis

1-2 Design of the Rotary Reactor used for Solution Phase Metal Vapour Synthesis

2-1 Quartz Vessel for Vacuum Pretreatment of Support Material

2-2 Low Temperature Anaerobic Vessel for Impregnation of Support Materials

2-3 Design of the Dual Electron Gun used in the Rotary MVS Reactor

2-4 Collection and Filtering Vessel for MVS Reaction Products

2-5 Glass Manifold for Transfer of Supported Metal-Cluster Samples to Sealed Ampoules

3-1 Typical CTEM Micrograph of a Pt/Al_2O_3 MVS Sample

3-2 Particle Size Analysis of the Ni/SiO_2 MVS-Generated Sample Pretreated at 200°C

3-3 Particle Size Analysis of the Ni/SiO_2 MVS-Generated Sample Pretreated at 400°C

3-4 Particle Size Analysis of the Ni/SiO_2 MVS-Generated Sample Pretreated at 600°C

3-5 Particle Size Analysis of the Ni/SiO_2 MVS-Generated Sample Pretreated at 725°C

3-6 Particle Size Analysis of the Pt/SiO_2 MVS-Generated Sample Pretreated at 200°C

3-7 Particle Size Analysis of the Pt/SiO_2 MVS-Generated Sample Pretreated at 400°C

3-8 Particle Size Analysis of the Pt/SiO_2 MVS-Generated Sample Pretreated at 600°C

3-9 Particle Size Analysis of the Pt/SiO_2 MVS-Generated Sample Pretreated at 800°C

3-10 The Effect of Support Pretreatment Temperature on Mean Particle Size

3-11 Average Metal Particle Sizes of MVS Materials Before and After Catalysis

3-12 Comparison of Average Particle Sizes between Ni/Pt Bimetallic and Unimetallic Pt MVS Samples

3-13 Particle Size Distributions of the Samples Produced in the Static MVS Reactor

4-1 Typical XPS Broadscan of Supported Metal Cluster Material

4-2 XPS Scan of Carbon 1s Peaks in a Typical Spectrum of Supported Cluster Materials

4-3 Typical XPS Scan of Fe(2p) Peak in Supported Metal Cluster Materials

4-4 Typical XPS Scan of Ru(3p) Peak in Supported Metal Cluster Materials

4-5 Typical XPS Scan of Pt(4f) Peak in Supported Metal Cluster Materials

4-6 Typical XPS Scan of Pt(4d) Peak in Supported Metal Cluster Materials

4-7 Typical XPS Scan of Ni(2p) Peak in Supported Metal Cluster Materials

5-1a Trends in Magnetic Resonance Parameters for Various Systems on Support Surfaces

5-1b The Temperature Dependence of Magnetic Resonance Linewidths

5-2 EPR/FMR Spectrum of a Ni/Al_2O_3 Material (800°C Pretreatment) taken at 123 K

5-3 EPR/FMR Spectrum of a Ni/Al_2O_3 Material (800°C Pretreatment) taken at 293 K

5-4 EPR/FMR Spectrum of a Ni/Al_2O_3 Material (800°C Pretreatment) taken at 533 K

5-5 EPR/FMR Spectrum of a Ni/Al_2O_3 Material (200°C Pretreatment) taken at 123 K

5-6 Model of Support Pretreatment and Nickel Particle Nucleation Processes for High-Temperature-Pretreated Alumina

5-7 Model of Support Pretreatment and Nickel Particle Nucleation Processes for Low-Temperature-Pretreated Alumina

5-8 Summary of the Synthesis, Anaerobic Heating and Oxidation of MVS-Generated Ni/Al_2O_3 Materials

6-1 Predicted IR Spectra of Adsorbed CO as a Function of Surface Coverage According to Local Field Effect Theory (Reproduced from Ref. 58)

6-2 IR Spectra of Two Binary Mixed-Isotope Carbonyls (from Ref. 55)

6-3 Simulated CO Spectra showing the Effects of Coverage and the Vibrational Coupling Force Constant

6-4 Simulated CO Spectra at Various Fractional Coverages for Equimolar Isotopic Mixtures

6-5 The Effect of the Vibrational Coupling Force Constant in Predicted Spectra of Equimolar Isotopic Mixture of ^{12}CO and ^{13}CO

6-6 IR Spectrum of Adsorbed CO on Supported Pt MVS Materials Pretreated at 200°C, at Full Surface Coverage

6-7 IR Spectrum of Adsorbed CO on Supported Pt MVS Materials Pretreated at 400oC, at Various Fractional Coverages

6-8 IR Spectrum of Adsorbed CO on Supported Pt MVS Materials Pretreated at 600°C, at Various Fractional Coverages

6-9 IR Spectrum of $^{12}CO/^{13}CO$ Mixture Adsorbed on an MVS-Generated Supported Platinum Material

6-10 IR Spectrum of ^{12}CO Adsorbed on a Pt MVS Sample After Ozidation

6-11 CO Stretching Frequency as a Function of Particle Size on Platinum

6-12 Coverage Dependent Frequency Shifts as a Function of Particle Size for CO Adsorbed on Platinum

6-13 A Model for CO Adsorption on Oxidatively Treated Platinum Cluster Surfaces

6-14 Total Hydrogen Uptake Isotherms for a Pt/SiO_2 MVS Material Following Various Pre-treatments

6-15 CO Adsorption Enthalpies on Platinum Surfaces Ranging from Bulk to Ultra-Small MVS-Generated Specimens

6-16 Hydrogen Adsorption Enthalpies on Platinum Surfaces Ranging from Bulk to Ultra-Small MVS-Generated Specimens

6-17 The Relationship Between the Promotion-Energy-Corrected Adsorption Enthalpy and Stretching Frequency upon Chemisorption for CO on Various Transition Metals

6-18 A Thermodynamic Description of the Size Dependence of CO Adsorption Enthalpies on Metal Particles

6-19a The Relationship Between CO Stretching Frequency Change and Particle Size

6-19b Factors which Influence the Particle Size Dependence of Heats of Adsorption of CO on Platinum

7-1 n-Butane Conversion Catalysis Results for Sample ASC-01

7-2 n-Butane Conversion Catalysis Results for Sample ASC-01 (Repeat Experiment)

7-3 n-Butane Conversion Catalysis Results for Sample EMR-6

7-4 n-Butane Conversion Catalysis Results for Sample EMR-3b

7-5 n-Butane Conversion Catalysis Results for Sample EMR-5

7-6 n-Butane Conversion Catalysis Results for Sample EMR-11a

7-7 n-Butane Conversion Catalysis Results for Sample EMR-11b

7-8 n-Butane Conversion Catalysis Results for Sample EMR-21a

7-9 n-Butane Conversion Catalysis Results for Sample EMR-21b

7-10 Postulated Surface Reaction Mechanism for n-Butane Conversion on MVS-Generated Supported Iron Catalysts

8-1 n-Butane Conversion Catalysis Results for Sample EMR-20

8-2 n-Butane Conversion Catalysis Results for Sample EMR-19

8-3 Selectivities at 300°C for n-Butane Conversion over MVS-Generated Pt/Ni (Al_2O_3) Particles

8-4 n-Butane Conversion Catalysis Results for a Static MVS Sample Produced from $Pt(N_2)_3$

8-5 The Packing Structure, Coordinate System and Filling Order Conventions for the NIO Bimetallic Surface Model

8-6 Possible Configurations for the Four-Atom Ensembles in the NIO Bimetallic Surface Model

8-7 Results from the NIO Bimetallic Surface Model

8-8 Results from the VSRO Bimetallic Surface Model

8-9 Results from the *Fully Segregated* Bimetallic Surface Model

9-1 Pretreatment Reactor / EXAFS Cell Used for Rigorously Anaerobic Sample Handling

9-2 Normalized Pt-L_{III} EXAFS Data Measured at 100 K

9-3 Fourier Transform Amplitude of the Pt-L_{III} EXAFS Data Measured at 100 K

9-4 Normalized Ni-K EXAFS Data Measured at 100 K

9-5 Fourier Transform Amplitude of the Ni-K EXAFS Data Measured at 100 K

9-6 A Structural Detail Model of the MVS-Generated Bimetallic Ni/Pt Particle

CHAPTER I

Introduction

The technique of Metal Vapour Synthesis (MVS) has been shown over the past few years, to yield a wide variety of interesting compounds and new materials formulated via these compounds. With respect to the production of organotransition metal compounds themselves, the MVS method has the advantage of being able to yield preparative scale quantities, whereas other methods such as matrix isolation can only produce microgram amounts of these products. As a direct result of the yield capability, various novel materials may also be generated, such as metal clusters, cluster compounds, films and carrier supported metal particle preparations. Collectively, these materials exhibit many unique properties, which facilitate their application to new technologies which are just beginning to be discovered. In the presently reported research are demonstrated, just a few of the fascinating properties of, and useful applications afforded by MVS generated materials. It was the particular focus of this research, to examine both unimetallic and bimetallic materials prepared by depositing MVS precursor compounds onto commonly used catalyst support materials such as silica and alumina.

Metal Vapour Synthesis involves basically, the generation of metal atom vapour and subsequent deposition of that vapour into a reactant matrix. This matrix may be a solid film of (usually organic) material, or a dynamically mixed liquid, solution or solid/liquid suspension. The various ways of generating the necessary flux of metal atoms include: resistance, inductance, electric arc, and laser furnaces, as well as cathode and magnetron sputtering. Probably the most widely used and versatile method however, is the electron beam type of furnace. The materials which are described here, were produced using this type of atom source. Andrews[1] presents a synopsis of both the technological developments in the design of electron guns for MVS, and a description of the principles of operation of these. The most important developments are the application of reverse polarity[2,3] beam sources (i.e., in which the target metal is maintained at a high positive potential, in order to minimize the destruction of product compounds by spurious ions, energetic secondary electrons and plasma discharges), and the incorporation of liquid nitrogen cooling[2] of the target hearth. This latter development permits the use of MVS with liquid phase reactant systems and refractory metals.

The types of reactors used for MVS can be grouped into two different classes: those which employ a static reaction vessel, and those in which the metal atom deposition occurs into a liquid film produced by the rapid rotation of the reaction vessel. Figures 1-1 and 1-2 show schematic representations of both types of reactor used in the present research.

The preparative-scale static reactor[4,5] (Figure 1-1) was designed to operate over the extended temperature range of 10 to 300 K. In this reactor, a film of solid substrate (this may be condensed from either a pure reactant liquid or vapour, or a solution of the reactant in an inert solvent) was deposited onto the inside surface of the cryogenically cooled cup, together with the metal atom flux. This is termed the cocondensation method. After rotating the cup assembly upward, reaction products were collected by controlled warming of the substrate beyond its point of fusion. The secondary reaction which yielded the oxide-supported materials was carried out by adding the oxide powder to the MVS precursor contained in the upright cup assembly. A means was available whereby ambient air was excluded from the reaction vessel.

In the rotary reactor (Figure 1-2), a film of liquid was maintained by spinning the spherical glass vessel. The atom flux was deposited into the film at the top of the reactor. The rotary reactor can also operate in the cocondensation mode if the reactant is vaporized together with the atom flux, and the products are deposited as a solid film on the reactor wall. For this purpose, a temperature controlled cannulator was included in the reactor design. Alternatively, the rotary reactor can be used for solution phase MVS preparations. In this method, the reactant and a liquid solvent are admitted together into the reactor during atom flux deposition. The products collected in the liquid film during the various syntheses which were carried out. The rotating vessel was immersed in a cooling bath in order to reduce the solvent vapour pressure sufficiently so that the electron gun was able to be operated. After the syntheses, the product containing solutions were transferred from the reactor via a collection tube, and were subsequently contacted with the catalyst support oxides. The design shown in the figure also includes the capability of maintaining sub-ambient temperatures and atmosphere isolation of the product during removal from the reactor and further handling.

Although both cocondensation MVS and solution phase MVS methodologies may be expected to produce the same supported cluster materials from a given atom/reactant system, this has been demonstrated not to be the case. Major differences lie within the diffusion and agglomeration kinetics during deposition and subsequent warm-up, and how they are affected by solid versus liquid phase media.

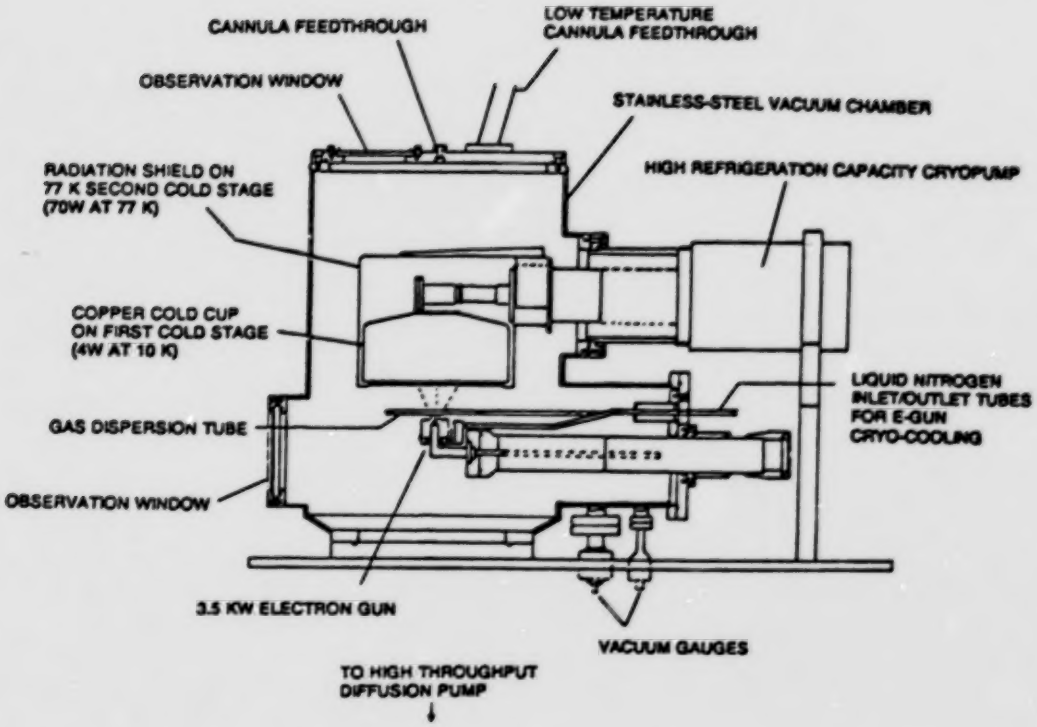

Figure 1-1 Design of the Static Reactor used for Metal Vapour Synthesis

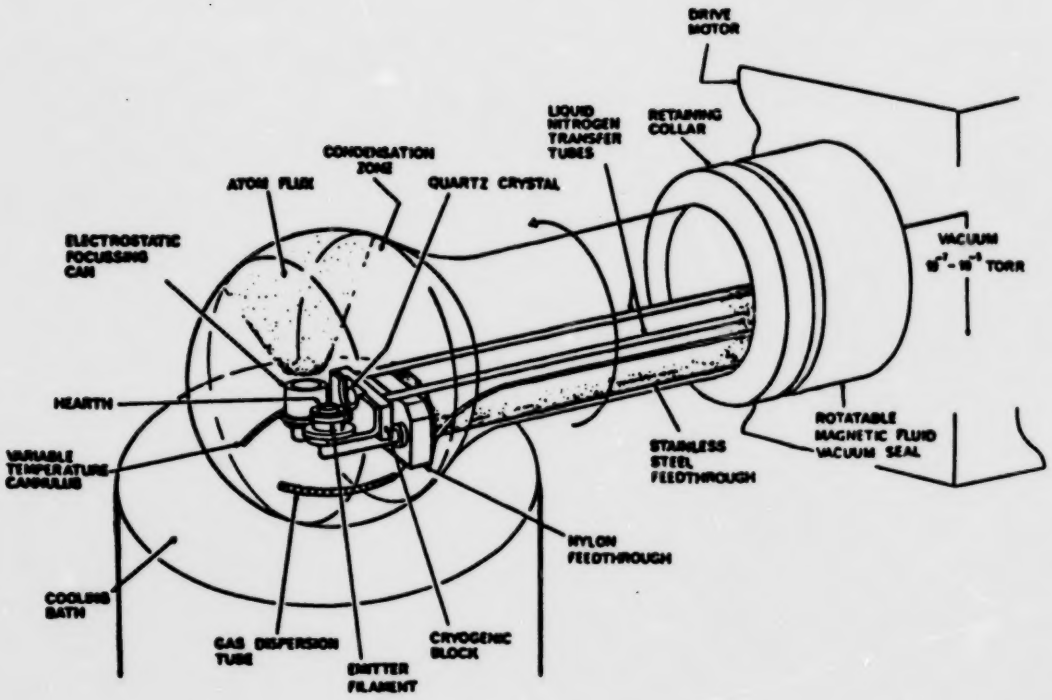

Figure 2-2 Design of the Rotary Reactor used for Solution Phase Metal Vapour Synthesis

Beyond the synthesis of MVS generated materials, it was of key interest to the presently reported research project to characterize the products as extensively as possible. In order to make best use of the available techniques for this purpose, two bimetallic systems were chosen for the study: Iron-Ruthenium and Nickel-Platinum, along with the series of related unimetallic preparations of all of these metals. The characterization techniques which have been used to acquire knowledge about these materials include:

- Bulk elemental analysis techniques such as Plasma Excitation and Neutron Activation Analyses.
- Conventional and Scanning Transmission Electron Microscopy (CTEM and STEM).
- Energy Dispersive X-ray Analysis (EDAX) coupled with STEM.
- X-ray Photoelectron (XPS) Spectroscopy.
- Magnetic characterization methods such as Ferromagnetic Resonance Spectroscopy (FMR), Electron Paramagnetic Resonance Spectroscopy (EPR), and Conduction Electron Spin Resonance Spectroscopy (CESR).
- Ultraviolet-Visible Absorption Spectroscopy (UVS).
- Fourier Transform Infrared (FTIR) Spectroscopy using carbon monoxide as an adsorbed probe molecule.
- Chemisorption, along with associated calorimetric measurements.
- Catalytic Testing, using the conversion of n-butane in a reducing (diluted hydrogen) atmosphere, as a probe reaction.
- Extended X-ray Absorption Fine Structure (EXAFS) Spectroscopy.

CHAPTER II

Synthesis of MVS Materials

2.1 Experimental Details

The materials dealt with in the presently reported research were silica and alumina supported clusters of iron, ruthenium and iron/ruthenium bimetallics, as well as nickel, platinum and nickel/platinum bimetallics. Most of these were produced through the use of liquid phase MVS to synthesize bis-toluene and tris-ethylene metal(0) organometallic precursors (in methylcyclohexane and toluene solutions), which were subsequently reacted with the high temperature vacuum pretreated oxide carriers. A few alumina-supported platinum samples were also produced in the preparative scale static reactor; these involved organometallic precursors which were synthesized in pure liquid cryogens (CO, N_2 and C_2H_4). All of the resulting materials were handled entirely in the absence of ambient air.

The reaction which leads to the final supported cluster products is believed to proceed[4] through the decomposition of the organometallic precursors by the OH groups found on the oxide surfaces. Once this first step has occurred, further precursors decompose at the site of the initial reactions; thus, nucleation continues until clusters of metal atoms have agglomerated on the carrier surface. It is important to note here that the tris-ethylene metal(0) compounds were chosen because of the similarity in decomposition temperature[5] of both the nickel and platinum compounds (which is about 273 K). Similarly, bis-toluene iron(0) and bis-toluene ruthenium(0) both decompose[6] at about 243 K. This will be demonstrated to be crucial in order to produce truly *bimetallic* clusters on a surface. It has been found that co-impregnation of mixed Fe and Ru cluster carbonyls[7] for example, yields only mixtures of highly dispersed unimetallic particles. This occurs because of the dissimilarity in decomposition temperature of such compounds.

2.1.1 Preparation of Reagents for MVS Reactions

Before proceeding with the actual metal vapour synthesis reaction, certain steps were required in order to prepare the solvent and the oxide support materials.

The solvents used were supplied as spectroscopic purity reagents, and were further pretreated by distillation and drying. Some of the preparations were conducted using solvents which were rigorously dried over metallic sodium, using benzophenone as an indicator. In other preparations, the solvents were dried over silica gel; comparison of resulting materials obtained through both solvent drying procedures, using all of the characterization methods available, showed no discernable differences in their properties. Before being used in the MVS reactions, the solvents were also subjected to freeze degassing. In this step, each solvent sample was cooled by immersing its container in liquid nitrogen, then removing the more volatile dissolved gases under vacuum. Degassing was required in order that during the metal vapour synthesis, the pressure in the reactor would be sufficiently low to permit operation of the electron gun, as well as to minimize extraneous oxidation processes.

The oxide support materials (silica and alumina samples) were also pretreated before use in all of the synthesis experiments. In the first stage of this treatment, large batches of material were calcined in flowing air at about 300°C for 5.0 hours. The quantities of material so treated were usually sufficient for several synthesis experiments; these were stored in airtight containers. The second stage of oxide pretreatment was carried out just prior to each synthesis run. In this stage, a pre-weighed quantity of oxide material (from the calcined stock) was placed into a quartz vacuum dehydration vessel as shown in Figure 2-1. The charge for typical syntheses was 4.0 to 10.0 g depending on the intended metal loading in the final product. The vessel was placed in a furnace capable of operating up to a maximum temperature of 800°C. The dehydration was carried out under vacuum pumping for 3.0 h, and typically reached a pressure of less than 100 mtorr by the end of the procedure. Most of the MVS materials were prepared on support surfaces which had been pretreated at either 200°C or 600°C, although some 400°C and 800°C preparations were also used. After being cooled to 25°C, the oxide samples were transferred under flowing dry argon into the vessel shown in Figure 2-2, and stored there until the organic precursor had been synthesized in the MVS reactor. For materials like SiO_2 and Al_2O_3, these combined pretreatments afford a means of controlling the surface hydroxyl concentration. It has been demonstrated by this research that this is a crucial parameter affecting both the particle size distribution of the metal clusters created on these surfaces, and their catalytic, electronic and other physicochemical properties.

2.1.2 The Metal Vapour Synthesis Reaction

In the present work, the MVS reaction and experimental conditions can best be described by example: in this case, the solution phase synthesis of tris-ethylene metal(0) complexes using methyl-

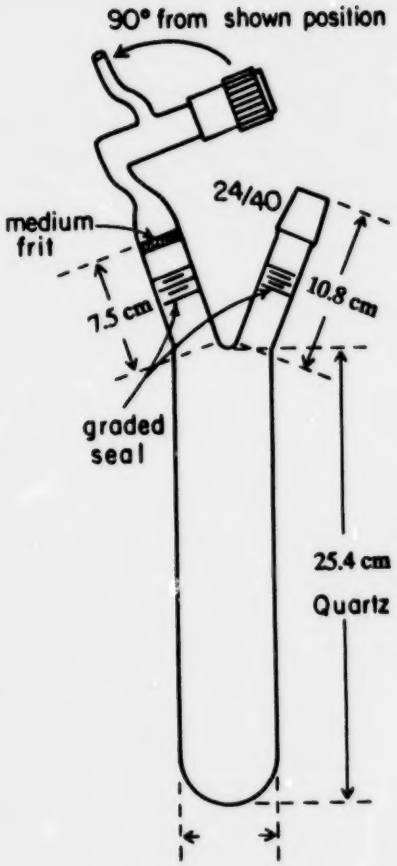

Figure 2-1 Quartz Vessel for Vacuum Pretreatment of Support Material

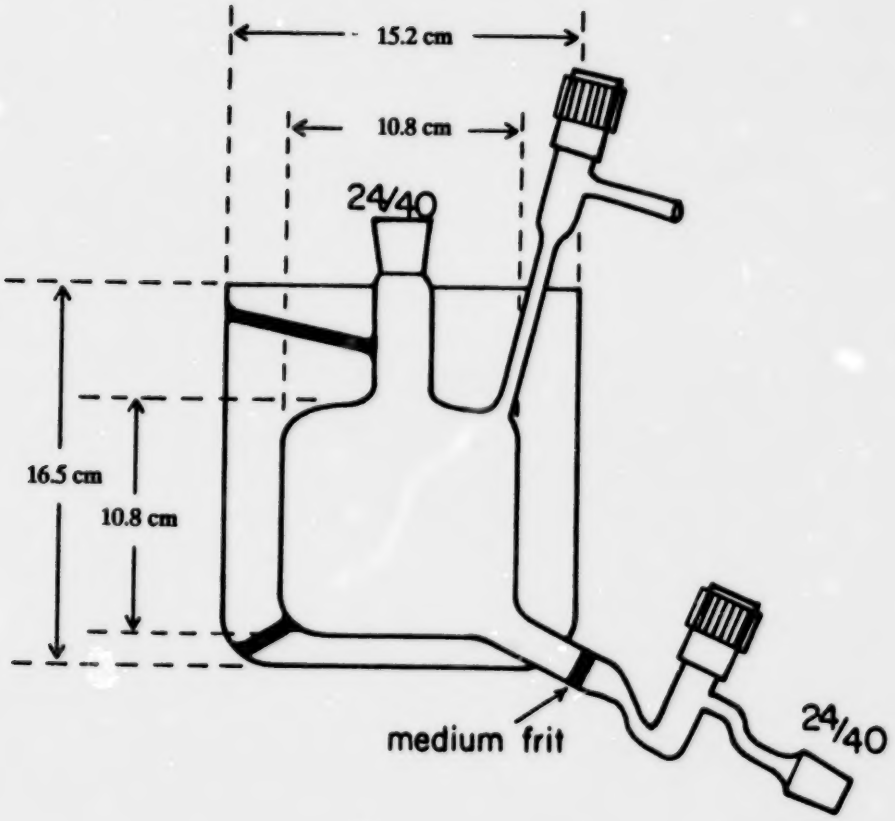

Figure 2-2 Low Temperature Anaerobic Vessel for Impregnation of Support Materials

cyclohexane as the solvent. In the present research, both Nickel and Platinum have been used with this reactant/solvent system.

In addition to the materials preparation procedures outlined above, there were some essential setup procedures which were carried out before the reaction was allowed to begin. First of all, each of the electron guns in the reaction vessel was equipped with an electron emitting filament. For this purpose, a length of 24 gauge thoriated tungsten wire (1% ThO_2 / 99% W) was formed into two hemicircular parts and clamped into place as shown in Figure 2-3. The height of the loop was adjusted so that a direct line of sight from the filament to the target metal was avoided; this was required in order that the emitted electrons could be properly focussed by the electrostatic screen (also shown in the figure). After the pre-weighed metal samples were placed in the centres of each of the target hearths, the focussing screens were put into place, and the height of each was adjusted so that the electron beam would remain focussed on the metal target throughout the synthesis run. The required position was such that the top surface of the piece of sample metal was located 4.5 to 5.5 mm below the top of the screen assembly. Before mounting the glass vessel onto the rotating seal gasket, it was necessary to ensure that the electrical leads which supply high voltage to the various parts of the electron gun assembly were separated well enough that during the run, arcing did not occur. Whenever a run was being conducted using only one kind of metal, both guns were charged with metal samples. This afforded the advantage that if one gun should fail for any reason, the second could be used to complete the run.

Once the glass vessel had been secured in place, it was tightened while rotating and with rough vacuum pumping in progress (this ensured a good seal by freeing gases which may sometimes be trapped in the vacuum sealing grease). Pumping was further continued with a 2300 $L \cdot s^{-1}$ diffusion pump, until a pressure of approximately 1×10^{-7} torr had been achieved. This served as a means of ensuring the absence of leaks, since it was well below the reaction operating pressure of ca. 2×10^{-5} torr.

Just prior to starting the reaction, the rotating vessel was cooled by raising a liquid nitrogen (or other) refrigeration bath into place around the bottom of the assembly. The level of liquid in the bath was maintained constant throughout the reaction. The electron gun was next energized (even in the case of bimetallic syntheses, the guns were used one at a time). The choice of focussing voltage and filament current were entirely dependent on the choice of metal being vapourized, and were determined by trial and error during preliminary experiments. The major criterion which establishes the optimum setting is to have a metal vapourization rate which will not cause the pressure inside the reactor to exceed about 3

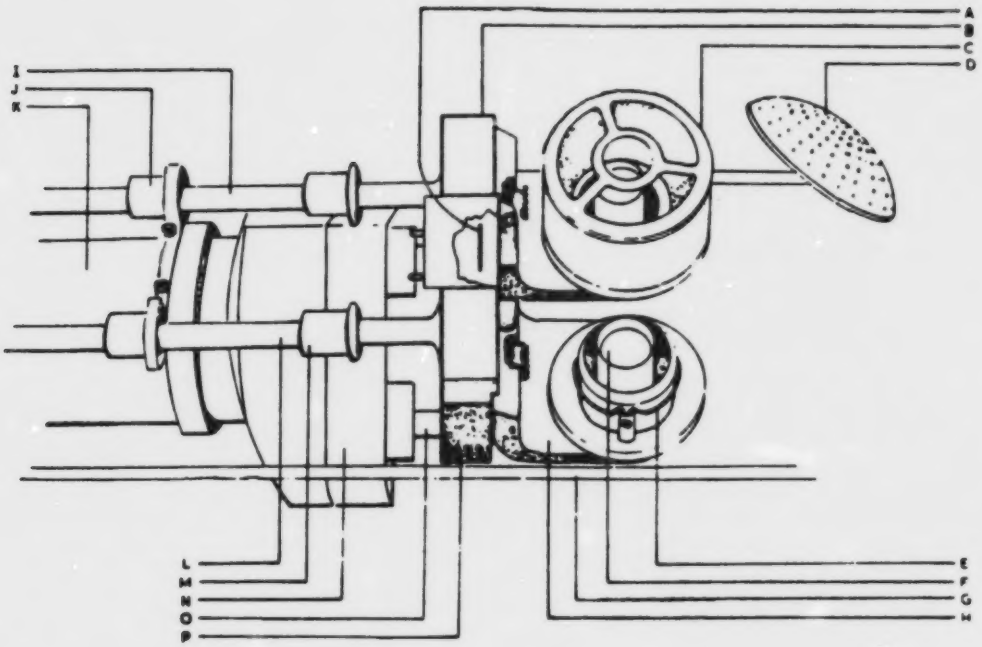

I. Liquid Nitrogen Transfer Tube
J. Teflon Collar for (I)
K. E-gun Support / Housing for Conduits
L. Liquid Nitrogen Outlet Tube
M. Teflon Collar
N. Nylon Flange
O. Cooling Water & Electrical Connection
P. Copper Cooling Block

A. Quartz Crystal Microbalance
B. Liquid Nitrogen Cooled Copper Block
C. Electrostatic Focusing Shield
D. Heated Ligand Inlet
E. Electron Emitting Filament
F. Target Metal Hearth
G. Product Removal Cannulus
H. Adjustable Support for Focussing Shield

Figure 2-3 Design of the Dual Electron Gun used in the Rotary MVS Reactor

x 10^{-5} torr (otherwise the electron gun's safety mechanism will cause it to shut off). In the case of nickel for example, the focussing voltage was usually about 2.6 kV, and the filament current was about 65 mA.

Immediately upon commencement of metal vapourization, both the reactant ethylene and solvent methylcyclohexane flows into the reactor were begun. Their flowrates were controlled by means of two needle valves and were adjusted such that the pressure remained between 1.0 x 10^{-5} and 2.0 x 10^{-5} torr; the amount of solvent was supplied in great excess with respect to the reactant. During the deposition, the total mass of metal vapourized was monitored (approximately) by using a quartz crystal detector equipped with an oscillator and frequency counter. By having the frequency calibrated with respect to the mass of metal which has condensed on it, the detector provided a means of controlling the metal vapourization rate. Unfortunately it cannot always be ensured that the flux of metal atoms condensing on the crystal surface, and that entering the reactant matrix are the same. As a result, an accurate value of the mass of metal vapourized was determined after the synthesis run, by weighing the metal sample and subtracting the weight from the initial sample weight. Metal atom deposition for this system was usually carried out for a period of two to three hours; this was sufficient for example, to provide a metal loading of about 2 wt% for Ni on 10.0 g of alumina support.

Once the required metal deposition was completed, the electron gun, reactant and solvent flows and rotation of the reactor were suut off, the refrigeration bath was removed from the reactor assembly, and the products were drawn from the reactor into a collection vessel (shown in Figure 2-4). In order to do this, the reaction vessel was brought to atmospheric pressure under argon, while the collection vessel was evacuated. During the transfer, the double walled tube leading from the bottom of the reaction flask was maintained sufficiently cool that the organometallic precursor material just synthesized did not decompose. Cooling of the transfer tube was achieved by passing a stream of N_2 gas through a liquid nitrogen heat exchange bath and then between the inner and outer walls of the transfer tube. By adjusting the gas flowrate, the temperature could be varied; a thermocouple and readout also allowed it to be monitored.

2.1.3 Support Impregnation Procedure

The glass vessels (Figures 2-4 and 2-2) used for collection of the precursor and contact of the precursor and oxide support materials respectively were both cooled by placing solid CO_2 and acetone in the outer chambers.

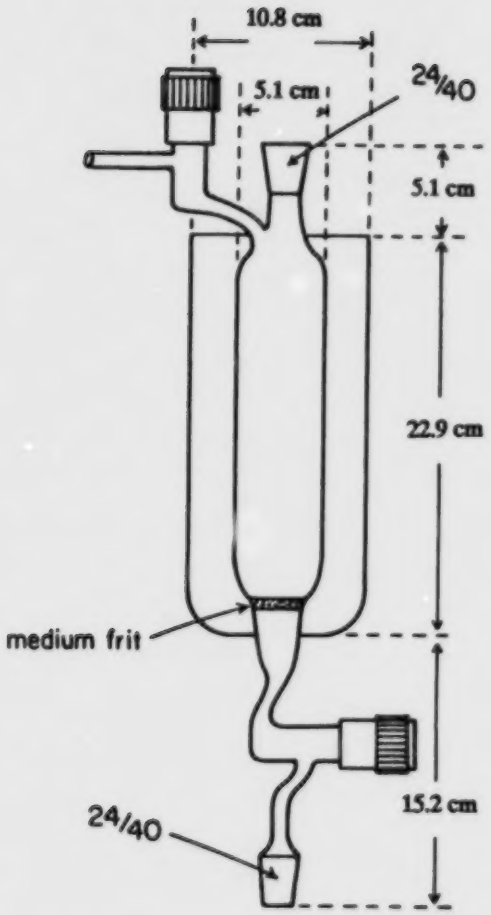

Figure 2-4 Collection and Filtering Vessel for MVS Reaction Products

The final step in the synthesis of supported metal cluster materials involved anaerobically placing the precursor solution into the oxide-containing vessel, magnetically stirring while maintaining the dry ice bath for 5.0 h, and finally allowing the material to warm to room temperature overnight. Subsequent to this, the excess liquid solvent was removed, first by drawing it through the fritted glass filter which retained the powder sample, and finally by vacuum pumping (at room temperature) until the pressure inside the vessel fell below 1.0×10^{-1} torr. The dry powder was then ready for storage. The glass vessel shown in Figure 2-5 provided the means by which small ampoules containing about 1.0 g of material each were sealed off and stored for future testing.

In the case of the Ru and Fe syntheses, in which toluene was used both as the reactant and the solvent, the flowrate of this substance during the reaction was such that there was a great excess with respect to molar metal deposition rate. The only other difference in experimental treatment between these two systems, was that the toluene runs were carried out at about -105°C, by using a pentane bath cooled by pumping liquid nitrogen through a heat exchange coil.

2.2 List of All Samples Produced

Table 2-1 lists all of the MVS generated, supported metal cluster material samples which have been synthesized. These are identified by serial numbers of the form EMR-N y, where the number N denotes the MVS run (and in cases where more than one support pretreatment was used, y denotes the letters a,b,c etc. which identify the support pretreatment temperature). The metal type(s), support type and nominal metal loading are given, as well as the characterization tests which have been employed in order to examine the material.

2.3 Bulk Elemental Analyses

The metal loading values reported in Section 2.2 are actually nominal values. This results, not only from the fact that the mass of support material (which is weighed before the vacuum pretreatment) changes, but that a substantial fraction of the metal which is vapourized is not incorporated into the final supported cluster material. From experience, the nominal loadings are calculated using the assumption that the efficiency with respect to metal incorporation (versus that vapourized) is 0.75. Because of this, bulk elemental analyses were carried out in order to determine somewhat more reliable estimates of the metal content of MVS products.

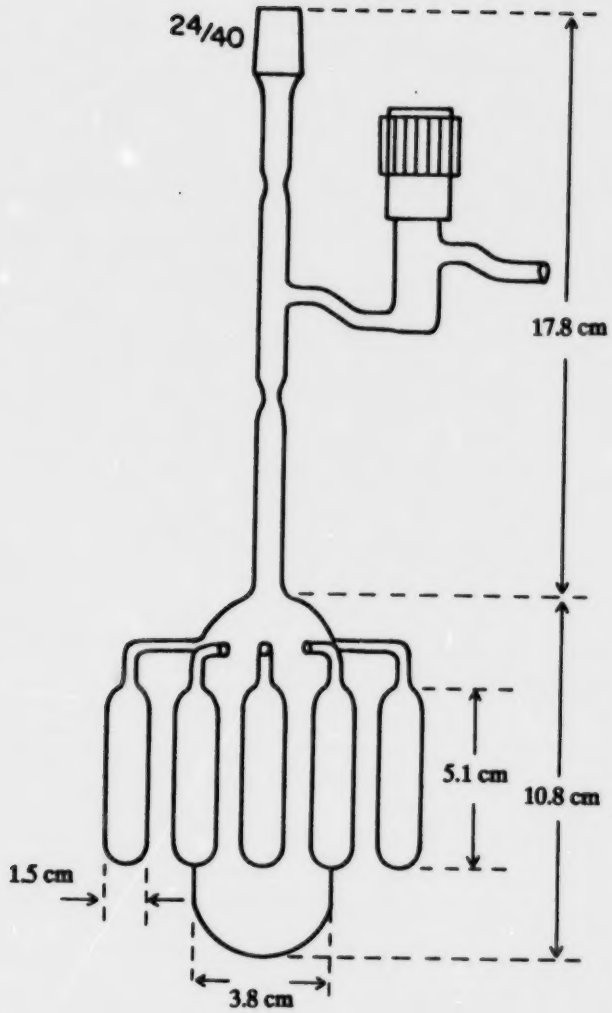

Figure 2-5 Glass Manifold for Transfer of Supported-Metal Cluster Sample to Sealed Ampoules

Table 2-1 List of All MVS Materials and Characterization Tests Made

SAMPLE	METAL A	METAL B	FRACTION METAL A	METAL LOADING (wt%)	SUPPORT (SLVNT)	VAC PRTMT (°C)	CHARACTERIZATION TESTS PERFORMED													
							CAT	CHZ	SEM	TEM	EDX	FMR	EPR	CSR	XPS	AUG	FIR	MIR	UVS	NAA	PEA
EMR-1 a	Ru		1.0000	2.0	A (TOL)	250									•						
EMR-1 b	Ru	Fe	0.6260	2.0	A (TOL)	250						•	•		•						
EMR-2 a	Fe		1.0000	0.7	A (TOL)	250						•	•		•						
EMR-2 b	Ru	Fe	0.6680	0.3	A (TOL)	250									•						
EMR-3 a	Fe		1.0000	0.5	A (TOL)	250						•	•		•						
EMR-3 b	Ru	Fe	0.7400	1.7	A (TOL)	250	•		•	•	•				•						
EMR-4	Fe		1.0000	1.5	A (TOL)	250	•		•			•	•		•						
EMR-5	Ru	Fe	0.5940	5.2	A (TOL)	250	•		•	•	•	•	•		•						
EMR-6	Ru		1.0000	3.2	A (TOL)	250	•			•	•	•	•		•						
EMR-7	Pt		1.0000	1.0	A (TOL)	250									•						
EMR-8	Pt		1.0000	1.4	M (TOL)	250			•												
EMR-9	Pt		1.0000	0.6	M (TOL)	250															
EMR-10 a	Pt		1.0000	1.3	M (TOL)	250															
EMR-10 b	Pt		1.0000	1.3	M-(TOL)	600															
EMR-11 a	Fe		1.0000	3.5	M (TOL)	250	•														
EMR-11 b	Fe		1.0000	3.5	M (TOL)	450	•														

CAT - Catalysis
CHZ - Chemisorption
SEM - Scanning Electron Microscopy
TEM - Transmission Electron Microscopy
EDX - Energy Dispersive X-ray Analysis

FMR - Ferromagnetic Resonance Spectroscopy
EPR - Electron Paramagnetic Resonance Spec.
CSR - Conduction Electron Spin Resonance Spec.
XPS - X-ray Photoelectron Spectroscopy
AUG - Auger Electron Spectroscopy

FIR - Far Infrared Spectroscopy
MIR - Mid Infrared Spectroscopy
UVS - Ultraviolet/Visible Spectroscopy
NAA - Neutron Activation Elemental Analysis
PEA - Plasma Emission Elemental Analysis

A - Alumina
S - Silica
M - Mixed Alumina/Silica

TOL - Toluene
MCH - Methylcyclohexane
THF - Tetrahydrofuran
PRY - Propylene

SAMPLE	METAL A	METAL B	FRACTION METAL A	METAL LOADING (wt%)	SUPPORT (SLVNT)	VAC PRTMT (°C)	CHARACTERIZATION TESTS PERFORMED														
							CAT	CHZ	SEM	TEN	EDX	FMR	EPR	CSR	XPS	AUG	FIR	MIR	UVS	NAA	PEA
EMR-12	Pt		1.0000	3.7	M (TOL)	250			•	•	•	•			•					•	
EMR-13	Pt		1.0000	10.8	M (TOL)	250			•			•								•	
EMR-14	Pt		1.0000	4.5	M (TOL)	250			•						•					•	
EMR-15	Pt		1.0000	5.2	M (THF)	250			•											•	
EMR-16	Pt		1.0000	3.4	M (PRY)	250			•											•	
EMR-17	Pt		1.0000	1.5	M (MCH)	250			•											•	
EMR-18 a	Pt		1.0000	0.6	M (MCH)	250															
EMR-18 b	Pt		1.0000	1.2	M (MCH)	500															
EMR-19 a	Ni		1.0000	1.7	S (MCH)	200	•		•	•		•	•		•					•	•
EMR-19 b	Ni		1.0000	2.0	S (MCH)	400			•	•		•	•		•					•	•
EMR-19 c	Ni		1.0000	1.7	S (MCH)	600	•		•	•		•	•		•					•	•
EMR-19 d	Ni		1.0000	2.0	S (MCH)	725	•		•	•		•	•		•					•	•
EMR-20 a	Pt		1.0000	2.2	S (MCH)	200	•	•	•	•		•	•		•				•	•	
EMR-20 b	Pt		1.0000	1.6	S (MCH)	400			•	•		•	•		•					•	
EMR-20 c	Pt		1.0000	1.7	S (MCH)	600	•		•	•		•	•		•					•	
EMR-20 d	Pt		1.0000	1.8	S (MCH)	800	•		•	•					•					•	

Table 2-1 Continued

SAMPLE	METAL A	METAL B	FRACTION METAL A	METAL LOADING (wt%)	SUPPORT (SLVNT)	VAC PRTMT (°C)	CHARACTERIZATION TESTS PERFORMED													
							CAT	CHZ	SEM	TEM	EDX	FMR	EPR	CSR	XPS	AUG	FIR	NIR	UVS	NAA	PEA
EMR-21 a	Fe		1.0000	3.9	A (TOL)	200	•		•			•								
EMR-21 b	Fe		1.0000	3.9	A (TOL)	600	•		•			•								
EMR-22 a	Ni		1.0000	2.0	A (MCH)	200	•			•		•			•					•	•
EMR-22 b	Ni		1.0000	2.0	A (MCH)	800	•			•		•	•		•					•	•
EMR-23 a	Pt		1.0000	3.0	A (MCH)	200	•			•	•				•					•	•
EMR-23 b	Pt		1.0000	3.1	A (MCH)	600	•			•	•				•					•	•
EMR-24 a	Pt	Ni	0.4400	2.8	A (MCH)	200	•			•					•					•	•
EMR-24 b	Pt	Ni	0.4400	3.0	A (MCH)	600	•			•					•					•	•
EMR-25 a	Pt	Ni	0.1667	1.4	A (MCH)	200	•			•					•					•	•
EMR-25 b	Pt	Ni	0.1667	1.5	A (MCH)	600	•			•					•					•	•
EMR-26 a	Pt	Ni	0.0476	1.8	A (MCH)	200	•														
EMR-26 b	Pt	Ni	0.0476	1.8	A (MCH)	600	•														
EMR-27 a	Pt	Ni	0.5000	2.0	A (MCH)	200	•			•	•									•	•
EMR-27 b	Pt	Ni	0.5000	2.0	A (MCH)	600	•			•	•									•	•
EMR-28 a	Pt	Ni	0.7500	3.4	A (MCH)	200	•			•	•									•	•
EMR-28 b	Pt	Ni	0.7500	3.9	A (MCH)	600	•			•	•									•	•
EMR-29 a	Pt		1.0000	1.4	S (MCH)	200				•								•	•	•	•
EMR-29 b	Pt		1.0000	2.4	S (MCH)	400				•								•		•	•
EMR-29 c	Pt		1.0000	2.2	S (MCH)	600				•								•		•	•
EMR-29 d	Pt		1.0000	2.4	S (MCH)	780				•										•	•

Table 2-1 Continued

In the present research, there were two methods (although others had been unsuccessfully attempted) which have been used to analyze some of the unimetallic Ni, Pt and Ni/Pt bimetallic samples. The first was a neutron activation technique, conducted at the Mining and Metallurgy Department, University of Toronto; the second was a plasma emission spectroscopic (PES) technique, conducted at the Department of Chemical Engineering, at the University of Waterloo. Both of these methods have been found to be in acceptable agreement with each other, and with the reported nominal metal content values of the samples tested.

The neutron activation method involves a primary irradiation of the sample by energetic neutrons from a Slowpoke™ reactor. This excites a radiative decay of the element sought in the sample. By calibrating the scintillation rate against that emanating from a standard of the same element and having known concentration, the fraction of metal in the sample being analyzed can be determined. This technique has the advantage that it is nondestructive (although the sample containers which were used, did require that the sample be air exposed). One disadvantage encountered when dealing with the bimetallic samples containing both Ni and Pt, was that the neutron activation excited both elements; the Pt decay had a much shorter half-life, so that the Ni concentration could be measured, provided that sufficient time was allowed until the Pt background signal had fallen to an acceptable level. This required 72 hours. Unfortunately, after this time there had been some loss in sensitivity for detection of the nickel scintillation signal above that of the background radiation signal. In using the same procedure for Pt determination, the measurement can be taken sooner, thus resulting in greater sensitivity for this element.

The PES technique (which incidentally has better sensitivity for quantitative determination of nickel), used an argon plasma excitation source into which solutions containing the analyte were injected directly. The induced atomic emission of each element has a characteristic set of spectral lines. Therefore, by examining the spectrum for a sample containing many elements, a qualitative analysis may be performed; or by measuring the intensity of the line corresponding to a particular element, a quantification of that element may be obtained. Once again, the measured intensities were compared against calibration standards. The advantages afforded by this technique, are that for most elements, the measured emission intensity is linear with respect to concentration over a dynamic range of nearly three orders of magnitude, and that concentrations of only a few parts per million can be easily measured. Also, interferences between elements in bimetallic samples are uncommon for most pairs of metals (and do neither affect the Ni/Pt nor the Fe/Ru systems).

Sample preparation required the complete dissolution of a known mass of material which was to be analyzed, and dilution to within the linear concentration range of the PES spectrometer. For this purpose, 10 ml of a solution of six parts (by volume) of HF, four parts HNO_3 and one part $HClO_4$ was used. In some cases, a second addition of 10 ml of aqua regia and/or warming to 60°C was also required to complete the digestion of the metal. Dilution was accomplished using 100.0 ml of a 50.00 $g \cdot L^{-1}$ H_3BO_3 solution and the necessary further quantity of distilled water. The same dissolution procedure was used for the standards, in which known masses of pure metals were digested.

Table 2-2 lists the results for several analyses of nickel, platinum and Ni/Pt bimetallic MVS materials. For all of these, the plasma emission and neutron activation analysis values are compared with the nominal metal contents as determined from the weight of vapourized metal.

The agreement between the results obtained under both techniques was within 10 % in several cases, although some large discrepancies were observed as well. A particular example of such is the Ni analysis of sample EMR-22, in which the PES value was in good agreement with the nominal nickel content, but the neutron activation measurement yielded a much lower value. At the present time the reason for the discrepancy is not clear; obviously the somewhat lower detection sensitivity of the neutron activation technique with respect to nickel is not sufficient to provide an explanation.

A feature which is apparent, is that results from both bulk analysis techniques were consistently lower than the calculated nominal content values. The trend is also more pronounced for samples which have higher metal loadings. It is probably the case that for this system, the estimate of 75% deposition efficiency was somewhat high. Furthermore, this efficiency seems to decrease as the total mass of metal vapourized in the synthesis run increases.

SAMPLE	SUPPORT	LOADING BY WEIGHT NICKEL ANALYSIS		
		Nominal Value	Plasma Emission	Neutron Actvation
EMR-19a	Silica	1.7	0.84	0.60
EMR-19b	Silica	2.0	0.98	0.67
EMR-19c	Silica	1.7	0.91	0.63
EMR-19d	Silica	2.0	0.94	0.66
EMR-22a	Alumina	2.0	1.67	0.59
EMR-22b	Alumina	2.0	1.67	0.44
EMR-24a	Alumina	0.7	0.60	0.38
EMR-24b	Alumina	0.8	0.72	0.36
EMR-25a	Alumina	0.8	0.60 (0.59)	0.40
EMR-25b	Alumina	0.9	0.18	0.38
EMR-27a	Alumina	0.5	0.30	0.24
EMR-27b	Alumina	0.5	0.47	0.34
EMR-28a	Alumina	0.3	0.30	0.07

SAMPLE	SUPPORT	LOADING BY WEIGHT PLATINUM ANALYSIS		
		Nominal Value	Plasma Emission	Neutron Actvation
EMR-29a	Silica	1.4	1.21	1.3
EMR-29b	Silica	2.4	1.83	1.7
EMR-29c	Silica	2.2	1.72	1.6
EMR-29d	Silica	2.4	1.79	1.7
EMR-24a	Alumina	2.0	1.28	1.1
EMR-24b	Alumina	2.2	1.28	1.7
EMR-25a	Alumina	0.6	0.5 (0.4)	0.4
EMR-25b	Alumina	0.7	-	0.4
EMR-27a	Alumina	1.5	1.20	0.8
EMR-27b	Alumina	1.5	1.23	1.4
EMR-28a	Alumina	3.1	2.80	1.7
EMR-28b	Alumina	3.5	-	2.3

Table 2-2 Bulk Elemental Analysis Results

CHAPTER III

Electron Microscopy Studies

In this study, there were two types of electron microscopy techniques employed to analyze MVS materials. Conventional Transmission Electron Microscopy (CTEM) gave the greatest spatial resolution in its imaging capability, while Scanning Transmission Electron Microscopy (STEM), although having somewhat lower resolution, was coupled with the technique of Energy Dispersive X-ray analysis (EDAX) in order to permit elemental analyses of surface domains using 1.0 nm by 1.0 nm resolution (maximum). The CTEM facility was located in the Medical Sciences Department at the University of Toronto, and the STEM-EDAX facility was located at the Institut de Recherches sur la Catalyse, C.N.R.S., Lyon, France.

A concise description of both CTEM and STEM principles of operation is presented by Delannay[8], and Gallezot[9] who also give details of the sample preparation techniques applicable to these studies.

3.1 CTEM Study of Particle Size Distributions

One of the key features of interest of MVS-generated supported metal particles, and in fact all highly dispersed supported metal catalysts however synthesized, is the nature of their particle size distributions. This concerns the sizes, variance among the sizes, shape and variance among the shapes of such particles. Through the application of electron microscopy, one can derive a wealth of information on the subject.

In the present study, the unimetallic Ni, Pt and Ni/Pt bimetallic system was selected; a systematic investigation was undertaken in order to examine many of the factors in the synthesis and treatment of these materials which govern the resulting nature of the particle size distributions. Among the parameters considered were:

- The pretreatment temperature (hence surface OH concentration) of the support material.
- The effect of trace water levels in the MVS solvent and reagents.
- The differences between silica and alumina as support materials.
- The effect of incorporating two metals as in the bimetallic samples.
- Changes induced by thermal treatments, oxidizing treatments, and use of the materials as catalysts

3.1.2 Analysis of CTEM Data

Transmission electron microscopy allows a sort of direct observation of supported metal particles on a catalyst surface. Although CTEM micrographs present a two-dimensional representation of what is, in reality a three-dimensional system, it is possible to measure the dimensions of a great number of individual particles on the support surface. Typically, for very small metal particles which appear to have spherical geometry (their two dimensional projections are *round*), one reports a diameter as the characteristic which is used to classify the various particles observed in a particular sample. This is not an ideal situation, insofar as such particles are not really spherical; it is the limited resolution of the TEM technique which produces the appearance of sphericity. One will generally accept this approximation however, since no more suitable characteristic is available.

For a given catalyst sample which exhibits a range of particle sizes, it is most convenient to apply statistical techniques in order to describe its nature. Normally, a population may be classified by two parameters: namely some form of average or mean value, and a measure of the breadth of the distribution. The most commonly used approach is to observe a sufficiently large and representative number of discrete metal particles. Following this, one calculates the mean and standard deviation of particle sizes for the entire population, as estimated by such observation.

The presentation of data begins by classifying the particle sizes into N evenly spaced intervals, and noting the number of particles counted within each range (eg. , 0.5-1.0, 1.0-1.5 nm, etc.). In this way, the observations can easily be depicted in the form of histograms.

The best developed method for extracting estimates of the two parameters used in characterizing the PSD of the metal particles, involves the use of the statistical Normal Distribution[8]. If it is

justifiable to assume that the individual particle diameters are randomly drawn from some normally distributed population, then the mean $< d_n >$ of such a population is estimated by:

$$< d_n > = \frac{\sum_{i=1}^{N} n_i d_i}{\sum_{i=1}^{N} n_i} \qquad [3.1]$$

where n_i is the number of particles having diameter d_i (which is the midpoint of the ith size interval), and the summation is carried out over all observed intervals from $i = 1$ to N (with N being the total number of size intervals).

Similarly, the standard deviation, which is a measure of the breadth of the distribution may be estimated by:

$$s_n^2 = \left[\frac{\sum_{i=1}^{N} n_i \left[d_i - < d_n > \right]^2}{\sum_{i=1}^{N} n_i} \right] \qquad [3.2]$$

One may also report the "area average" particle size. This is given by the following:

$$< d_s > = \frac{\sum_{i=1}^{N} n_i d_i^3}{\sum_{i=1}^{N} n_i d_i^2} \qquad [3.3]$$

where n_i and d_i are defined as in [3.1] and [3.2]. This representation, when presented in the form of a histogram displays the fraction of the total surface area possessed by the particles whose diameters fall within each of the size intervals. It is important to note that an implicit assumption of spherical geometry is contained within [3.3].

In a similar manner, the "volume average" is given by:

$$< d_v > = \frac{\sum_{i=1}^{N} n_i d_i^4}{\sum_{i=1}^{N} n_i d_i^3} \qquad [3.4]$$

for which the histogram representation shows the fraction of the total metal volume which is occupied by all of the particles whose diameters are within the ith size class.

The population distributions whose means are estimated by each of [3.1], [3.3] and [3.4] have slightly differing estimates of their standard deviations, which may be calculated using:

$$\frac{s_n}{<d_n>} = \frac{s_s}{<d_s>} = \frac{s_v}{<d_v>} \qquad [3.5]$$

The main reason for having three different bases for representing particle size distributions is to allow for comparisons with other experimental techniques[8,11]; in chemisorption measurements for example, the area basis PSD is determined, and in FMR measurements, it is the volume basis PSD which is obtained directly. It is possible to interconvert between these representations, but in so doing one must always make an assumption about the particle geometry (eg. cubic, hemispherical, etc.).

Another frequently reported parameter which is intended to describe the nature of supported metal catalysts, is the dispersion. This may be defined as the fraction of active atoms (i.e. the metal) which is exposed on the catalyst surface. In the extreme limit that every metal atom is a surface atom, the dispersion has a value of unity. It is possible to achieve this in real catalytic systems, especially in the case of MVS generated specimens in which the metal particles typically have diameters smaller than 1.5 nm. As particle sizes increase, the dispersion decreases; for spherical particles, the dispersion is inversely proportional to the particle diameter. One can clearly see that even for catalyst particles which are still considered to be small according to conventional standards (eg. 10 nm), that very few of the metal atoms present are actually catalytically useful.

In practice, one cannot *count* the surface atoms, so as to employ the above definition of dispersion. Even methods which do attempt to measure the amount of metal surface area (such as

chemisorption) have limitations. It is therefore more suitable in many cases to make, once again, the assumption of spherical geometry in order to approximate the dispersion. This may be done from TEM data by using the following:

$$D = \frac{fA}{\rho \delta N_o} \frac{S}{V} \qquad [3.6]$$

where D is the dispersion, A is the atomic weight of the metal atoms, ρ is the bulk density of the metal, δ is the average surface area occupied by a single metal atom, N_o is Avogadro's number, and f is a correction factor which represents the fraction of the metal which is actually accessible to reactants in a catalytic run or chemisorption measurement. The ratio $\frac{S}{V}$ is the surface area to volume ratio, which can be replaced by the quantity $\frac{6}{d}$ for either spherical or cubic metal particles. The quantity d, above represents the diameter in the spherical case, or the length of one edge for the cubic case.

It must be pointed out that the parameter δ has, itself some dependence on size[11]. For large particles whose shape is quite spherical, this dependence may often be ignored without causing any significant error. However, for small clusters whose nuclearity is only 10 or 20, this is not the case. The calculation of dispersion may still be accomplished by using other approximations which will be seen to suffice. Even for the small particles mentioned above, if close packed configurations may be assumed, the variation of the parameter δ with nuclearity is not severe; an average may be estimated by knowing values of δ for various crystal faces, and obtaining a weighted mean of these.

In calculating D from TEM micrographs, values will tend to overestimate those obtained through other methods such as chemisorption. This is because TEM measurements do not eliminate particles which are not accessible to gas molecules. That is, TEM data correspond to the maximum value of $f = 1$ in equation [3.6]. Different estimates may also be calculated depending on which basis is chosen for the average to be used in equation [3.6]. The dispersions calculated from a given micrograph will be largest if the number basis n is used, and smallest if the volume basis v is used.

There is one last consideration which pertains to the use of statistical treatment of TEM data. Often, a qualitative observation of the histograms shows that the assumption that the particle sizes are drawn from a normal distribution is not valid. This is especially the case when the mean lies much closer to the minimum of the size range than to its maximum. In such cases, it is generally suitable to assume that the logarithms of the particle sizes are normally distributed. This is commonly called the log-normal

distribution[8]. If this system is being used, the above formulae may simply be used by replacing $\log_e(d_i)$ where d_i appears, and carrying out the indicated summations. The resulting averages are then reported by taking the exponential of the sum. As an example of this, the formulae for number average and (number average) standard deviation would become:

$$\langle d_n \rangle = \exp\left[\frac{\sum_{i=1}^{N} n_i \log_e d_i}{\sum_{i=1}^{N} n_i}\right] \qquad [3.7]$$

$$s_n^2 = \exp\left[\frac{\sum_{i=1}^{N} n_i \left(\log_e \frac{d_i}{\langle d_n \rangle}\right)^2}{\sum_{i=1}^{N} n_i}\right] \qquad [3.8]$$

The expressions which are used to calculate the area and volume basis parameters can be similarly modified. If the usual normal distribution is used to analyze data to which the log-normal distribution applies, the average particle sizes will tend to be somewhat overestimated.

3.1.3 Results of the CTEM Study of Surface Hydroxyl Effect

One of the major goals of this investigation was to discover how the mean metal cluster size, spread of the cluster distribution, and the dispersion were affected by the degree of surface hydroxylation of the silica support, using Ni and Pt organometallics as exemplary metal atom precursors. In both cases, the metal atom carrier was the zerovalent tris-ethylene metal complex dissolved in methylcyclohexane at temperatures of about 190 K. The metal loading was maintained in the 1.6 to 2.2 wt% range, and the surface hydroxyl concentration of the silica was varied from 1 to 5 [OH] groups per square nanometre according to pretreatment techniques described elsewhere[10]. The choice of Ni and Pt on silica relates to their distinct redox properties, and further to the ease with which good contrast between the metal and support in TEM micrographs may be obtained[11].

A typical CTEM micrograph is shown in Figure 3-1. This example shows an alumina-supported unimetallic platinum specimen. The good degree of contrast between the metal particles and this support is evident. Furthermore, the (111) lattice spacing of the alumina has been resolved. This latter observation provides a reliable internal calibration scale, which allows one to avoid the usual uncertainties in

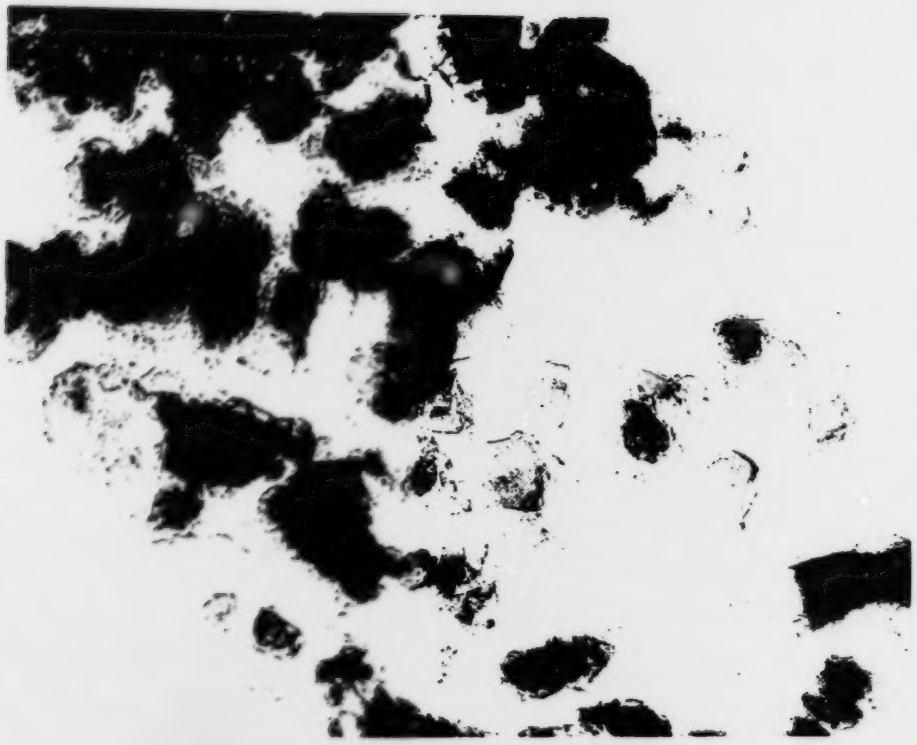

Figure 3-1 Typical CTEM Micrograph of a Pt/Al_2O_3 MVS Sample

calculating the magnification factor. In the case of silica, no such lattice image is resolvable, however these samples were handled in identically the same manner as the alumina-supported ones.

For the analysis of each of the micrographs, a large number (between 300 and 700) of particles was chosen at random for each sample. These were classified according to the number of particles which fell into various size intervals. A summary of the data is presented in Table 3-1.

PRETREATMENT TEMPERATURE	< 0.60 (nm)	0.82 - 1.63 (nm)	1.63 - 2.45 (nm)	2.45 - 3.26 (nm)	TOTAL COUNT
200°C	51.2	41.2	6.2	1.4	299
400°C	82.6	16.7	0.7	-	606
600°C	79.0	21.0	-	-	310
800°C	43.2	53.5	3.3	-	459

Table 3-1 a Particle Size Distribution of Silica-Supported Nickel Clusters

PRETREATMENT TEMPERATURE	< 0.60 (nm)	0.82 - 1.63 (nm)	1.63 - 2.45 (nm)	2.45 - 3.26 (nm)	TOTAL COUNT
200°C	51.2	41.2	6.2	1.4	299
400°C	82.6	16.7	0.7	-	606
600°C	79.0	21.0	-	-	310
800°C	43.2	53.5	3.3	-	459

Table 3-1 b Particle Size Distribution of Silica-Supported Platinum Clusters

Note: Particle Counts are normalized to give percentage of total falling within each range.

Results were analyzed and presented by a computer program (a listing is given in Appendix A), and are depicted in Figures 3-2 through 3-9. These include the histogram representations, average diameter and standard deviations, as well as the dispersion estimates for the number, area, and volume basis PSD 's. Each sample is detailed in one figure. In all cases involving these samples, it was determined that the log-normal distribution was most appropriate; numerical values were calculated accordingly.

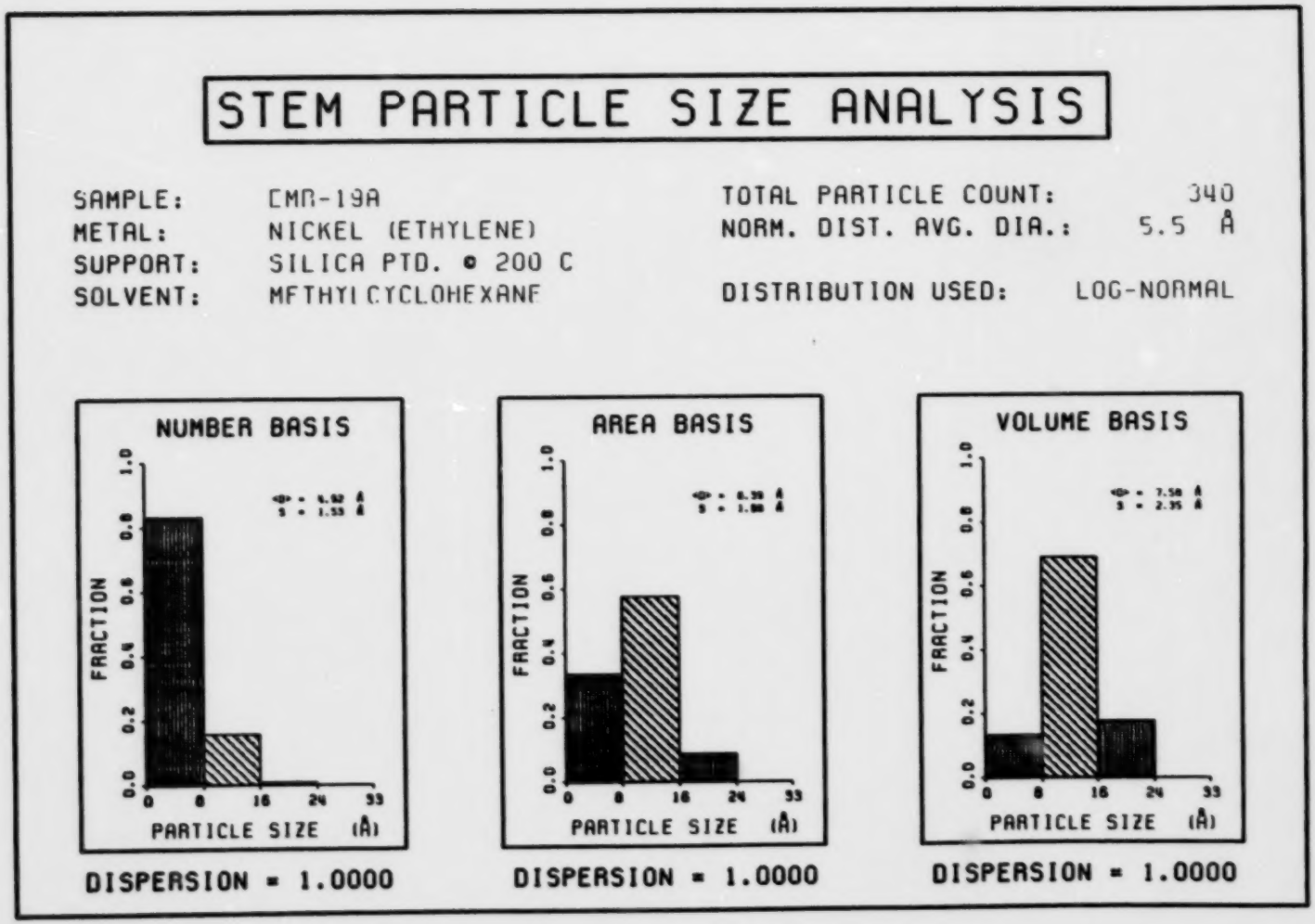

Figure 3-2 Particle Size Analysis of the Ni/SiO_2 MVS-Generated Sample Pretreated at 200°C

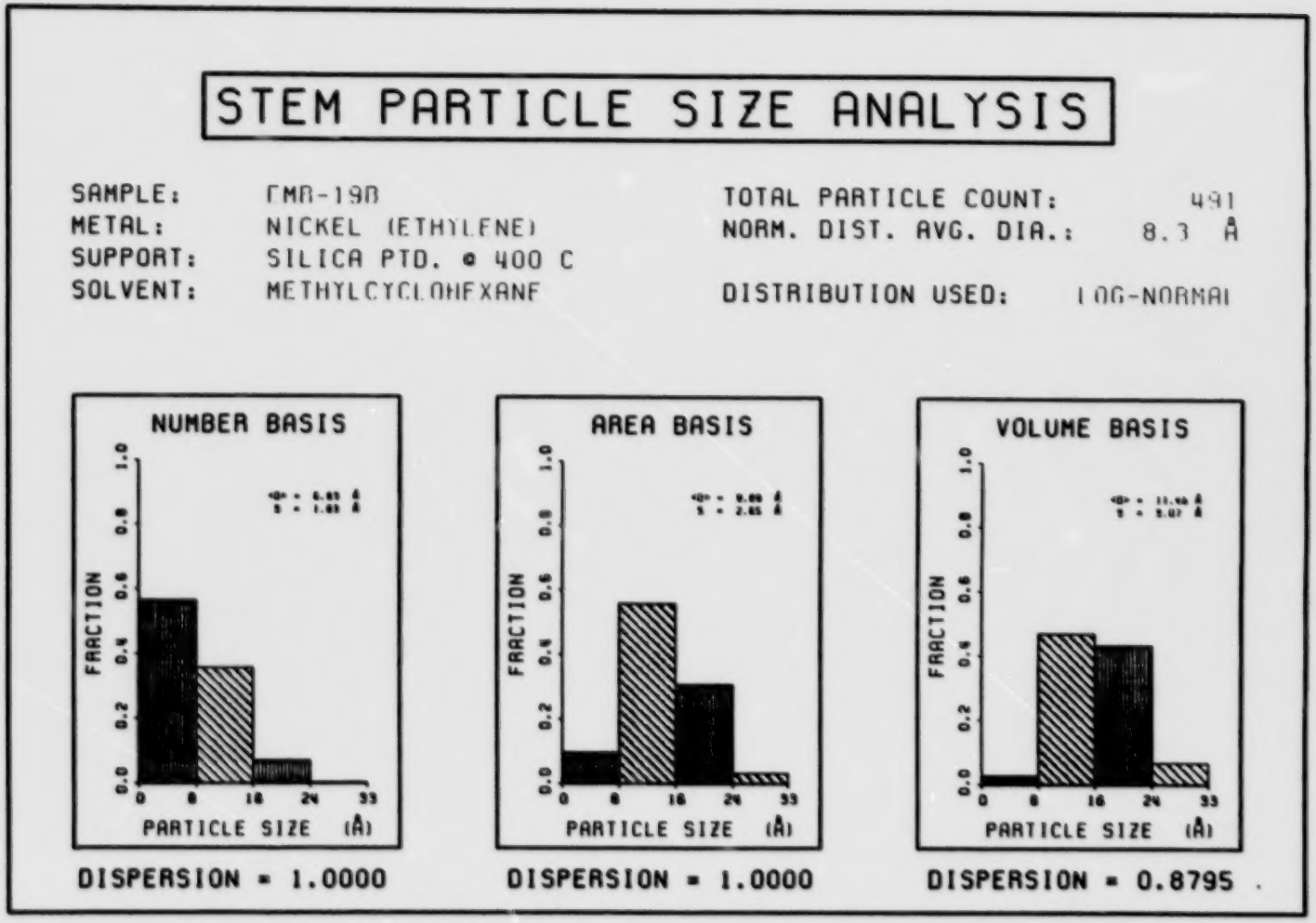

Figure 3-3 Particle Size Analysis of the Ni/SiO_2 MVS-Generated Sample Pretreated at 400°C

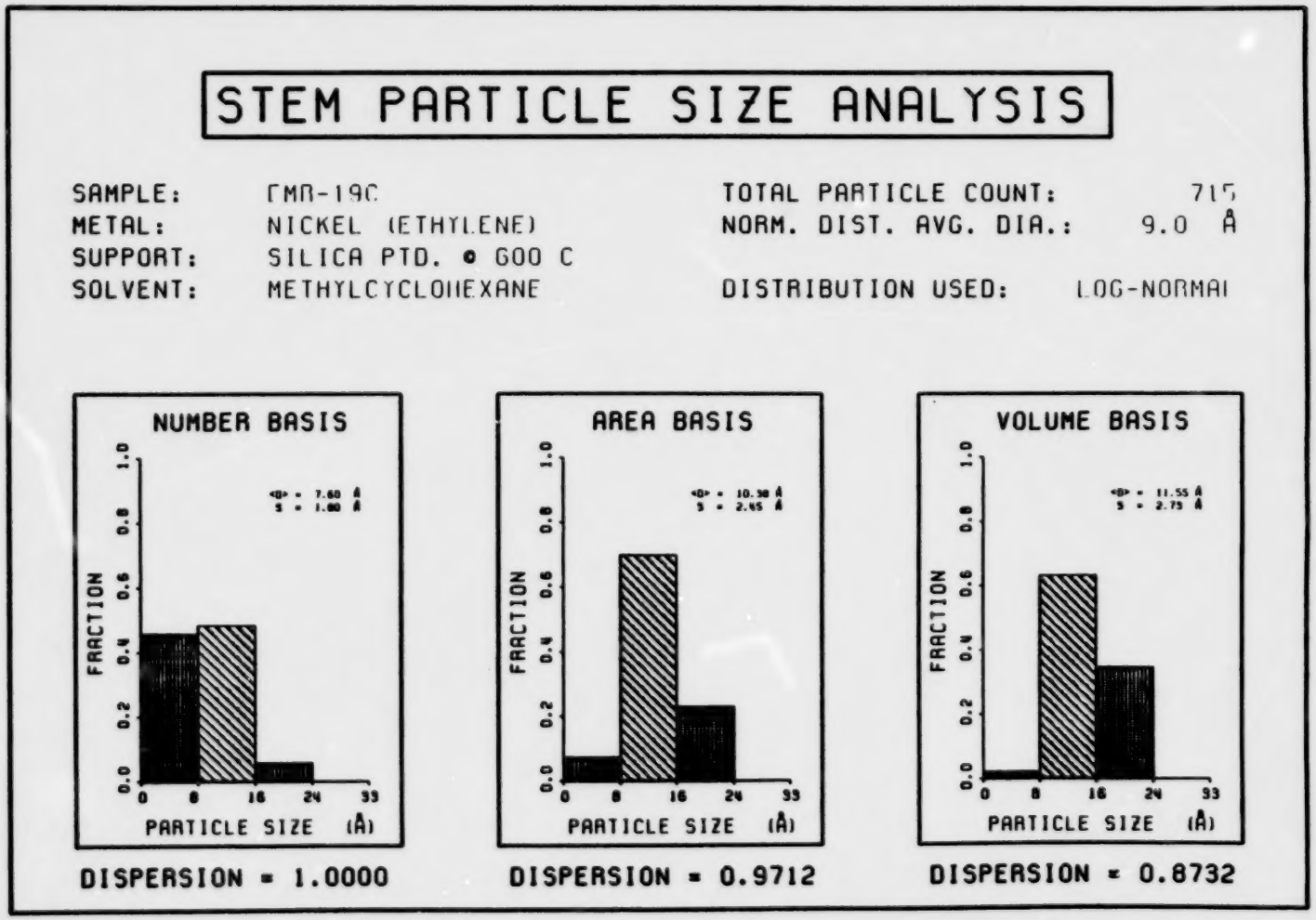

Figure 3-4 Particle Size Analysis of the Ni/SiO_2 MVS-Generated Sample Pretreated at 600°C

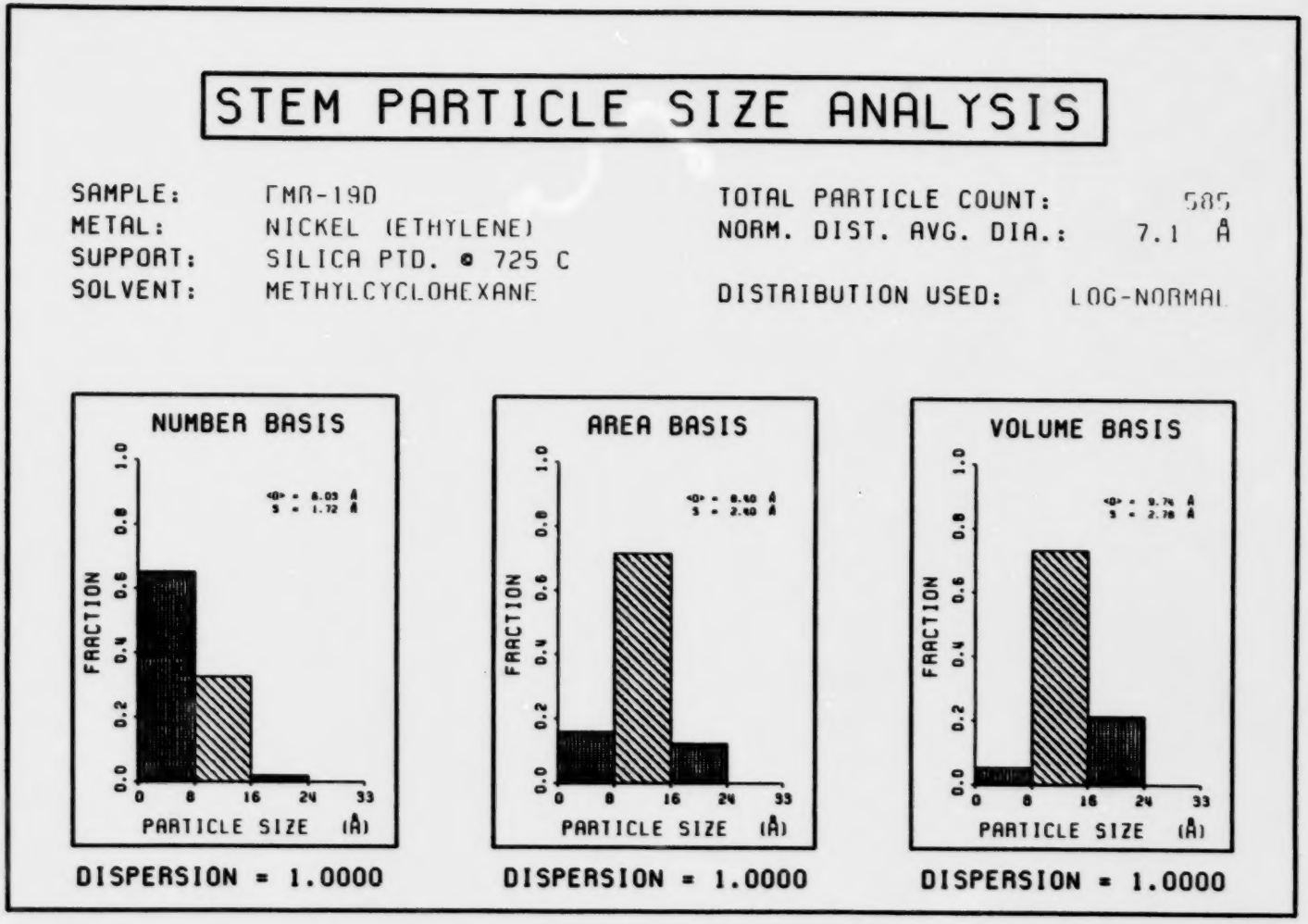

Figure 3-5 Particle Size Analysis of the Ni/SiO_2 MVS-Generated Sample Pretreated at 725°C

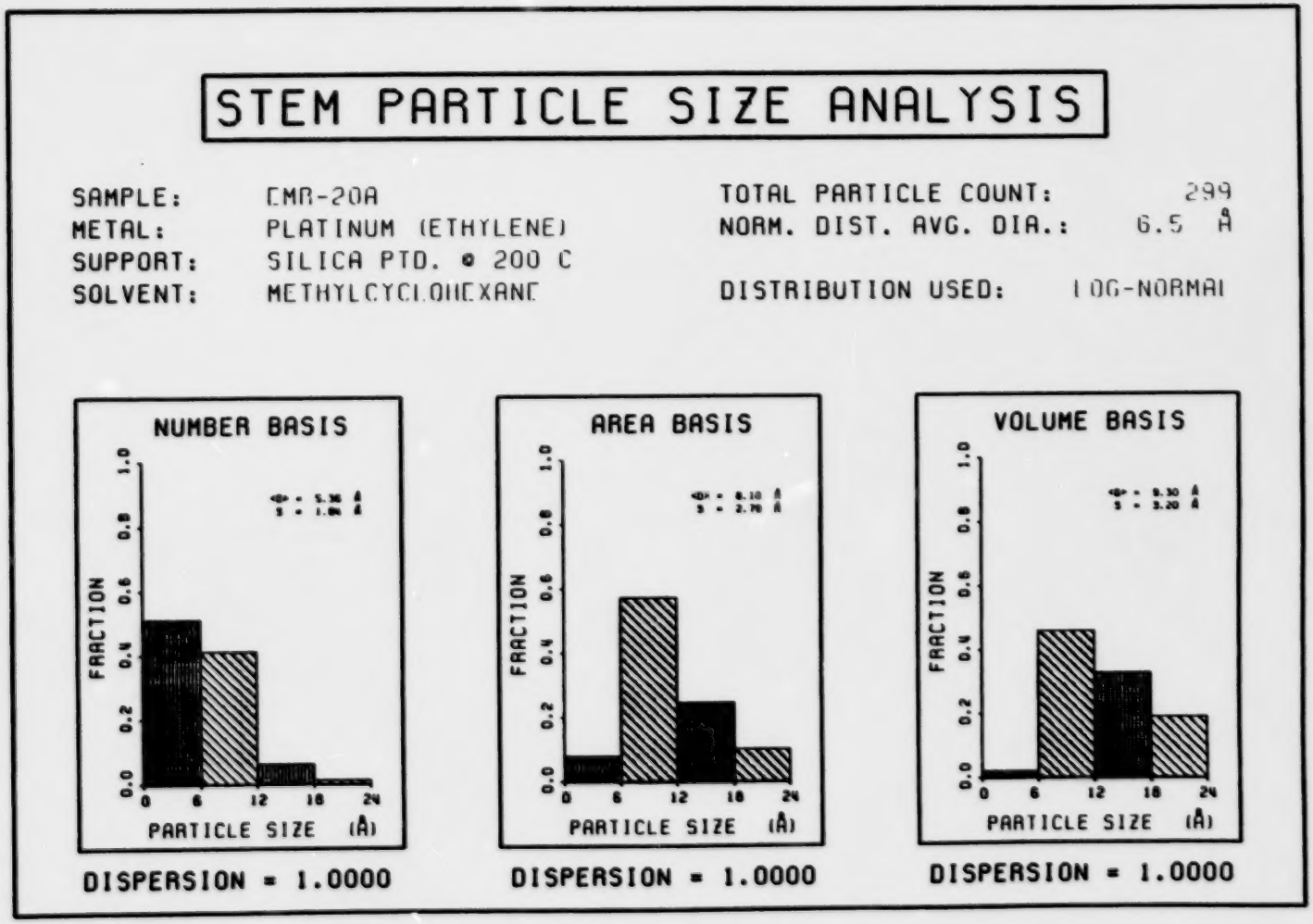

Figure 3-6 Particle Size Analysis of the Pt/SiO_2 MVS-Generated Sample Pretreated at 200°C

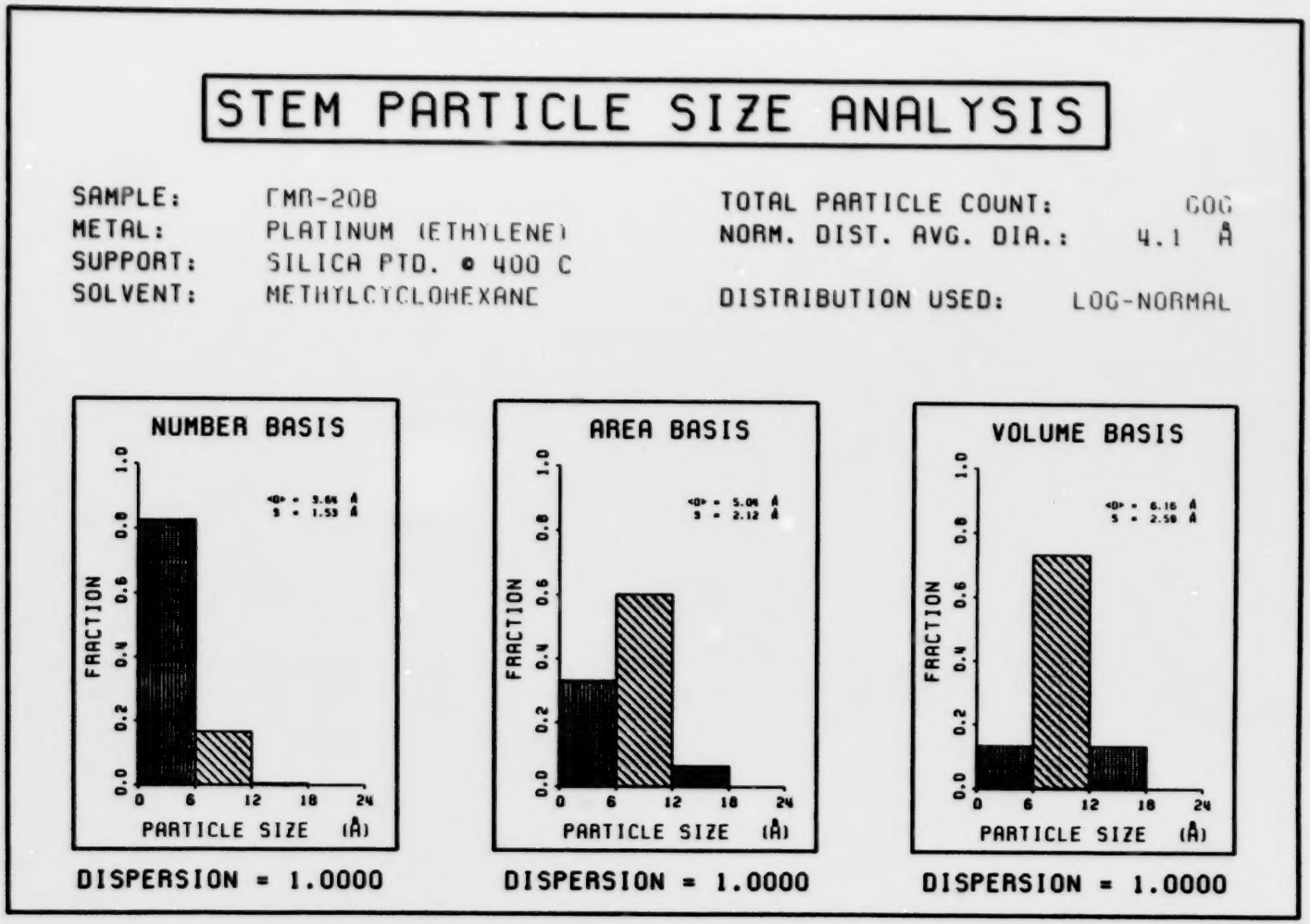

Figure 3-7 Particle Size Analysis of the Pt/SiO_2 MVS-Generated Sample Pretreated at 400°C

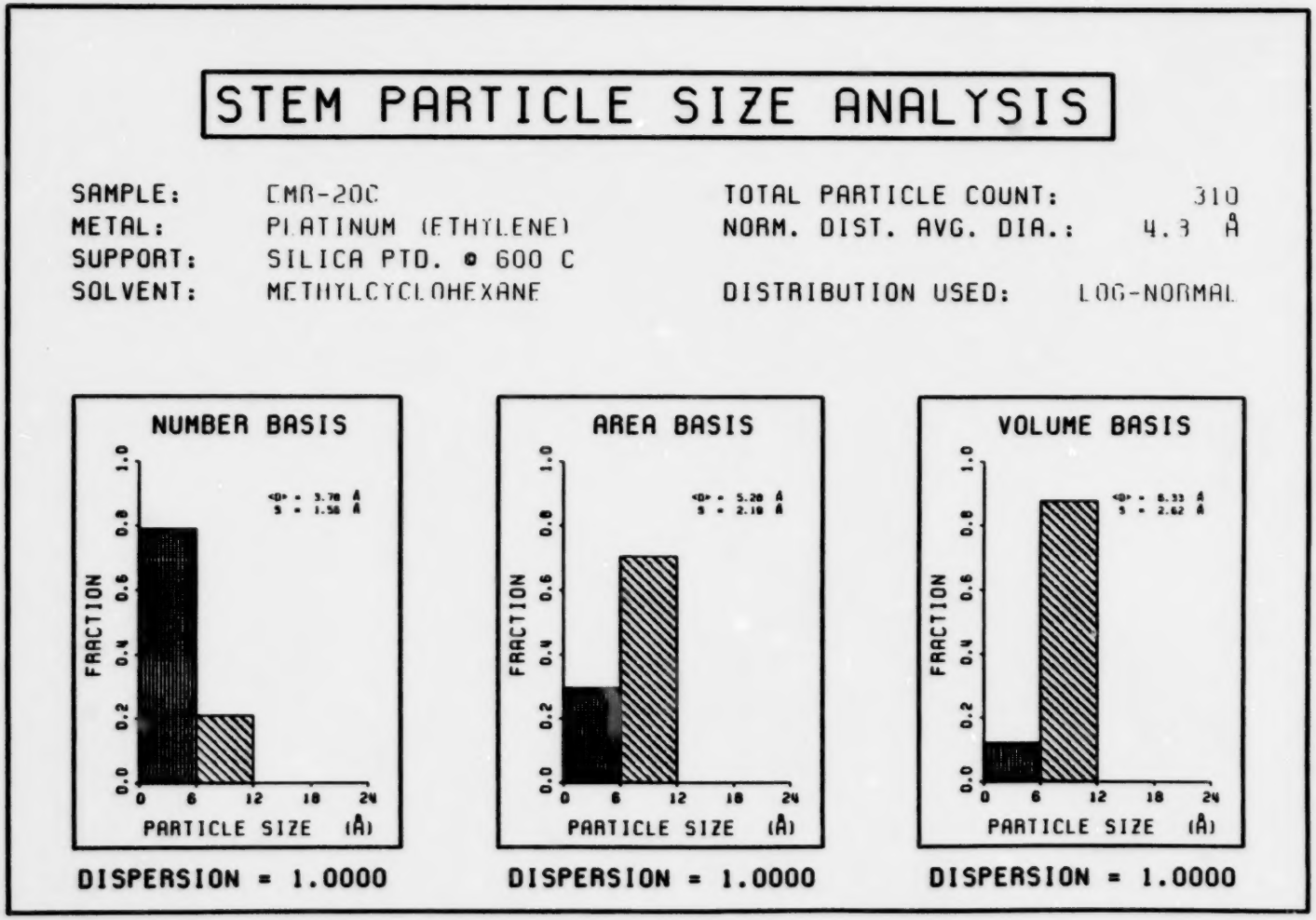

Figure 3-8 Particle Size Analysis of the Pt/SiO_2 MVS-Generated Sample Pretreated at 600°C

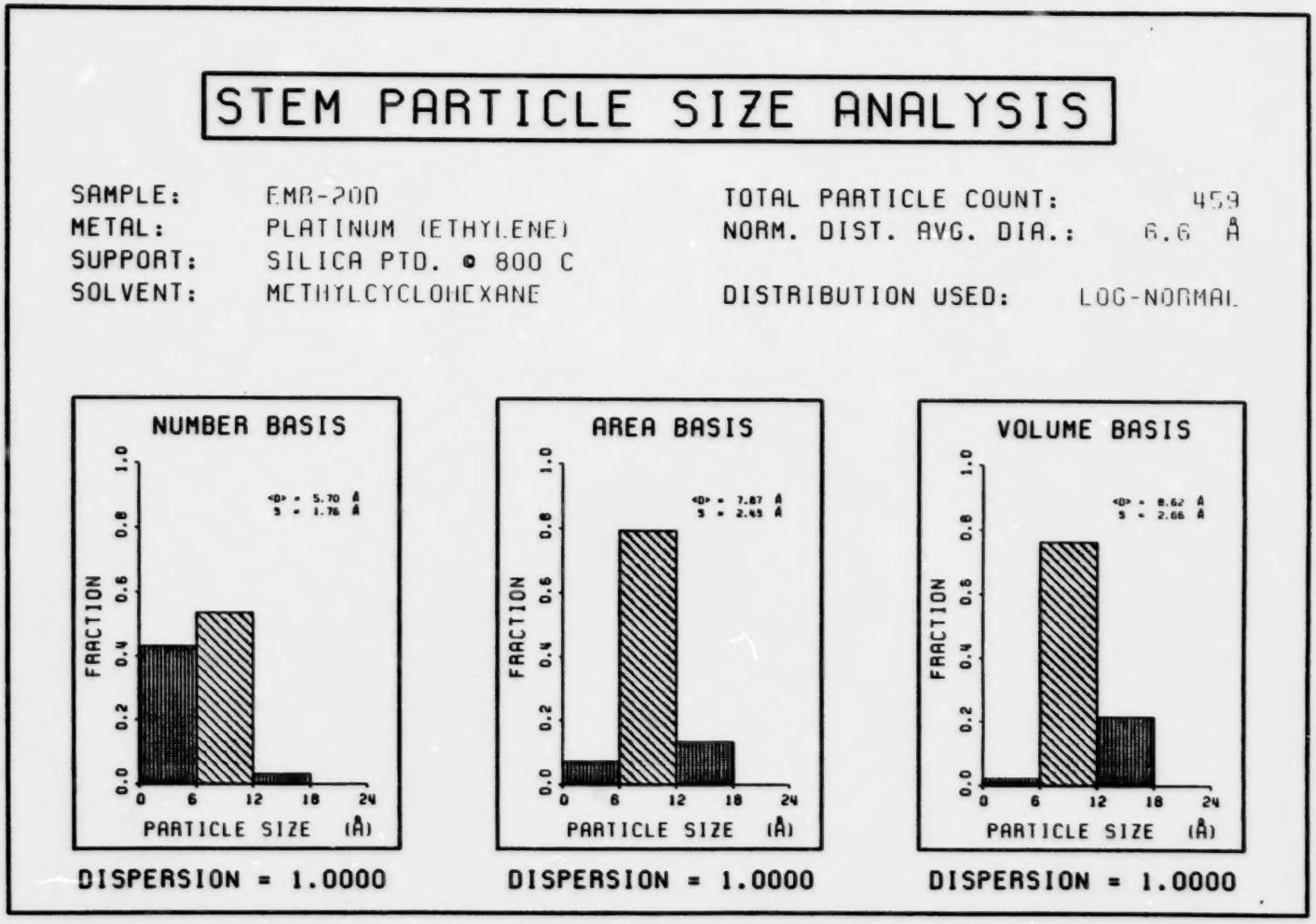

Figure 3-9 Particle Size Analysis of the Pt/SiO_2 MVS-Generated Sample Pretreated at 800°C

By inspection of the histograms, one can readily see that the average particle sizes for Ni and Pt cluster materials prepared by the MVS method are all below 1.0 nm. Thus, in these materials, dispersions of unity have been realized. The distributions appear to be unimodal in all observed cases, and have rather narrow standard deviations. In all samples, there were no particles larger than 3.5 nm which could be seen, and there is no other evidence to suggest their presence.

Figure 3-10 shows the average particle size values for the four nickel and four platinum samples (each representing a different vacuum pretreatment temperature of the silica support prior to impregnation with MVS precursor). For both metals, the variation between the largest and smallest of the averages is only 0.2 nm. This is within the experimental error associated with the measurement, hence it may be concluded that the resulting average particle size does not depend on initial surface hydroxyl concentration in the range of 1 to 5 per square nanometre.

3.1.4 CTEM Study of Support Choice,Treatments, and Bimetallic Incorporation

The same analysis procedure which was applied to the silica-supported MVS clusters revealed that the alumina-supported specimens also showed a lack of correlation between average particle sizes and the support pretreatment temperature (pretreatments of 200 and 600°C only were examined). The average particle sizes for these samples were found to be virtually superimposable onto the corresponding points for the silica supported materials shown in Figure 3-10. Such observation is somewhat surprising, in that SiO_2 and Al_2O_3 are known, not only to have considerably different surface OH concentrations, but to have different acid strengths[16] of these surface groups. It is therefore apparent that although the OH groups may yet be involved in metal nucleation, the differences in concentration and acidity which have been examined in the present study, (at the total metal loading levels used) are not manifest in particle size differences.

Another question regarding the sizes of supported metal particles, probes the effect of various treatments of the MVS generated materials after their synthesis. This consideration is of obvious importance to the use of these materials as catalysts: one is interested in the fate of the particles when exposed to various atmospheres at sometimes high temperatures. One method used to address the question, was an examination of several of the previously discussed samples after their use in a catalytic

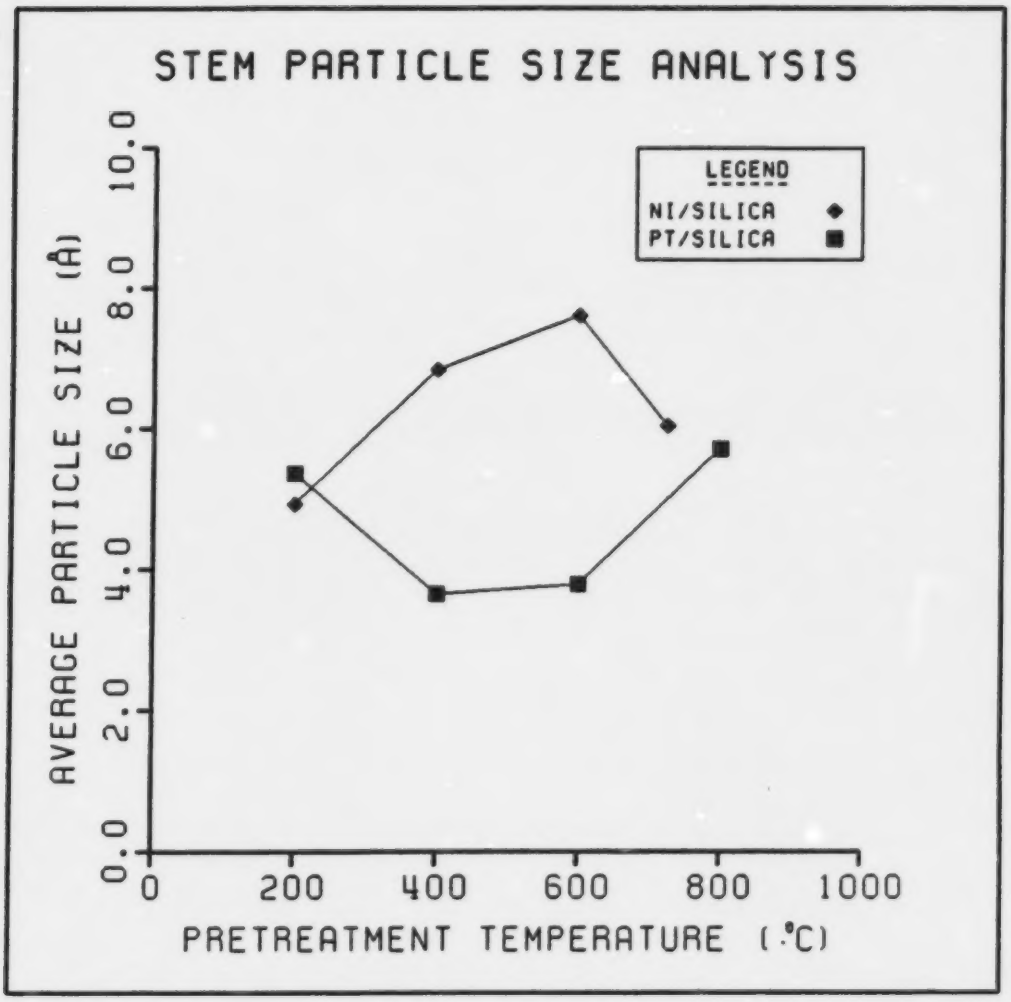

Figure 3-10 The Effect of Support Pretreatment Temperature on Mean Particle Size

reaction. The complete experimental details are presented in Chapter VII, but here it is pointed out that the conditions involved reducing atmospheres, temperatures as high as 400°C, and exposure times in excess of twenty hours. Figure 3-11 shows data for the Pt/SiO_2 materials both before (from Figure 3-10) and after catalysis[a]. From inspection of the data, it is clear that some degree of sintering had taken place during the use of these materials as catalysts. The average size of the supported particles, for all pretreatment temperatures shown increased to about 1.3 nm. That the pretreatment temperature had no observed effect on the ultimate particle sizes is not unexpected, since both the original sizes and the catalytic results were virtually identical for the four samples. As compared with conventional heterogeneous catalysts of this type (i.e. Pt/SiO_2), the degree of sintering is very mild[17]; many other systems demonstrate a sufficient degree of sintering that particles of several hundred angstroms are often observed. This is therefore, one unique property of MVS generated supported metal materials. It should also be pointed out that the nickel materials were subject to similarly mild sintering in these experiments.

An analysis of representative Pt/Ni bimetallic samples is summarized in Figure 3-12, superimposed onto the Pt unimetallic results from Figure 3-10. The virgin bimetallic samples had particle sizes which were (as one would expect) in the same range as both of the unimetallic series of samples.

3.1.5 CTEM Study of MVS Materials Produced in the Static Reactor

Three samples of alumina-supported platinum MVS materials were synthesized using the static reactor technique, and cocondensation methodology. This allowed the examination of specimens produced through the intermediacy of organometallic precursors other than tris-ethylene platinum(0) in methylcyclohexane. One of the three materials was synthesized from the tris-ethylene complex, however this was generated in pure liquid ethylene rather than in methylcyclohexane solution; the other two were synthesized from a tris-dinitrogen and tetracarbonyl platinum(0) complex, respectively.

As was discussed in the experimental section, although the tris-ethylene complex can be easily synthesized at temperatures higher than 77 K, a *gettering* solvent is necessary in order that the vapour pressure be sufficiently low to permit operation of the electron gun. In the static reactor, pure ethylene can be used, as the operating temperature can be arranged to be much lower. The two other organometallics cannot be synthesized even at liquid nitrogen temperatures. In the case of the tris-dinitrogen compound, this is so because its decomposition temperature[23] is 70 K. In the case of the tetracarbonyl

---

a of the four virgin samples, three (as shown) were available for analysis after catalysis.

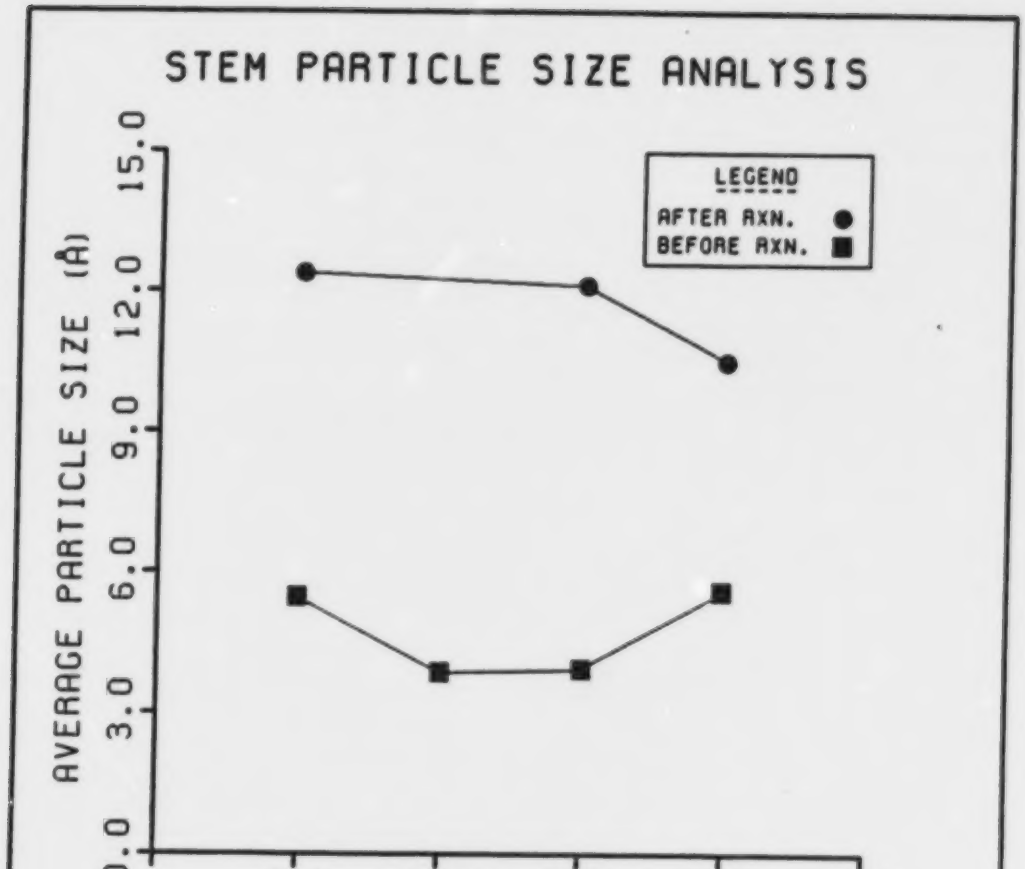

Figure 3-11 Average Metal Particle Sizes of MVS Materials Before and After Catalysis

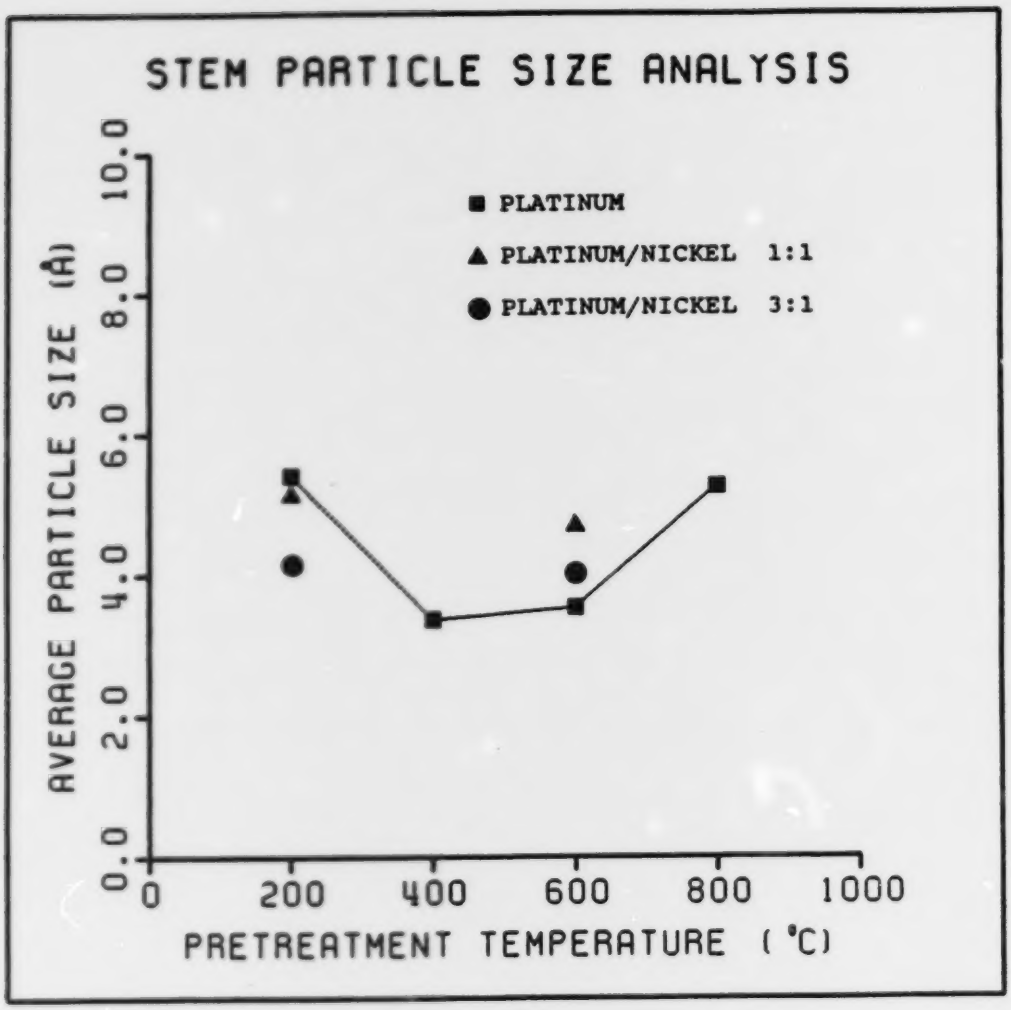

Figure 3-12 Comparison of Average Particle Sizes between Ni/Pt Bimetallic and Unimetallic Pt MVS Samples

compound, although the decomposition temperature[24] is 146 K, direct synthesis via reaction between Pt atoms and carbon monoxide will not occur[25] above 20 K. An attempt to synthesize the compound at higher temperatures would result in the formation of polynuclear platinum carbonyls and/or colloidal platinum, hence ultimately generating much larger supported metal particles.

CTEM particle size analyses for the three static phase MVS materials are shown in Figure 3-13. Immediately, one can see that the ethylene and carbonyl precursor complexes yielded particle size distributions which were virtually identical to those stemming from the use of the solution phase tris-ethylene type compounds. Noting that precursor/carrier contact was effected at temperatures just above 77 K, it can be concluded that such a procedure brought solvated mononuclear entities to the carrier surface before reaction there to form the anchored metal species. This was well demonstrated in all cases to be crucial in order to produce extremely small (subnanometre) metal clusters. Since the contact procedure involved melting of the MVS product before reaction with the surface, the tris-dinitrogen compound decomposed before being anchored to the carrier. Along with the decomposition, a certain degree of agglomeration is evidenced to have occurred; this explains the considerably larger resultant particle size distribution. It can be seen, that for the $Pt(N_2)_3$ case alone, no particles smaller than 0.5-1.0 nm were observed. Furthermore, the breadth of the distribution was much wider than for any other of the MVS samples examined. Interestingly, although the average particle sizes of reductively treated solution phase MVS materials were very similar to the static MVS $Pt(N_2)_3$ virgin material (i.e., about 1.2 to 1.3 nm), they had a much narrower range of particle sizes. It seems apparent that the surface mobility which gave rise to the sintering of anchored particles in hydrogen at 300°C, is more restricted than the solution phase mobility of precursors which gave rise to the formation of polynuclear platinum clusters or colloidal platinum before they became carrier-anchored. This demonstrates that the extremely small MVS-generated virgin particles have better resistance to sintering than many conventional catalysts, and that such materials, when they do sinter, can yield better defined and more uniform active surfaces for catalysis.

A general conclusion which can be drawn from the combined solution-phase and static-phase studies, is that the smallest available particle sizes were achieved by supplying solvated single metal atoms to the carrier surface. Because the zerovalent, thermally unstable precursors were delivered under extremely mild conditions, the genesis of anchored clusters was able to be carried out under conditions of absolute minimum surface mobility of metal atoms.

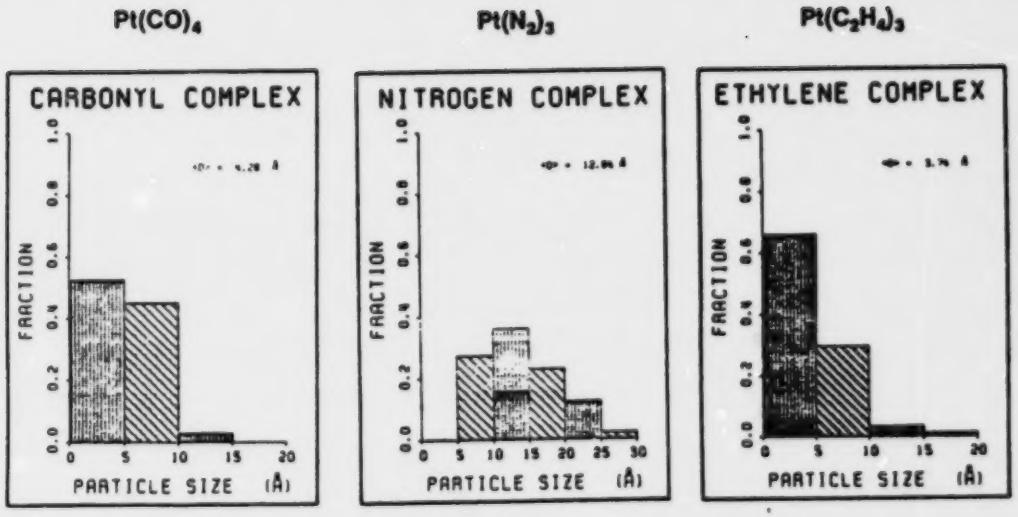

Figure 3-13 Particle Size Distributions of the Samples Produced in the Static MVS Reactor

3.2 STEM-EDAX Investigation of Fe/Ru Bimetallics

The first attempt at using the EDAX probe as a means of analyzing individual supported particles was carried out on bimetallic iron/ruthenium samples. The objective of this preliminary study was to determine whether the supported particles actually contained both metals, or whether the synthesis had produced an array of unimetallic particles which were only intermingled on the surface. Since this qualitative result, and possibly estimates of the iron to ruthenium atomic ratios was the only information sought, it was deemed unnecessary to keep the specimens air isolated. Although it might be speculated that oxygen exposure could cause surface mobility of the metals (possibly allowing proximal unimetallic particles to combine at that time), experience with these metals[18] has shown such not to be the case, unless higher temperatures are also used. Furthermore, the observation that the particles after air exposure were still smaller than 1.0 nm discredits the idea of agglomeration being promoted by non-anaerobic conditions.

In the investigation of the Fe/Ru samples, both CTEM and STEM-EDAX were employed. The preliminary CTEM work began with an optimization of the sample preparation technique and the choices of instrument operating parameters, to the point at which the fringe pattern of the alumina (support) lattice was clearly resolved. Under such conditions, the observed particles were determined to be only slightly larger that the lattice spacing. For the (111) crystal face, the spacing has been determined[19] to be 0.456 nm. The various higher index crystal faces for alumina have smaller spacings such that they could not be resolved no matter how the instrument was operated. It may therefore be concluded that the average particle size as estimated from this CTEM study of the bimetallic materials was about 0.6 nm; for a Ru/Al_2O_3 unimetallic sample which was also analyzed, the observed particle size range was 0.6 to 0.8 nm. Because of the extremely small size of these particles, the scanning microscope (STEM) could not resolve distinct particles. However, a large number of 1 x 1 nm analysis windows were examined, and in no instance was a sector found in which only one of the metals was present. If one takes into account the average distance between individual particles on the support surface (as determined by the CTEM analyses), at least some of the STEM-EDAX analysis windows must have achieved single-particle measurements. It will be shown later that for the Ni/Pt bimetallic system, in which distinct particles were in fact analyzed, all observed particles contained two metals. It is further noteworthy that the measured

average Fe/Ru atomic ratio was 1.8; the calculated ratio based on the masses of metal incorporated during the synthesis was 1.5.

In addition to the MVS generated bimetallic material, two control samples were also analyzed under identical conditions. These were both bimetallic (in the bulk sense) iron/ruthenium preparations supported on MgO (100 m^2/g as per the method[7] of Choplin et al.). Table 3-2 provides a comparison of the EDAX results for these samples. Both of the conventional materials were prepared by the thermal decomposition of carbonyl type compounds. In one case a heteronuclear cluster precursor: $H_2FeRu_3(CO)_{13}$ was used, and in the other case, two mixed homonuclear cluster carbonyls ($Fe_3(CO)_{12}$

PRECURSOR COMPLEX	METAL LOADING (by weight)	PARTICLE SIZE (nm)	Fe/Ru ATOMIC RATIO	
			PRECURSOR	CLUSTERS
A	0.80	1.0 - 1.5	0.33	0.30
B	1.10	1.0 - 5.0	0.33	*
C	5.20	0.6 - 0.8	1.50	1.80

Precursor Complexes

A $H_2FeRu_3(CO)_{13}$

B Mixed $Fe_3(CO)_{12}$ and $Ru_3(CO)_{12}$ in 1:3 Fe:Ru Atomic Ratio

C MVS Fe/Ru Bimetallic Material

Figure 3-2 EDAX Analysis for Supported Iron/Ruthenium Particles from Various Precursors

and $Ru_3(CO)_{12}$) in the same atomic ratio as the heteronuclear precursor were used. The loadings were 0.8 and 1.1 wt% respectively, whereas for the MVS material, the loading was 5.2 wt%. It is interesting upon first inspection, that the particle sizes for the reduced carbonyl-precursor materials were much larger than those of the MVS materials, even though the overall loading was much higher for the latter.

In comparing the two conventional materials, the EDAX results indicated that only the heteronuclear precursor yielded bimetallic particles on the support surface, having the same atomic ratio (within experimental error) as the precursor nuclei. The mixed carbonyls produced distinct unimetallic

particles. This was observed despite the fact that from the size of these particles, it is known that the inital three-atom precursors had agglomerated to form clusters of several hundred atoms on the carrier surface. The growth of such clusters without resulting in bimetallic incorporation, has been attributed[7] to the difference in decomposition temperatures for the iron and ruthenium carbonyls, and is cited as the reason for genesis of bimetallics from mixed Fe and Ru bis-toluene compounds (whose decomposition temperatures are very similar)

3.3 STEM-EDAX Study of the Nickel/Platinum System

Based on the results obtained for the iron ruthenium system, a STEM-EDAX study was undertaken to examine the nickel/platinum/bimetallic system. As before, it was of fundamental interest to verify that the synthesis had indeed produced bimetallic clusters on the support surface, and to determine whether the composition of these was similar to that of the bulk MVS material. Furthermore, new types of experiments were carried out, in which STEM-EDAX measurements were made in conjunction with various treatments of the MVS generated materials; these provided more information about the nature of the metal particles, their interaction with the surface, and their interaction with other chemical species to which they are often exposed.

It was readily observed that once again, bimetallic particles were produced, and that their compositions were a reflection of the bulk material composition. A more indepth set of experiments revealed however, that the atomic composition of the particles showed some (albeit narrow) distribution. This will be discussed later, especially with reference to its relevance in formulating a bimetallic structure model which accounts for the observed catalytic activity patterns of these materials. The qualitative observation that separate unimetallic particles did not result, is again in agreement with the proposal that similarity of decomposition temperature of the precursors[5,6,7] is required to give rise to bimetallic clusters.

A preliminary examination of two of the bimetallic samples was conducted in exactly the same manner as the examination of the Fe/Ru samples. The virgin materials contained supported particles which were only observed with the aid of CTEM; in the STEM instrument, it was necessary to analyze many 1 x 1 nm windows and infer that both metals were found within such analysis zones. Furthermore, in the CTEM observations, there were extremely few observable clusters. It was speculated that probably most of the metal atoms in the system were isolated, or had nucleated only to the extent of a few atoms (hence being too small to be resolved even by CTEM methods). Upon medium temperature reduction

of the materials, a high density of easily seen particles was revealed. Another interesting observation of the virgin samples was that during exposure to the electron beam in the STEM instrument, which can cause local heating of the region being observed to temperatures as high as 200°C, some motion of the image was noted. This was not the same kind of motion as that which results from charging of the specimen granules, but was instead attributed to the thermally induced desorption of organic residues from the surface. Such a phenomenon was never observed for the reduced samples.

It was determined that the virgin samples contained both metals uniformly distributed over the carrier surface, although the form of these metals may have been as organometallic entities merely chemisorbed thereupon (even though the initial tris-ethylene precursors would not be likely to have retained their integrity).

One of the experiments involving treatments of the virgin materials was a byproduct of one of the sample preparation techniques. In order to help disperse the specimen granules onto the carbon-coated copper sample grid, a solvent suspension technique was used for some of the samples. The particular solvent choice was absolute ethanol. Application of the technique involved first preparing a suspension of about 1 mg of sample powder in 5 ml of the alcohol, using a sonic frequency of 3 MHz. A drop of the suspension was then taken, immediately placed on the specimen grid, and allowed to dry for approximately two hours. Observation of the samples prepared in this manner showed that metal particles were observed both on the oxide support, and on the carbon film which was underlying the specimen granules. Also, although many of the particles were small (i.e., 1-2 nm), several larger particles (up to 10 nm) were also detected. The observations were entirely different for specimens which were prepared by dispersing dry powders onto the grids. Thus it was concluded that for virgin sample materials, ethanol is capable of resolvating the metal which is initially found on the support surface; during subsequent drying, metal particles can redeposit on the carrier surface and on the carbon film of the specimen grid. Furthermore, whatever the chemical state of the resolvated metal, it is obvious that a substantial degree of agglomeration occurs during the solvation-redeposition process.

A STEM-EDAX examination of the materials subjected to the ethanol suspension procedure revealed several interesting features of the reformed metal particles. Most striking of these was that the off-support particles were very platinum rich relative to the overall composition. When the metal species were resolvated from the surface, it is apparent that there was a preference for platinum to be more easily removed. In consideration of the ease with which platinum and nickel are oxidized, this is an expected observation, since the bonding of the original precursor entities to the carrier is believed[4,20] to be favored by ease of partial oxidation of the metal in such an organometallic. This observation also provided some

evidence that for virgin materials, much of the metal was not already associated with bimetallic clusters. If this were so, it would be difficult to explain how resolvation could have selectively removed platinum from such clusters. A more likely explanation is that much of the surface metal was in the form of (possibly as of yet mononuclear) adsorbed organometallics, the platinum containing examples of such being more easily removed from the surface. It is important to note here, that after being subjected to hydrogen reduction, the MVS generated particles did not resolvate in ethanol. This treatment (which was essentially the same as that used for pretreatment of the MVS materials as catalysts) therefore established the bimetallic clusters which were observed to be well anchored to the surface, and which homogeneously reflected the bulk composition of the material.

The discovery of the resolvation phenomenon suggests several further experiments which could expand the understanding of the structure of MVS materials. One of these would involve reductive treatments of the sample using a range of temperatures in small increments up to 200°C. For each such sample, the quantity of resolvatable metal would be determined[a], and plotted against the reduction temperature. From this, it would be ascertained at which temperature metals were fixed to the surface (this information being available for any metals either alone or in bimetallic combinations). Furthermore, if it turned out that the resolvated metal was in the form of a single, spectroscopically identifiable species (for which the Gibbs' free energy of formation could be determined as a function of temperature), one could carry out the resolvation measurements over a range of temperatures, and hence plot the fraction of metal removed versus the free energy of formation of the removed species. If the experimental conditions were such that the resolvated metal in solution was in equilibrium with the solid sample, then the slope of the above plot would yield a description of the heterogeneity of particle-surface binding energies.

The samples which had been reduced were examined in detail, using STEM-EDAX, particularly since these are believed to represent the materials which are used as catalysts. This was the first examination in which isolated particles could be seen and hence unequivocally analyzed by EDAX. Table 3-3 presents the results for a number of single particle measurements of the 1:1 atomic ratio sample. Listed within the table are measurements of the compositions of nine individual 1.5 nm particles, as well as four replicate measurements on one of these. The purpose in taking such measurements, was to allow both an

---

a spectroscopically, by measuring the concentration of metal from a known quantity of MVS material and known volume of solvent.

SCAN IDENTIFIER	OBSERVED Pt/Ni RATIO	SCAN IDENTIFIER	OBSERVED Pt/Ni RATIO
A	0.533	G	0.583
B	0.800	H	0.686
C	1.297	I-1	0.912
D	1.262	I-2	1.030
E	1.212	I-3	0.787
F	0.442	I-4	1.259

TABLE 3-3a EDAX Analysis Results for Bimetallic Ni/Pt Particles Produced by MVS

SUMMARY	AVERAGE RATIO	STANDARD DEVIATION	NUMBER OF OBSERVATIONS
Particles	0.970	0.2054	9
Replicate	0.997	0.0404	4

TABLE 3-3b Statistical Summary of Averages and Variances

assessment of the compositional variance, and the variance which was attributable to experimental error. In the following discussion, it is shown that statistical tests can be applied in order to demonstrate that the observed variance exceeds that which is explainable by random experimental error.

As shown in the table, the variances[a] for experimental error (replicate measurements of the same particle) and composition ratio measurements of different particles are respectively, 0.0404 and 0.2054. These values have three and eight degrees of freedom corresponding to four and nine values respectively. According to the method outlined by Snedecor and Cochrane[21], the ratio of these variances:

---

a as calculated according to equation [3-2]. By convention, the variance s^2 is the square of the standard deviation.

s_p^2/s_m^2 (where the subscripts p and m refer to different particle and measurement error variances) is represented by the F-distribution with (8;3) degrees of freedom. Thus, the observed ratio is 5.084, and the tabulated value of the F-distribution (for the appropriate degrees of freedom) is 5.250 at the 80% confidence level. This may be interpreted as follows: we had made the null hypothesis that $\sigma_p^2 = \sigma_m^2$ (σ^2 is the true population variance of which s^2 is the estimator). From the value derived using the F-distribution, it is shown that two variances could differ by enough so that their ratio was greater than 5.25 due to random chance alone, 20% of the time if the experiment were repeated *ad infinitum*. By the conventions of this type of statistical analysis, the evidence is rather weak for accepting the null hypothesis; however, there is neither any evidence to suggest that assuming the composition to vary from particle to particle is in error. It will be shown later that this statement is consistent with further experimental results.

That the statistical test yielded much less conclusive evidence than that which was sought, immediately suggests that more data are required. For example, if both of the variances had had eight degrees of freedom, (given the same numerical values) the appropriate confidence level at which the null hypothesis could be accepted would have been slightly better than 95%. It is also important to note that the replicate measurements need not come from a single particle. This would present a great experimental limitation, since one can seldom make more than about four EDAX measurements before the specimen would move under the influence of the electron beam. An appropriate experimental program would be to make groups of quadruplicate measurements on several particles; this would result in greater degrees of freedom for the estimates of both variances. Such work should be attempted in the future.

CHAPTER IV

Characterization by X-ray Photoelectron Spectroscopy

Examination of supported cluster and other catalytic materials is routinely carried out using X-ray photoelectron spectroscopy (XPS). This is a surface technique by virtue of the rather low escape depths of photoelectrons from such samples; in the case of supported metal materials, the region probed is typically to about 2.0 nm below the surface. The technique provides information mainly about the electronic structure of the material investigated, although some structural details are often revealed as well.

A brief, yet sufficiently comprehensive description of the theory and experimental details of XPS (and its particular application to catalytic materials) is presented by Delannay[64]; a more intensive examination of the topic is given in Reference 65. In the present material, only a very general treatment of the theory will be provided, along with the experimental details which are particular to the present experimental investigation.

4.1 General Theory

Photoelectron spectroscopy concerns the ejection of electrons from a sample by sufficiently energetic radiation. This can be in the UV-visible range, which will cause ionization of valence band electrons, or in the x-ray part of the spectrum, which will cause ejection of core level photoelectrons. The ejected electrons, in order to be released from the sample and subsequently detected, will have some kinetic energy. By measuring this energy, and relating it to the initial energy of the x-ray radiation, it is possible to determine the *binding energy* of the particular core level electron. The exact value of the binding energy (i.e., the energy required to remove the electron from its orbital in the sample to the vacuum level of the XPS instrument) is indicative, not only of the element and particular core level from which the electron came, but also of the oxidation state and other features of its electronic environment. These features can include crystal field and other symmetry effects, as well as the size of metal clusters in which the element is found. Electronic environment effects are observed as shifts in the measured binding energy

with respect to the binding energy of the same core level in an isolated, zerovalent atom of the same type. Typically for transition metals, binding energies for deep core level electrons (for example a Pt(4f) level) become shifted upward by about 0.8 to 1.0 eV per valence number as the metal atom is oxidized. Since, under available experimental conditions the electron energies can usually be resolved within 0.2 eV or so, it is possible to use XPS to determine oxidation states. It is also obvious that partial charge transfer (amounting to considerably less than a full valence state) can also be revealed. This is particularly important in studies of supported metal cluster materials.

Another possible cause for shifts in the determined location of core level binding energy peaks, is related to the size of metal clusters. Though not significant for either bulk metal samples, or large particle clusters (above 10 nm), the typical size-related shifts for the present materials can also be on the order of 1 or 2 eV. The direction of the shift is an increase upon going from *bulk* to ca. 1 nm particles. This raises the immediate difficulty of deconvoluting the two sources of upward energy shifting, before XPS results can be interpreted. Fortunately, it will be seen that there are several situations in which comparisons can be made by examining different MVS materials which have the same sizes. Probably the most informative of these is to study bimetallic samples, and compare those results with the corresponding unimetallic samples, all of which have the same size particles. Such has the potential of revealing the effect each metal has on the electronic environment of the other.

A phenomenon known as shakeup is sometimes seen to occur in certain XPS processes. It is caused by a simultaneous excitation of a second electronic level in the atom, occurring with the photoejection of the first. This is indicated in a spectrum, by the presence of small[a] peaks located at several eV higher than the XPS peaks to which they correspond. Shakeup is not a generally observed phenomenon, but rather occurs in only certain special cases. One such example is for 2p photoemission peaks in transition metals having unpaired (i.e., these are paramagnetic) d electrons. Whether or not shakeup structure is observed for a particular p level of a particular element, is intimately related to its oxidation state in the sample, but also reflects the spin state and symmetry of the species involved.

The intensities of XPS peaks are directly related to the concentration of the particular element in the surface region of the sample being examined. However, every core level of every element has a

---

a the reason why shakeup features are seen as small shoulders on the parent XPS peaks, is that only a certain fraction of the total photoemissions occur with simultaneous shakeup.

different probability of photoemission; hence quantitative comparisons require a correction for this. Normally, the photoionization cross sections for the various elements of interest are known, and therefore the ratios of peak intensities in a measured XPS spectrum to that of a reference peak in the same spectrum will provide correction factors for determining surface concentrations of the various elements. In samples of the present type, quantitative results are somewhat questionable, since the definition of what is the *surface region* is rather vague. Even the concept of electron escape depth is difficult to conceptualize because of the fact that the system is composed of dense 1 nanometre metal particles, less dense support grains, and pore spaces under high vacuum.

4.2 Experimental Details

One of the major difficulties in performing XPS analyses of oxide supported metal cluster materials, is that these are insulators. Due to this, the photoionization process causes a buildup of positive charge on the sample; this generally reaches a stable average value of a few eV rather rapidly. If not eliminated, this charging would have the effect of producing an apparent shift in the binding energy (to higher values since the extra positive charge would cause more energy to be required to remove the photoelectrons to the vacuum level of the instrument). An even more troublesome complication in XPS is that the charge is not homogeneously distributed about the sample surface. The effect of such inhomogeneity in the local charge, is to cause extreme broadening of the peaks.

There were two separate techniques which were used in order to overcome the charging problems. In the first case, the overall buildup of positive charge was compensated by using a low-energy electron flood gun. This provided a controlled current of electrons of usually between 1.0 and 5.0 eV, which balanced the charge lost by photoionization. In calculating the binding energies, the energy of the flood electrons was taken into account.

The use of the flood gun alone cannot correct the problem of differential charging however. This latter was accomplished by grounding the sample as much as possible. For that purpose, two techniques have been attempted in the present study. Both of these are similar in principle; namely that MVS material grains (which are desired to be as small as possible) were placed in intimate contact with some conducting medium. The two such media were a foil of indium (into which the powder sample was pressed) and a very fine copper grid placed on top of the powder sample. Adequate results were obtained using both methods, however it was found that the indium foil was slightly more reliable in terms of yielding good reproducibility and XPS lineshapes which are indicative of properly corrected differential charging.

The actual method used in determining observed binding energies did not involve a direct subtraction of the flood gun potential. Rather, an empirical approach was used, which took advantage of the carbonaceous impurities always present in samples being analyzed. If one examines the spectral region at which the carbon 1s peak is located, a doublet is seen to occur. This actually represents two forms of carbon: one which was in the indium foil, and one which was on the surface of the sample. The latter was in the form of various hydrocarbons adsorbed onto the sample surface. Even in the extremely clean MVS and static MVS preparations, this carbon is unavoidable.

The carbon peak associated with the grounding foil (or grid) was observed to remain at a constant binding energy value when the flood gun potential was varied, while that associated with the sample was flood gun voltage dependent. The assumption that carbon on the sample surface (being in intimate contact therewith) would experience the same difference in potential due to the flood gun, vacuum potential of the XPS instrument, etc., as the other elements in the sample, allowed the true binding energies for all peaks to be obtained. The calculation simply involved shifting all of the peaks by the same amount as that required to match the carbon 1s peak to its literature value[68] of 285.0 eV.

In a large number of the spectra, core level peaks for the various metals were observed to be broadened with respect to those observed in bulk samples. This was directly caused by differential charging; the use of either grids or foil helped, but does not eliminate charging perfectly. In order to determine the location of the peaks therefore, a curve fitting technique was used.

The curve fitting procedure was conducted by using 100% Gaussian lineshapes. In all of the cases, both peaks of a split doublet were fitted together. The number of Gaussians in each fitting operation was variable, but subject to the constraints of fixed linewidth, peak separation and ratio of intensities (these parameters being taken from spectra obtained on samples which were conducting, hence in which broadening was absent). The implicit assumption is then that the final number and amplitude of the Gaussians, gives an indication of the number and relative population of energetically distinct environments of the element to which the XPS peak corresponds. Typically, for the present materials, between three and six Gaussians were found to represent the observed spectral patterns.

4.3 Results and Discussion of XPS Investigations

The results are presented in three subsections. In the first, the trial runs in which conditions were optimized (particularly those relating to charging problems) in order to achieve acceptable XPS

spectra are considered. The remaining two sections present results from an investigation of the iron/ruthenium bimetallic system and the nickel/platinum bimetallic system respectively.

In all XPS spectra obtained for these samples, broad scan ranges of 0 to 1000 eV (binding energy) were collected. A typical example is shown in Figure 4-1. In this spectrum, which was for a Ni unimetallic material on alumina, peaks corresponding to nickel, aluminum, oxygen, carbon and indium have been indicated along with the particular core level involved.

4.3.1 Charging Problems, Referencing and Curve Fitting

As previously discussed, correct binding energies were determined by referencing the C(1s)peak associated with the surface carbon, to a standard value. In Figure 4-2, an example of the XPS data and curve fit for the signal in the carbon 1s region are presented. This was recorded for the non air-exposed sample EMR-20b. The largest peak (indicated at 285.08 eV) corresponds to the carbon contained in the indium foil. The other contributors to the observed signal (which could be displaced by varying the flood gun potential) arose from the adventitious carbon on the sample. The value used to correct all of the other peaks in the spectrum was the largest surface carbon peak, namely the one located at 281.31 eV. Thus, a value of 3.69 eV was added to the measured binding energies for the other peaks.

The uncertainty in estimating binding energies under the present set of experimental conditions is quoted as ±0.2 eV. This was arrived at by examining the run to run reproducibility of such values. The major source of this uncertainty and limitation on any further improvement, was the differential charging problem. It is however true that at this level of accuracy, subtle charge transfer effects may be elucidated; both bimetallic incorporation, and the results of various (eg. oxidative, reductive) treatments can be explored by XPS.

4.3.2 Examination of Unimetallic Fe, Ru, and Bimetallic Materials

Typical examples of the doublet peaks for both Fe(2p) and Ru(3p) are presented in Figures 4-3 and 4-4 respectively. Also displayed in these figures are the Gaussian curves used to fit the spectra. The binding energies for iron and ruthenium in both unimetallic samples, and bimetallic materials containing both of these are listed in Table 4-1.

The binding energies reported for both iron and ruthenium are for the 3/2 peak of the doublet shown in Figures 4-3 and 4-4 (which are 2p and 3p for Fe and Ru respectively). This choice is based on the convention of using the more intense of the two peaks, and allows comparison with reported literature

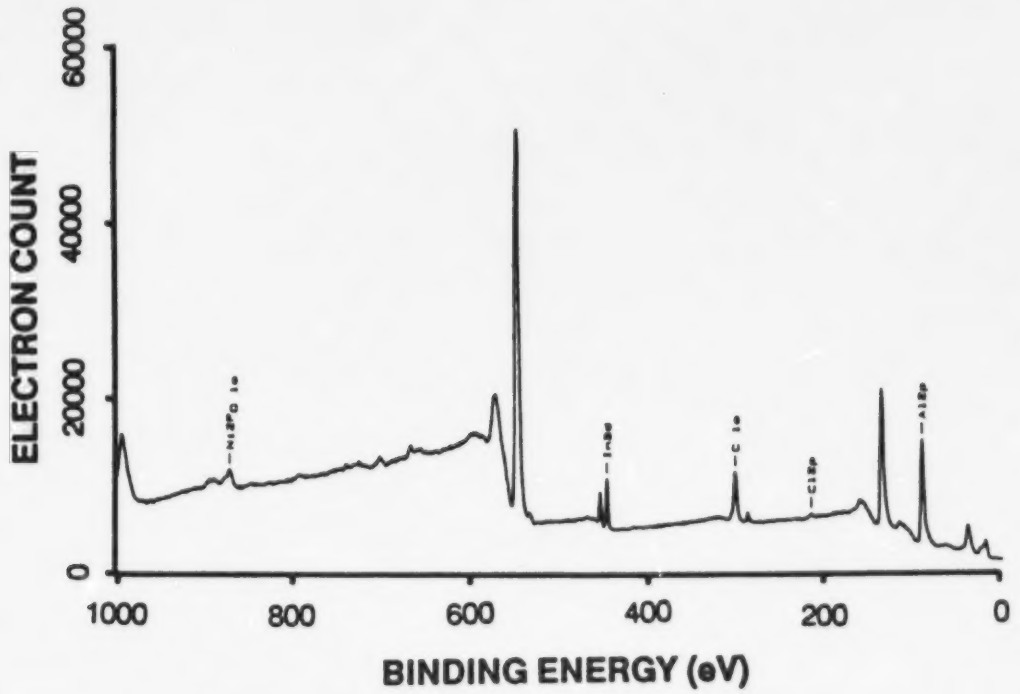

Figure 4-1 Typical XPS Broadscan of Supported Metal Cluster Material

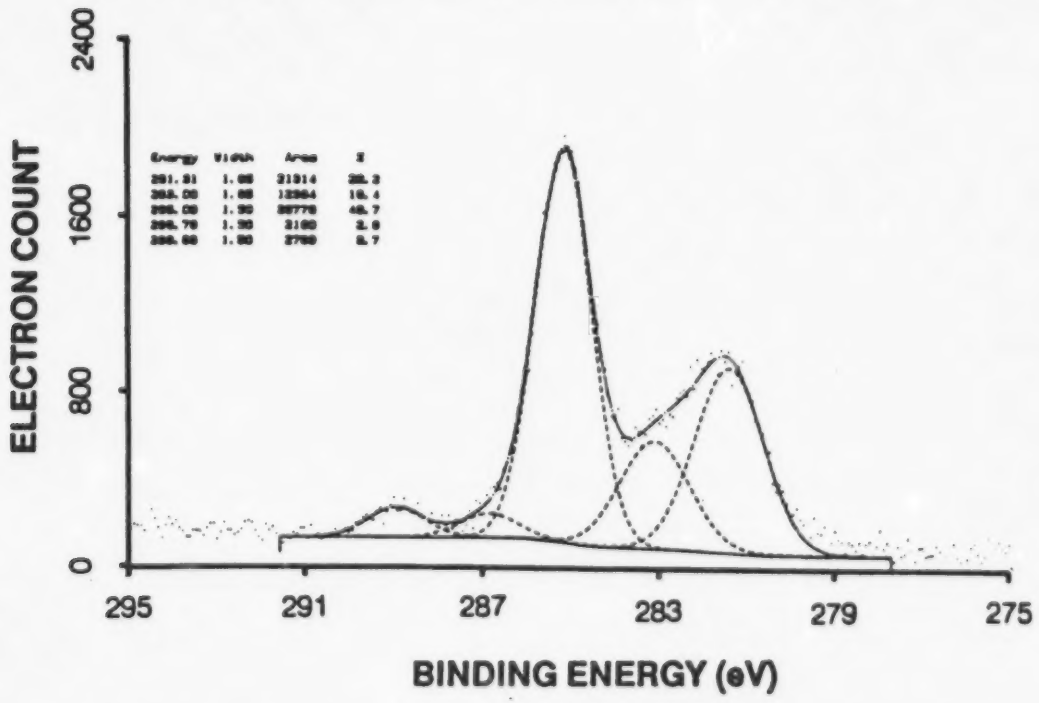

Figure 4-2 XPS Scan of Carbon 1s Peaks in a Typical Spectrum of Supported Cluster Materials

SAMPLE	Fe ATOMIC FRACTION (Total Metal Loading)	BINDING ENERGIES (eV)	
		Fe($2p_{3/2}$)	Ru($3p_{3/2}$)
EMR-6	0.00 (3.2 wt%)	-	462.7
EMR-4	1.00 (1.5 wt%)	710.4	-
EMR-3b	0.25 (1.7 wt%)	*	463.7
EMR-5	0.60 (5.2 wt%)	710.0	463.7

* signal should have been present but was too weak to detect

TABLE 4-1a Measured XPS Binding Energies for Fe/Ru MVS Materials on Alumina

SAMPLE	Fe ATOMIC FRACTION (Total Metal Loading)	BINDING ENERGIES (eV)	
		Fe($2p_{3/2}$)	Ru($3p_{3/2}$)
EMR-6	0.00 (3.2 wt%)	-	462.8
EMR-4	1.00 (1.5 wt%)	711.7	-
EMR-3b	0.25 (1.7 wt%)	710.8	463.0

TABLE 4-1b Measured XPS Binding Energies for Hydrogen Reduced Fe/Ru MVS Materials on Alumina

values. For the Fe($2p_{3/2}$) peak, binding energies of about 711.0 eV are assigned[67] to bulk Fe_2O_3; bulk metallic Fe has a reported Fe($2p_{3/2}$) binding energy of 706.8 eV. It is apparent therefore that the iron present in the MVS materials should be considered to exist in an oxidized form; however, this is not sufficient to conclude that this be Fe^{+3}, since the size of the supported iron (or iron containing bimetallic) particles is in the range where a shift of about 1.0 to 2.0 eV should be expected. Thus it might be speculated that the average formal oxidation state of the Fe would lie between +2 and +3. In order to verify this however, one would require a standard of comparable size and known oxidation state. A further

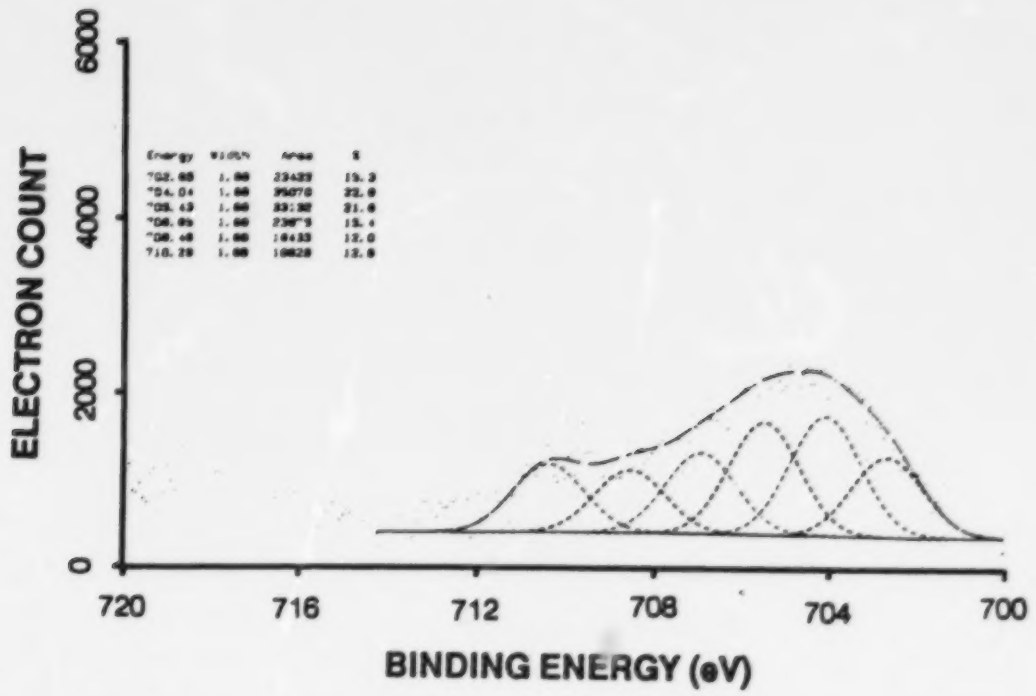

Figure 4-3 Typical XPS Scan of Fe(2p) Peak in Supported Metal Cluster Materials

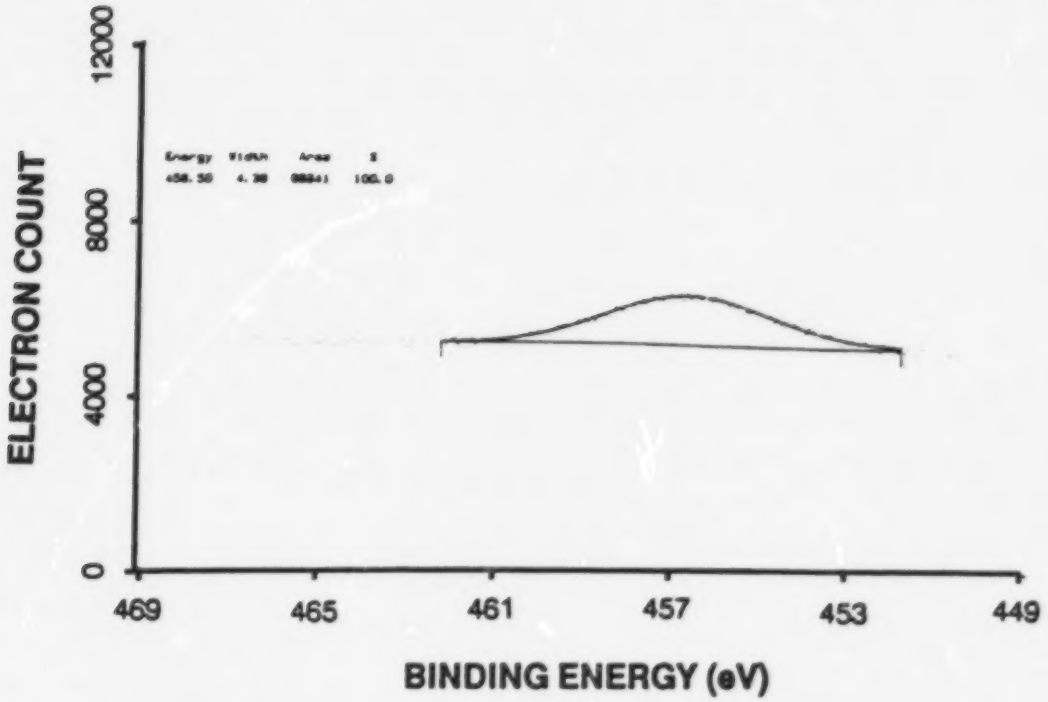

Figure 4-4 Typical XPS Scan of Ru(3p) Peak in Supported Metal Cluster Materials

experiment, which could possibly provide evidence for valence states lower than +3, would involve oxidation of the present materials and rerunning of the XPS spectra (of course, one would also have to ensure that such treatment did not affect the average particle sizes).

The identification of oxidized Fe on the support surface poses further questions as to the detailed nature of such an occurrence. One possibility is that the surface Fe resides in the form of isolated Fe^{+3} ions. Isolated surface species of this type have been reported[69] for copper, and could as easily result for iron (especially in consideration of the fact that in MVS, zerovalent species are delivered to the surface as mononuclear precursors). Furthermore, this possibility cannot be ruled out on the basis of the CTEM examination reported earlier, since Fe clusters were not observed directly until the samples had been subjected to treatments which themselves could have led to particle agglomeration. Other possibilities for the nature of surface iron include both superparamagnetic and ferromagnetic clusters of (for example) Fe_2O_3. Assignment of one or more of the above possibilities could be accomplished through the application of a Mössbauer spectroscopic study; although in order to differentiate between isolated iron centres as well as the two cluster models, this would have to be a temperature and magnetic field dependent investigation.

Unfortunately, the Fe($2p_{3/2}$) signal in the ruthenium rich virgin bimetallic was not sufficiently strong that a reliable binding energy could be obtained. This was also caused by the low total metal loading in that sample. It may be possible to reexamine the sample using a considerably longer scanning time, in order to collect better data.

The Ru($3p_{3/2}$) binding energies measured for the virgin MVS materials ranged from 462.7 to 463.7 eV. As with iron, this is a value consistent with oxidized Ru, although a direct interpretation in terms of formal oxidation state is not possible under the present conditions. Most striking about the measurements, was that incorporation of Fe in the bimetallic samples seemed to cause an increase of about 1.0 eV in the Ru($3p_{3/2}$) binding energy. Simultaneously, a decrease of about 0.4 eV was observed for the Fe($2p_{3/2}$) value. This may be regarded as evidence of a bimetallic interaction between the two metals; furthermore, it is consistent with the expected transfer of negative charge from Ru to Fe. Although the level of experimental uncertainty (ca. $\pm$0.2 eV) would preclude quantitative statements about the relative magnitudes of the two binding energy shifts, that the Ru shift is larger may be rationalized in terms of a greater difference in charge per Ru atom (since the sample was Fe rich). In the case of the hydrogen reduced samples, similar charge transfer was observed. In the latter case however, there was no significant difference in the Ru($3p_{3/2}$) binding energy between the unimetallic and bimetallic samples, while the difference was about 0.9 eV for the Fe($2p_{3/2}$) value. This is again consistent with the argument based on

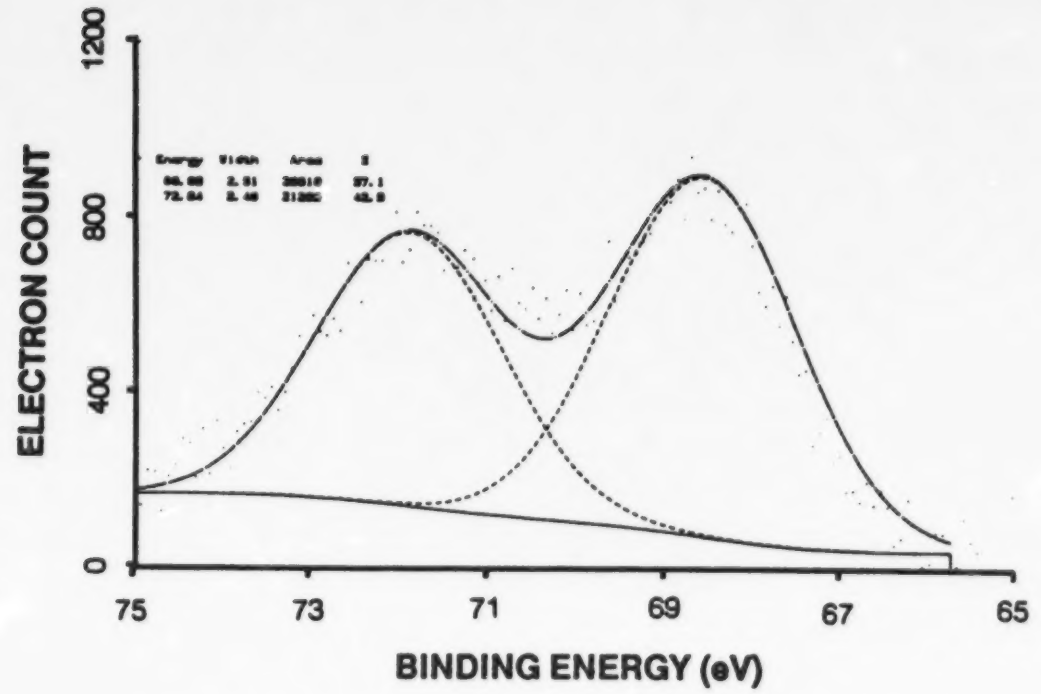

Figure 4-5 Typical XPS Scan of Pt(4f) Peak in Supported Metal Cluster Materials

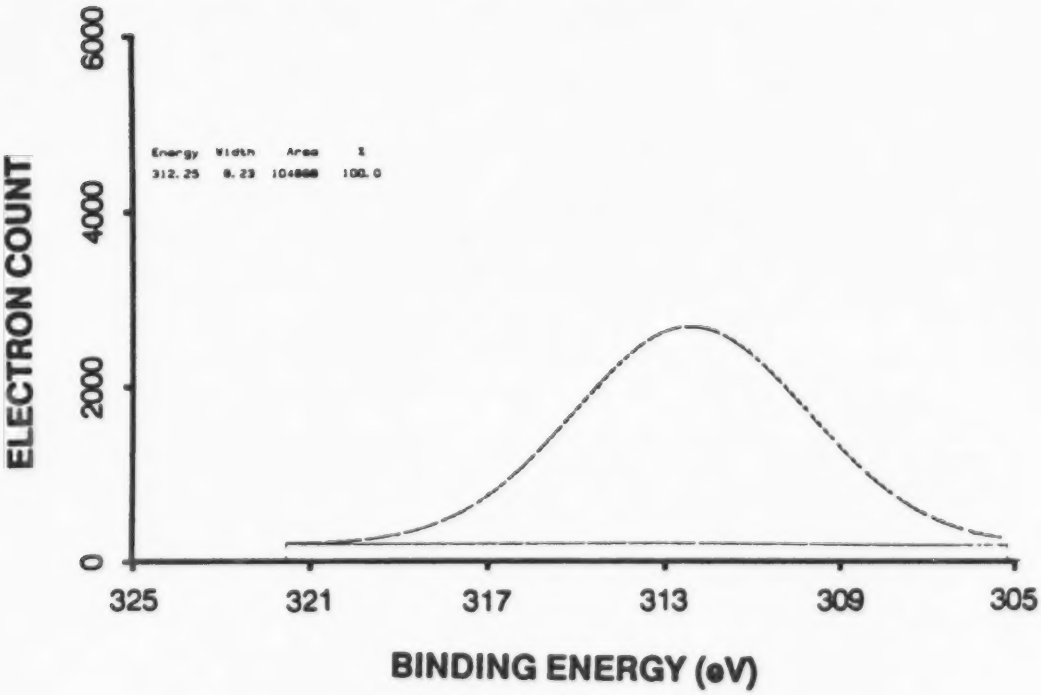

Figure 4-6 Typical XPS Scan of Pt(4d) Peak in Supported Metal Cluster Materials

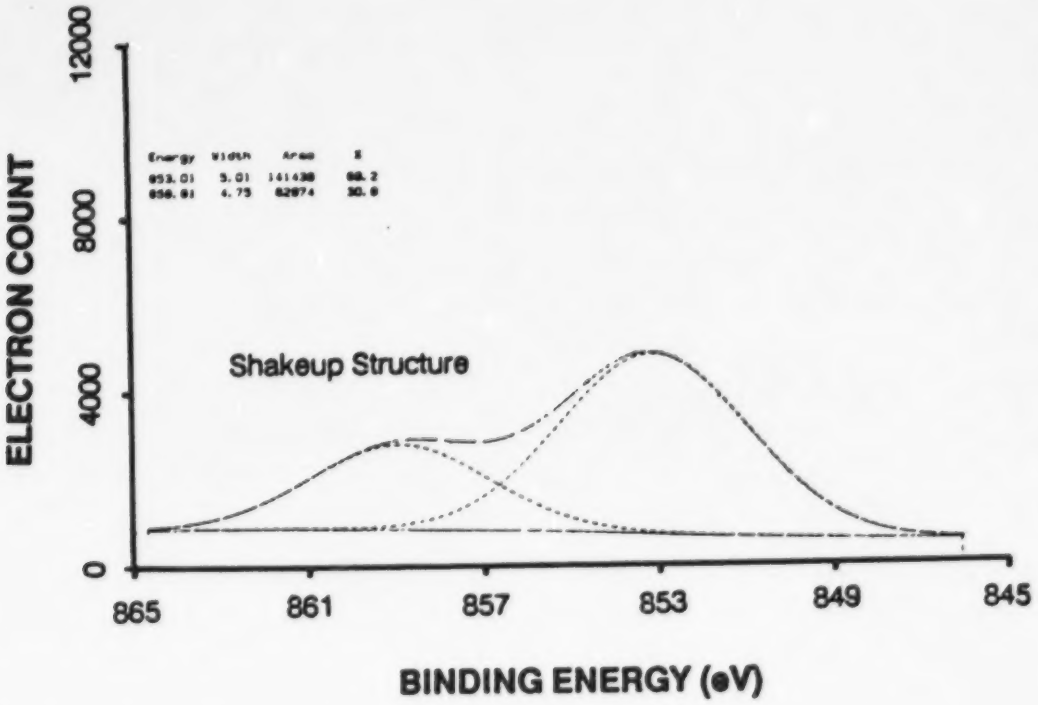

Figure 4-7 Typical XPS Scan of Ni(2p) Peak in Supported Metal Cluster Materials

SAMPLE	NICKEL FRACTION	AIR EXPOSURE	BINDING ENERGIES (eV)		
			Ni ($2p_{3/2}$)	Pt ($4f_{7/2}$)	Pt($4d_{5/2}$)
EMR-20a	0.00	NO	-	71.4	-
EMR-20b	0.00	NO	-	71.8	-
EMR-20b	0.00	YES	-	72.3	-
EMR-20c	0.00	NO	-	71.9	314.5
EMR-20c	0.00	YES	-	72.4	-
EMR-20d	0.00	YES	-	72.0	-
EMR-23a	0.00	NO	-	-	315.3
EMR-19a	1.00	NO	855.6	-	-
EMR-22a	1.00	NO	856.0	-	-
EMR-22b	1.00	NO	856.0	-	-
EMR-24a	0.44	NO	856.0	-	315.4

TABLE 4-2a Measured XPS Binding Energies for Ni/Pt MVS Samples

SAMPLE	Ni ATOMIC FRACTION (Total Metal Loading)	BINDING ENERGIES (eV)	
		Ni($2p_{3/2}$)	Pt($4d_{5/2}$)
EMR-22	1.00 (2.0 wt%)	854.6	-
EMR-24	0.00 (3.1 wt%)	-	315.5
EMR-27	0.50 (2.0 wt%)	856.8	315.1

TABLE 4-2b Measured XPS Binding Energies for Hydrogen Reduced Ni/Pt MVS Materials on Alumina

the atomic fraction of each metal present in the samples. In the runs in which hydrogen reduced samples were examined, it was the ruthenium-rich bimetallic which was studied.

A mildly surprising result can be observed by comparing the Fe($2p_{3/2}$) binding energy values for sample EMR-4 both before and after reduction. It would appear that the *reduced* sample was in fact slightly more oxidized. It is not unreasonable however to speculate that the ultra-small iron particles actually experienced a more oxidizing environment by being raised to a temperature of 300°C while in intimate contact with a highly acidic support surface (even though the ambient atmosphere contained 25% H_2).

From the results presented in Chapter VII, the concept that addition of Ru in bimetallic supported MVS preparations leads to enhanced reducibility of the Fe, is consistent with catalytic results on these bimetallics. Although such reduction can be of an extent much less than one formal oxidation number, it may certainly be sufficient to cause a readily observable difference in catalytic activity and selectivity.

4.3.3 Examination of the Unimetallic Ni, Pt and Bimetallic Materials

Examples of narrow range XPS scans of the Pt($4f_{7/2}$), Pt($4d_{5/2}$) and Ni($2p_{3/2}$) peaks are presented in Figures 4-5, 4-6 and 4-7 respectively. The results of binding energy determinations for various unimetallic Ni, Pt and bimetallic Ni/Pt samples are recorded in Table 4-2. Among the experiments conducted were comparisons between anaerobic and air exposed platinum/silica samples. Also the data allow comparisons between silica and alumina as the support material (in unimetallic Pt examples), and

a similar examination of the effect of bimetallic incorporation to that which was reported for the iron/ruthenium system.

The reason why both Pt($4f_{7/2}$) and Pt($4d_{5/2}$) values are reported in the present study, is that for alumina supported samples, the Al(2p) peak interferes with the Pt($4f_{7/2}$) peak. Therefore, Pt($4d_{5/2}$) binding energies have been reported instead. The intensity of this alternate peak was still about 50% of that of the Pt($4f_{7/2}$) peak; thus there was no experimental difficulty in using it. For one of the Pt/SiO_2 samples, both Pt binding energies are reported, but generally only one was measured.

Examination of the platinum binding energies revealed little difference with respect to support pretreatment temperature, for the silica-supported virgin materials. In all of the cases, the values were consistent[67,71] with literature values for Pt(0). Although they were slightly shifted upward from the bulk Pt(0) values, the shifts are well within the range expected on the basis of size effects alone.

The Pt($4f_{7/2}$) values reflect modest increases (ca. 0.5 eV) for virgin samples which were air exposed. Considering the size of the platinum particles (which are known to have essentially unitary dispersion), dissociative chemisorption of a monolayer of oxygen, resulting from the air exposure, would have been expected to produce a stiochiometry very close to PtO (i.e., 1:1). Hence, unless adsorptive bonding of a much weaker nature had occurred, at monolayer coverage, the small binding energy shift is indicative of incomplete surface oxidation of the clusters. It must be noted that for PtO, a shift of at least 2.0 eV relative to Pt(0) should have been observed if complete formation of $(PtO)_n$ had taken place. It is also important to consider the lack of peak broadening upon oxygen adsorption. This provides evidence that the charge transfer involved in the chemisorptive bonding of the oxygen is completely delocalized. The observed peak widths, along with the 0.5 eV shift would seem to suggest that the most appropriate model for the air exposed system, is that of a 1:4 O:Pt stoichiometry having a fully (fourfold) bridged-bonded structure. The infrared data (dealing with CO adsorption after air exposure on these same materials) reported in Chapter VI, are also consistent with this model. The reader will likely recall that after adsorption of some oxygen on the platinum materials, a reactive removal (forming CO_2) and CO replacement was not seen to occur; rather, CO stretching frequency shifts were better explained by considering that enough room on the surface was available for CO and (probably dissociated) O_2 to co-adsorb.

The shift of about 0.8 eV upon comparison of alumina and silica-supported platinum clusters (in the virgin materials) may be regarded as evidence of a support effect which is electronic in nature. The magnitude of the shift seems surprisingly high, but once again the level of experimental error should be

considered. It is not beyond reason to suggest that the binding energy shifts could be closer to between 0.4 and 0.5 eV.

Interestingly, a comparison of the Pt($4d_{5/2}$) binding energies for alumina supported uni- and bimetallic platinum particles indicates that no observable charge transfer took place between the two metals when Ni was also incorporated in the virgin samples.

The results for the Ni($2p_{3/2}$) binding energies shown in Table 4-2a demonstrate very similar effects experienced by Ni, as for Pt. A difference of about 0.4 eV was observed, comparing SiO_2 and Al_2O_3 as the support materials (with the Al_2O_3 having, as one would expect, a slightly greater potential for withdrawing charge from the cluster). Furthermore, again examining the binding energies observed for the uni- and bimetallic virgin materials, one finds that metal to metal charge transfer did not take place.

The Pt($4d_{5/2}$) binding energies tabulated in both parts of Table 4-2 are consistent with zerovalent platinum, while the Ni($2p_{3/2}$) values are all consistent with those measured for oxidized nickel[70]. In the case of the hydrogen reduced samples, the differences in Pt($4d_{5/2}$) binding energies between the unimetallic and bimetallic samples are likely within experimental error, although one might alternatively conclude that a very slight difference in valence state did exist. The Pt($4d_{5/2}$) binding energy values were not significantly changed by the hydrogen reduction procedure, which is entirely as expected on the basis that the virgin materials contained Pt(0).

The Ni(2p3/2) binding energy value for the reduced EMR-22 (unimetallic) sample is 2.2 eV lower than that of the corresponding, hydrogen reduced bimetallic. Actually this value is consistent with bulk NiO, whereas the values near 856.0 eV could possibly be assigned[70] to species such as Ni_2O_3 or $Ni(OH)_2$. However, the most reasonable explanation for the lack of upward shift, in the unique case of reduced EMR-22, is that of size effects. The electron microscopy and EXAFS (Chapter IX) work have revealed that the reduced unimetallic MVS material had an average particle size larger than 1 nm, while the other samples were considerably smaller[a]. It is perhaps rather unfortunate that the above noted size

---

a in the case of the reduced bimetallic sample, in which the nickel and platinum phases of an individual particle are known (cf. EXAFS study, Chapter IX) to be segregated, XPS size effects would be expected to be related to the size of the nickel phase.

effects tend to obscure conclusions that one might otherwise be able to make regarding metal-to-metal charge transfer in this system.

The occurrence of shakeup structure (as indicated in Figure 4-7) for supported nickel cluster materials is somewhat unusual. It should be noted that although the figure shows only one member of the Ni(2p) doublet and its shakeup signal, similar shakeup structure occurred as well on the (not shown) Ni($2p_{1/2}$) peak. The relative intensities and distance from the parent peaks were the same for both. The existence of this structure cannot be explained[72] by either Ni^0 or low spin Ni^{+2} (such as in model compounds having square planar geometry). Therefore, it would suggest possibly high spin Ni^{+2}. The validity of this notion is strengthened by the observations of superparamagnetic Ni particles within the present work (cf. Chapter V on Electron Paramagnetic Spectroscopy experiments). As is discussed in that chapter, such particles are believed to be anchored to the surface by oxidized nickel, i.e., Ni^{+2} species.

4.4 Summary of the XPS Study

All of the XPS data collected during this group of experiments show good agreement with those data obtained via other techniques (FTIR & Chemisorption, EPR/FMR, catalytic results etc.). They also fit well with expected trends, as discussed in the relevant literature; a particular consequence of the present observations is that they provide good evidence for unusually low valence states[a] (compared with conventional supported materials of even larger particle sizes).

An interesting difference between the Ni/Pt pair and the Fe/Ru pair was the tendency for the latter to experience metal to metal charge transfer, while in the former case, such was not as convincingly observed (although metal to carrier charge transfer was significant, at least for the virgin materials). At the present time, sufficient data are not available to demonstrate whether metal to surface charge transfer would occur to a similar extent in the Fe/Ru system.

A first attempt at rationalizing this behaviour involved considering the Pauling electronegativity values of the elements in question. As it turned out however, the differences between the

---

a one may recall for example, that the European standard Pt/SiO_2 material (discussed in greater detail in Chapter VIII) was found to contain Pt(II); also, states of Ru lower than +3 are uncommon for materials produced by hydrogen treatment of typically used Ru(III) precursors.

electronegativities of Fe and Ru, and those of Ni and Pt are both 0.37 (in Pauling's units). Hence, the XPS results are not satisfactorily explained by comparing the electronegativities of the zerovalent elements. Using the Allred-Rochow system of electronegativities, one would expect that the Fe/Ru system should be the one for which metal to metal charge transfer would not occur. This is even less consistent with the present results.

A more realistic treatment of the concept of how likely charge transfer is, between various elements, involves standard redox potentials[73]. Of course, one cannot obtain such values for supported cluster systems, but the use of acidic solution data is not entirely without value; furthermore, what is sought is only a qualitative explanation. The reader will be aware that both silica and alumina are mildly to strongly acidic carrier materials, hence this choice is reasonable.

In applying the redox treatment of the observations, the XPS data were used to choose reasonable oxidation states for each of the elements. These were assumed to be Pt^0, Ni^{+2}, Ru^{+2} and Fe^{+3}. Table 4-3 shows the standard reduction potentials for these oxidation states to their most likely alternative states. In the case of Ni, both the 0 and +1 states are considered in the table, however the qualitative picture is the same whichever is used. The standard cell potentials obtained by coupling the Fe/Ru and Ni/Pt pairs are respectively, +0.521 V and -1.347 V. This demonstrates that oxidation of Ru^{+2} to Ru^{+3} and simultaneous reduction of Fe^{+3} to Fe^{+2} is thermodynamically allowed, while a similar charge transfer for Pt^0 and Ni^{+2} (or Ni^{+1}) is not. Of course, this is a rather oversimplified analog to the supported cluster systems, however its usefulness is obvious.

Both of the models used to explain the patterns of catalytic selectivities for the two bimetallic systems, are reinforced by the present XPS results. The Fe/Ru model was based on assumptions related to (and requiring) electron transfer, vis a vis the concept that incorporation of Ru allowed the Fe also present to be more *reducible*. The same model also provided an explanation of the effects of increased loading in unimetallic iron samples, diminishing the average Fe oxidation state (since the surface is believed to have only a limited capacity for oxidizing incoming precursor atoms).

The bimetallic surface model which has been invoked to explain the catalytic results on the Ni/Pt system, was founded on the assumption that the observed phenomena were not due to electronic interactions, but rather, a solely geometric effect. Since the present XPS data reveal only weak evidence of barely measurable electronic interactions in the bimetallic system, there is some justification for rejecting a competitive model, which would explain the catalytic selectivities according to a perturbation of the electric field experienced by the reactant(s) when the second metal is incorporated.

	E_o (V)
$Ni^{+2} + 2e^- \longrightarrow Ni^0$	-0.257
$Pt^0 \longrightarrow Pt^{+2} + 2e^-$	-1.090
$Pt^0 + Ni^{+2} \longrightarrow Pt^{+2} + Ni^0$	-1.347
$[Ni(CN)_4]^{-2} + e^- \longrightarrow [Ni(CN)_3]^{-2} + CN^-$	-0.401
$Fe^{+3} + e^- \longrightarrow Fe^{+2}$	+0.771
$Ru^{+2} \longrightarrow Ru^{+3} + e^-$	-0.249
$Fe^{+3} + Ru^{+2} \longrightarrow Fe^{+2} + Ru^{+3}$	+0.521

Table 4-3 Standard Reduction Potentials for Fe, Ru, Ni and Pt in Acidic Aqueous Media

CHAPTER V

Magnetic Resonance Characterization Studies

Ferromagnetic Resonance (FMR) and Electron Paramagnetic Resonance (EPR) spectroscopies have been utilized in the task of characterizing MVS generated supported metal cluster materials. These techniques are not only useful in terms of examining the magnetic properties of such materials, but since the magnetic properties themselves reflect a great deal of information about the spatial, structural and electronic nature of the specimens, they can provide a very detailed description of MVS products.

The application of magnetic resonance characterization methodology is presented here by using but a few examples of the MVS materials which have been synthesized during the research project. In particular, supported nickel cluster materials have been studied in some detail, however an extension of the presently reported study to iron containing specimens (and possibly even platinum containing specimens, for which the technique of Conduction Electron Spin Resonance (CESR) would be employed) would have been equally feasible.

5.1 General Theory of Ferromagnetic and Paramagnetic Resonance

5.1.1 Analytical Capabilities of Magnetic Resonance Spectroscopy

In dealing with supported metal materials, the following form of a spin Hamiltonian is applicable[74] in order to describe the energy of the transitions which are of interest.

$$\hat{H} = \beta \, \mathbf{H} \cdot \mathbf{g} \cdot \hat{\mathbf{S}} + \hat{\mathbf{S}} \cdot \mathbf{A} \cdot \hat{\mathbf{I}} + \hat{\mathbf{S}} \cdot \mathbf{D} \cdot \hat{\mathbf{S}} \qquad [5.1]$$

This expression is simplified relative to the general form of a spin Hamiltonian, since it only considers isolated paramagnetic centres (which may be atoms, ions or molecules). Smaller terms involving crystal field, nuclear Zeeman, nuclear hyperfine and nuclear quadrupole effects, have not been included in [5.1]. The terms which have been included relate to the resonances caused by the applied magnetic field of the spectrometer (through the magnetogyric g-tensor), interactions of the electronic and nuclear

spins (through the nuclear hyperfine tensor $\hat{A}$), and zero-field interactions (through the spin-spin splitting tensor $\hat{D}$). The information contained by these three tensors provides extensive characterizational data about the paramagnetic systems for which they can be determined. In practice[75], their values are elucidated by using the spin Hamiltonian [5.1] to perform computer simulation (i.e., curve fitting) of recorded EPR/FMR spectra. An important aspect of this simulation requires the correct orientation of the axes of the paramagnetic centres in the material being examined, with respect to the axis of the applied magnetic field of the spectrometer. Also, the proper averaging over all possible orientations of the paramagnets must be carried out in the case of microcrystalline and amorphous materials.

Elucidation of the electronic Zeeman g-tensor yields a description of both the ground state and excited state electronic orbital configurations of the paramagnetic system. Furthermore, from the pattern into which components of this tensor may be split, one can draw conclusions regarding the symmetry of the environment of the paramagnetic centres.

The electronic spin - nuclear spin coupling term provides insight into the isotropic and dipolar contributions of the hyperfine and superhyperfine tensor $\hat{A}$. From this, it is possible to derive information about the unpaired electron spin density residing in s, p, d, etc. orbitals of the atoms constituting a paramagnetic centre.

The fine structure (spin-spin) coupling term becomes relevant only in systems where $s>½$ (i.e., high spin systems of isolated paramagnets). The $\hat{D}$ tensor components relate details about the spin-orbit, dipole-dipole and exchange coupling terms. This is useful (in high spin systems) for extracting the energy level characteristics of atomic and molecular orbitals which experience spin orbit coupling; mean distances between electronic spins which are magnetic-dipole coupled; and exchange energies.

Up to this point in the theoretical discussion, systems of isolated or *magnetically dilute* paramagnets have been considered. In dealing with supported metal cluster materials, this is not the only situation which is of interest. It is often essential to include terms in the spin Hamiltonian to account for weak but significant interactions between the paramagnetic centres. These are in the form of distance dependent dipole-dipole and exchange coupling components included in the fine structure term (as pointed out by Abragham and Bleany[74] and by Weltner[75]). In the analysis of EPR lineshapes for systems which experience such interactions, one uses a pairwise interaction model (which includes an appropriate distribution of distances between the paramagnetic centres) in order to deconvolute dipole broadening and exchange narrowing contributions.

The transition between systems which may be regarded as isolated paramagnets and those which are more appropriately described[76] in terms of dominant inter-paramagnetic interactions is expected to be related to the progression of sizes of supported metal clusters. In the case where positive exchange energies are involved, one would be dealing with multi-domain ferromagnets, which with decreasing particle size become single-domain superparamagnets. It is precisely these systems (and ranges of particle sizes) which were of greatest interest in the present study; a concise treatment[13] of their ferromagnetic resonance properties is presented in the following section.

5.1.2 Magnetic Resonance Spectroscopy Theory

The resonance condition for absorption of microwave radiation by a paramagnetic material (such as in an EPR/FMR experiment) is given by the following expression:

$$h\nu = g\beta H_o = h\omega_{res} \qquad [5.2]$$

where h represents the wavelength of the microwave radiation, and H_o is the externally applied magnetic field vector. The resonant frequency may be further expressed as:

$$\omega_{res} = \gamma H_o = \frac{g\beta}{h} H_o \qquad [5.3]$$

by rearrangement of [5.2]. The above is applicable to the case of non interacting paramagnetic centres.

In solid samples, the theoretical treatment must be concerned with strong exchange interactions between atoms; essentially all unpaired electron spins will be coupled at temperatures well below the Curie Temperature T_c. Here, the exchange integral J has a positive value, and excitation of the sample results in a spontaneous magnetization of the ferromagnetic state. The ferromagnetic state typically has a magnetic moment which is four to five orders of magnitude larger than that of an isolated paramagnetic system. The total magnetic moment precesses about the direction of the applied field vector, at an angular frequency which is given by:

$$\omega_{res} = \gamma H_{eff} \qquad [5.4]$$

In this expression, the effective resonance field H_{eff} has two contributions given by:

$$H_{eff} = H_R + H' \qquad [5.5]$$

in which H_R is the resonance field position, and H' is an adjustment arising from the magnetic anisotropy field. As will be discussed in greater detail later, H' is dependent on the nature of the specimen, particularly on both its size and shape.

A ferromagnetic particle having dimensions below those of a Weiss domain (about 10 nm) has an axis of easy magnetization, much like that of a single crystal. In the absence of an applied magnetic field, the total magnetic moment of such a particle remains aligned with this axis. The temperature dependence of the total magnetic moment of a single domain ferromagnet is similar to that of a paramagnetic ion or molecule, however the major difference between the two systems, is that the former has a total moment which is thousands of times greater than that of the latter. This effect in single domain ferromagnetic particles has been termed superparamagnetism. The temperature dependence of the magnetic moment, in these situations, is formally described[13] by the Langevin equation.

When examining ferromagnetic particles, it is usually found that exchange coupling dominates over dipole-dipole coupling. This leads to an observation of rather narrow FMR lines. With progressively smaller ferromagnetic particles, thermal randomization of the magnetic moments greatly reduces the total magnetization, thus leading to a decrease in the dominance of exchange coupling. As the relative contribution of the dipole-dipole coupling therefore increases, a broadening of the FMR signal takes place. Another size dependent feature, is that the temperature dependence of larger particle ferromagnetic resonance line widths is quite distinct from that of smaller particle superparamagnetic resonance line widths. In the case of ferromagnetic nickel particles for example, FMR linewidths are almost invariant between 4 and 300 K, then show broadening as the temperature approaches the Curie temperature (which for Ni, is 631 K). In the contrasting case of superparamagnetic nickel particles, the approach to the Curie point produces line narrowing. The latter effect can be attributed to the aforementioned thermal randomization of the magnetization vector of the particle, which brings about a reduction in the effective anisotropy by averaging the internal anisotropy field.

5.1.3 Contrast and Comparison of EPR and FMR Resonances

According to the previous sections, there are many factors which affect the magnetic resonance linewidths, as well as the lineshapes and g values. Figure 5-1 presents a summary of the factors and their relationships to the observed spectroscopic patterns. The following is a somewhat more detailed contrast between EPR and FMR than that which has already been discussed.

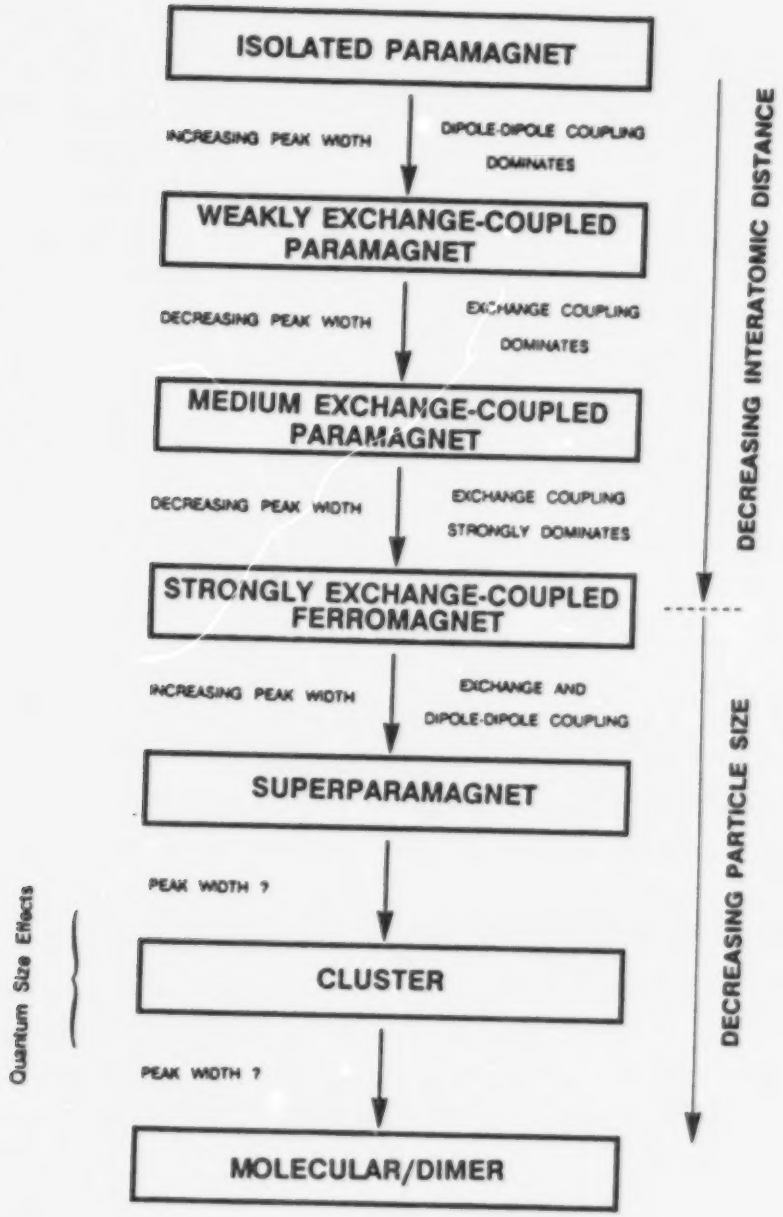

Figure 5-1 a Trends in Magnetic Resonance Parameters for Various Systems on Support Surfaces

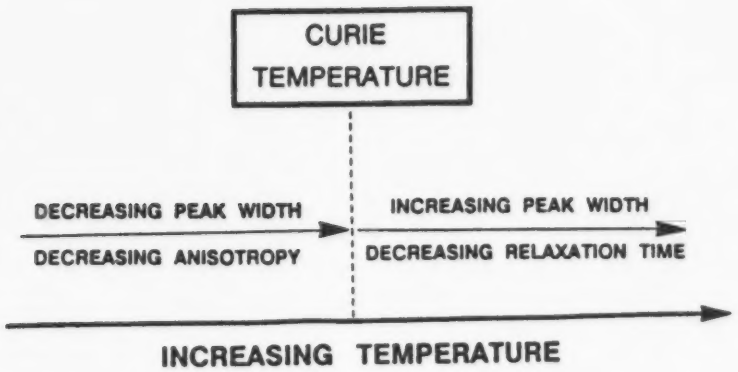

Figure 5-1 b The Temperature Dependence of Magnetic Resonance Linewidths

It is interesting that EPR and FMR resonances can often be observed in the same experiment. The major phenomenological difference[13,74,75,76] between the two is that FMR signals involve the collective magnetic moments of many paramagnetic centres within a particle, whereas EPR signals are produced by the excitation of isolated (or having insignificant interactions) paramagnetic centres.

In the FMR situation, the observed resonance position is shifted from that given by:

$$H_o = \frac{h\nu}{g\beta} \qquad [5.6]$$

due to magnetic anisotropy field contributions (shape, magnetocrystalline and magnetostriction influences). Also, these same contributions give rise to broadening and distortion of the observed lineshape. In superparamagnetic particles, internal anisotropy fields are encountered as a result of preferred orientations of the magnetization vectors. When the anisotropy energy becomes comparable to the thermal energy kT, an averaging of the anisotropy field is caused by rapid thermal fluctuations of the magnetization vector. This results in a reduction in the effective anisotropy observed.

At the (X-band) frequencies used in collecting EPR/FMR data, the measurement time is about 0.1 ns. Whenever the fluctuation time of the magnetization vector is well below this value, the particle will behave as a superparamagnet, and whenever it is much greater, the particle will be ferromagnetic. At some temperature defined as the *blocking temperature*[13], the experimental measurement time and the magnetic fluctuation time will be equal.

5.2 Special Magnetic Properties of Nickel

Nickel is a particularly favorable material to study using FMR spectroscopy, because of its low value[76] of the bulk magnetocrystalline anisotropy field. This is given, in general by:

$$H_A = \left| \frac{2K_1}{M_s} \right| \qquad [5.7]$$

where K_1 is the first order magnetocrystalline anisotropy constant, and M_s is the saturation magnetization. Furthermore, the relatively low Curie temperature is advantageous. Both iron and cobalt have considerably larger magnetocrystalline anisotropy values and higher Curie temperatures[76]. Because in the case of nickel, complications due to magnetic anisotropy are not severe, one can directly obtain thermomagnetic curves[13] from a temperature dependent survey of FMR signal intensities. This is useful in demonstrating superparamagnetic behaviour (which yields straightforward limits on the possible sizes of the metal clusters examined), determining the Curie temperature of the system being analyzed, and using these to establish the particle size distribution of the sample.

The observations of superparamagnetic behaviour may be easily discerned from the FMR data, by noting a shift in the line position toward the true g-value upon increasing the temperature. This results from a corresponding increase in the extent of averaging out the magnetic anisotropy field; thus the anisotropy becomes small relative to the intrinsic linewidth of the FMR signal. With increasing temperature, the observed linewidth also becomes narrower and approaches the intrinsic linewidth, which is itself temperature dependent (due to relaxation time effects).

The limiting g-value (which corresponds to the absence of anisotropy) is represented by:

$$g_{app} = \frac{h\nu}{\beta H_R} \qquad [5.8]$$

and is equal to the g-value for the bulk material. For fcc nickel, this is reported[76] to be between 2.21 and 2.22.

Signal intensities in FMR/EPR spectroscopy are determined by taking the double integral (over the required band) of the derivative signal which was recorded in the instrumental run. It provides a measure of the magnetic susceptibility of the material which was analyzed. The magnetic susceptibility versus temperature or *thermomagnetic* curves can be used to estimate the particle size distributions of paramagnetic supported metal cluster samples. In order to accomplish this, it is necessary to utilize either Langevin[13] functions to fit the thermomagnetic curves, or in the case of the smallest particles (for which quantum size effects play an important role), Brillouin[77] functions. These functions are theoretical expressions for the magnetic susceptibility; each is size dependent. Therefore, the methodology required to extract particle size distribution estimates from real data obtained for a polydisperse sample, would be to fit a weighted series of Langevin (or Brillouin) functions to the thermomagnetic curve. The weighting would be based on particle size distributions expressed in polynomial form. The available resolution in this procedure would depend on the degree of the polynomial chosen, however successful application of this would in turn depend on the intrinsic noise level in the magnetic susceptibility curves.

The Langevin and Brillouin functions are both expressed in terms of the volume of the paramagnetic particles. The P.S.D. therefore obtained would be the volume basis representation. As with the P.S.D. determined by chemisorption methods (area basis representation), and the number basis P.S.D. from CTEM measurements, all can be interconverted by assuming a geometry for the particles.

One possible advantage of the magnetic method of extracting particle size distributions, is that unlike the other two methods there is a capability of also elucidating the particle shapes. This can in principle, be accomplished by examining the asymmetry of the derivative lineshape[13]. These asymmetry parameters can further provide insight into the metal particle / support surface interactions. For this purpose, one examines contributions to the anisotropy term arising from shape and magnetostriction (stress/strain) factors. It is also possible[13] to treat more complex distortions of FMR lineshapes using these same factors in the computer simulation (fitting) of the recorded experimental data.

5.3 Experimental Details

5.3.1 Procedure and Spectrometer Details

EPR/FMR spectra were collected for powder samples. As with most of the experimental work detailed in this document, anaerobic conditions were maintained for all of the runs, except those in which a deliberate oxidation of the sample material was desired. The mass of sample typically required was about 100 mg for the MVS materials. This material was introduced into the instrument in 3 mm i.d. (iron free) quartz tubes.

The EPR spectrometer used, was a Varian E4 model. The sample, when introduced into the microwave cavity of the instrument was able to be cooled to temperatures as low as 6 K (although for the present study acceptable results were obtained at a minimum temperature of 123 K), and heated to temperatures well above ambient. The highest temperature used to record data in this study was 533 K.

Spectra were collected using the X-band microwave frequency (9.4 GHz) at optimum power settings between 0.1 and 10.0 mW. The magnetic field range scanned was from 0 to 6000 G of applied field. The calibration required in order to determine exact g-values was accomplished by running EPR spectra of the standard DPPH (diphenyl picryl hydrazyl) along with each experimental run.

5.3.2 Experiments Conducted

As stated in the introduction, only nickel samples were examined in the presently reported work. These were the alumina supported specimens; the reason for their choice in preference to the silica supported MVS materials, was that the particular silica has an iron impurity content sufficiently high to be troublesome, whereas the alumina does not. Both the sample whose support was pretreated at 200°C and whose support was pretreated at 800°C were investigated.

The behaviour and temperature dependence of the magnetic properties were examined for virgin materials, as well as materials which were subjected to oxidation (both by air exposure at ambient temperatures, and the very severe treatment with undiluted O_2 at 260°C). In order to conduct a thorough investigation of the temperature dependent behaviour, several heating/cooling cycles were performed. This afforded the possibility of observing whether various phenomena were reversible or not.

5.4 Results of the EPR/FMR Investigation

5.4.1 Supported Nickel Sample on High Temperature Pretreated Support

Perhaps the more interesting of the two samples examined via magnetic characterization methods, was the Ni/Al_2O_3 MVS material whose support was pretreated at 800°C. This was the carrier surface which would have been expected to have the lowest initial hydroxyl concentration before impregnation of the tris-ethylene nickel(0) precursor. The EPR/FMR spectrum for this sample, measured at 123 K, is presented in Figure 5-2. The broad, almost isotropic signal (having a measured g-value of 2.145 and peak-to-peak width of ca. 880 G) has, superimposed on it, a triplet of resonance lines whose shape indicates orthorhombic symmetry. The g-values for the three resonances were 2.870, 2.138 and 2.051. The broad FMR resonance is attributed to nickel clusters, while the orthorhombic triplet of EPR features indicates a paramagnetic Ni^{+1} centre which is anchored to the surface. That this species is indeed interacting with the surface, can be concluded on the basis of the low degree of symmetry; if such unpaired electron density were delocalized on a nickel cluster (of nearly spherical shape) a more isotropic signal would have been observed. The extremely unusual valence state of +1 for nickel has been observed in other carrier-supported systems (generated by thermal and photolytic reduction of the nickel +2 state). The supports included various oxides and zeolites. As an example of this, a Ni^+ / SiO_2 material was found[13,84] to have orthorhombic g-tensor values of 2.64, 2.30 and 2.015.

The temperature dependence of the above observations provides considerably more information about carrier supported MVS nickel materials. Upon warming the sample to 293 K, and reexamining the magnetic resonance spectrum, it was found that the Ni^{+1} signal was no longer observable, and that the basically unperturbed (although somewhat less intense) FMR signal remained. This spectrum is shown in Figure 5-3. The process was completely reversible on re-cooling the sample to 123 K.

In a further experiment, the same sample was heated to 533 K. The corresponding EPR/FMR spectrum is shown in Figure 5-4. As before, there was a disappearance of the Ni^{+1} signal, but contrastingly the FMR signal also changed. The g-value shifted to a new position of 2.004 (from the former value of 2.145); also, the peak-to-peak linewidth decreased slightly from 880 to 840 G. When a final spectrum for this series was taken, again at 123 K, the Ni^{+1} feature returned, however the FMR signal had irreversibly changed: the g-value was slightly shifted from its original value of 2.145 to 2.169, and the linewidth increased from 880 G to 1100 G.

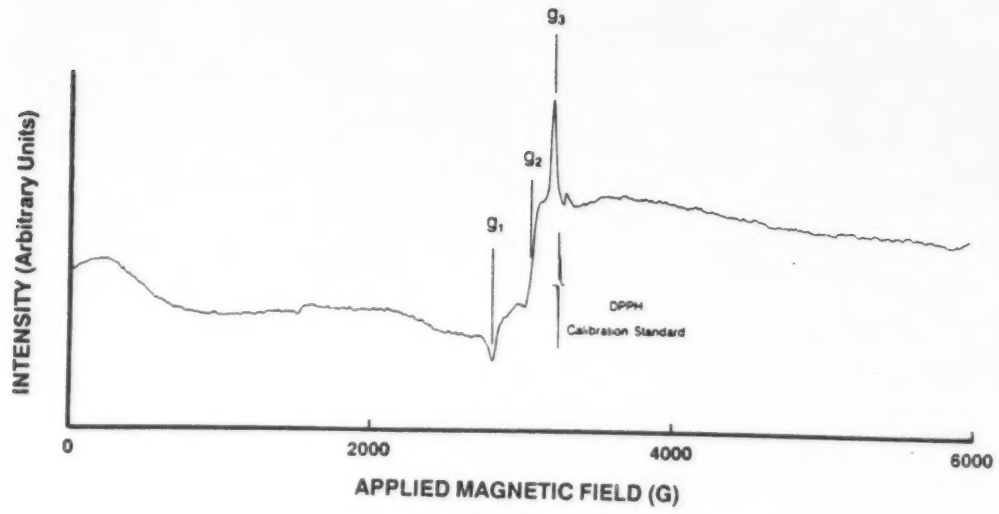

Figure 5-2 EPR/FMR Spectrum of a Ni/Al_2O_3 MVS Material (800°C Pretreatment) Taken at 123 K

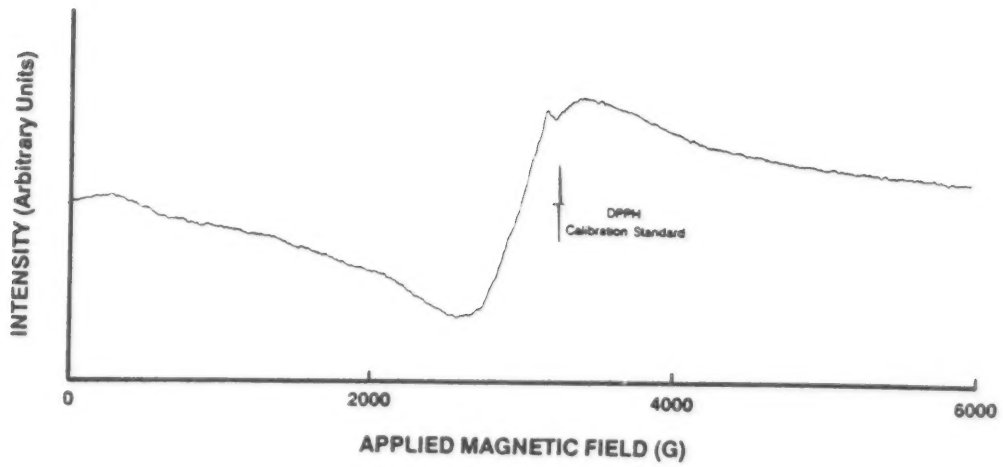

Figure 5-3 EPR/FMR Spectrum of a Ni/Al_2O_3 MVS Material (800°C Pretreatment) Taken at 293 K

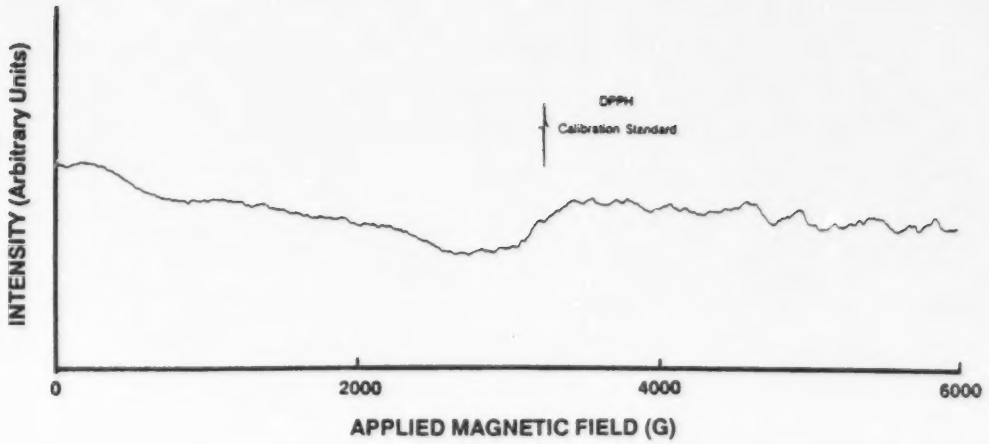

Figure 5-4 EPR/FMR Spectrum of a Ni/Al_2O_3 MVS Material (800°C Pretreatment) Taken at 533 K

A different experiment, in which the 800°C pretreated nickel sample was oxidized (even ambient temperature exposure to air was sufficient) demonstrated that the Ni^{+1} signal was not seen. It should be pointed out here that the likeliest change (i.e., creation of Ni^{+2}) would produce an EPR silent entity. In addition to this effect, air exposure caused an irreversible change in the characteristics of the FMR features. The signal itself became temperature independent after oxidation of the sample, and the g-value relocated to a value near 2.000 (with the peak width becoming approximately 800 G).

5.4.2 Supported Nickel Sample on Low Temperature Pretreated Support

The other MVS material subjected to EPR/FMR experiments was the nickel/alumina material for which the support pretreatment temperature was 200°C, and hence which would have a relatively higher degree of initial surface hydroxylation.

As before, the initial spectrum was recorded at a temperature of 123 K. This is presented in Figure 5-5. The most obvious similarity between the initial spectra for the two samples, was the presence of the broad FMR signal attributed to supported nickel clusters. However, for this sample the Ni^{+1} spectral features were not observed.

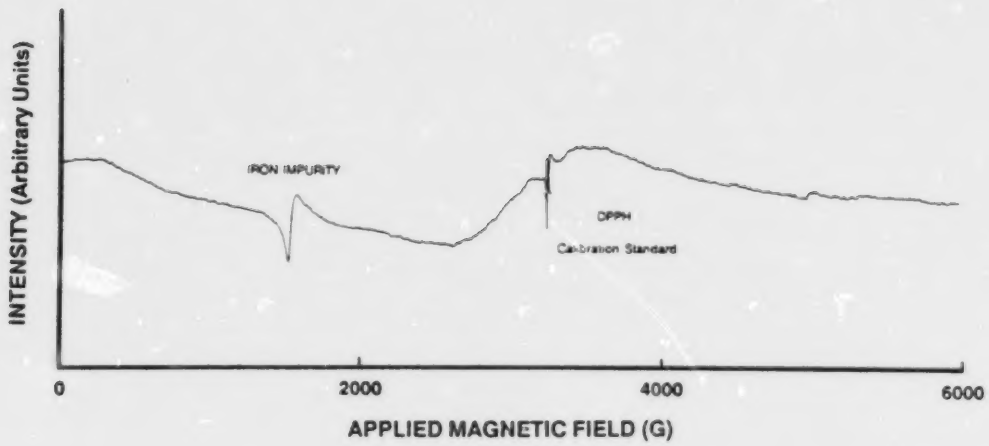

Figure 5-3 EPR/FMR Spectrum of a Ni/Al_2O_3 MVS Material (800°C Pretreatment) Taken at 293 K

The remaining observations of thermomagnetic behaviour, with the concomitant changes induced by the various treatments and temperatures at which spectra were collected, revealed that the two samples were very similar (other than for the absence of Ni^{+1}).

5.5 Discussion of Magnetic Resonance Spectroscopy Results

The structure of the alumina support material has a defect spinel crystal lattice[78], which when thermally treated can have surface groups which display amphoteric properties. Such surface groups are often described[79] as Brønsted acid (terminal -OH), coordinatively unsaturated oxygen Lewis base (terminal -O) and oxygen vacancy Lewis acid (Al^{+3}) sites. Through the application of analytical techniques[79] such as surface titrations, calorimetry, vibrational spectroscopies and MAS-NMR, much is now known about the effects of thermal treatment of aluminas on the distribution and properties of the different surface groups. In fact, one can easily achieve a good degree of control of the desired surface characteristics of the carrier. At treatments around 200°C, the Brønsted sites remain dominant, at 400-500°C a roughly equal number of Brønsted and Lewis acid sites will be produced; at 800 to 1000°C, there would be mainly Lewis acid sites (for a material whose BET surface area was around 200 m^2/g).

The nature of the Lewis acid and base sites also depends on their coordination numbers. With lower coordination number, the terminal -O (Lewis base) sites become more strongly basic; similarly the Lewis acid sites become more strongly acidic with decreasing coordination number [80,81,82,83].

It is obvious that the available degree of control of the characteristics of carrier materials is potentially useful in studying the anchoring and nucleation of supported metal clusters, the charge transfer effects experienced by the clusters, and the degree of resistance to sintering possessed by such clusters.

Considering the EPR/FMR results for the two samples which were investigated, it is immediately apparent that the properties of the nickel clusters were indeed sensitive to the population and characteristics of the surface groups on the carrier prior to the precursor impregnation. This result was not well emphasized by many of the other analytical techniques used. For example, neither CTEM particle sizes nor catalysis results revealed any but the most subtle differences between the 200°C and 800°C pretreated MVS nickel samples.

5.5.1 High Temperature Support Pretreated Material

The nucleation of the supported clusters on the 800°C pretreated carrier can be conceptualized by the simple model as shown in Figure 5-6. Removal of surface bound H_2O (dehydration and dehydroxylation) leads to the system which is depicted in the middle portion of the figure. The characteristics are: relatively few remaining terminal -OH groups (these being very spread apart), and a high concentration of Lewis acid (terminal -O) and Lewis base (Al^{+3}) groups[78-83]. During the impregnation of the zerovalent nickel precursor, one might envisage the interaction of Ni^0 with the surface Brønsted acid groups yielding anchored Ni^{+1} centres. This process, although no observation has yet been attempted in order to verify it[a], could involve the simultaneous evolution of H_2 (alternatively the H atoms could abstract O atoms, resulting in H_2O production). It should be mentioned here, that the resulting Ni^{+1} entity has orthorhombic (eg. C_{2v}) symmetry.

For the 800°C pretreated surface, having low total OH population, only a fraction of the nickel precursor delivered would be required to react with all of the Brønsted acid groups. The remaining nickel precursor molecules (readily yielding their Ni^0 atoms) agglomerate on the initially formed Ni^{+1} anchors,

---

a such a determination would be hindered by the very likely adsorption of the hydrogen onto the surface.

thus producing Ni_n^{+q} clusters in the final material. Both the ultimate nuclearities and charge values are dependent upon the total amount of precursor, and the details of the impregnation process.

It is also possible to speculate on the simultaneous agglomeration of a certain amount of Ni^0 on the -O and Al^{+3} surface groups. Clusters thus formed could be well isolated from the Brønsted acid site clusters, or alternatively they could be in the proximity of these. It is actually considered unlikely that stable clusters would agglomerate via interaction with the -O groups, since such clusters would be electron rich (partial negative charge). Contrastingly, the clusters which might be expected to agglomerate at Al^{+3} centres would, like those agglomerated at -OH centres, be electron poor.

This model is entirely consistent with the EPR/FMR observations of a Ni^{+1} species in a field of orthorhombic symmetry, coexisting with superparamagnetic Ni_n clusters. The orthorhombicity is a direct result of the interaction of the Ni^{+1} entity with the surface.

There is also evidence against postulating that the virgin MVS material could contain surface anchored $Ni^{+1}(C_2H_4)_x$ (where x = 1 or 2). In an EPR study of supported $Ni^{+1}(C_2H_4)$ on Ca-X zeolite[84], g-values of 2.643, 2.460 and 1.973 were determined. These are quite different from those determined in the present magnetic resonance study.

The thermomagnetic behaviour of the MVS generated nickel particles in the temperature range of 123 to 533 K, followed the expected trend for superparamagnetic species. It may therefore be concluded on the basis of the size dependent blocking temperature[13,76], that these particles were definitely smaller than 5 nm.

The observations of almost isotropic lineshapes and small changes in the peak-to-peak linewidths over the range of 123 to 293 K, imply that the carrier supported nickel clusters had almost spherical shape. This is very interesting in the light of CTEM particle size determinations (wherein the reader may recall that the particles have been observed to be of subnanometre dimensions). The resolution of shapes, which would require three dimensional information, is not available in the CTEM method. Now that the assumption of spherical geometry may be taken to be valid, it becomes easy to interconvert, and hence compare the particle size distributions obtained using different analytical methods (CTEM, Chemisorption, and FMR/EPR).

At the high temperature limit of the observations (533 K), the g-value of 2.004 was found to be quite different from that for bulk nickel[76] (namely about 2.22). This implies that either the particles had

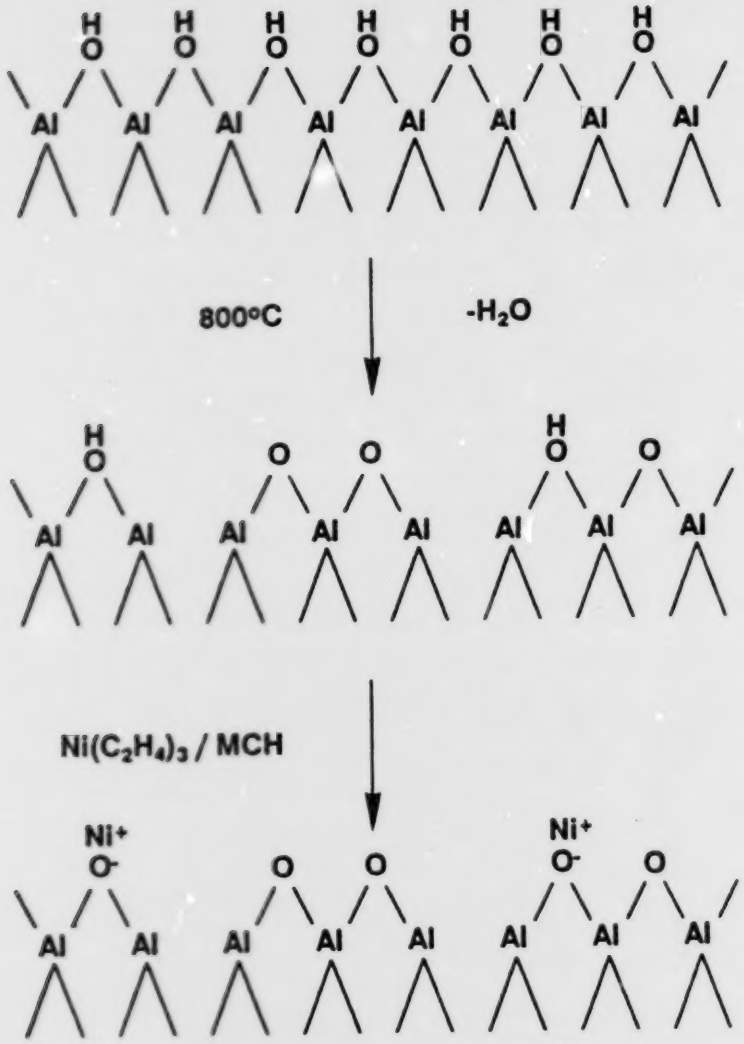

Figure 5-6 Model of Support Pretreatment and Nickel Particle Nucleation Processes for High-Temperature Pretreated Alumina

a net charge different from zero, or that they were small enough to experience quantum size effects. In the event that quantum size effects did control the magnetic properties of the clusters under these circumstances, a treatment of the data would require a quantum mechanical approach rather than a classical one. For such an approach, one would be concerned with the question as to whether the average spin magneton number of nickel was cluster size dependent[77].

Another aspect of the temperature dependent magnetic behaviour of the system suggested the possibility of an interaction between the Ni^{+1} and Ni_n^{+q} entities at the support surface. This was reflected in the rather unusual relaxation behaviour of the Ni^{+1} surface site, which in turn can best be explained by the close proximity of some other paramagnetic or superparamagnetic centre. A fully consistent description of the system could even be that the nickel clusters are anchored by the Ni^{+1} entities.

The present data do not provide evidence against the existence in the system, or participation in surface anchoring, of Ni^{+2}. This species is EPR silent as a result of either local crystal field distortions, and/or extremely fast relaxation effects[13,74,75,76]. Furthermore, until a quantitative estimate of the number of nickel atoms (both as Ni^{+1}, and in the agglomerated clusters) can be made, it is not possible to conclude that the actual Ni^{+1} concentration could be very small.

The final EPR/FMR spectrum taken at 123 K, following heating to 533 K showed a small increase in the g-value (from 2.145 to 2.169) and an increase in the peak-to-peak width (from 880 to 1100 G) with maintenance of the almost isotropic lineshape. This is indicative of sintering, however this is very minimal, and consistent with both chemisorption and CTEM (following catalysis) results. In no observed case, for any high temperature treatment, did the average particle size surpass 2.0 nm. The resistance to sintering is thought to be a direct manifestation of the effect of anchoring by Ni^{+1} (and likely also Ni^{+2}) surface sites.

It may be unequivocally stated that air or O_2 oxidation of the MVS material gave rise to an irreversible annihilation of the Ni^{+1} species. Conversion of this to Ni^{+2} is the only reasonable fate of such. Furthermore, the oxidative treatment caused changes in the g-value and peak width of the nickel FMR signal, and the introduction of temperature invariance of the FMR parameters, which are consistent with its conversion to supported $(NiO)_n$. To be somewhat more concise at this point, other stoichiometries (as suggested by the IR/chemisorption of CO on platinum data) for the new phase are possible. The NiO stoichiometry of 1:1 would be correct if the oxidative treatment caused a monolayer of oxygen atoms to be adsorbed onto the (unitarily dispersed) nickel particle surface.

5.5.2 Low Temperature Support Pretreated Material

A model, very similar to that proposed for the 800°C pretreated surface system, is depicted in Figure 5-7. The thermal dehydration/dehydroxylation once again produces a loss of H_2O, but at 200°C the ultimate Brønsted acid (OH) group concentration on the surface remains much higher. As a direct result of this, the probability of having many pairs of vicinal OH groups is also quite high. As shown in the lower portion of Figure 5-7, the incoming Ni^0 precursors, with the loss of H_2 (from reaction with the surface OH groups) and their ligands, can form Ni^{+2} surface species. These, just as with the Ni^{+1} anchors on the other surface, could be envisaged to have acted as nucleating centres for other incoming precursor molecules. This model is consistent with the observed absence of Ni^{+1} for the present sample material. The Ni^{+2} species in this model are also depicted as having a geometry which entails orthorhombic symmetry.

In the low temperature pretreated sample, there was again evidence for superparamagnetic nickel clusters, in fact quite similar to those synthesized on the high temperature pretreated carrier. This is provided by the form, and especially the temperature dependence of the observed FMR data. Because of the similarity in these two samples, it can be concluded that the size and shape of the nickel clusters was very similar in both cases. This agrees with the CTEM work, in which the size similarity was very clearly demonstrated; and also with the catalytic data, which revealed virtually no differences in selectivity or activity for the two materials.

Since, once again there was very high resistance to sintering, some form of efficient surface anchoring of the particles is implied. Although Ni^{+2} could not be directly observed in these experiments, it would be difficult to explain the thermal stability of the particles without assuming anchoring. In further comparison with the other sample, the oxidative treatments produced the same irreversible effects; these would be entirely consistent with the formation of supported oxide clusters (eg. $(NiO)_n$, etc.) anchored to the surface by Ni^{+2}.

5.6 Summary of the EPR/FMR Study

The application of magnetic resonance spectroscopic examinations of Ni/Al_2O_3 MVS materials has revealed several interesting characteristics of such samples, as well as demonstrating the potential importance of this analytical technique.

The information regarding the size of the MVS generated nickel clusters has been found to agree with all of the size estimates obtained through other techniques. In addition, the magnetic resonance characterization has produced some knowledge of the shape of the surface clusters; for the materials examined, a (nearly) spherical geometry has been deduced.

There was strong evidence according to results of the magnetic resonance studies, that an important feature of the MVS generated supported metal particles, was their anchoring to the carrier surface by a charge transfer mechanism. This almost certainly involved Brønsted acid groups which were found on the initially unimpregnated carrier material, after it was pretreated according to carefully controlled procedures. Because of the charge transfer anchoring, the materials gave extremely good resistance to sintering, in both reducing and oxidizing atmospheres, and at high temperatures.

The most appropriate description of the particle/surface anchor, according to the present results, seems to be Ni^{+1} or Ni^{+2} depending on the initial surface population of Brønsted -OH groups. In cases where Ni^{+1} was observed, it was also found to be quite easily oxidized to Ni^{+2}. A summary of all of the reactions involved throughout this study is shown in Figure 5-8.

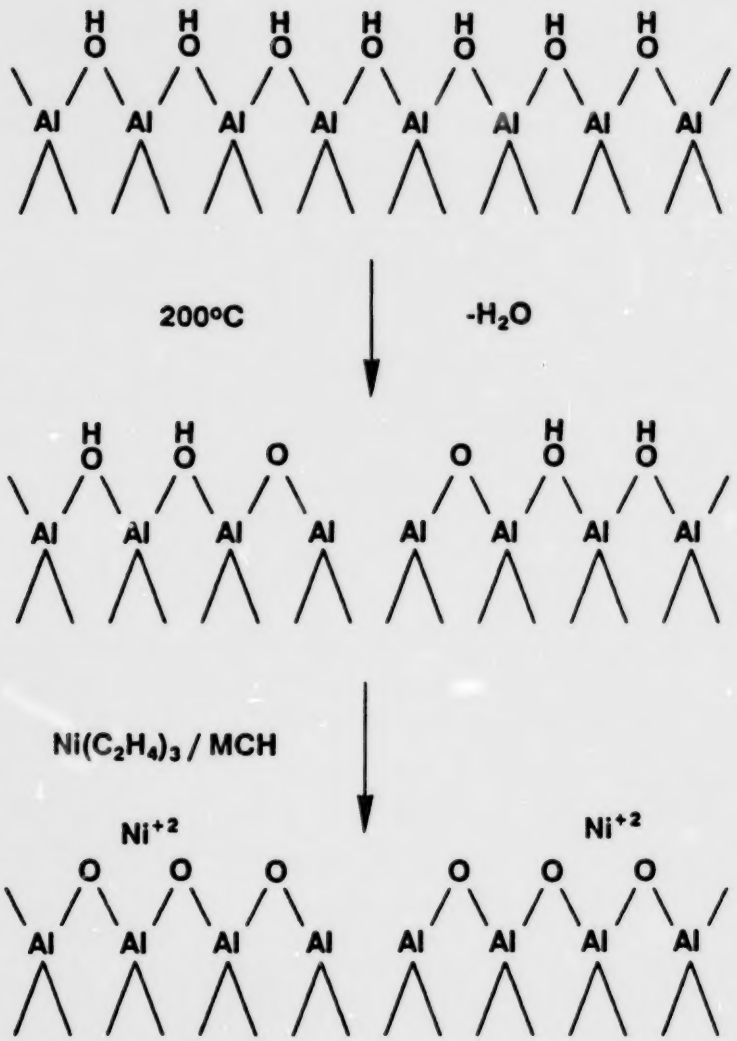

Figure 5-7 Model of Support Pretreatment and Nickel Particle Nucleation Processes for Low-Temperature Pretreated Alumina

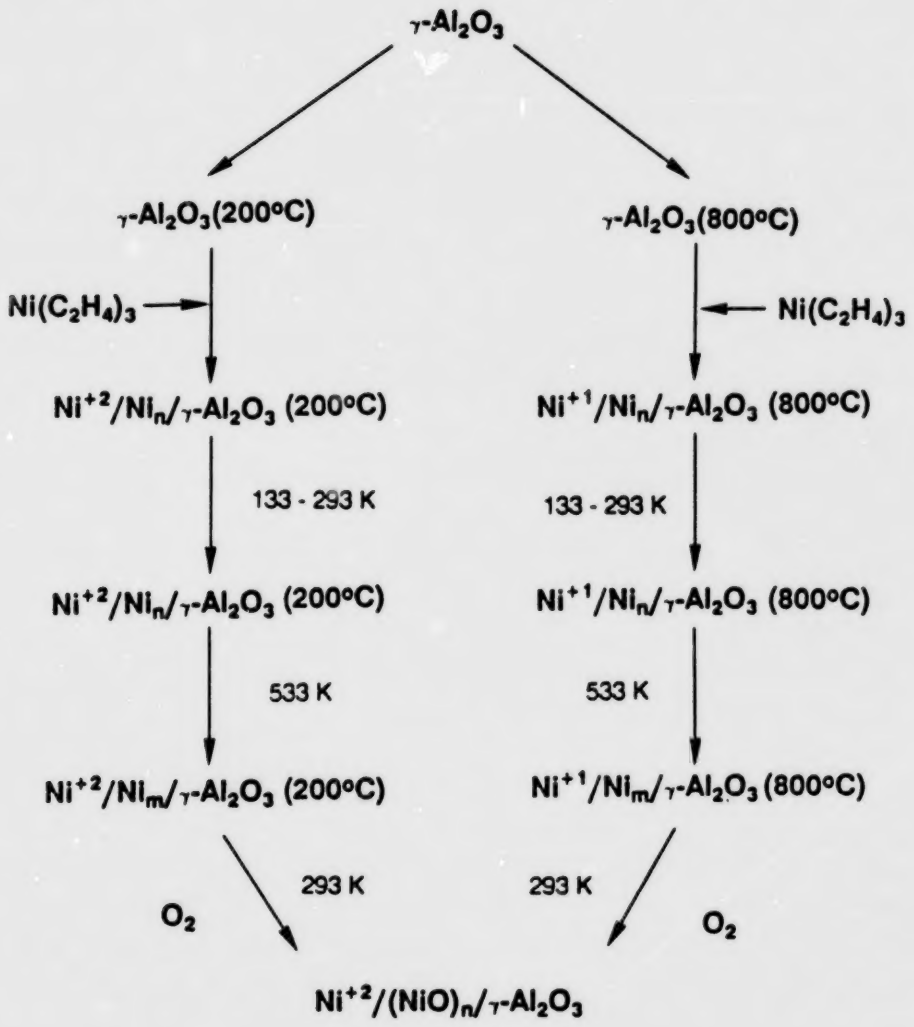

Figure 5-8 Summary of the Synthesis, Anaerobic Heating and Oxidation of MVS Generated Ni/Al_2O_3 Materials

CHAPTER VI

Chemisorption Studies

The use of chemisorption in examining supported metal cluster materials is perhaps one of the most routinely applied characterization techniques. The direct relationship between this phenomenon and catalysis is obvious, yet it will also be seen that chemisorption can be employed to investigate many of the physical properties of these materials as well. Of particular interest here, is the fact that MVS generated supported particles are of such a size that new chemisorption and related phenomena have been observed.

6.1 Mid Infrared Examination of CO Chemisorption on Pt/SiO2

The chemisorption of carbon monoxide onto platinum surfaces, studied through the use of mid-infrared spectroscopy is one of the most extensively mentioned topics in the catalytic literature[52]. This has been applied, not only to bulk metal, thin films and single crystal systems, but also to supported particle preparations (of various size regimes), and to related compounds of the $Pt_n(CO)m$ type (in most cases). It is noteworthy that due to the extremely small size of MVS clusters, such samples represent the greatest departure from the *flat* surface, which has yet been examined using the present technique.

The frequency of the carbonyl stretching mode in chemisorbed CO can be affected by a rather large number of factors which include: the form of the surface (whether small particle or single crystal), the particular crystal face, the particle size, the fractional surface coverage, electronic interaction with the support, and the surface-bonding stoichiometry. Furthermore, experiments in which mixtures of ^{12}CO and ^{13}CO are co-adsorbed or exchanged can provide additional physical information through observations of the coverage dependence of the peak intensities, the shifts of the peak positions, and the lineshapes. Much recent work[53,54,55,56,57,58] has been devoted to the use of isotopic mixtures in order to probe the physical mechanisms which account for both the frequency and intensity changes in IR spectra with respect to surface coverage.

6.1.1 Theory of Coverage Dependent Behaviour

In order to account for the observed changes in CO spectra on metals, as the fractional coverage is varied, it becomes clear that at least five mechanisms may contribute. Of these, a smaller number will usually be seen to dominate. The five mechanisms are:

- Local Field Effects which influence the optical properties of oriented submonolayer coverages of CO on metals.
- Electrodynamical Dipolar Coupling between CO molecules, acting through space.
- Vibrational Coupling between CO molecules, acting through common bonding electrons.
- Chemisorptive Bond Strength Variations in M=CO, acting through the metal.
- Repulsion Effects between vicinal chemisorbed CO molecules.

Of the five mechanisms listed, three are thought[55] to dominate. These are the Local Field Effects, Electrodynamical Dipolar Coupling, and Vibrational Coupling (through metal).

6.1.1.1 Local Field Effects

When electromagnetic radiation interacts with an adsorbed molecule on a surface, the electric field will be different from that of the incident radiation if it were propagating in a vacuum. This is a result of the induction of dipoles (and higher order multipoles) in neighboring molecules, by the incident light. Such a phenomenon accounts for observed[63] solvent-dependent spectral line shifts.

The effect which such local fields have on optical properties has been discussed by Dignam and Moskovits[58]. According to the applicable theory, the dielectric constant of a monolayer of thickness d, and having a density of N molecules per unit area is given by:

$$\varepsilon_n = \frac{1+\left(\frac{4\pi N}{d}\right)\alpha_n}{1-\left(\frac{4\pi N}{3d}\right)\alpha_n} \qquad \varepsilon_t = \frac{1+\left(\frac{4\pi N}{d}\right)\alpha_t}{1-\left(\frac{4\pi N}{3d}\right)\alpha_t} \qquad [6.1]$$

where the subscripts n and t represent polarization normal and tangential to the surface respectively, and the α values are the molecular polarizabilities. Both the dielectric constant and the polarizabilities may be complex. Using this expression, one may then state the fractional decrease in reflectance which is a result of the presence of the adsorbed layer:

$$\left.\frac{\Delta R}{R_o}\right|_p = -8\pi d\nu \cos\varphi \ \text{Imag}\left[\frac{\varepsilon_t-\varepsilon_m}{1-\varepsilon_m}\left(1+\frac{1-\frac{1}{\alpha_m\varepsilon_t}}{\cot^2\varphi-\frac{1}{\varepsilon_m}}\right)\right] \qquad [6.2]$$

$$\left.\frac{\Delta R}{R_o}\right|_s = -8\pi d\nu \cos\varphi \ \text{Imag}\left(\frac{\varepsilon_t-\varepsilon_m}{1-\varepsilon_m}\right) \qquad [6.3]$$

$$\alpha_m = \left(\frac{\varepsilon_n}{\varepsilon_t}\right)\left(\frac{\varepsilon_t-\varepsilon_m}{\varepsilon_n-\varepsilon_m}\right) \qquad [6.4]$$

and where the subscripts p and s refer to polarization of the incident light respectively parallel and perpendicular to the plane of incidence. Here, φ is the angle of incidence, ε_m is the dielectric constant of the metal substrate (reflecting surface), and ν is the frequency of the incident light.

If the case of infrared radiation impinging on strongly reflecting surfaces (which is representative of most metals) is considered, the perpendicular attenuation given by [6.3] will reduce to zero, and the above equations may be simplified to:

$$\left.\frac{\Delta R}{R_o}\right|_p = -8\pi d\nu \sin\varphi \tan\varphi \ \text{Imag}\left(1-\frac{1}{\varepsilon_n}\right) \qquad [6.5]$$

$$\alpha_m = \frac{\varepsilon_n}{\varepsilon_t} \qquad [6.6]$$

Through the combined use of equations [6.1] and [6.5], the decrease in reflectance can be examined as a function of coverage. If, for simplicity, one imposes a Lorentzian lineshape:

$$\alpha_n = \frac{s}{\nu_o^2 + i\gamma\nu - \nu^2} \qquad [6.7]$$

as the form of the molecular polarizability, where ν_o is the centre frequency, γ is the linewidth and s is a constant related to the line intensity; the reflectance attenuation may be expressed as:

$$\left.\frac{\Delta R}{R_o}\right| = -8\pi d\nu \sin\varphi \tan\varphi \ \text{Imag}\frac{\Gamma}{1+\frac{2}{3}\Gamma} \qquad [6.8]$$

where,

$$\Gamma(\nu) = \frac{4\pi\left(\frac{N}{d}\right)s}{\nu_o^2 + i\gamma\nu - \nu^2} \qquad [6.9]$$

Taking the first derivative of equation [6.8], and setting it equal to zero in order to obtain the value of the frequency corresponding to the maximum, one obtains:

$$\nu_{max}^4 = \nu_o^4 + \frac{4}{3}\beta\nu_o^2 + \frac{4}{9}\beta^2 \qquad [6.10]$$

where,

$$\beta = 4\pi\left(\frac{N}{d}\right)s \qquad [6.11]$$

Expanding ν_{max} as a power series in terms of β, than assuming that β is small enough so that only the first order terms are significant, the following approximation may be obtained for the spectral position of the maximum reflectance attenuation:

$$\nu_{max} = \nu_o + \frac{4}{3}\pi\left(\frac{N}{d}\right)\left(\frac{s}{\nu_o}\right) \qquad [6.12]$$

By examining this equation, it can be seen that (to first order) the peak will move to higher frequencies in a linear fashion with respect to increasing surface coverage. Furthermore, this shift depends only on the

parameter s (which is an indication of the oscillator strength of the IR absorber); it is not, according to the present theory, a function of the Lorentzian linewidth.

Figure 6-1 shows predicted IR spectra for carbon monoxide adsorbed on metal surfaces as a function of coverage. These depict results which are due only to local field effects. In observed[64] spectra for CO on platinum(111), the actual spectral shifts were about three times larger than those predicted by local field effect theory alone. For this reason, the present theory will be included, but combined with other phenomena (to be discussed in the following sections) in order to model coverage dependence in experimental data.

6.1.1.2 Dipolar and Vibrational Coupling Effects

Although quite different physical phenomena, dipolar coupling and vibrational coupling have been treated together by Moskovits and Hulse[55] using a single model for the interactions of vibrating CO molecules. The two couplings are considered in terms of a harmonic vibrational potential:

$$V = \frac{1}{2}\sum_{i=1}^{N} f_r Q_i^2 + \sum_{i>j=1}^{N} \beta_{ij} Q_i Q_j \qquad [6.13]$$

where for N vibrating oscillators, f_r is a force constant and Q_i is the displacement coordinate of the oscillator. The $\sum \beta_{ij} Q_i Q_j$ cross term represents the vibrational coupling, wherein the parameter β_{ij} includes both dipolar (through space) and vibrational (through metal) contributions. The above expression was demonstrated to be useful for predicting both coverage dependent frequency shifts, and the intensity patterns for isotopic mixtures of ^{12}CO and ^{13}CO. In applying the theory, CO was assumed to be adsorbed randomly on a planar section of a (100) fcc lattice. Thus, the CO molecules in the model had parallel dipoles, normal to the surface. In order to simulate coverage dependent effects in the analysis, the number of adsorbed CO molecules was kept constant (at fifty), and the size of fcc lattice segment was varied.

A relatively simple extension of the analysis can be accomplished by also including the possibility of having some angle between the vibrating dipoles. This is obvious in the treatment of CO adsorption and its coverage dependence on small particles. At the present time, computer models capable of analyzing such systems are in existence[65] and were routinely used as part of the research reported here.

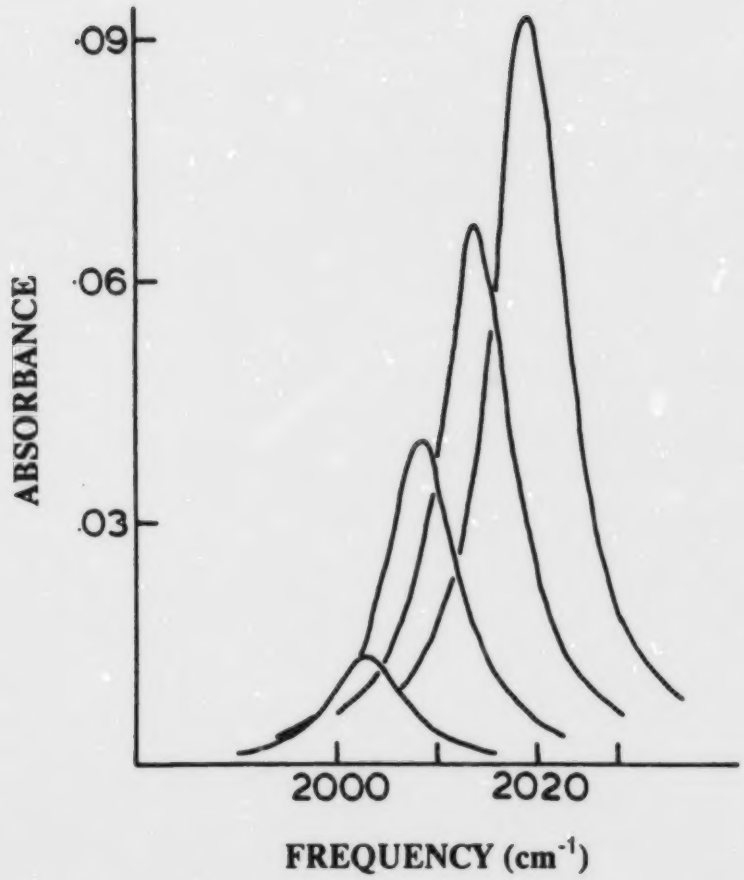

Spectra of submonolayers of a diatomic such as CO on a metal surface, showing the shift in the frequency at which maximum absorbance occurs with increasing coverage. Spectra shown were calculated with $s = 4 \times 10^{-19}$ cm, $\gamma = 9$ cm^{-1}, $\nu_o = 2000$ cm^{-1}, $d = 3$ Å, $\theta_{mc} = 84°$ and coverages of 1,3,5 and 7×10^{14} molecules/cm^2.

Figure 6-1 Predicted IR Spectra of Adsorbed CO as a Function of Surface Coverage According to Local Field Effect Theory (Reproduced from Ref. 58)

6.1.1.3 Through Space Electrodynamical Dipolar Coupling

The coupling cross terms discussed in the previous section have been considered by involving the constant β_{ij}. For dipolar coupling, this is given by:

$$\beta_{ij} = \frac{1}{R_{ij}^3}\left[\left(\frac{\partial\mu}{\partial Q_i}\right)\Big|_{Q_i=0}\left(\frac{\partial\mu}{\partial Q_j}\right)\Big|_{Q_j=0}\right] \qquad [6.14]$$

where μ is the dipole moment of the CO molecules, and R_{ij} is the distance between them. The mathematical form of this expression has been demonstrated[55] to be correct, however the magnitude of this interaction proves to be too weak to account for either the observed frequency shifts or the isotopic intensity ratios.

6.1.1.4 Through Metal Vibrational Coupling

Another possible model for the form of the parameter β_{ij} would be to use the value of the interaction force constant directly, that is:

$$\beta_{ij} = f_{rr} \qquad [6.15]$$

Within this representation, the vibrational coupling is seen to result from the fact that both oscillators interact through the common molecular orbital which they share. This is therefore a *through metal* phenomenon, and applies to systems in which no more than one CO molecule is bound to each metal atom.

Application of this theory (even using a simplified version which only considered nearest neighbor coupling to be significant) demonstrated that observed spectral shifts and isotopic intensity ratios were much better explained than by the dipolar coupling theory.

The same authors[55] considered two model metal carbonyl systems, as a means of examining the effect of adsorption angle. In that study, mixed isotope spectra were collected. Figure 6-2 shows the structures of the two compounds, as well as the IR spectra which reveal important differences in the intensity ratios of the peaks corresponding to the two isotopes (in the figure, the * symbol has been used to indicate the ^{13}CO peaks).

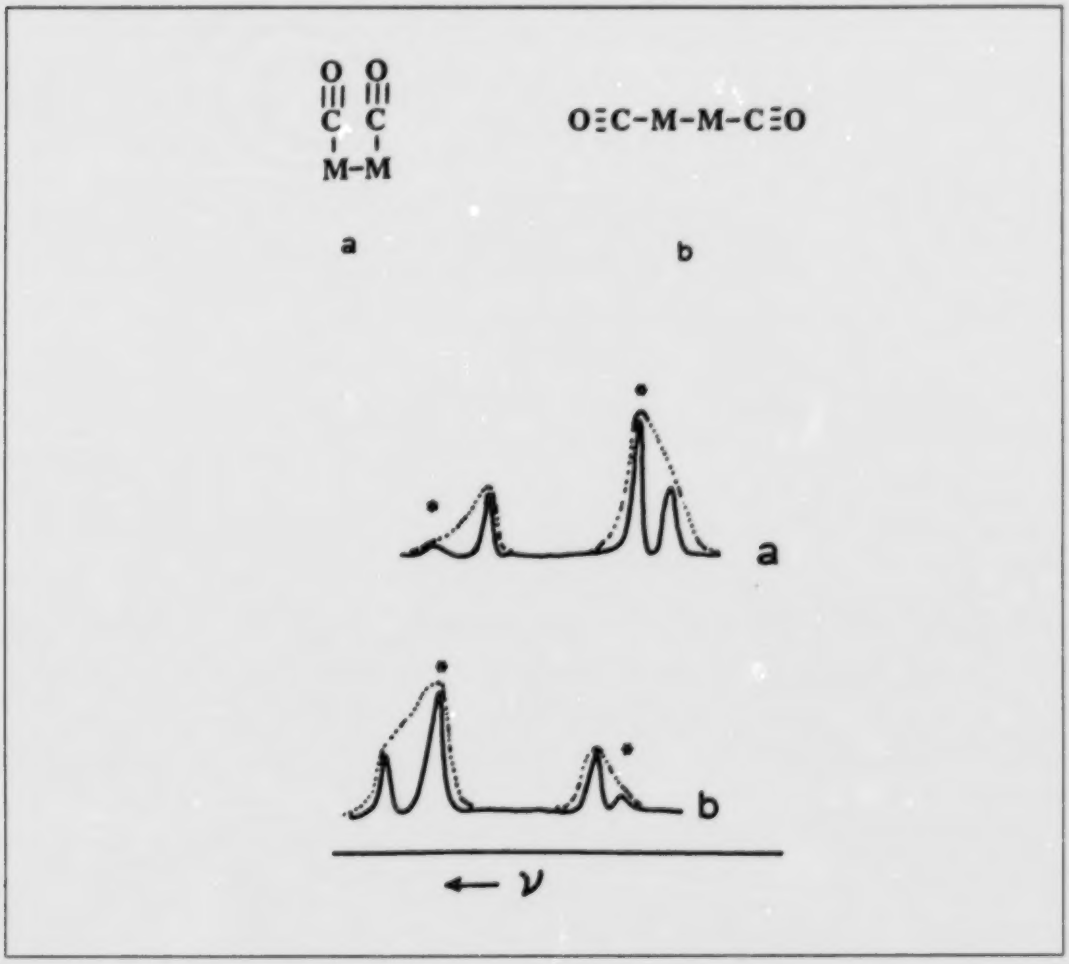

Figure 6-2 IR Spectra of Two Binary Mixed-Isotope Carbonyls (from Ref. 55)

Further application of this theory examined the effects of various fractional coverages and values of the force coupling constant f_m using both ^{12}CO and equimolar mixtures of ^{12}CO and ^{13}CO. Figures 6-3 through 6-5 illustrate the intensity patterns and spectral shifts expected on the basis of vibrational coupling. Typical values of the required coupling force constants have been determined for a number of stable carbonyl compounds. These are listed in Table 6-1.

Using a value of 1.0 mdyne/nm for the force constant f_m, the vibrational coupling theory predicts maximum frequency shifts of 20 cm^{-1} for systems having $N = 4$ nearest neighbors, and 30 cm^{-1} for those having six. In order to predict larger shifts, f_m values in the range of 2.0 to 5.0 mdyne/nm would be required.

Such would suggest some form of enhanced communication between the adjacent CO molecules; possibly this could involve bonding.

6.1.2 Results of IR Examination of Adsorbed CO

A study was conducted in which several Pt/SiO_2 samples in the form of thin pressed wafers were exposed to adsorbent gases, then examined using a highly sensitive Fourier Transform Infrared Spectrometer (Nicolet™ 20 SXB model). Various procedures were employed, including controlled dosing with CO and isotopic mixtures, desorptions, and treatments involving these at various temperatures. Experiments involving oxidations and sintering were also conducted.

As shown in Figures 6-6, 6-7 and 6-8, three spectra were recorded at full coverage for Pt/SiO_2 samples whose supports were vacuum pretreated at 200, 400 and 600°C. All of these displayed a single IR band centered at about 2064 cm^{-1}. In order to carry out an investigation of the coverage dependence of this band, stepwise vacuum desorption runs were conducted employing temperatures ranging from 25 to 150°C. The additional results are also shown in the figures. In all three cases, there was a red shift of at least 66 cm^{-1} (noting that the lowest observable spectrum had a singleton peak position of approximately 1998 cm^{-1}). Examination of the literature has revealed that this is the largest such shift, as of yet reported for supported particle systems. This may possibly be a manifestation of the fact that the present materials represent surfaces having greater curvature than any other conventional materials.

In addition to the observed red shifts and decreases in band intensities upon desorption of the CO, there was a pronounced increase in the bandwidth and a distinct development of asymmetry of the lineshape. The asymmetry had the important feature of appearing as a broadening toward the low frequency side of the band.

In a parallel study using ^{13}CO, similar effects were observed. The band position corresponding to full coverage occurred at 2014 cm^{-1}, and decreased to about 1964 cm^{-1} upon desorption to the minimum observable coverage.

Results for a mixed isotope study on these samples are presented in Figure 6-9. In the particular experiment, the nearly equimolar mixture of 0.45 mole fraction ^{12}CO was used.

Examination of the spectra shows two bands which were resolved, having peak positions of 2048 cm^{-1} and 2016 cm^{-1} and almost equal intensities. The band corresponding to ^{13}CO was found to lie within

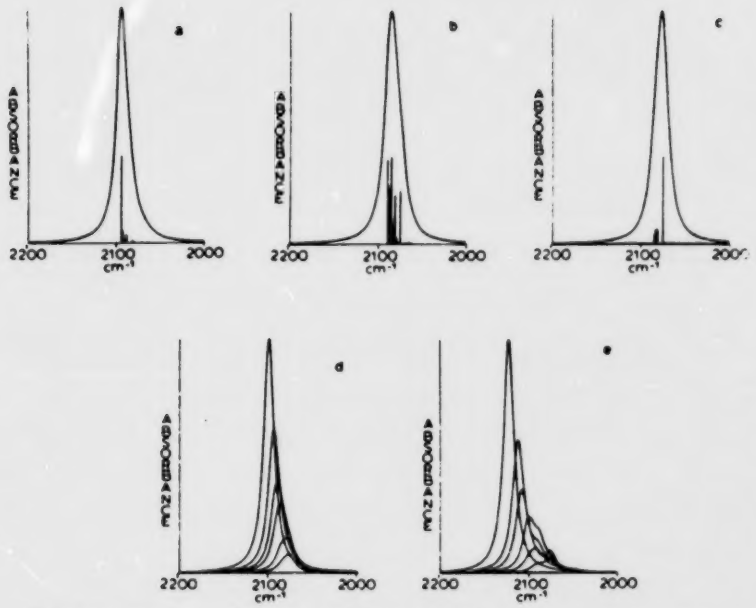

Calculated spectra for ^{12}CO on (100) fcc face. (a–c) Spectra obtained for coverage values of 0.69, 0.39 and 0.10, respectively. The vertical bars give the frequencies and absorption intensities of individual normal modes making up the "observed" spectrum (solid line). (d) A superposition of spectra calculated for coverage values of 0.10, 0.21, 0.39, 0.51, 0.69 and 1.0 scaled according to coverage. Spectra a–d, calculated with f_{rr} = 0.1 mdyn/A. (e) Same ad d but with f_{rr} = 0.2 mdyn/A to show more clearly the broadening at intermediate coverages and subsequent narrowing at high coverages of the spectral linewidths.

Figure 6-3 Simulated CO Spectra Showing the Effects of Coverage and the Vibrational Coupling Force Constant (Ref. 58)

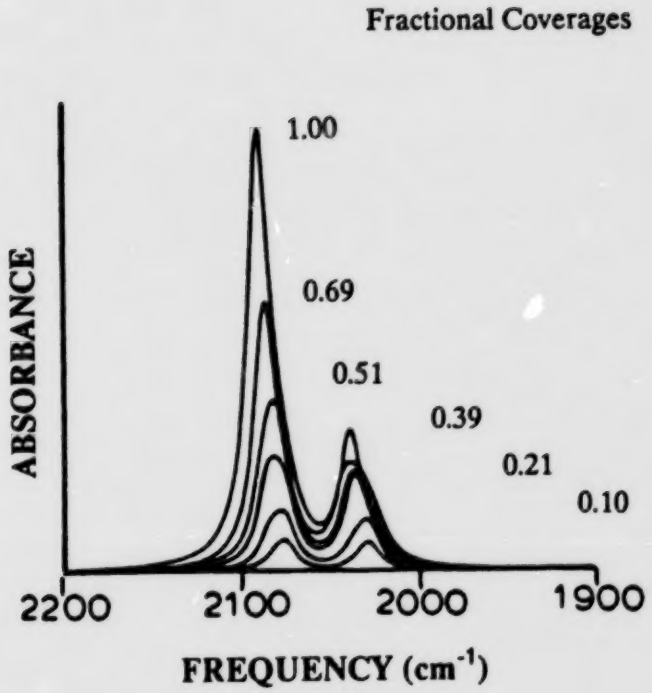

Note: Values Calculated using f_{rr} = 1.0 mdyne/nm

Figure 6-4 Simulated CO Spectra at Various Fractional Coverages for Equimolar Isotopic Mixtures (Ref. 58)

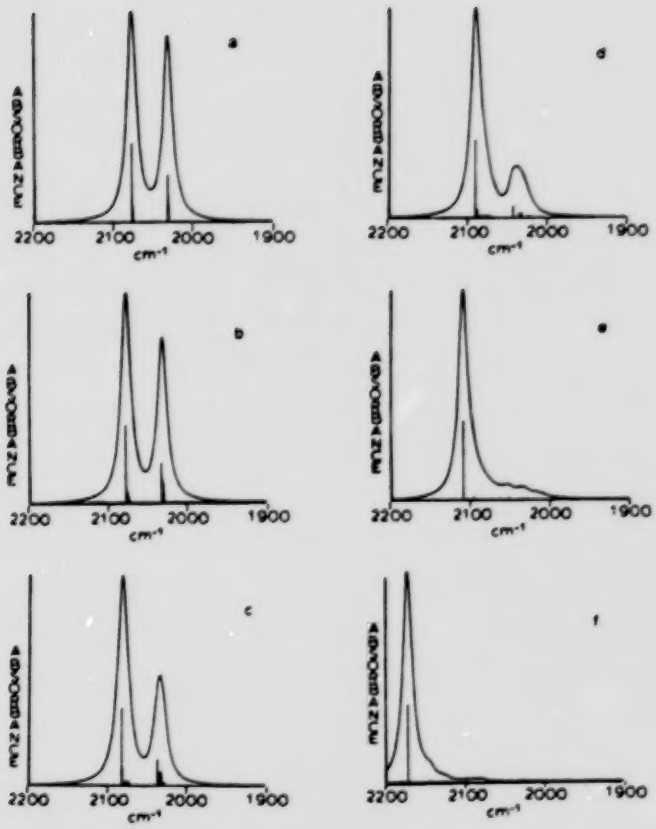

The effect of the value of f_{rr} on the spectrum of an equimolecular mixture of ^{12}CO and ^{13}CO adsorbed on a (100) fcc crystal face at full coverage. (a–f) f_{rr} = 0.01, 0.02, 0.05, 0.1, 0.2, 0.5, respectively.

Figure 6-5 The Effect of the Vibrational Coupling Force Conatant in Predicted Spectra of Equimolar Isotopic Mixture of ^{12}CO and ^{13}CO (Ref. 58)

Compound		f_{rr} (mdyn/A)
$Ni(CO)_2$		0.83
$Ni_2(CO)_2$ (bridge)		0.81
$Cu(CO)_2$		1.08
$Ni_2(CO)_2(N_2)_2$		0.80
$Ni(CO)_3N_2$		0.53
$Cu(CO)_3$		0.62
$Ni(CO)_4$		0.30
		0.35
$Pt(CO)_4$		0.26
$Pd(CO)_4$		0.24
$Cr(CO)_6$		0.26 (cis)
$Mo(CO)_6$		0.27 (cis)
$W(CO)_6$		0.30 (cis)
$Mn_2(CO)_{10}$		0.20 (1,2) [a]
	on same metal	0.24 (1,10)
		0.39 (1,3)
	across M–M bond	0.07 (1,6)
		0.08 (9,10)

[a] Numbers in parentheses refer to the numbering scheme below.

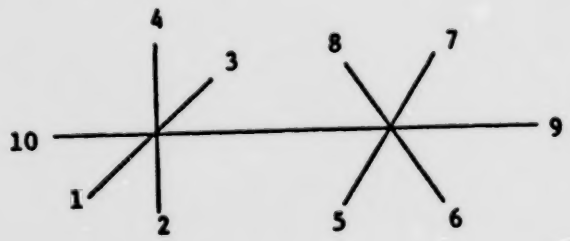

Table 6-1 Force Constants for Carbonyl Stretch-Stretch Coupling in Several Compounds (from Ref. 58)

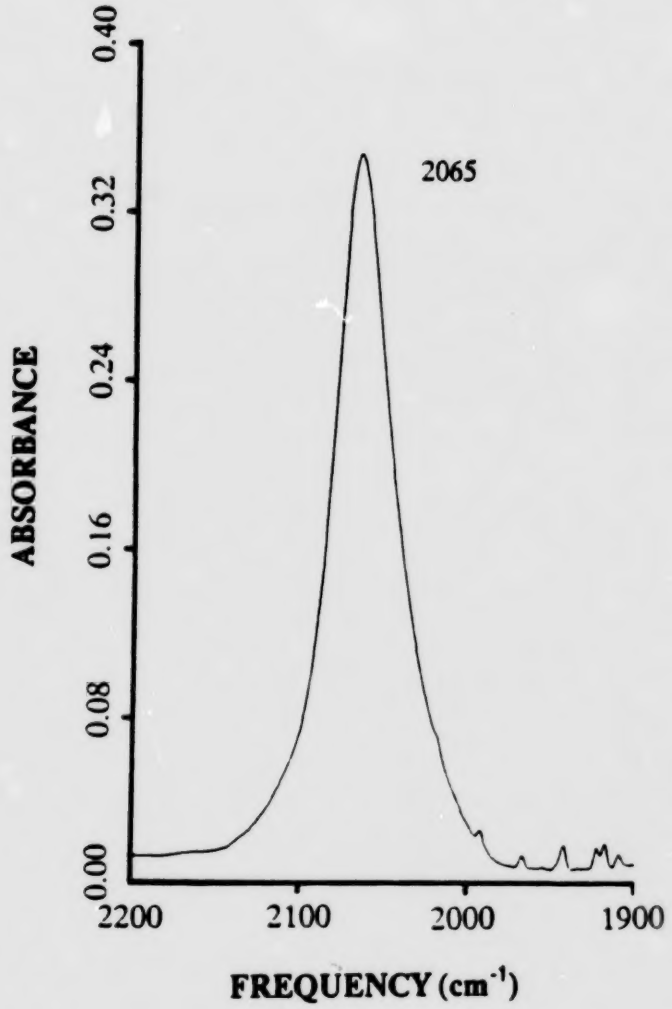

Figure 6-6 IR Spectrum of Adsorbed CO on Supported Pt MVS Material Pretreated at 200°C, at Full Surface Coverage

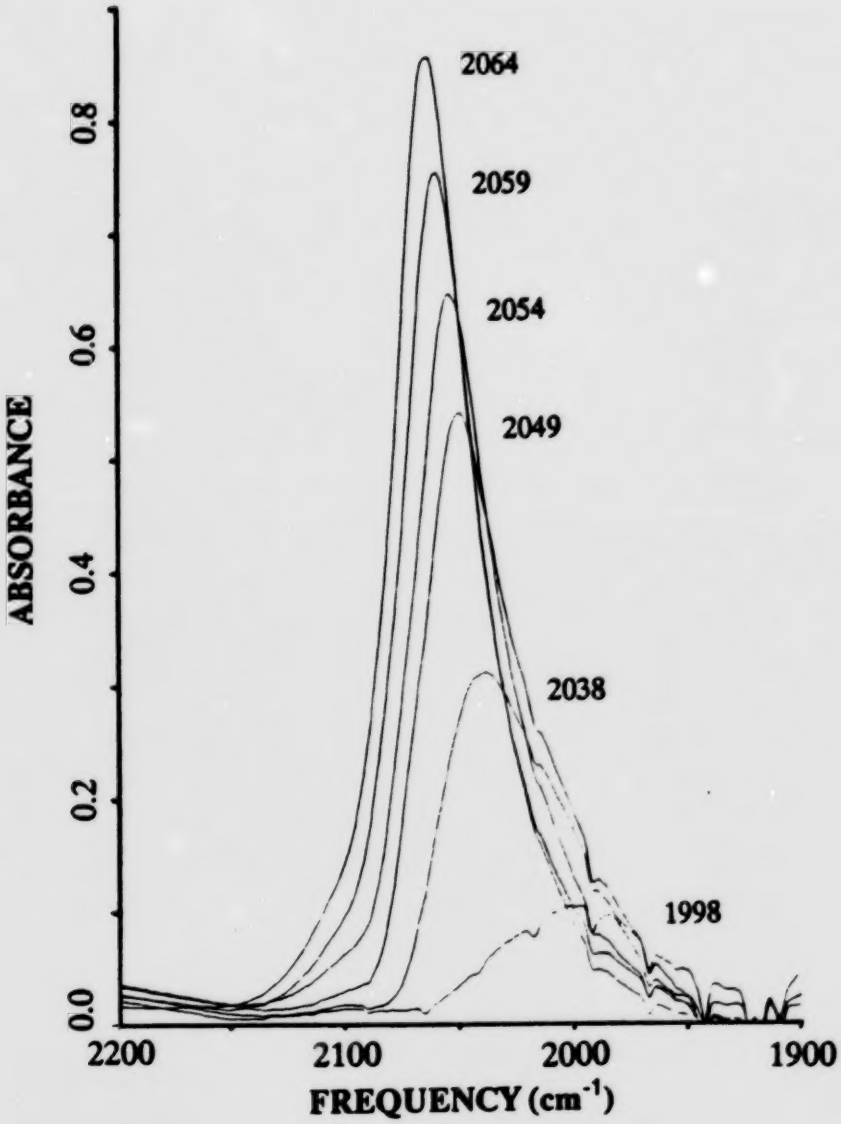

Figure 6-7 IR Spectrum of Adsorbed CO on Supported Pt MVS Material Pretreated at 400°C, at Various Fractional Coverages

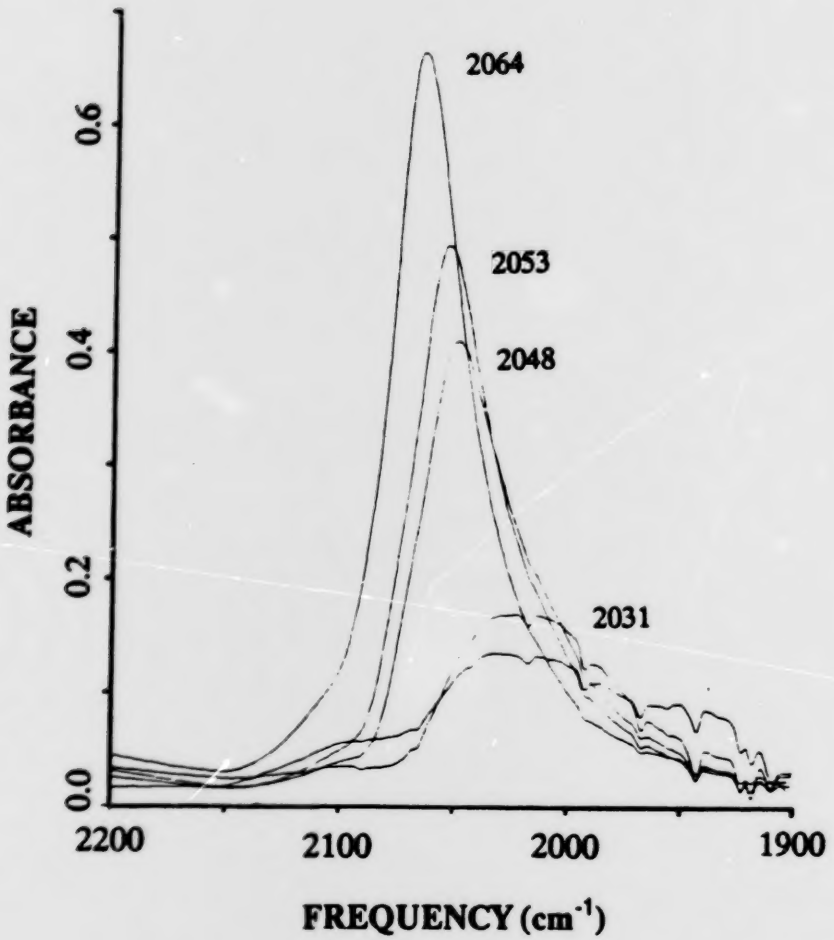

Figure 6-8 IR Spectrum of Adsorbed CO on Supported Pt MVS Material Pretreated at 600°C, at Various Fractional Coverages

2 cm^{-1} of its position, as observed in the pure ^{13}CO results, however the ^{12}CO peak was redshifted by approximately 16 cm^{-1} from its pure ^{12}CO value.

In a final experiment belonging to this group, an oxidative treatment was applied to one of the virgin samples, prior to CO chemisorption and examination in the FTIR. The sample whose support was pretreated at 600°C was subjected to an atmosphere of 101.3 kPa of O_2, at a temperature of 150°C for 60.0 min. Following this, a full-coverage adsorption of ^{12}CO was carried out. The results for this experiment are shown in Figure 6-10. Comparing this with the results for ^{12}CO adsorption on the corresponding virgin sample, a blue shift of 13 cm^{-1} is seen to have ocurred, in addition to a marked narrowing of the IR absorption band.

6.1.3 Discussion of IR Results for CO Adsorption

Upon examining the location of full coverage peak maxima, for the materials used in the IR experiments, it was readily seen that the support pretreatment temperature (hence the degree of surface hydroxylation of the support) did not affect the results. The direct implication of this, is that there were no significant electronic differences among the samples. Such a conclusion is fully consistent with many of the other results obtained, particularly those from X-ray photoelectron spectroscopy. Furthermore, these same results were consistent with expectations (for subnanometre particles), made on the basis of studies of larger particles, planar surfaces and mononuclear model compounds of platinum. Figure 6-11 shows a plot of the full-coverage peak CO stretching frequency as a function of particle sizes; the present data have been included in the figure, and can be seen to demonstrate behaviour consistent with the other data. In a similar manner, the coverage dependent frequency shifts also demonstrate the expected behaviour, as shown in Figure 6-12.

In order to explain the unusually large coverage-dependent frequency shift (66 cm^{-1}), and unusually low peak position (2064 cm^{-1}) at full coverage, one must employ the through metal vibrational coupling model. Neither the local field nor the electrodynamical (dipole-dipole) coupling models were adequate for that purpose. Furthermore, fairly large values of f_{rr} were also required. All of this is consistent with what is expected for CO, strongly chemisorbed onto extremely small platinum clusters.

The mixed isotope ^{12}CO / ^{13}CO results (including both the frequencies and intensity patterns) were also well explained in terms of the through metal vibrational coupling model. This reinforces the notion of significant pairwise interactions between the adsorbed CO molecules, which occur through the metal/metal bonds in the ultra-small clusters.

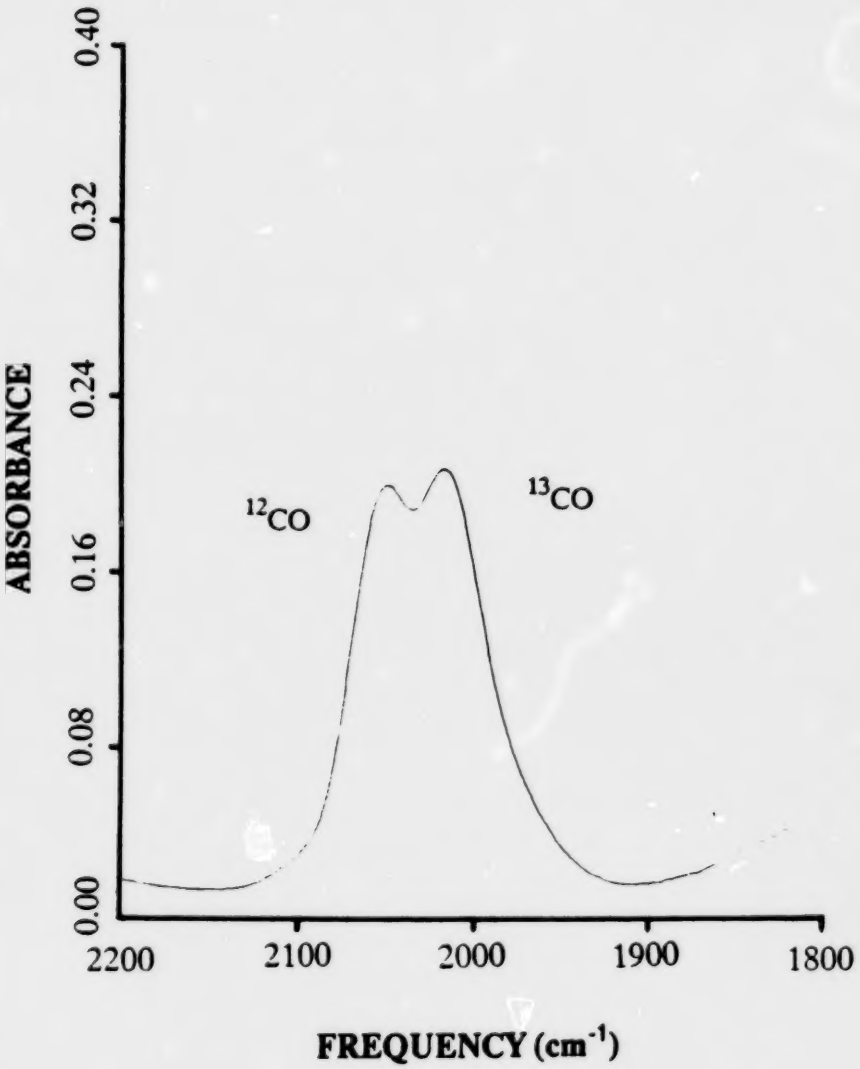

Figure 6-9 IR Spectrum of a $^{12}CO/^{13}CO$ Mixture Adsorbed on an MVS Generated Supported Platinum Material

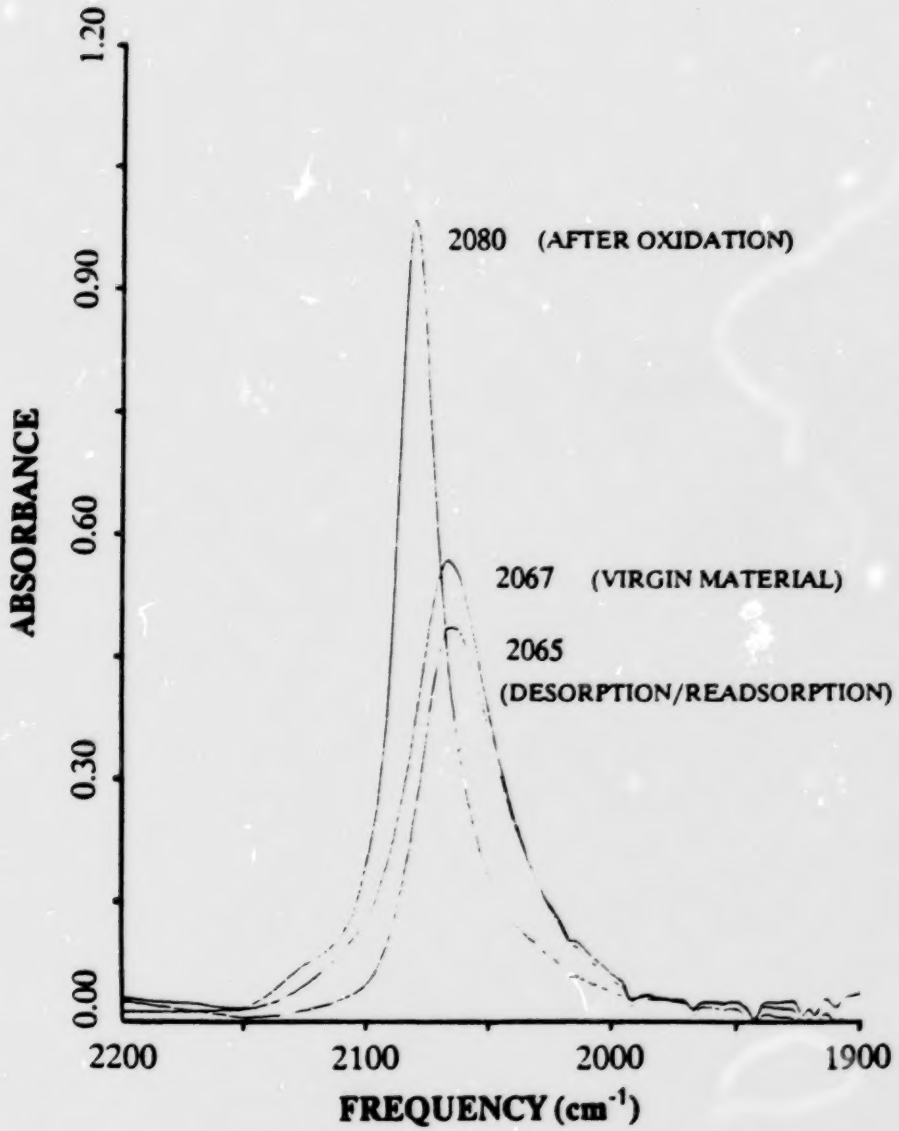

Figure 6-10 IR Spectrum of ^{12}CO Adsorbed on a Pt MVS Sample After Oxidation

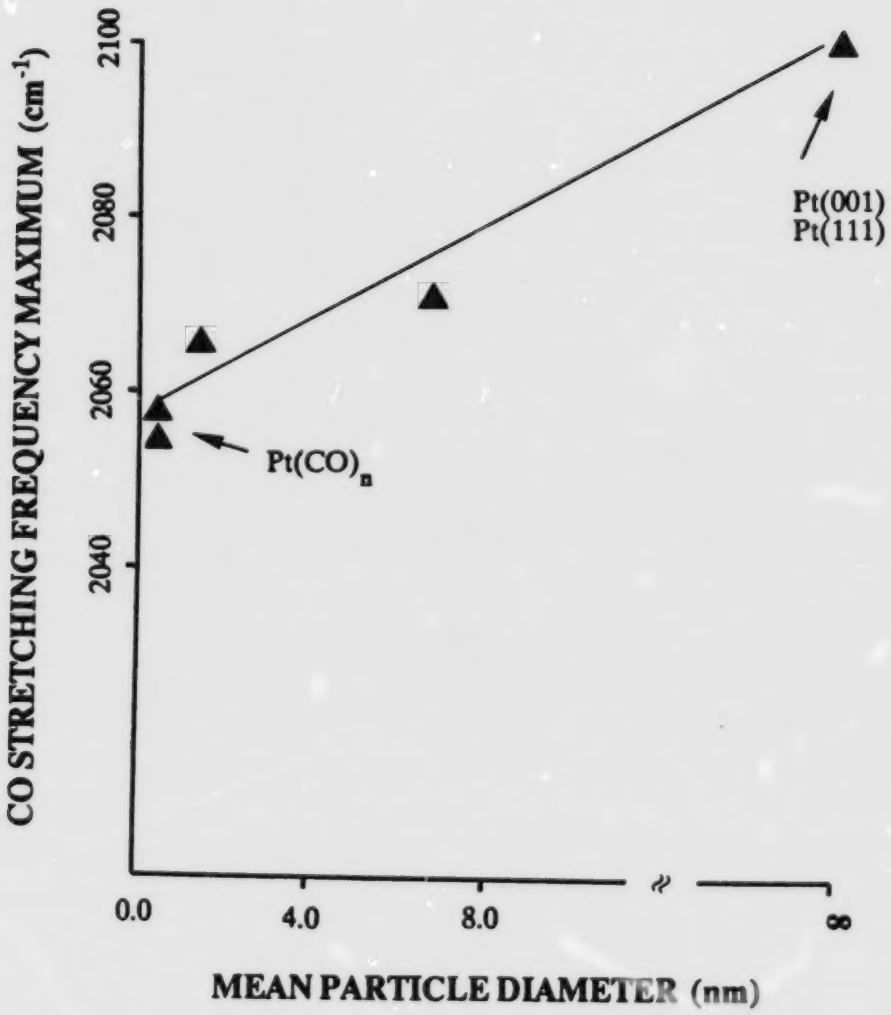

Figure 6-11 CO Stretching Frequency as a Function of Particle Size on Platinum

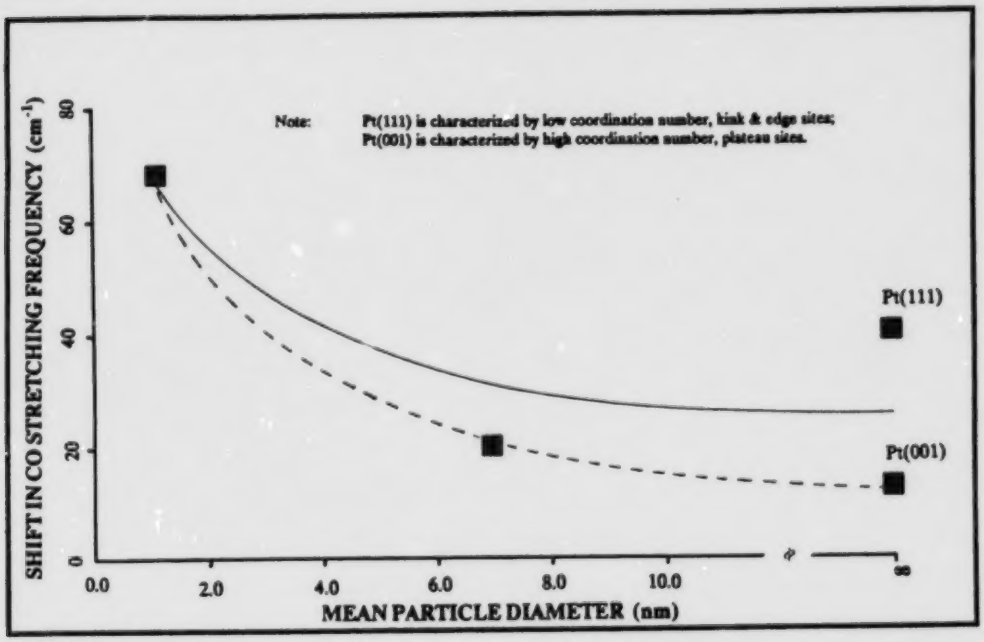

Figure 6-12 Coverage Dependent Frequency Shifts as a Function of Particle Size for CO Adsorbed on Platinum

The observation of increasing linewidth along with the aforementioned asymmetry as the fractional coverage is decreased, is expected[56] for a system in which CO adsorption forms islands at submonolayer coverages. According to this model, some of the CO molecules are completely surrounded by neighboring CO molecules, while others (namely those which occur at the island edges) encounter a less symmetrical environment. At less than full coverages, the resultant differences in coupling force constants would give rise to the pronounced band broadening and the observed asymmetry; such effects would become more apparent with decreasing CO coverages.

The concept of formation of small islands of adsorbed CO (instead of either a uniform and sparse coverage, or formation of one big island) is considered as a thermodynamic rather than a kinetic phenomenon[56]. This is thought to be a manifestation of the competition between interactive (attractive) forces between the CO molecules and the entropy term. Under equilibrium conditions, these two opposing forces become balanced.

Considering chemisorptive bonding in terms of the conventional $\sigma - \pi^*$ (donor acceptor) molecular orbital model, the coverage dependent behaviour can also be explained. According to the model, one expects higher CO stretching frequencies for adsorbed entities which exist on low index (eg. 001) planes, and lower frequencies for those adsorbed on high index planes (eg. 111). This results from the fact that the low index species are found in relatively symmetrical environments (high coordination and more planar surface structure), whereas the higher index species *see* more edges, kinks and a generally lower overall coordination. The shifting to lower frequency with decreasing coordination is interpreted in terms of the enhanced delocalization of charge from the metal orbitals into the π^* orbitals (having appropriate symmetry) of the adsorbed CO. An extreme case of this low coordination is represented by Pt(CO); in observed spectra, it indeed had the lowest full coverage CO stretching frequency of any terminally bound system. The presently reported value of 2064 cm^{-1} for the full coverage CO frequency was the lowest for any supported Pt cluster system yet investigated. Such was expected on the basis of the extraordinarily small sizes of these clusters.

As has been alluded to earlier, it is appropriate to consider for systems of such small dimensions, that the dipoles of the adsorbed CO molecules may not be parallel to each other (and thus neither perpendicular to the metal surface). The previously employed through space electrodynamical (dipole-dipole) and through metal vibrational coupling models can be easily modified to reflect this. The necessary angular dependence of the harmonic vibrator potential (cf. equation 6.13) can be introduced through the use of the geometrical factor ϕ_{ij}, as shown in the following:

$$V = \frac{1}{2} \sum_{i=1}^{N} f_r Q_i^2 + \sum_{i>j=1}^{N} \phi_{ij} \beta_{ij} Q_i Q_j \qquad [6.16]$$

It is clear that this slightly modified model could account for the large shifts in frequency with respect to fractional coverage. Also, such a treatment must be considered in explaining the ^{12}CO / ^{13}CO results as well. At the present time, calculations are recommended which would use various model mixtures of the two isotopes on Pt_8 cubic and Pt_{13} cubo-octahedral clusters, in order to simulate the observed coverage-dependent IR spectra. The exercise would furthermore provide considerable information about β_{ij} and also about the phenomenon of CO island formation on these surfaces.

In the set of results concerning the oxidative treatments of the supported platinum materials, the observations included a blue shift of the CO frequency from 2067 cm^{-1} to 2080 cm^{-1} upon oxidation, and a narrowing of the peak itself. These are not consistent with a mechanism[60] involving only the removal

of chemisorbed oxygen (through reaction with gaseous CO, to form CO_2) and its replacement by chemisorbed CO, since this would not explain a blue shift of 14 cm^{-1}.

A more plausible model for the oxidative treatment process would involve either an oxygen promoted cluster growth, or oxidation of the metal itself, or possibly both.

In the first case, some growth phenomena have already been observed for these materials. According to work done by Professor A. Vannice (Pennsylvania State University, 1985) on these samples, at 300°C growths[a] to between 1.2 and 1.5 nm were reported. The CTEM observations presented in Chapter III, on materials used for the catalysis experiments (taken to temperatures as high as 400°C), confirmed such growth results. In the FTIR treatments, somewhat milder temperatures (150°C) could be expected to have given rise to a lesser (though not necessarily zero) degree of agglomeration. Observations of the CO frequency at full coverage for 7.0 nm Pt clusters showed a value of 2070 cm^{-1}, which is lower than the corresponding value for the oxidized specimens in the present study.

Altogether, these results suggest that the post-oxidative-treatment CO adsorption could be best explained[60] by dissociative O_2 adsorption and CO adsorption simultaneously on the Pt clusters. This is illustrated for a cubic model cluster, in Figure 6-13. In this interpretation, the blue shift can be attributed to a charge depletion of the metal cluster which is brought about by the coadsorption of oxygen (i.e., oxidation reduces the extent of $\sigma - \pi^*$ bonding in the Pt-CO subsystem). It should also be recognized[60] that the mere presence of adsorbed oxygen could contribute to the observed shift by simply leading to stronger CO-CO coupling (such could arise through a geometrical effect: crowding, for example). Of course, it would be extremely difficult to separate and quantify charge depletion and enhanced vibrational coupling effects, especially in the very small size regime.

The concept that (under the conditions used to oxidize these samples) complete surface coverage by oxygen did not take place, is consistent with information provided by the XPS measurements reported in Chapter IV. Those data showed that the binding energy shifts were too small to indicate

---

a the Vannice results (by chemisorption) indicated average sizes in the 1.4 to 2.0 nm range. These are area basis values however, which roughly correspond to 1.2 to 1.5 nm using the number basis convention.

complete oxidations, which would have corresponded to stoichiometries such as PtO, for example. It was however observed that some degree of oxidation had occurred.

6.2 Adsorption Enthalpy Studies on Supported Platinum Materials

A number of experimental runs were conducted, in which CO, H_2 and O_2 were adsorbed onto silica supported MVS platinum materials. These were also conducted by A. Vannice at the Pennsylvania State University. Through an analysis of the molar uptake data, it was possible to determine average particle sizes for the Pt clusters, and to make comparisons between the values thus obtained, and those obtained by CTEM analyses. Additional experimental work on these materials involved measuring the heats of chemisorption of the various gases. Comparisons in this case were made with results for other platinum particles ranging in size from molecular model compounds to bulk metallic Pt. In addition, an interesting contrast between platinum and palladium adsorption enthalpies was found and is discussed here.

6.2.1 Experimental Details

Samples subjected to both uptake and calorimetric measurements were transferred into the appropriate apparatus under anaerobic conditions, by using a protective stream of dry nitrogen. In order to obtain measurable extents of chemisorption, it was necessary to carry out various elevated temperature pretreatments of the samples. The particular details of these are presented in the tables of results. The sequences of gas adsorptions used to determine the adsorption enthalpies are similarly listed in the results tables.

Following the necessary pretreatments, samples placed into the measurement apparatus were divided into two portions. The calorimetric measurements were conducted on portions of about 18 mg., and the uptake measurements required the remainder of the charge (which was approximately 400 mg.).

The chemisorption isotherms used to determine monolayer uptake quantities, hence average particle sizes, were obtained at ambient temperatures. The monolayer coverages were calculated by extrapolating the linear segments of the measured isotherms to zero pressure. In the case of hydrogen adsorption, the total quantities of reversibly and irreversibly adsorbed gas were determined by readsorption following evacuation.

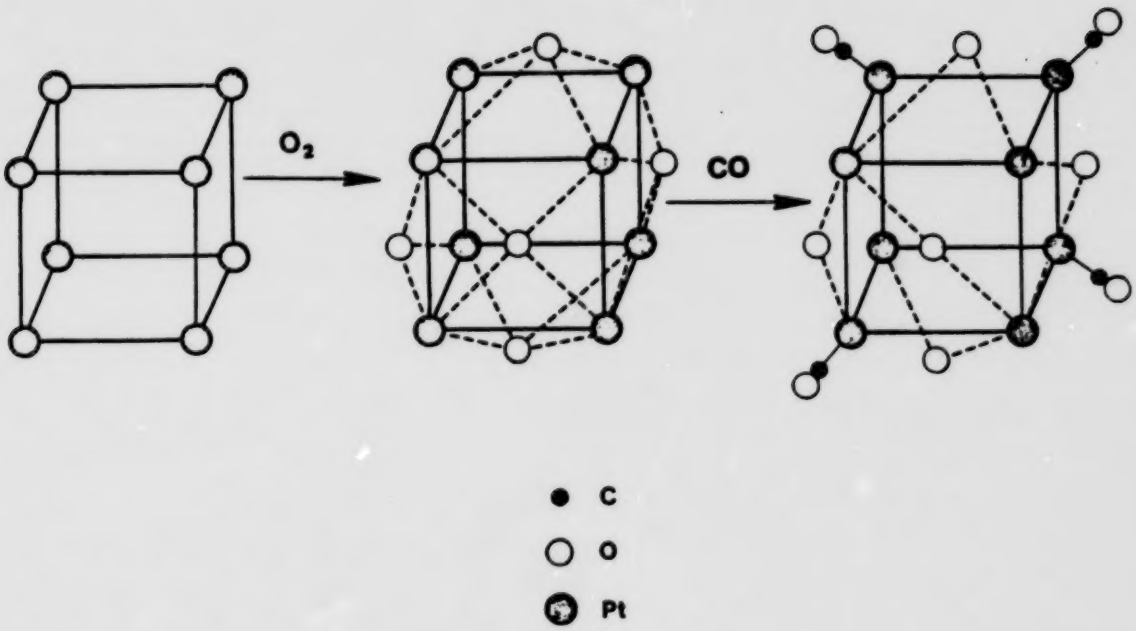

Figure 6-13 A Model for CO Adsorption on Oxidatively Treated Platinum Cluster Surfaces

In a similar manner as for hydrogen, the CO coverage was determined by calculating the difference between reversibly and irreversibly adsorbed material, at an equilibrium partial pressure of 75 torr.

The calorimetric runs were conducted also using partial adsorbate pressures of 75 torr, and temperatures of 300 K. In order to express the average particle size from these data, the fraction of exposed metal D was first estimated using the total H_2 uptake values, then the particle size in nm was calculated using:

$$d = \frac{1.13}{D} \qquad [6.17]$$

The experimental errors reported to be associated with the calorimetric measurements gave total uncertainties of about ±3 kcal/mol for the adsorption enthalpies quoted in the present results.

6.2.2 Chemisorption and Calorimetric Results

A representative group of hydrogen uptake isotherms (for the EMR-20c sample: 1.7 wt% Pt/SiO_2; 600°C support pretreatment) showing the total coverages for three different sample pretreatments is shown in Figure 6-14. A summary of all of the uptake measurements, including oxygen as well, is presented in Table 6-2, along with the average particle diameters thus determined and comparisons of those with CTEM particle diameters.

Calorimetric data showing the heats of adsorption for oxygen, heats of reaction for subsequent hydrogen titration, and heats of adsorption for CO are presented in Tables 6-3, 6-4 and 6-5 respectively.

6.2.3 Discussion of Results

It is clear upon inspection of all of the particle size values reported here, that in no case did severe agglomeration take place. Even where oxidative high temperature treatments were used, the average particle size remained below about 2 nm.

The comparisons between particle sizes by CTEM measurement and those obtained by the present chemisorption study seem to show some disagreement. It must be realized however, that the CTEM values are for materials which were introduced into the instrument without prior treatment, whereas the chemisorption values were only attainable after various agglomeration-inducing treatments. The CTEM particle size values for MVS materials after use as catalysts were in much better agreement with the chemisorption results: values of about 1.3 to 1.6 nm were measured in both CTEM and chemisorption studies (in the latter case, referring to only the reductive and inert treatments).

It is quite apparent that the stability of MVS generated Pt clusters, even though these are extremely small, is very good. This applies to situations involving high temperatures as well as atmospheres ranging from highly reducing to highly oxidizing.

An interesting property of the adsorption enthalpies for CO on platinum, is that they were not observed to depend on the size of such particles. This result is valid for particles as large as 100 nm and as small as 1 nm (i.e., including the present MVS materials). Furthermore, it has been noted for unsupported (ultra fine powder) platinum, as well as for various support materials such as alumina, silica, mixed aluminosilicates, and titania. These carrier materials represent a full range of strongly basic to strongly acidic surfaces. A plot of CO adsorption enthalpies versus particle size is shown in Figure 6-15,

including the present results, which superimpose well (within experimental error) with the remaining literature data. The value of the adsorption enthalpy, in all MVS cases ranged from 26.6 to 31.4 kcal/mol.

A plot of H_2 adsorption enthalpy for various sizes of Pt particles is presented in Figure 6-16. As can be readily seen, there is again an invariance of the value with respect to particle size; also, the present data are completely in agreement with all of the other results indicated.

An even more fascinating property of CO adsorption enthalpies on small supported metal clusters appears when one compares platinum with palladium. In this latter case, Vannice[61] has discovered that there is a size dependence. In order to understand the reason for this, it is useful to begin by considering the relationship[63] between adsorption enthalpies for CO on various metals, and the corresponding shifts in IR frequency for CO adsorbed on the same group of metals. The IR frequencies in question are similar to those observed for metal carbonyls[63].

A plot of $\Delta H_{ads} + \frac{E^*}{10}$ versus ΔF_{CO} yields a monotonically increasing function, as illustrated in Figure 6-17. This is almost identical to a plot of D^* versusΔF_{CO}. In this plot ΔH_{CO} is the initial heat of adsorption, and the termE^* is the d^n promotion energy. D^* is the metal/carbon bond energy in the binary carbonyl, corresponding to the same valence state as the surface metal species. The factor of 1/10 in the former relationship arises from the empirical relationship:

$$D^* = -21.92 + 87.83\,(\Delta F_{CO})^{\frac{1}{2}} - 23.21\,\Delta F_{CO} \qquad [6.18]$$

used to express D^*: the difference between the heat of adsorption and D^*, when plotted against E^* yielded a slope[63] of 1/10.

The correlation between ΔH_{CO} andΔF_{CO} implies that the surface atoms to which the CO molecules are chemisorptively bound, exist in some valence state having a promotion energy which depends monotonically upon E^*. Such dependence may possibly be related to the coordination number of the surface metal atoms, hence in the case of extremely small particles, one might expect a pronounced size effect. Incorporating this idea results in the thermodynamic cycle shown in Figure 6-18, in which the enthalpy of adsorption has been referenced to the valence state of the surface metal atoms according to:

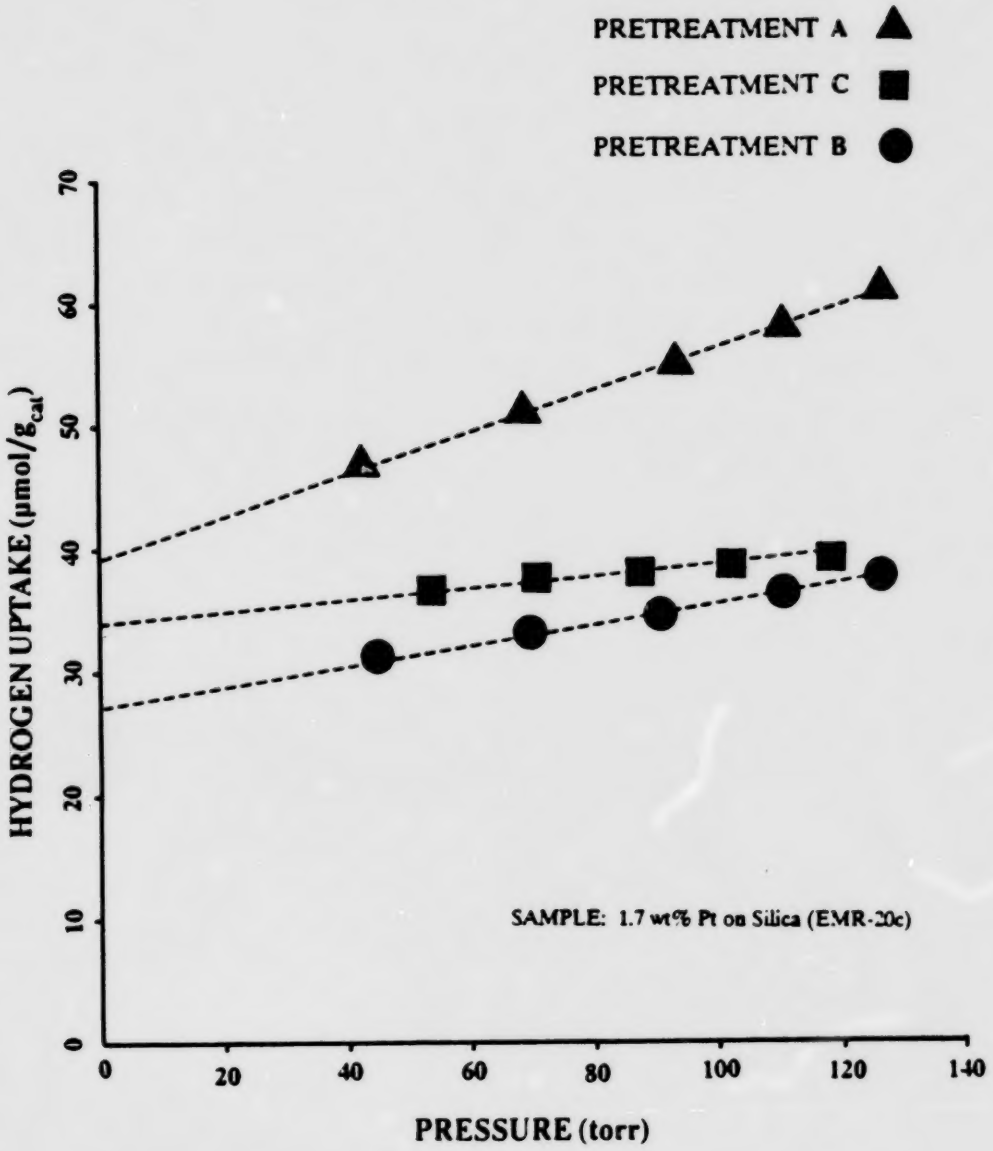

Figure 6-14 Total Hydrogen Uptake Isotherms for a Pt/SiO_2 MVS Material Following Various Pretreatments

SAMPLE	EXPT	HYDROGEN UPTAKE (μmol/g)			OXYGEN UPTAKE (μmol/g)	DIAMETER (nm)	
		TOT	REV	IRR		ADSPTN	CTEM
[illegible]	1 A				7.1	0.81	
	2 D	31.6	10.0	21.6			2.00
[illegible]	1 A	40.0	16.3	23.7		1.20	0.53
	2 B	27.8	12.6	15.2		1.60	
	3 A				11.8		
[illegible]	* D	35.2	10.9	24.3		1.40	
[illegible]	1 A	40.4	16.2	24.1		1.30	0.79
	2 B	31.8	13.0	18.8		1.60	
	3 A				12.5		

EXPERIMENT IDENTIFIERS

1 Hydrogen Adsorption (average of two runs)

2 Oxygen Adsorption followed by Hydrogen Titration (one or two runs)

3 CO Adsorption

A Pretreatment by Evacuation (1.0 h @ 473 K)

B Pretreatment by H_2 Reduction (1.0 h @ 473 K)

C Pretreatment by Reduction in 20% H_2 / Inert (1.0 h @ 573 K); then Evacuation 1.0 h @ 573 K, adsorption system) or Argon Purging (4 to 5 h @ 298 K)

D Pretreatment by Calcination in 20% O_2 (1.0 h @ 573 K); Evacuation (1.0 h @ 573 K); Reduction in 20% H_2 (1.0 h @ 573 K); Evacuation (1.0 h @ 573 K).

* This sample was given Pretreatment D, after a calorimetric experimental measurement. After the pretreatment, it was subjected to the same measurement again.

Table 6-2 Results of Adsorption Measurements made Prior to Calorimetric Studies

	PRETREATMENT	H_2 UPTAKE			ENERGY CHGE.			ADS. ENTHALPY			PARTICLE DIAMETER
		TOT	REV	IRR	TOT	REV	IRR	TOT	REV	IRR	(nm)
	C	32.4	12.7	19.7	551.7	169.3	382.4	17.0	13.3	19.4	2.00
	C	26.6	15.6	11.0	441.3	178.5	262.8	16.6	11.4	23.9	1.90
	D+C	31.6	10.9	20.7	509.4	152.5	356.9	16.1	14.0	17.2	1.60
	C	26.0	13.2	12.8	395.0	172.9	222.1	15.2	13.1	17.4	2.00

Table 6-3 Heats of Chemisorption of Hydrogen on Pt/SiO_2 MVS Samples

SAMPLE*	UPTAKE (μmol/g)	ENERGY CHANGE (cal/g)	ADSORPTION ENTHALPY (kcal/mol)
EMR-20 a	25.1	1.2121	48.3
EMR-20 b	17.7	1.0034	56.7
*EMR-20 c	22.5	1.2732	56.6
EMR-20 d	19.5	1.0131	52.0

Table 6-4 a Heats of Chemisorption of Oxygen on Pt/SiO_2 MVS Samples

SAMPLE	UPTAKE (μmol/g)	ENERGY CHANGE (cal/g)	ADSORPTION ENTHALPY (kcal/mol)
EMR-20 a	84.9	2.1061	24.8
EMR-20 c	66.2	1.8103	27.3
*EMR-20 c	80.0	2.1048	26.3
EMR-20 d	68.3	1.4551	21.3

* sample was given pretreatment D and previously subjected to calorimetric run

Table 6-4b Reaction Enthalpies for Subsequent Hydrogen Titrations

	EXPERIMENTAL SEQUENCE	UPTAKE (μmol/g)	ENERGY CHANGE (cal/g)	ADSORPTION ENTHALPY (kcal/mol)
	C 1	50.2	1.5140	30.2
	C 2	42.7	1.2430	29.1
	C 1	46.0	1.3367	29.1
	C 2	40.7	1.1868	29.2
	C 1	44.6	1.3986	31.4
	C 2	39.9	1.1908	29.8
	C 1	48.3	1.2855	26.6
	C 2	42.6	1.1728	27.5

* sample was given pretreatment D and previously subjected to calorimetric run

Table 6-5 Heats of Chemisorption of Carbon Monoxide on Pt/SiO_2 MVS Samples

$$\Delta H_{CO} = \Delta H^{*}_{CO} + \frac{E^{*}}{N}$$

Here, ΔH^{*}_{CO} is the enthalpy referenced to the valence state of the surface metal atoms, and N is the coordination number of these (N = 1,2,3,...,9) with respect to other metal atoms.

Examining a further aspect of particle size effects for CO adsorption on Pt, one finds that there is a monotonic dependence of the frequency shift[a] upon particle size. The dependence, as shown in Figure 6-19, is valid for the size range extending from 0.6 nm to bulk surfaces.

The observation[61] of essentially invariant enthalpies of chemisorption with respect to particle size can be rationalized in terms of two opposing (size dependent) effects; the change in ΔH^{*}_{CO} accompanying changes in particle size is counterbalanced, in the case of platinum, by a change in the E^{*}/N term

---

a comparing the CO stretching frequency of the adsorbed entity to that of the free molecule.

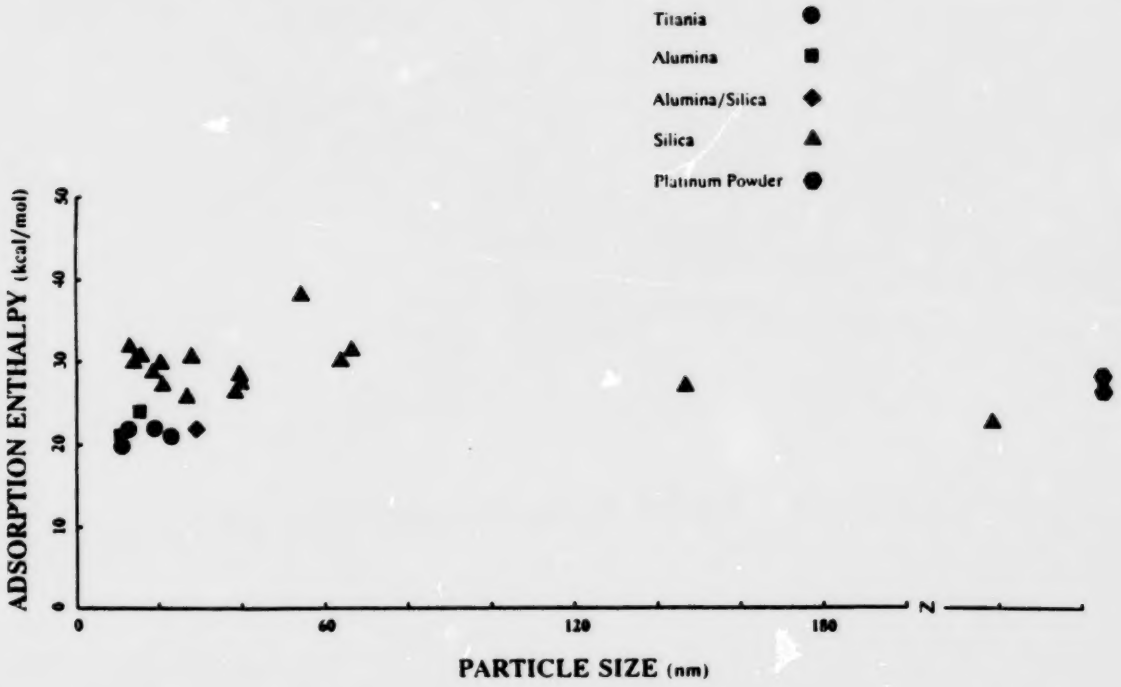

Figure 6-15 CO Adsorption Enthalpies on Platinum Surfaces Ranging from Bulk to Ultra-Small MVS-Generated Specimens

(since N is related to particle size). This overall invariance is illustrated in the lower portion of Figure 6-19. The counterbalancing contributions by ΔH°_{CO} and E^*/N are expected to be most pronounced with very small particle sizes.

As a contrast to the special case of platinum, Vannice and his coworkers[61] have made similar observations of CO adsorption of palladium. In the latter case, the promotion energy E^* is expected to be much less important than for platinum. The dependence of ΔH_{CO} on N will therefore not be opposed as it would in the Pt case; the result is that for Pd clusters, CO chemisorption enthalpies do in fact depend on their sizes.

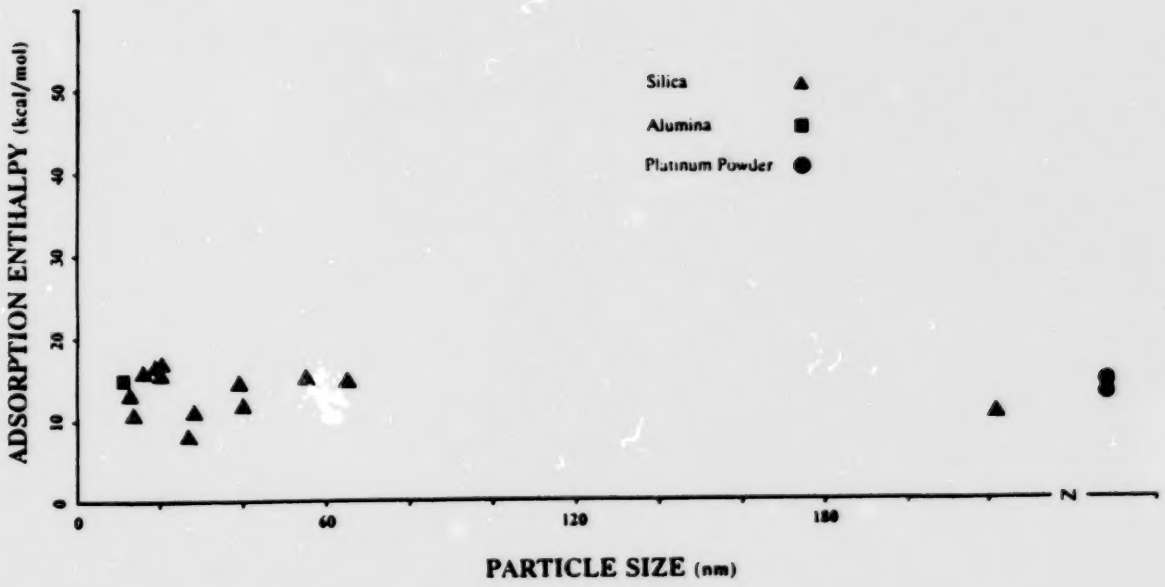

Figure 6-16 Hydrogen Adsorption Enthalpies on Platinum Surfaces Ranging from Bulk to Ultra-Small MVS-Generated Specimens

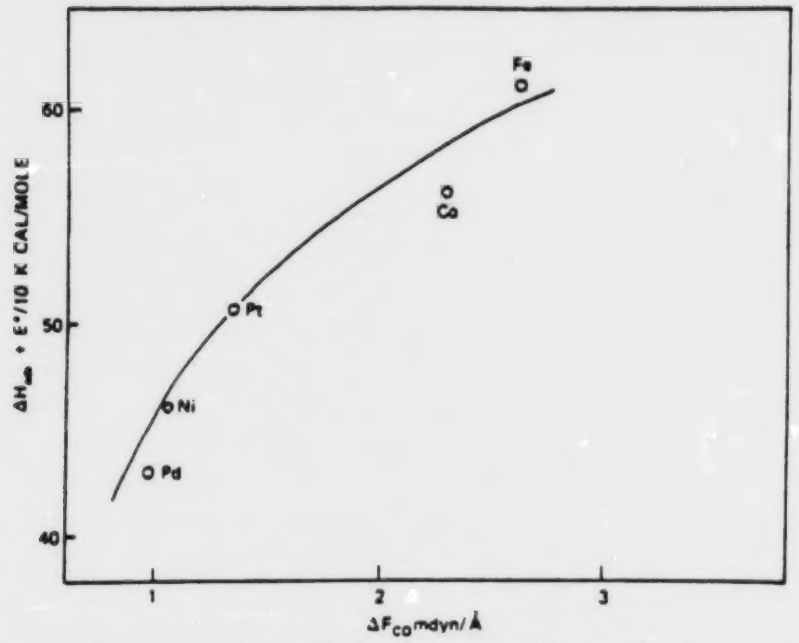

The quantity, $\Delta H_{ads} + E^*/10$, plotted against ΔF_{CO} for CO chemisorbed on various metals.

Thermodynamic Properties of Chemisorbed CO

Metal	ΔF_{CO}[a]	ΔH_{ads}[b]	$\Delta H_{ads} + E^* 10$
Fe	2.63	46	61.3
Co	2.31	48	56 0
Ni	1.07	42	46.2
Pd	0.99	43	43 0
Pt	1.16	49	50.7

[a] Units are mdyn Å; obtained from data in table using the Cotton-Kraihanzel approximation.
[b] Initial heats of adsorption in kcal mole: D Brennan and F. H. Hayes, *Phil. Trans.* 4, 258, 347 (1965).

Figure 6-17 The Relationship Between the Promotion-Energy-Corrected Adsorption Enthalpy and Stretching Frequency Change upon Chemisorption for CO on Various Transition Metals

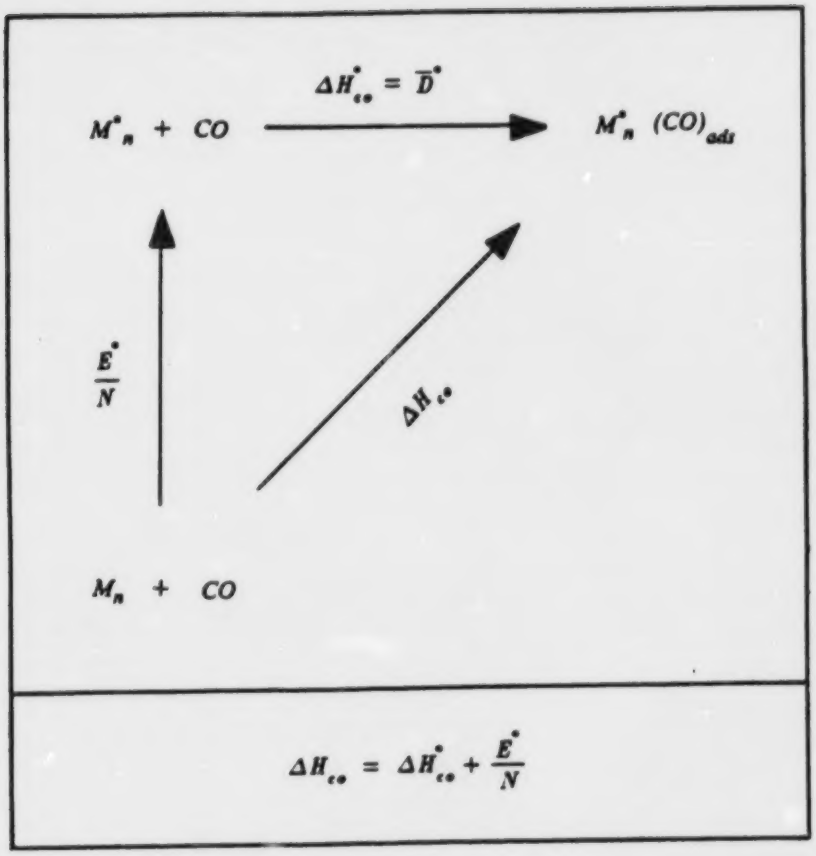

Figure 6-18 A Thermodynamic Description of the Size Dependence of CO Adsorption Enthalpies on Metal Particles

FIGURE 6-19 a

The Relationship Between CO Stretching Frequency Change and Particle Size for CO Adsorption on Supported Platinum Particles

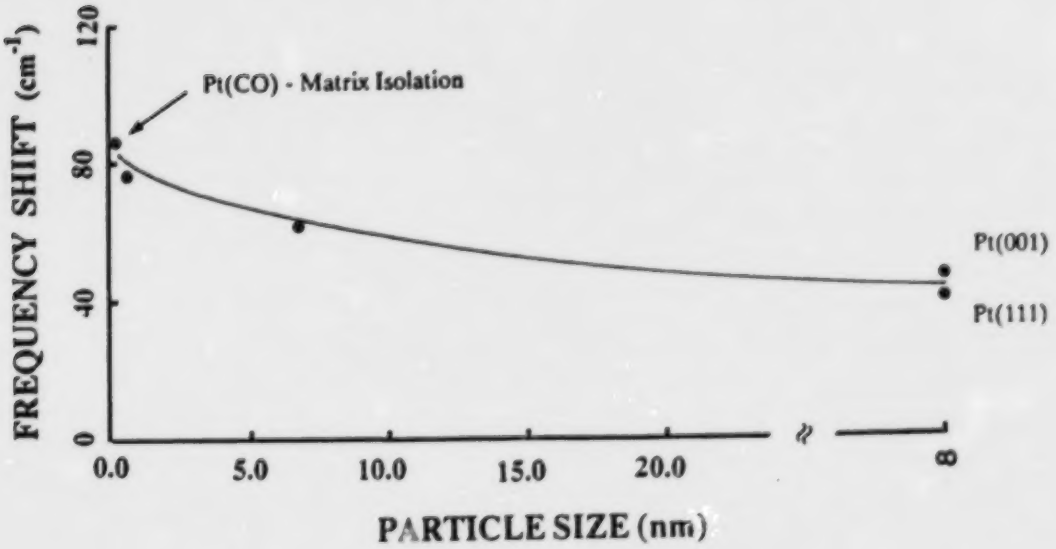

FIGURE 6-19 b

Factors which Influence the Particle Size Dependence of Heats of Adsorption of CO on Platinum

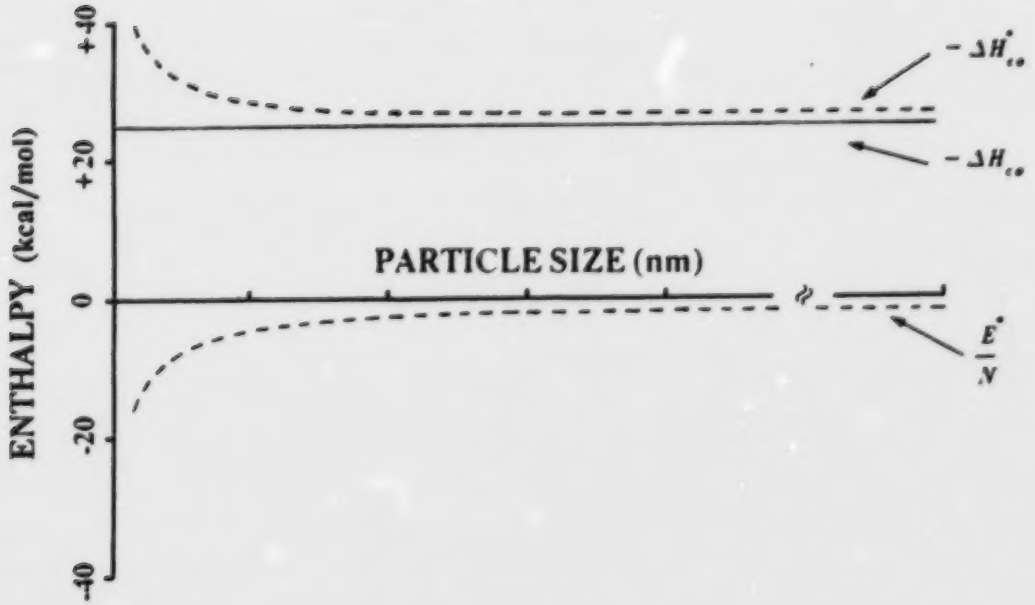

CHAPTER VII

Catalysis on the Iron, Ruthenium and Iron/Ruthenium Bimetallic MVS Materials

A study of metal vapor synthesized oxide supported ruthenium, iron and ruthenium/iron bimetallic catalysts has been conducted using the conversion of n-butane as a probe reaction. Examination of the conversion of n-butane showed that hydrogenolysis, dehydrogenation and isomerization of the reactant were all observed. A mechanism has been proposed in order to explain the distribution of reaction products for several of the samples.

7.1 Introduction and Literature Review

A brief review of some of the literature pertaining to the bimetallic catalysis experiments which have been performed, is presented here. This is divided into two major sections: that regarding reactions on the Ru/Fe supported surface, and that pertaining to the preparation of supported materials in general (i.e., the effect of various parameters on the size, structure and oxidation state of metal particles).

7.1.1 Catalysis on Similar Bimetallic Materials

Sinfelt[28] has included data on hydrocarbon conversion over Ru/Cu catalysts on silica. In the case of cyclohexane conversion, the unimetallic Ru catalyst has been reported to produce both dehydrogenation (aromatization) and hydrogenolysis reactions; the latter being the minor reaction by about an order of magnitude. Incorporation of various fractions of Cu in the catalysts produced a decrease in activity for both conversion reactions, however, the selectivity toward hydrogenolysis decreased as more Cu was incorporated.

Experiments conducted on the above systems using ethane showed only hydrogenolysis, this being sharply decreased by increasing incorporation of Cu in the Ru catalysts. Copper is not catalytically active for these reactions, hence results were rationalized on the basis of a geometric effect in which copper atoms block surface sites of the active metal. It is accepted that hydrogenolysis would require a large

number of Ru atoms as a catalytic surface site, therefore incorporation of small fractions of Cu causes a great reduction in the relative number of these.

Other examples of supported MVS generated bimetallics containing Co have been produced by Klabunde[29]. The reaction systems investigated included hydrogenation and isomerization of olefins and dienes. The other metals used in the bimetallics were Fe, Mn, and Cr. All of these (though most significantly Mn) increased the overall activity with respect to that of pure Co. In this study, the results were rationalized on the basis of electronic effects (i.e. the oxidation state of each metal is perturbed by the presence of the other), although the possibility of geometric and ensemble effects was not entirely ruled out.

7.1.2 Particle Size Effects

Various studies of catalysis on supported unimetallics have been performed in order to investigate the effects of particle size on both the total activity and selectivities of these materials.

Kitajima et al.[30], have prepared via thermal decomposition of a Ru(0) organometallic complex, highly dispersed catalysts. Through the use of various pretreatment conditions (particularly temperature) and metal loadings, they have created various distributions of average particle size. This was determined by both hydrogen chemisorption and electron microscopy. The hydrogenation of both cyclohexene and benzene was examined. In both reactions, sharp maxima were found in the overall conversion rates versus particle diameter; for benzene this occurred at about 2.2 nm, and for cyclohexene, at about 3.6 nm.

In work with methylcyclopentane conversion, Sachtler et al.[31] have also assembled evidence for the effects of particle dispersion (hence particle size) on reaction rates.

Whyte[32] has compiled an extensive review of techniques for determining the particle sizes of supported metallic catalysts. These include chemisorption, X-ray line broadening, electron microscopy, small angle X-ray scattering and magnetic methods. In addition, a review of the effects of particle size on catalysis was also presented. The author pointed out that for many systems, there may not be a size effect with respect to certain reactions. It is generally accepted that size dependence usually results in systems in which the reactant is multiply bound to the surface.

7.1.3 Preparation of Catalysts

A study of small Fe particles on MgO has been carried out by Boudart et al.[33], in which the size range from 1.5 to 30.0 nm has been explored. As has been well established, support interactions lead to irreducibility of small Fe particles. MgO is less acidic than alumina or even silica, hence zerovalent iron is more easily produced on such surfaces. Nevertheless, Fe(II) was also observed to be contained in the catalyst particles. The concentration of Fe(II), as determined by magnetic susceptibility measurements, was found to remain essentially constant as the bulk Fe concentration was varied from 1 to 40 wt %. This may possibly be interpreted as indicating that Fe(II) was preserved through support interactions, and that Fe(0) produced during the hydrogen reduction (standard catalyst pretreatment) nucleated on these smaller clusters. This principle was also discussed by Bonneviot et al.[13,34] for Ni/silica catalysts. In the very small particle size regime, they observed (using EPR and FMR spectroscopies) that the unusual Ni(I) state occurred; this is thought to provide the sites by which nickel crystallites are *anchored* to the support surface. The FMR method[13] has also proved to be of great interest in providing data on the size distribution (as opposed to the average size only) and particle shape. Briefly, these are obtained from the temperature dependence of the FMR lineshape asymmetries and double-integrated intensities.

In work with three iron containing bimetallic preparations (with Ru, Os and Co), Choplin et al.[7] have used TEM and high spatial resolution X-ray analysis to study the composition of very small surface crystallites after reductive pretreatment. The crystallites were on the order of 1 - 5 nm in all cases. All of the samples were prepared via decarbonylation of polynuclear metal cluster compounds such as $H_2FeRu_3(CO)_{13}$. A comparison was made between materials which were prepared using heteropolynuclear compounds (like the above example), and codeposited mixtures of homopolynuclear precursors (a 3:1 mixture of $Ru_3(CO)_{12}$ and $Fe_3(CO)_{12}$ corresponds to the above). It was concluded that only the heteronuclear precursors yielded bimetallic metal particles upon treatment at 400°C. The composition of these particles was found to have the same ratio of metals as in the precursor compound used. In the case of the mixtures, only crystallites of Ru, Co or Os formed; the Fe was detected, however it was evenly dispersed on the support, and was believed to be entirely in the oxidized form. It was proposed that the existence of heterogeneous metal-metal bonds in the precursor compounds was required for the formation of bimetallic particles. Also noted, was the difference in decomposition temperatures which is known for the individual components of the mixtures. This was speculated to produce separate metal phases during the decarbonylation step.

In a similar preparation of Fe/Rh bimetallics through the thermal decomposition of mixed chlorides on silica (the above work[7] utilized a partially dehydroxylated MgO as the support), Ichikawa et

al.[12] found direct evidence for the existence of Rh-Fe bonds. This was accomplished through the use of EXAFS and Mössbauer spectroscopy. In samples having Fe:Rh ratios lower than about 0.3, the Fe was found to be in the form of Fe(III), and at the metal/support interface (where these were bound to both Rh(0) and lattice oxygen atoms). At higher Fe ratios, the excess Fe was found to be in the Fe(0) state, and on the surface of the bimetallic particles. Based on the elucidated structural form, catalytic properties such as unusually high methanol/ethanol yields in CO hydrogenation reactions, and good resistance to sintering were explained.

7.2 General Catalysis Results

A series of six preliminary n-butane conversion experiments on the Iron/Ruthenium Bimetallic (including unimetallics as well) system has been completed. Samples subjected to catalytic testing were loaded into a glass microreactor of 2 cm^3 volume, under completely anaerobic conditions. The material was retained in the reactor by a fritted glass disk 1.0 cm in diameter. Typical quantities were about 100 mg, and formed catalyst beds having depths of less than 1.0 cm. In all cases, the catalyst samples were pretreated in a stream of 25 % hydrogen in argon (total flowrate 50 cm^3/min @ STP) for 2.0 h at 300°C before the butane reactant stream was admitted. Data were recorded only after a steady level of catalytic activity had been reached; in all cases concerning the present materials, this occurred quite rapidly, usually requiring only 10 min.

All of the catalytic data for the experiments using iron and ruthenium containing catalysts were recorded at steady state, using the following gas flowrates (@ STP): n-Butane 8.0 cm^3/min, Hydrogen 30.0 cm^3/min, and Argon 30.0 cm^3/min; at various temperatures. In all cases, the reactor was operated in the differential mode, with maximum total conversions less than 2 %. The product stream emanating from the reactor was analyzed online, using packed column gas chromatography. For this purpose, a Porasil™-C column using n-octane as the stationary phase was used. The gas chromatograph was operated isothermally at 60°C and a pressure of approximately 325 kPa, using dry, oxygen free nitrogen as the carrier gas. The range of temperatures examined was 150°C to 429°C (although smaller ranges were used for individual samples depending on their overall activity.

Table 7-1 lists the six experiments which were performed. Samples 1 and 2 were of a catalyst prepared in 1984. The first analysis was carried out in 1985 January; the second is a later duplication of this. This pair of experiments was performed as a control, in order to ensure that the reactor system, GC

[redacted]	SAMPLE
1	1.7 wt% RuCl3 on SiO2 (ASC-1)
2	1.7 wt% RuCl3 on SiO2 (repeat)
3	3.2 wt% Ru on Al2O3 (EMR-6)
4	1.5 wt% Fe on Al2O3 (EMR-4)
5	1.7 wt% (3:1) Ru/Fe on Al2O3 (EMR-3b)
6	5.2 wt% (2:3) Ru/Fe on Al2O3 (EMR-5)

Table 7-1 List of Preliminary Experiments Performed on Iron, Ruthenium and Iron/Ruthenium Bimetallic MVS Materials

etc. were operating reliably, and to verify adequate reproducibility of results between two independent experimenters.

The remaining four experiments examine a pure Ru, pure Fe and two Ru/Fe bimetallic sets of MVS generated catalysts. Each of these was chosen from the more heavily loaded of the samples prepared thus far.

Experimental results for all samples presented here are in the form of figures which contain a table and three plots for each run. These list reaction and GC operating conditions, individual rates of production for the various product species, the total reaction rate, selectivities with respect to the various products, selectivities according to reaction mechanism and Arrhenius parameters. Arrhenius data are given only for the total rate of consumption of butane.

7.2.1 Control Experiment

Figure 7-1 corresponds to the experiments conducted in 1985, whereas Figure 7-2 corresponds to the duplicate experiment presently performed. The temperature range covered was the same in both cases however, exact duplication of each datum was not carried out.

SAMPLE: ASC-1 1.7 wt% RuCl3 on Silica
MASS: .1300 g

DATE: 1985 January 11
EXPERIMENTER: JG

REACTANTS: n-Butane 8.0 cm3/min
Hydrogen 30.0 cm3/min
Argon 30.0 cm3/min

GC COLUMN: Porasil-C
CARRIER GAS: Nitrogen
COLUMN TEMP: 40.0 C

PRESSURE: 293.0 kPa

SPECIES IDENTIFICATION

A. methane
B. ethane/ethylene
C. propane
D. propylene
E. iso-butane
F. n-butane
G. iso-butene
H. trans-2-butene
I. cis-2-butene

REACTION RATES (mol/h g)

TEMP (C)	SPECIES A	B	C	D	E	F	G	H	I	TOTAL CONVERSION
172.	1.221 -5	3.721 -6	5.461 -6	.000 0	.000 0	-9.008 -6	.000 0	.000 0	.000 0	.0029
204.	1.478 -4	2.793 -5	3.138 -6	.000 0	.000 0	-5.328 -5	.000 0	.000 0	.000 0	.0169
210.	1.338 -4	1.935 -5	2.155 -6	.000 0	.000 0	-4.474 -5	.000 0	.000 0	.000 0	.0142
231.	6.643 -4	8.061 -5	7.230 -6	.000 0	.000 0	-2.118 -4	.000 0	.000 0	.000 0	.0673
253.	1.894 -3	1.427 -4	9.773 -6	.000 0	.000 0	-5.521 -4	.000 0	.000 0	.000 0	.1754
277.	5.189 -3	1.527 -4	7.501 -6	.000 0	.000 0	-1.379 -3	.000 0	.000 0	.000 0	.4382

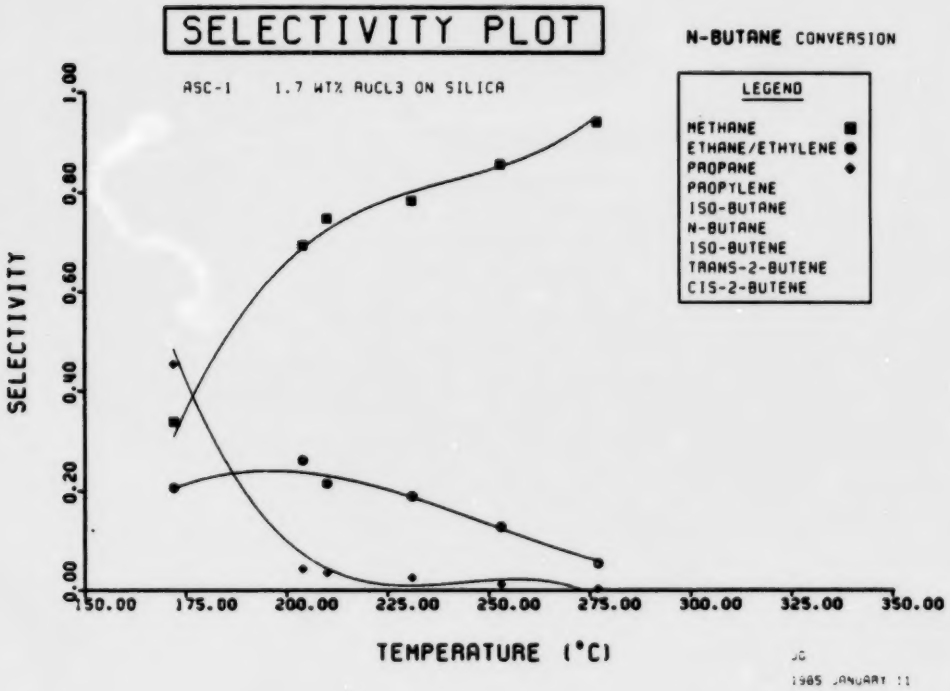

Figure 7-1 n-Butane Conversion Catalysis Results for Sample ASC-01

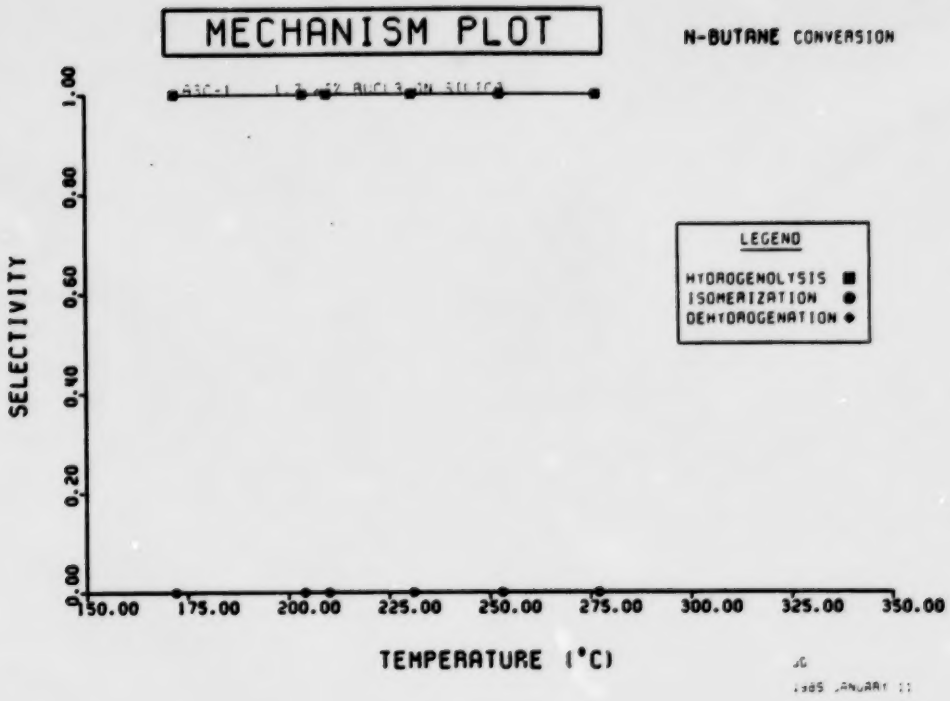

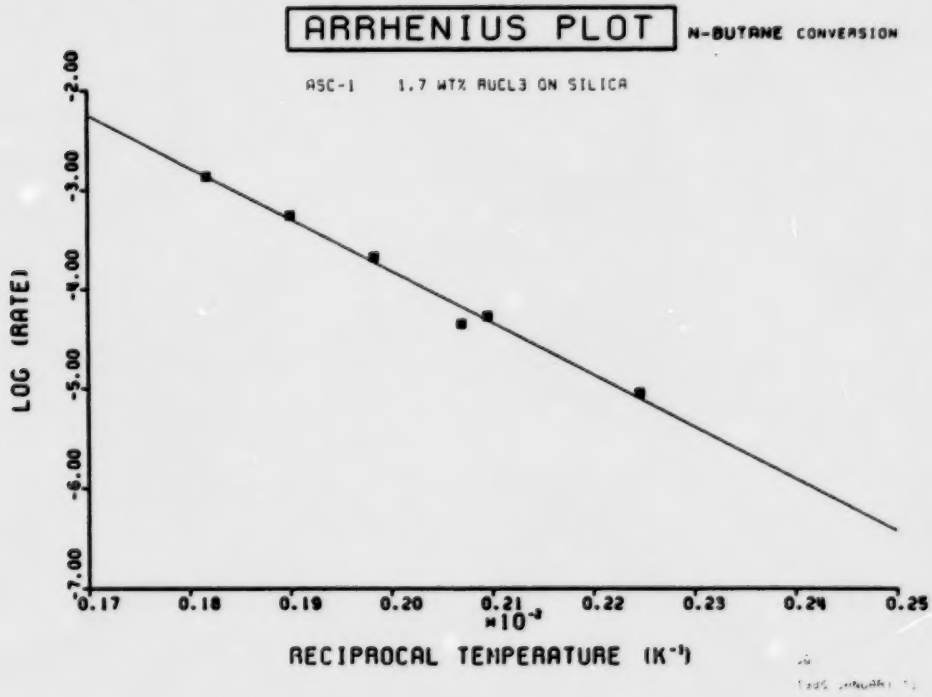

Figure 7-1 Continued

SAMPLE: ASC-1 1.7 wt% RuCl3 on Silica
MASS: 1400 g

REACTANTS: n-Butane 8.0 cm3/min
Hydrogen 30.0 cm3/min
Argon 30.0 cm3/min

DATE: 1986 March 27
EXPERIMENTER: RAP

GC COLUMN: Porasil-C
CARRIER GAS: Nitrogen
COLUMN TEMP: 40.0 C

PRESSURE: 293.0 kPa

SPECIES IDENTIFICATION

A. methane
B. ethane/ethylene
C. propane
D. propylene
E. iso-butane
F. n-butane
G. iso-butene
H. trans-2-butene
I. cis-2-butene

REACTION RATES (mol/h g)

TEMP (C)	SPECIES A	B	C	D	E	F	G	H	I	TOTAL CONVERSION
150.	4.239 -7	3.150 -7	1.262 -7	.000 0	.000 0	-3.192 -5	2.162 -5	.000 0	.000 0	.0006
231.	2.093 -6	2.420 -5	3.935 -6	.000 0	2.446 -7	-8.814 -5	2.051 -5	.000 0	.000 0	.0024
231.	2.038 -6	2.550 -5	4.146 -6	.000 0	4.351 -7	-8.812 -5	2.088 -5	.000 0	.000 0	.0024
246.	5.611 -6	4.482 -5	6.162 -6	.000 0	.000 0	-1.673 -4	.000 0	.000 0	.000 0	.0045
253.	9.044 -6	5.840 -5	7.233 -6	.000 0	.000 0	-2.607 -4	.000 0	.000 0	.000 0	.0070
253.	1.095 -5	6.556 -5	7.687 -6	.000 0	.000 0	-3.123 -4	.000 0	.000 0	.000 0	.0084
277.	3.427 -5	5.190 -5	3.523 -6	.000 0	.000 0	-8.854 -4	.000 0	.000 0	.000 0	.0238

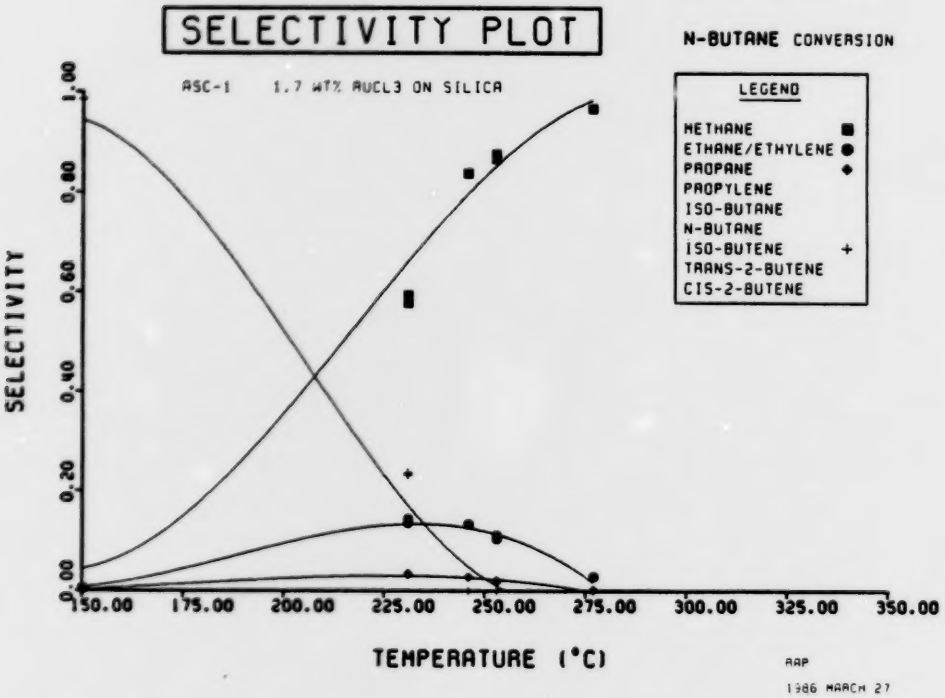

Figure 7-2 n-Butane Conversion Catalysis Results for Sample ASC-01 (Repeat Experiment)

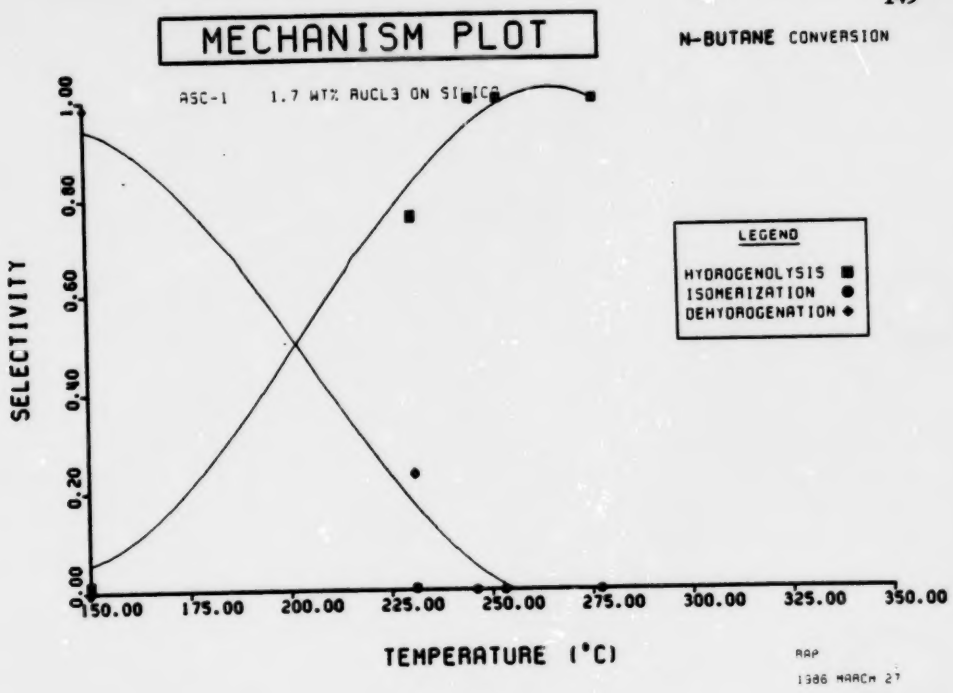

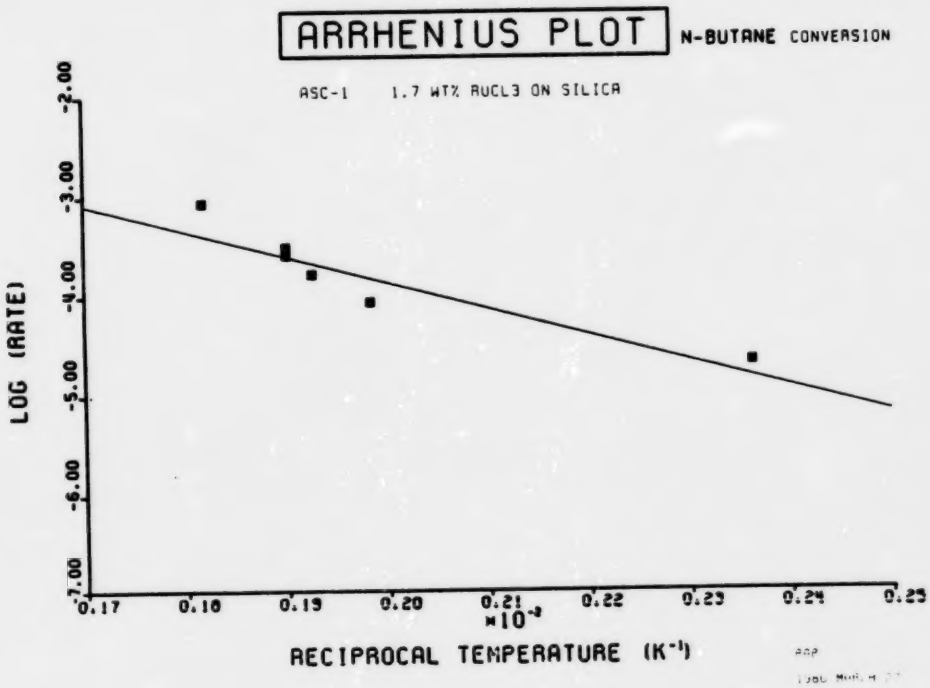

Figure 7-2 Continued

The two sets of results are characteristically the same: only propane, ethane and methane were produced. At lower temperatures, the selectivity toward the higher weight alkanes was greater. In the present experiment, some production of iso-butene was also indicated. This was observed only at 231°C, at which temperature the overall reaction rate was very low. Hence, this result is rather doubtful in its validity.

Quantitatively, the selectivities observed in the two experiments agree quite well. The present results seem to indicate a lower selectivity toward methane than for the original experiment, in the range of lower temperatures. This could possibly be accounted for by considering the iso-butene production. Since the rate observed was just above the limit of detection, earlier results may have ignored such data. By so doing, a re-plot of Figure 7-2 would be much more similar to Figure 7-1.

The Arrhenius plots are also very similar in comparison with each other. In Figure 7-2, the data point at 150°C represents a barely detectable total conversion, hence it is subject to a high degree of experimental uncertainty. Neglecting the point at 150°C, the activation energy and preexponential factor would be 116.52 kJ/mol and 1.019 x 10^8 mol/h·g respectively. These agree very well with the values observed for the original experiment. Activation energies on the order of about 100 kJ/mol are typical, according to previous work with several Ru preparations from various precursors[43]. Similar values are also reported for Iridium[36] which would be expected to agree with those of Ru, based on the work of Dalla Betta et al.[42].

7.2.2 MVS Generated Ruthenium Catalyst

The pattern of selectivities for sample EMR-6 (Figure 7-3) is quite similar to that of the ASC-1 Ruthenium halide sample. The notable exception is for production of iso-butane (isomerization reaction), which has a rate comparable to that of production of the higher mass alkanes (propane and ethane). At temperatures below 275°C, this is the major product, having a selectivity of about 40%, whereas each of the hydrogenolysis products accounts for ca. 20% of the butane consumption.

The Arrhenius activation energy for this experiment is also on the order of about 100 kJ/mol. As indicated on the plot, the data (which were recorded from two days' experimentation), appear to form two distinct curves. The lower of these, was obtained on the first day. After cooling to 25°C in argon, and repeating measurements in the same temperature range the following day, data for the upper curve were collected. The generation of two apparently parallel Arrhenius lines with the passage of time is indicative of changes in the number of active catalyst sites. This is usually attributed to sintering. As indicated by other measurements presented elsewhere in this document (CTEM and FMR/EPR), metal particles on

SAMPLE: EMR-6 3.2 wt% Ru on Alumina
MASS: 2000 g
DATE: 1986 April 02
EXPERIMENTER: RAP

REACTANTS: n-Butane 8.0 cm3/min
Hydrogen 30.0 cm3/min
Argon 30.0 cm3/min

GC COLUMN: Porasil-C
CARRIER GAS: Nitrogen
COLUMN TEMP: 40.0 C
PRESSURE: 293.7 kPa

SPECIES IDENTIFICATION

A. methane
B. ethane/ethylene
C. propane
D. propylene
E. iso-butane
F. n-butane
G. iso-butene
H. trans-2-butene
I. cis-2-butene

REACTION RATES (mol/h g)

TEMP (C)	SPECIES A	B	C	D	E	F	G	H	I	TOTAL CONVERSION
250.	1.622 -6	3.153 -7	6.007 -7	.000 0	7.313 -7	-1.745 -6	.000 0	.000 0	.000 0	.0000
275.	1.090 -5	2.329 -6	3.205 -6	.000 0	3.947 -6	-1.024 -5	.000 0	.000 0	.000 0	.0003
300.	1.845 -4	3.309 -5	2.591 -5	.000 0	3.157 -5	-1.137 -4	.000 0	.000 0	.000 0	.0029
325.	6.580 -4	9.247 -5	5.225 -5	.000 0	6.009 -5	-3.100 -4	.000 0	.000 0	.000 0	.0079
350.	1.613 -3	1.644 -4	6.636 -5	.000 0	6.661 -5	-6.016 -4	.000 0	.000 0	.000 0	.0181
350.	1.888 -3	2.070 -4	7.654 -5	.000 0	7.605 -5	-7.088 -4	.000 0	.000 0	.000 0	.0207
250.	2.443 -5	7.152 -6	8.816 -6	.000 0	9.538 -6	-2.583 -5	.000 0	.000 0	.000 0	.0007
250.	2.693 -5	8.155 -6	9.882 -6	.000 0	1.016 -5	-2.838 -5	.000 0	.000 0	.000 0	.0045
275.	2.007 -4	5.747 -5	4.860 -5	.000 0	6.004 -5	-1.754 -4	.000 0	.000 0	.000 0	.0042
275.	1.886 -4	5.509 -5	4.646 -5	.000 0	5.688 -5	-1.664 -4	.000 0	.000 0	.000 0	.0132
300.	8.933 -4	1.845 -4	9.917 -5	.000 0	1.279 -4	-5.178 -4	.000 0	.000 0	.000 0	.0129
300.	8.694 -4	1.808 -4	9.786 -5	.000 0	1.262 -4	-5.074 -4	.000 0	.000 0	.000 0	.0176
325.	1.804 -3	2.658 -4	9.821 -5	.000 0	1.113 -4	-7.680 -4	.000 0	.000 0	.000 0	.0203
332.	2.209 -3	2.530 -4	6.964 -5	.000 0	6.685 -5	-7.977 -4	.000 0	.000 0	.000 0	.0184
350.	1.794 -3	2.214 -4	9.083 -5	.000 0	9.525 -5	-7.225 -4	.000 0	.000 0	.000 0	.0186
350.	1.800 -3	2.262 -4	9.208 -5	.000 0	9.659 -5	-7.289 -4	.000 0	.000 0	.000 0	.0186

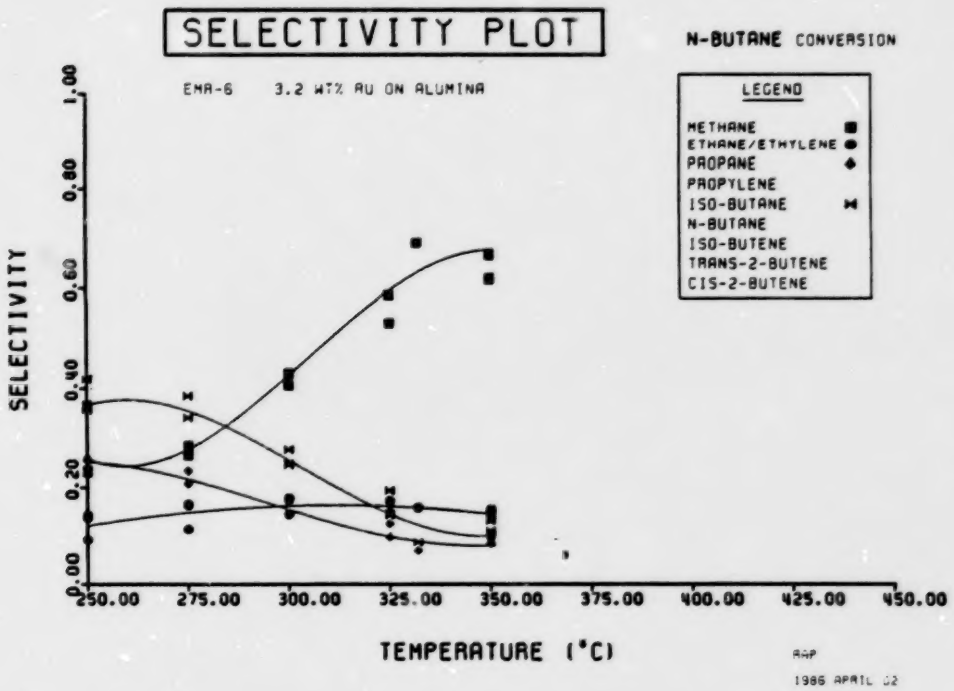

Figure 7-3 n-Butane Conversion Catalysis Results for Sample EMR-6

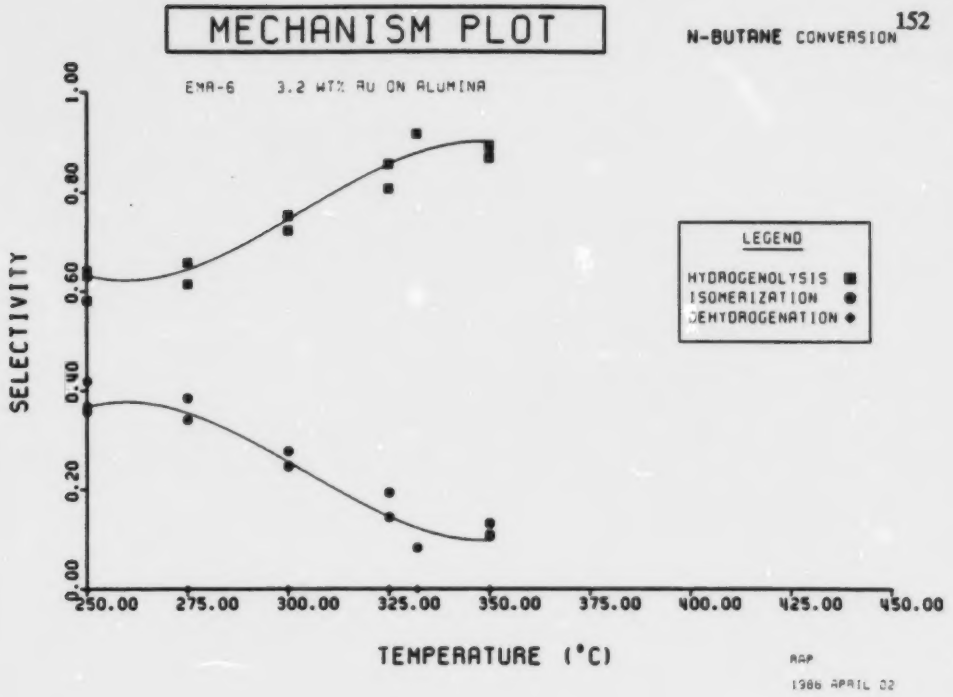

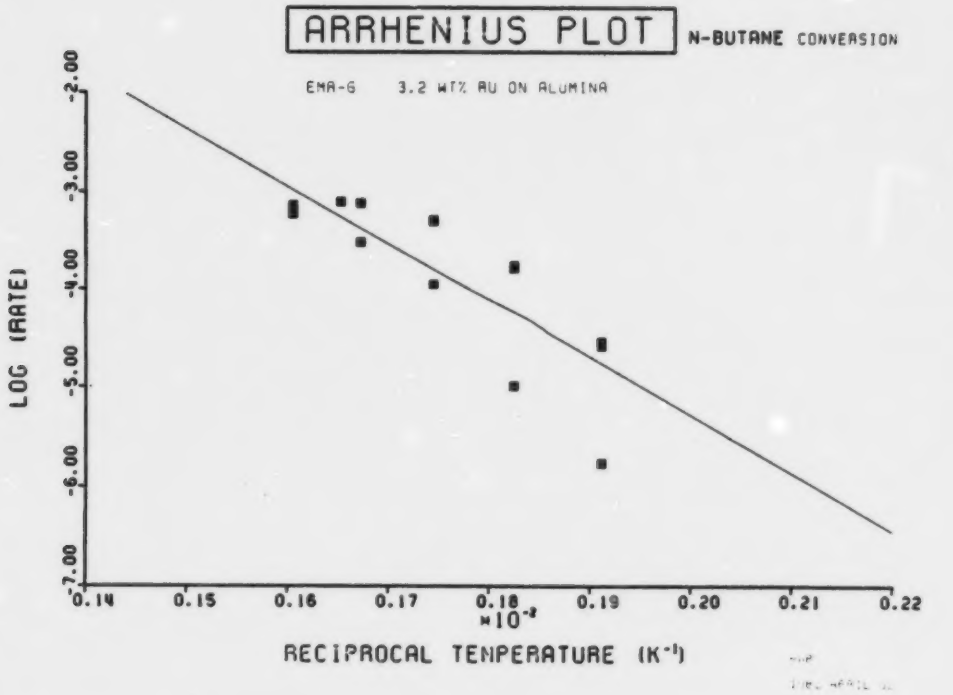

Figure 7-3 Continued

the support surface have been observed to increase in size over the temperature range examined here. It is interesting to note the increase in total activity as sintering takes place. This notion is in agreement with Sinfelt's suggestion[38] that adsorption sites for species to undergo hydrogenolysis may actually consist of ensembles of many metal centres. Mild sintering of extremely small crystallites (1 to 2 nm) could be therefore, reasonably expected to increase overall activity.

A further noteworthy feature of the Arrhenius plot for this sample, is the levelling off at temperature values greater than about 300°C. This behaviour (showing a rather characteristic shape) has been discussed by Hudgins et al.[39] for a variety of catalytic systems. It demonstrates the influence of transport phenomena (heat and mass) in determination of the overall reaction rate. These data do not however indicate which of internal heat, external heat, internal mass or external mass transfer effects are responsible. This observation points out a possible problem with further experiments, and is closely related to the difficulty experienced in preparing uniformly impregnated support materials. Calculations may be performed in order to estimate safe ranges of experimental conditions in which to operate, however these (in their presently available form) require the assumption of uniformly distributed catalyst sites within every catalyst particle (macroscopic).

7.2.3 MVS Generated Iron Catalyst

An MVS generated unimetallic Fe (1.5% on alumina) material was subjected to the same pretreatment and reaction conditions as the other samples. Using temperatures up to 410°C, no reaction whatsoever was observed. Although Fe is not normally considered to be an important hydrogenolysis catalyst, this total lack of activity may be caused by the irreducibility of Fe(III) on an alumina support having a significant surface concentration of OH groups. This observation was recently reported by Itchikawa[12]. The EPR/FMR data reported in Chapter V also provide evidence of the existence of Fe in this sample, entirely in the form of iron(III) oxide.

7.2.4 MVS Generated 3:1 Ru/Fe Bimetallic Catalyst

Results for the first bimetallic experiment of this group are presented in Figure 7-4. At temperatures below 350°C, the selectivities showed an unusually high predominance of the isomerization reaction over hydrogenolysis. Between 350 and 400°C, these selectivities all fell off quite sharply, as the selectivity toward olefin production (dehydrogenation reaction) increased. At 400°C, the distribution of products was about 40% trans-2-butene, 20% each of cis-2-butene and iso-butene, and less that 10% alkanes. There were also traces of propylene and presumably ethylene (since the GC column used was not capable of distinguishing ethylene from ethane) produced. It may be speculated that these result from

SAMPLE: EMR-3b 1.7 wt% Ru/Fe (3:1) on Alumina
MASS: 1.365 g
DATE: 1986 April 24
EXPERIMENTER: RAP

REACTANTS: n-Butane 6.0 cm3/min
Hydrogen 30.0 cm3/min
Argon 30.0 cm3/min

GC COLUMN: Poras:1-C
CARRIER GAS: Nitrogen
COLUMN TEMP: 40.0 C
PRESSURE: 293.0 kPa

SPECIES IDENTIFICATION

A. methane
B. ethane/ethylene
C. propane
D. propylene
E. iso-butane
F. n-butane
G. iso-butene
H. trans-2-butene
I. cis-2-butene

REACTION RATES (mol/h g)

TEMP (C)	SPECIES A	B	C	D	E	F	G	H	I	TOTAL CONVERSION
300.	9.045 -7	3.363 -7	.000 0	.000 0	6.105 -7	-1.905 -6	.000 0	.000 0	.000 0	.0000
325.	1.693 -6	1.381 -6	1.648 -6	.000 0	3.482 -6	-6.332 -6	.000 0	.000 0	.000 0	.0001
350.	1.332 -5	6.500 -6	5.308 -6	.000 0	9.388 -6	-1.365 -6	.000 0	1.156 -6	.000 0	.0023
378.	4.259 -5	1.257 -5	1.350 -5	1.145 -5	1.895 -5	-7.756 -6	1.831 -6	3.626 -6	1.953 -6	.0131
400.	1.001 -4	2.475 -5	2.257 -5	3.184 -5	2.348 -5	-1.422 -5	3.249 -6	6.398 -6	3.659 -6	.0243
400.	1.055 -4	2.575 -5	2.331 -5	3.317 -5	2.344 -5	-1.381 -5	3.341 -6	5.445 -6	3.773 -6	.0431
400.	1.395 -4	2.642 -5	2.621 -5	3.295 -5	2.370 -5	-1.456 -5	3.302 -6	6.477 -6	3.707 -6	.0267
400.	1.362 -4	3.122 -5	2.677 -5	3.985 -5	2.376 -5	-1.615 -5	3.609 -6	7.134 -6	4.175 -6	.0276
400.	1.161 -4	2.777 -5	2.612 -5	3.036 -5	2.478 -5	-1.338 -5	2.990 -6	5.869 -6	3.336 -6	.0225
405.	1.279 -4	2.995 -5	2.707 -5	3.345 -5	2.487 -5	-1.413 -5	3.178 -6	6.239 -6	3.562 -6	.0240
402.	1.240 -4	2.951 -5	1.471 -5	2.982 -5	2.555 -5	-1.282 -5	2.887 -6	5.669 -6	3.216 -6	.0217
405.	2.198 -6	4.663 -5	2.923 -5	6.778 -5	2.812 -5	-1.565 -5	3.394 -6	6.745 -6	3.671 -6	.0262
401.	2.126 -6	4.720 -5	3.872 -5	3.336 -5	3.708 -5	-1.289 -5	2.822 -6	5.508 -6	2.881 -6	.0219
402.	1.781 -6	4.036 -5	3.510 -5	2.914 -5	3.321 -5	-1.159 -5	2.642 -6	5.031 -6	2.656 -6	.0196
402.	1.726 -6	3.792 -5	3.260 -5	2.940 -5	2.857 -5	-1.192 -3	2.661 -6	5.108 -6	2.779 -6	.0202

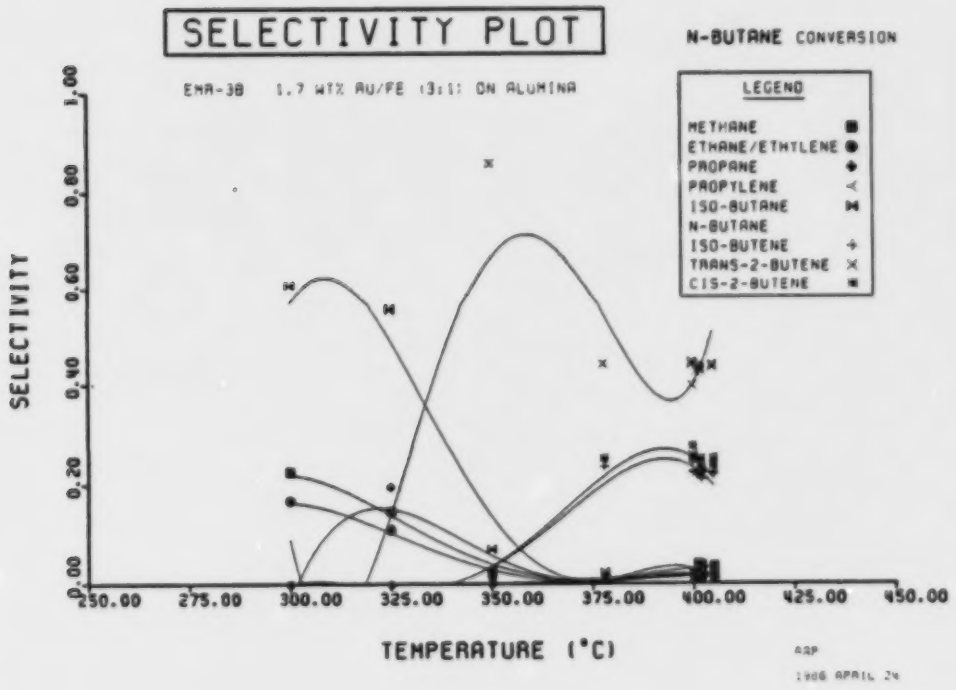

Figure 7-4 n-Butane Conversion Catalysis Results for Sample EMR-3b

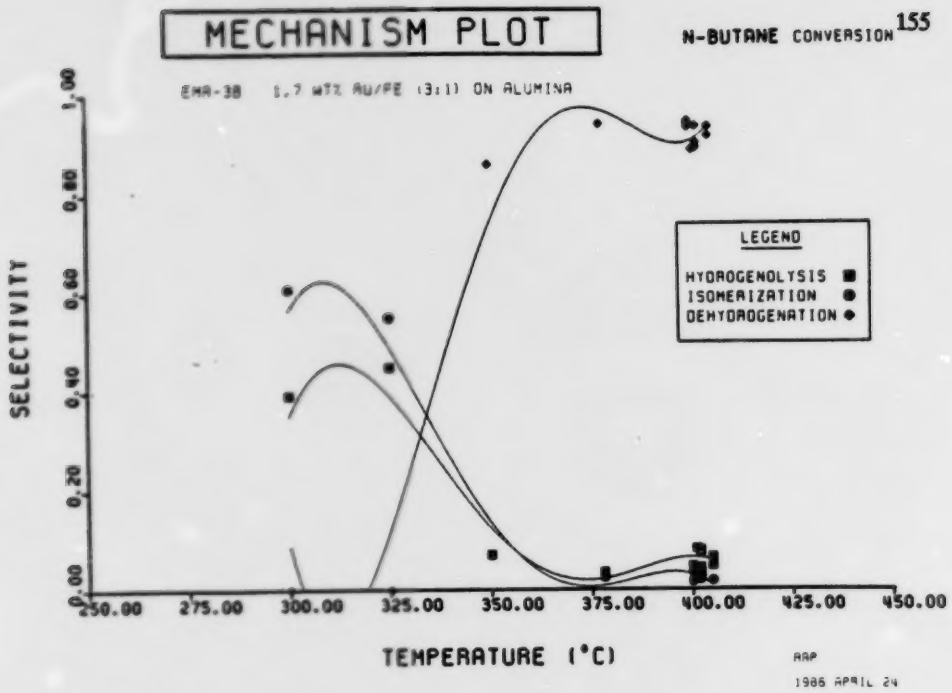

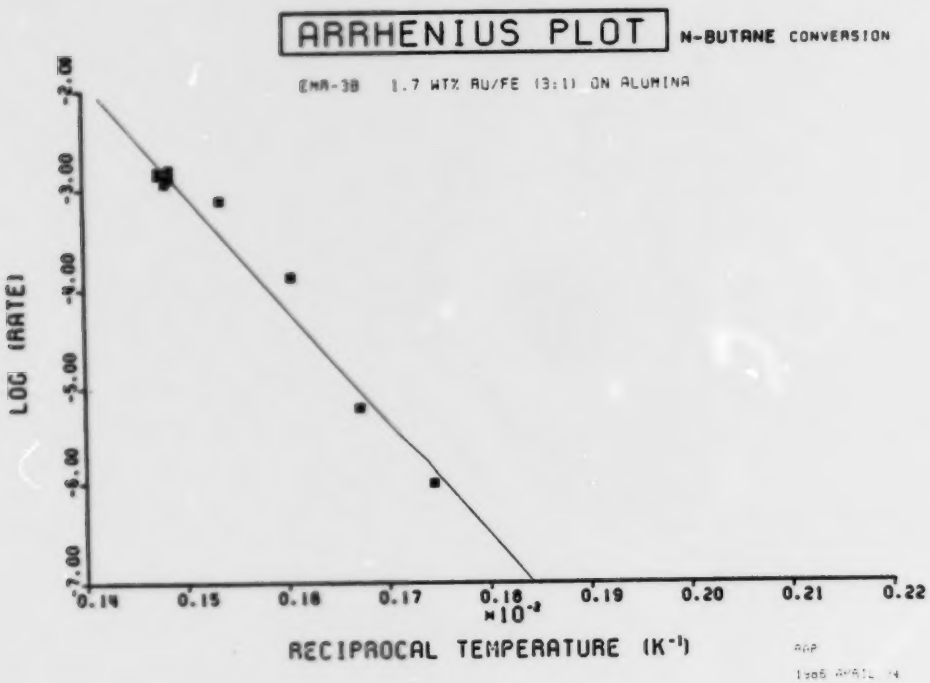

Figure 7-4 Continued

hydrogenolysis products which undergo further reaction. Such may involve re-adsorption of propane or ethane from the gas phase to the dehydrogenation sites, or a surface spillover phenomenon of these species. An experiment designed to elucidate this mechanism could possibly be carried out by varying the reactor space velocity; the use of propane hydrogenolysis could further simplify the analysis to differentiate between the primary and secondary type reactions.

It may also be speculated that zerovalent (or lower than +3 valence) iron is the active dehydrogenation site. This suggestion is based on Itchikawa's observation[12] that the presence of Rh (hence one might speculate similar behaviour for Ru as well) makes Fe more reducible under the conditions used.

The Arrhenius plot for this experiment shows good linearity, however the observed activation energy is about 225 kJ/mol. This value is probably a reflection of the dehydrogenation reaction alone.

7.2.5 MVS Generated 2:3 Ru/Fe Bimetallic Catalyst

The final n-butane conversion experiment of this group was performed on a second Ru/Fe bimetallic sample. This was for EMR-5, an iron rich sample having a higher total loading than the previous bimetallic (the total loading was 5.2 wt%; Ru:Fe was 0.60). The results are shown in Figure 7-5.

At temperatures below roughly 275°C, the only observed reactions were hydrogenolysis and a minor amount of isomerization. This bimetallic sample differed from the ruthenium rich sample, both in that isomerization selectivity was low in this temperature range, and that the selectivity toward ethane was almost twice as great as that toward methane/propane. The selectivity toward isomerization increased somewhat with increasing temperature; it reached a maximum of about 40% at 300°C.

Above 300°C, the selectivity toward methane increased to about 60%, with ethane selectivity being about 25%, and selectivities for isobutane and propane both being between 10 and 20%. It is obvious from the fact that there was much more methane than propane in the effluent stream, that the feed butane underwent successive hydrogenolysis reactions during its residence in the reactor.

As with the other bimetallic sample, dehydrogenation was observed at the high end of the temperature range examined. However, whereas in the Ru rich sample, this was first detected at 350°C, in the present sample, dehydrogenation was only observed above 400°C. Among the dehydrogenation products, the distribution was very similar for both bimetallics. The trans-2-butene showed a selectivity about twice as great as that of the iso and cis products.

SAMPLE: EMR-5 5.2 wt% Ru/Fe (2:3) on Alumina
MASS: 2427 g
DATE: 1986 May 22/23
EXPERIMENTER: RAP

REACTANTS: n-Butane 8.0 cm3/min
Hydrogen 30.0 cm3/min
Argon 30.0 cm3/min

GC COLUMN: Porasil-C
CARRIER GAS: Nitrogen
COLUMN TEMP: 40.0 C
PRESSURE: 293.0 kPa

SPECIES IDENTIFICATION

A. methane
B. ethane/ethylene
C. propane
D. propylene
E. iso-butane
F. n-butane
G. iso-butene
H. trans-2-butene
I. cis-2-butene

REACTION RATES (mol/h g)

TEMP (C)	SPECIES A	B	C	D	E	F	G	H	I	TOTAL CONVERSION
200.	1.722 -6	1.223 -6	5.380 -7	.000 0	2.418 -7	-1.685 -6	.000 0	.000 0	.000 0	0001
200.	1.742 -6	1.386 -6	6.370 -7	.000 0	2.182 -7	-1.814 -6	.000 0	.000 0	.000 0	0001
200.	1.551 -6	1.340 -6	5.676 -7	.000 0	3.054 -7	-1.884 -6	.000 0	.000 0	.000 0	0001
225.	9.407 -6	7.751 -6	3.167 -6	.000 0	1.067 -6	-9.670 -6	.000 0	.000 0	.000 0	0003
225.	8.542 -6	7.428 -6	3.116 -6	.000 0	1.351 -6	-9.537 -6	.000 0	.000 0	.000 0	0003
250.	5.335 -5	4.220 -5	1.605 -5	.000 0	1.362 -5	-6.010 -5	.000 0	.000 0	.000 0	0018
250.	4.656 -5	3.951 -5	1.535 -5	.000 0	1.270 -5	-5.560 -5	.000 0	.000 0	.000 0	0017
250.	4.586 -5	4.010 -5	1.573 -5	.000 0	1.317 -5	-5.647 -5	.000 0	.000 0	.000 0	0017
277.	2.558 -4	1.662 -4	5.155 -5	.000 0	8.546 -5	-2.712 -4	.000 0	.000 0	.000 0	0082
275.	2.192 -4	1.526 -4	5.346 -5	.000 0	8.370 -5	-2.541 -4	.000 0	.000 0	.000 0	0077
350.	2.013 -3	3.294 -4	4.667 -5	.000 0	5.092 -5	-7.530 -4	.000 0	.000 0	.000 0	0227
353.	1.883 -3	3.531 -4	6.988 -5	.000 0	8.434 -5	-7.840 -4	.000 0	.000 0	.000 0	0237
353.	1.810 -3	3.287 -4	7.149 -5	.000 0	8.702 -5	-7.575 -4	.000 0	.000 0	.000 0	0229
384.	2.154 -3	2.600 -4	6.007 -5	.000 0	3.592 -5	-7.344 -4	.000 0	.000 0	.000 0	0222
384.	1.987 -3	3.125 -4	7.093 -5	.000 0	7.844 -5	-7.797 -4	.000 0	.000 0	.000 0	0235
411.	1.701 -3	2.355 -4	8.913 -5	9.344 -6	9.762 -5	-7.709 -4	5.646 -5	.000 0	.000 0	0233
401.	3.639 -4	1.473 -4	8.262 -5	.000 0	1.415 -4	-3.681 -4	.000 0	.000 0	.000 0	0111
401.	2.787 -4	1.189 -4	7.348 -5	.000 0	1.257 -4	-3.106 -4	.000 0	.000 0	.000 0	0094
351.	1.655 -3	3.252 -4	9.303 -5	.000 0	1.149 -4	-7.610 -4	.000 0	.000 0	.000 0	0230
352.	1.622 -3	3.241 -4	9.730 -5	.000 0	1.222 -4	-7.626 -4	.000 0	.000 0	.000 0	0230
381.	1.835 -3	2.904 -4	7.500 -5	.000 0	7.883 -5	-7.439 -4	.000 0	.000 0	.000 0	0224
381.	1.818 -3	2.923 -4	8.176 -5	.000 0	8.854 -5	-7.504 -4	.000 0	.000 0	.000 0	0226
429.	1.659 -3	1.944 -4	7.760 -5	2.106 -5	7.128 -5	-9.948 -4	1.080 -4	1.013 -4	6.818 -5	0300
429.	1.612 -3	1.636 -4	7.809 -5	2.839 -5	7.239 -5	-1.162 -3	1.461 -4	2.922 -4	1.367 -4	0351

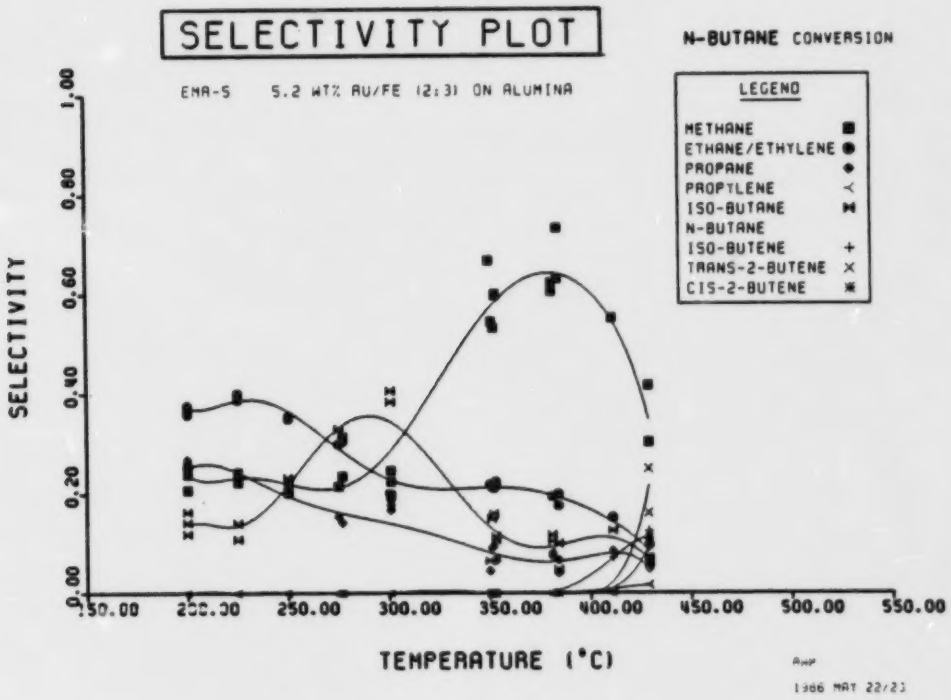

Figure 7-5 n-Butane Conversion Catalysis Results for Sample EMR-5

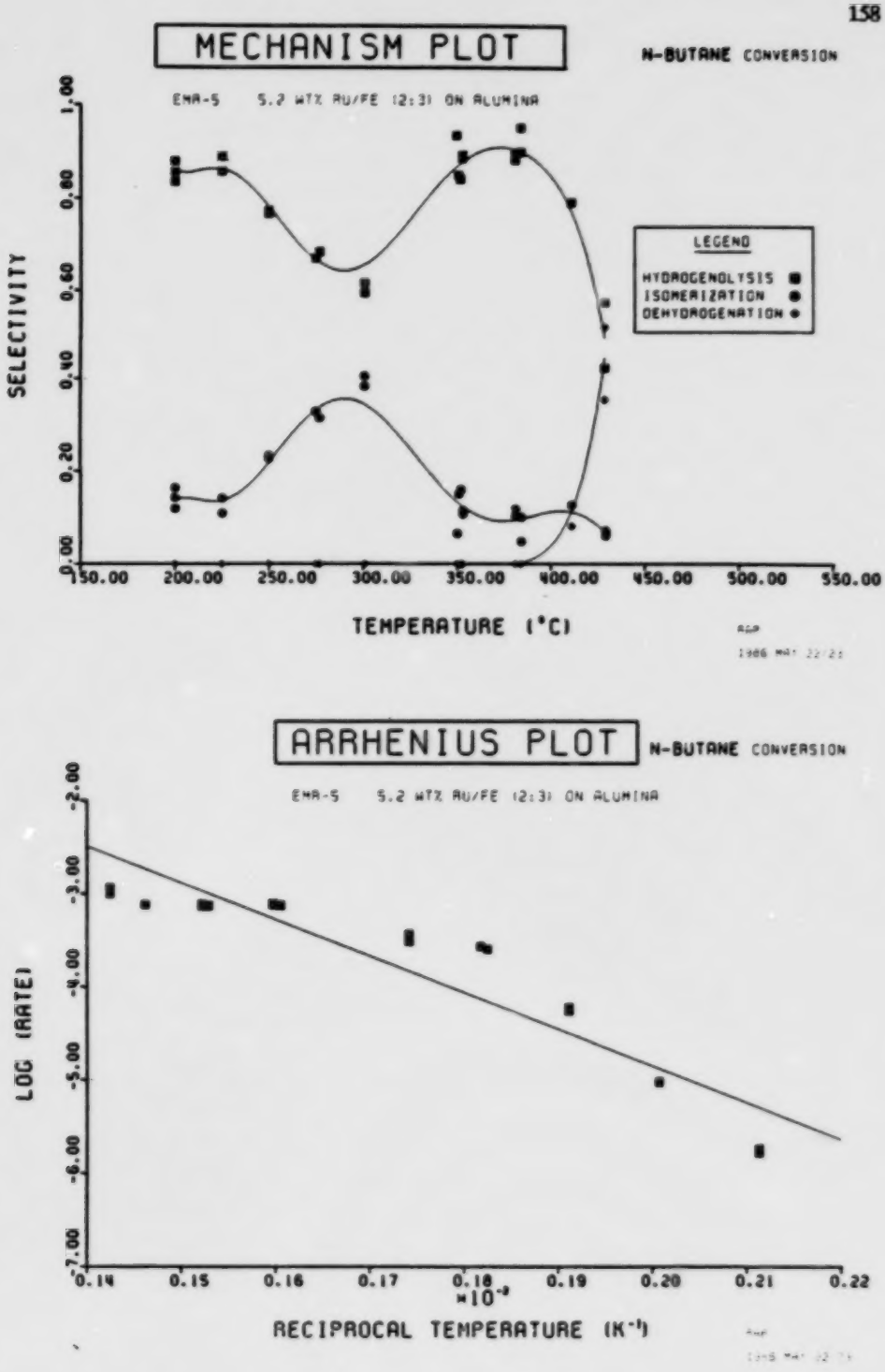

Figure 7-5 Continued

The Arrhenius plot for this sample shows better linearity in the lower temperature range than it does above 375°C. Again, there was a levelling off, indicative of transport inclusions. This is not unexpected, since at a total loading of 5.2 wt%, the total conversion was relatively high. The activation energy was lower than the usual 100 kJ/mol for hydrogenolysis. If however, the points in the high temperature range (where transport effects are observed) were neglected, the typical value for E_a would result. Because of the late appearance of any significant amount of dehydrogenation, the activation energy was much lower than for the Ru rich bimetallic sample (which was strongly influenced by that reaction, having E_a = 225 kJ/mol).

7.2.6 Control Experiment for Support Activity

A n-butane conversion run was carried out on an unimpregnated sample of each of support materials discussed in this chapter. This was done in order to verify that the catalytic activity measured was not a result of the support itself.

At temperatures below 400°C, there were only observations of barely detectable quantities of ethane. This would not cause problems in the interpretation of results, since such levels have been customarily ignored in drawing conclusions in previous experiments.

7.3 Additional Studies on Heavily Loaded Iron Catalysts

Based upon analysis of the first set of Fe, Ru and Fe/Ru MVS generated catalysts, there remained several unanswered questions. The most pressing of these centred around the role of the Fe valence state, and its effect on catalytic activity. According to the literature, the two major factors which can affect the oxidizability of Fe are the total metal loading employed, and the composition and pretreatment conditions of the support material. Further experiments were conducted in order to examine these.

The experiments in this group allow a preliminary examination of two factors, namely the choice of support material, and the support pretreatment temperature. In all, there are four samples having about the same total Fe loading; a high and low pretreatment temperature were used to prepare samples from a pure alumina support, and a 6% silica/94% alumina material.

Results are presented in Figures 7-6 through 7-9, and a qualitative comparison of the catalytic behaviour of these materials is presented in Table 7-2.

SAMPLE: EMR-11a 3.5 wt% Fe on SMR-6 support (pt. 250 C) DATE: 1986 Sept 08
MASS: 5426 g EXPERIMENTER: RAP

REACTANTS: n-Butane 8.0 cm3/min GC COLUMN: Porasil-C
Hydrogen 30.0 cm3/min CARRIER GAS: Nitrogen
Argon 30.0 cm3/min COLUMN TEMP: 60.0 C PRESSURE: 306.8 kPa

SPECIES IDENTIFICATION

A. methane
B. ethane/ethylene
C. propane
D. propylene
E. iso-butane
F. n-butane
G. iso-butene
H. trans-2-butene
I. cis-2-butene

REACTION RATES (mol/h g)

TEMP (C)	SPECIES A	B	C	D	E	F	G	H	I	TOTAL CONVERSION
100.	.000 0	6.678 -8	.000 0	.000 0	7.846 -8	-1.122 -5	1.111 -5	.000 0	.000 0	.0008
100.	.000 0	5.658 -8	.000 0	.000 0	7.211 -8	-1.119 -5	1.109 -5	.000 0	.000 0	.0008
100.	.000 0	.000 0	.000 0	.000 0	5.432 -8	-1.121 -5	1.115 -5	.000 0	.000 0	.0008
200.	1.743 -7	8.019 -8	3.455 -8	.000 0	2.140 -8	-1.114 -5	1.101 -5	.000 0	.000 0	.0008
200.	4.728 -7	4.462 -7	2.005 -7	.000 0	2.110 -8	-1.179 -5	1.127 -5	.000 0	.000 0	.0008
300.	3.696 -5	5.298 -6	6.997 -7	.000 0	6.704 -7	-2.471 -5	1.163 -5	.000 0	.000 0	.0017
300.	2.574 -5	4.321 -6	6.695 -7	.000 0	6.422 -7	-2.140 -5	1.166 -5	.000 0	.000 0	.0014
400.	6.637 -6	1.120 -6	3.802 -7	3.807 -6	2.896 -7	-1.140 -4	3.231 -5	4.807 -5	2.800 -5	.0077
450	8.233 -7	1.833 -7	2.542 -8	2.368 -6	.000 0	-1.499 -4	4.854 -5	5.888 -5	4.037 -5	.0101

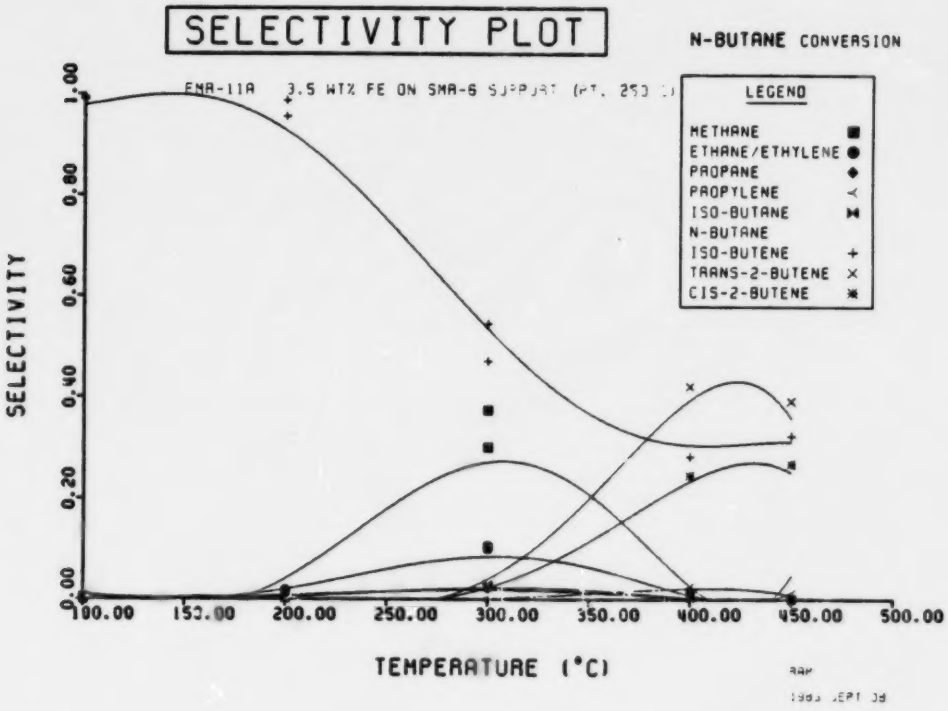

Figure 7-6 n-Butane Conversion Catalysis Results for Sample EMR-11a

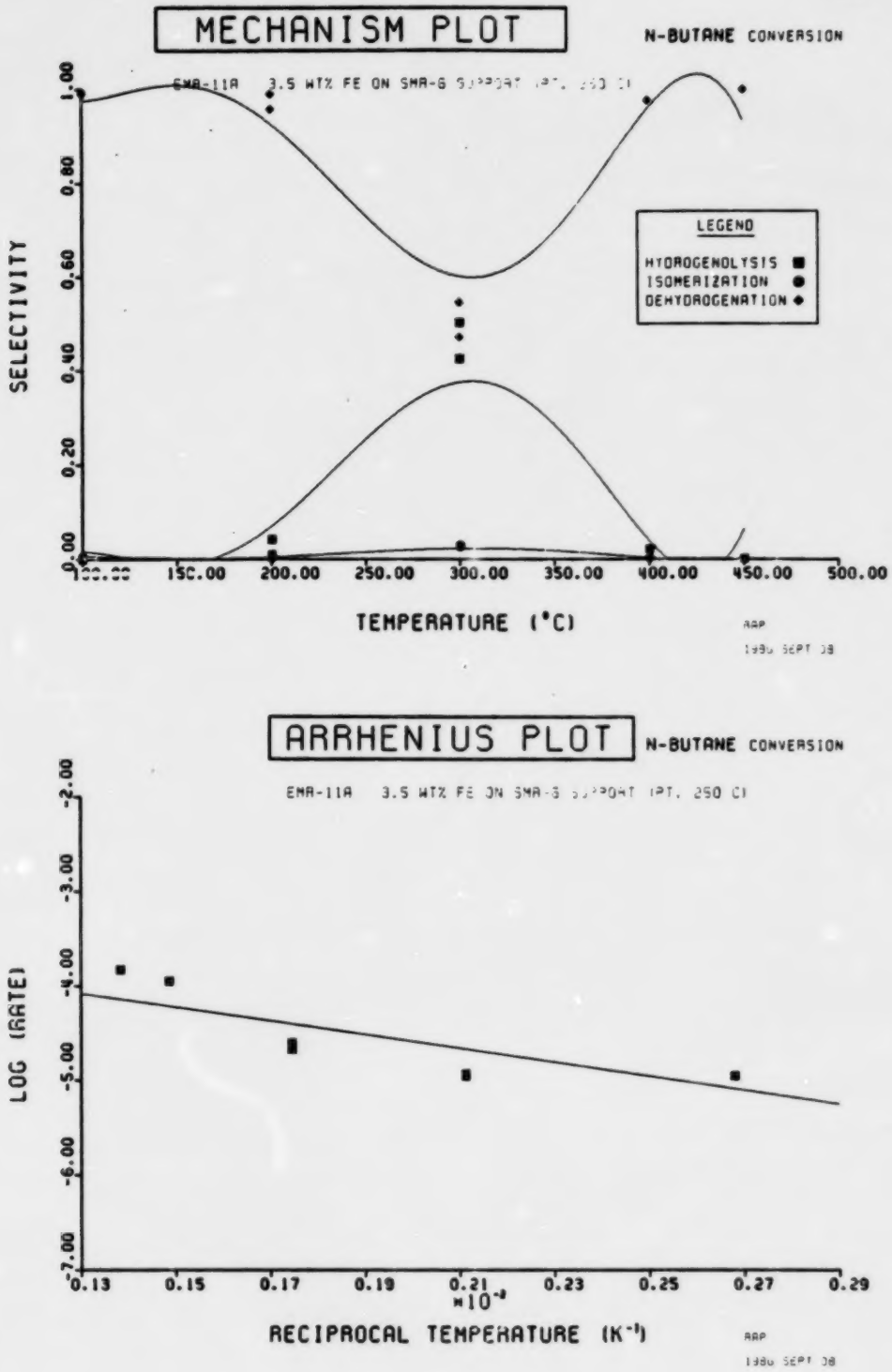

Figure 7-6 Continued

SAMPLE: EMR-11b 3.5 wt% Fe on SMR-6 support (pt. 450C) DATE: 1986 Aug 21
MASS: .3734 g EXPERIMENTER: RAP

REACTANTS: n-Butane 8.0 cm3/min GC COLUMN: Porasil-C
Hydrogen 30.0 cm3/min CARRIER GAS: Nitrogen
Argon 30.0 cm3/min COLUMN TEMP: 60.0 C PRESSURE: 317.2 kPa

SPECIES IDENTIFICATION

A. methane
B. ethane/ethylene
C. propane
D. propylene
E. iso-butane
F. n-butane
G. iso-butene
H. trans-2-butene
I. cis-2-butene

REACTION RATES (mol/h g)

TEMP (C)	SPECIES A	B	C	D	E	F	G	H	I	TOTAL CONVERSION
25.	.000 0	7.226 -7	6.402 -6	.000 0	3.356 -6	-5.415 -5	4.563 -5	.000 0	.000 0	.0025
25.	.000 0	4.672 -7	8.520 -7	.000 0	2.329 -6	-6.472 -5	4.152 -5	.000 0	.000 0	.0021
25.	.000 0	2.993 -7	4.271 -7	.000 0	1.222 -6	-2.675 -5	2.506 -5	.000 0	.000 0	.0012
50.	.000 0	2.126 -7	5.082 -7	.000 0	1.048 -6	-2.260 -5	2.105 -5	.000 0	.000 0	.0010
50.	.000 0	1.837 -7	5.931 -7	.000 0	9.486 -7	-1.936 -5	1.787 -5	.000 0	.000 0	.0009
100.	.000 0	1.162 -7	7.902 -7	.000 0	8.095 -7	-1.460 -6	.000 0	.000 0	.000 0	.0001
100.	.000 0	1.009 -7	8.884 -7	.000 0	7.415 -7	-1.455 -6	.000 0	.000 0	.000 0	.0001
200.	.000 0	.000 0	1.330 -6	.000 0	6.710 -7	-1.668 -6	.000 0	.000 0	.000 0	.0001
300.	.000 0	.000 0	1.690 -6	.000 0	5.460 -7	-1.814 -6	.000 0	.000 0	.000 0	.0001
360.	2.545 -7	.000 0	1.890 -6	.000 0	4.823 -7	-4.833 -5	2.482 -5	2.155 -5	.000 0	.0022
390.	1.623 -7	.000 0	1.727 -6	.000 0	3.877 -7	-4.110 -5	2.339 -5	1.598 -5	.000 0	.0019
420.	.000 0	.000 0	1.454 -6	.000 0	3.250 -7	-4.771 -5	2.644 -5	1.986 -5	.000 0	.0022

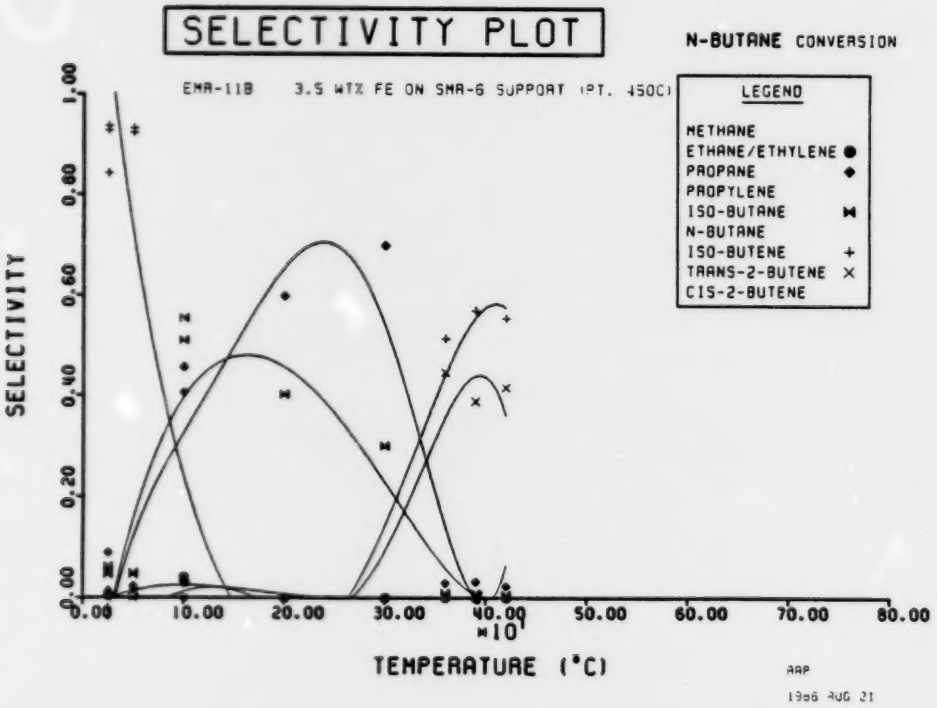

Figure 7-7 n-Butane Conversion Catalysis Results for Sample EMR-11b

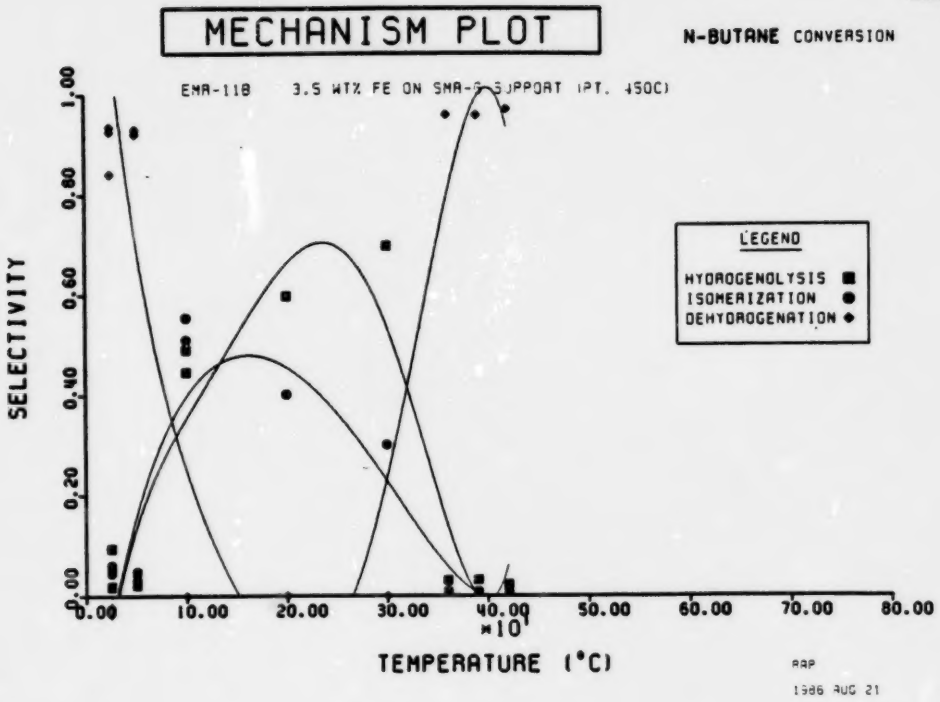

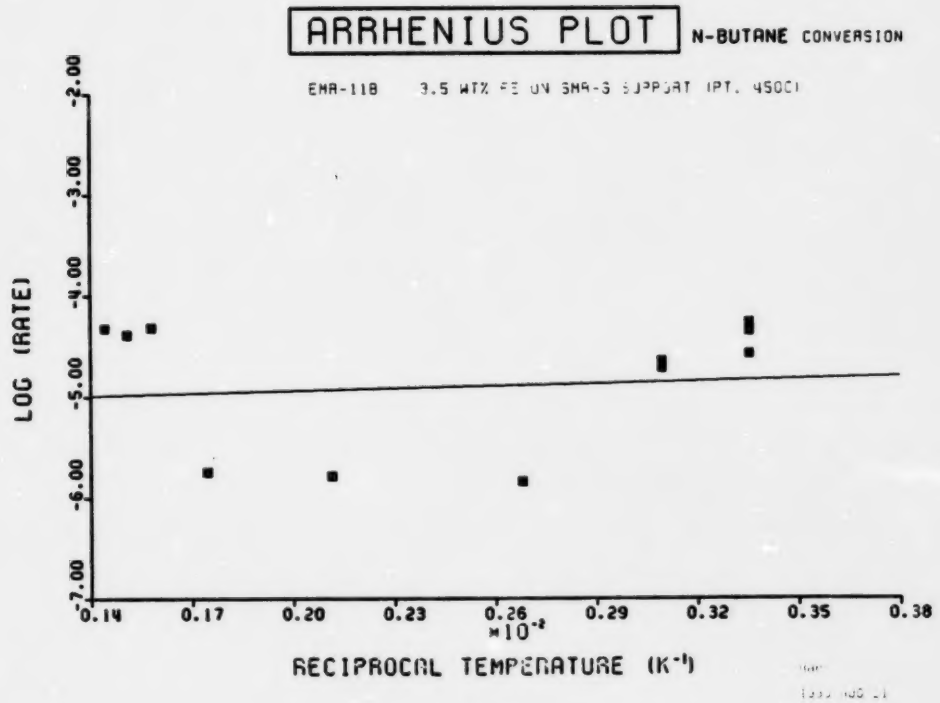

Figure 7-7 Continued

SAMPLE: EMR-21a 3.8 wt% Fe on Alumina (pt. @ 200 C) DATE: 1986 October 07
MASS: .3295 g EXPERIMENTER: RAP

REACTANTS: n Butane 8.0 cm3/min GC COLUMN: Porasil-C
Hydrogen 30.0 cm3/min CARRIER GAS: Nitrogen
Argon 30.0 cm3/min COLUMN TEMP: 60.0 C PRESSURE: 324.1 kPa

SPECIES IDENTIFICATION

A. methane
B. ethane/ethylene
C. propane
D. propylene
E. iso-butane
F. n-butane
G. iso-butene
H. trans-2-butene
I. cis-2-butene

REACTION RATES (mol/h g)

TEMP (C)	SPECIES A	B	C	D	E	F	G	H	I	TOTAL CONVERSION
301.	4.907 -7	.000 0	.000 0	.000 0	.000 0	-1.227 -7	.000 0	.000 0	.000 0	.0000
301.	4.900 -7	.000 0	.000 0	.000 0	3.660 -7	-4.885 -7	.000 0	.000 0	.000 0	.0000
353.	6.990 -6	9.949 -8	4.139 -8	1.023 -6	.000 0	-5.026 -5	.000 0	2.851 -5	1.916 -5	.0014
353.	1.108 -5	1.434 -7	5.559 -8	1.225 -6	2.993 -8	-5.299 -5	.000 0	2.912 -5	2.004 -5	.0015
380.	4.675 -5	4.465 -7	1.202 -7	2.711 -6	1.261 -7	-8.670 -5	.000 0	4.213 -5	3.041 -5	.0024
427.	5.574 -5	5.908 -7	7.065 -8	5.327 -6	1.187 -7	-3.182 -4	5.093 -5	1.463 -4	1.026 -4	.0089
429.	3.217 -5	3.800 -7	5.530 -8	4.134 -6	.000 0	-3.202 -4	5.735 -5	1.480 -4	1.035 -4	.0089

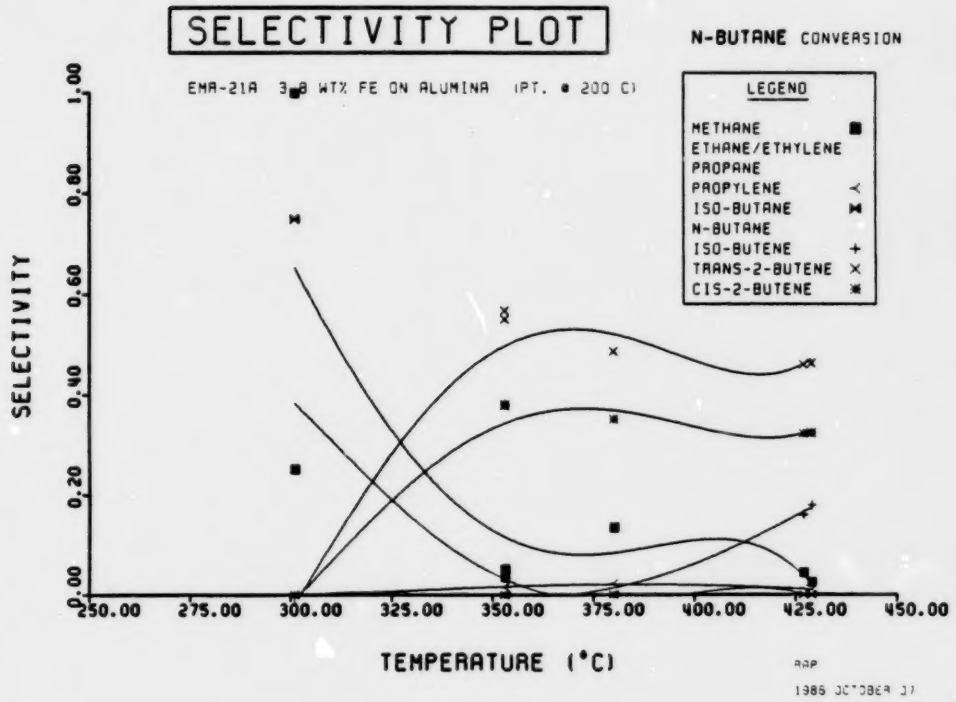

Figure 7-8 n-Butane Conversion Catalysis Results for Sample EMR-21a

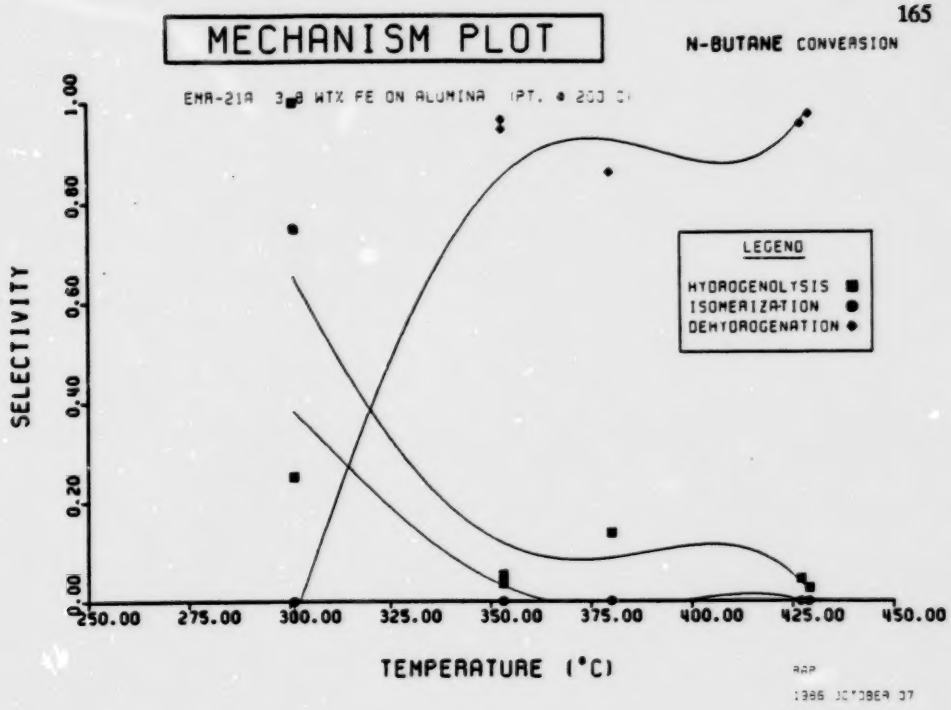

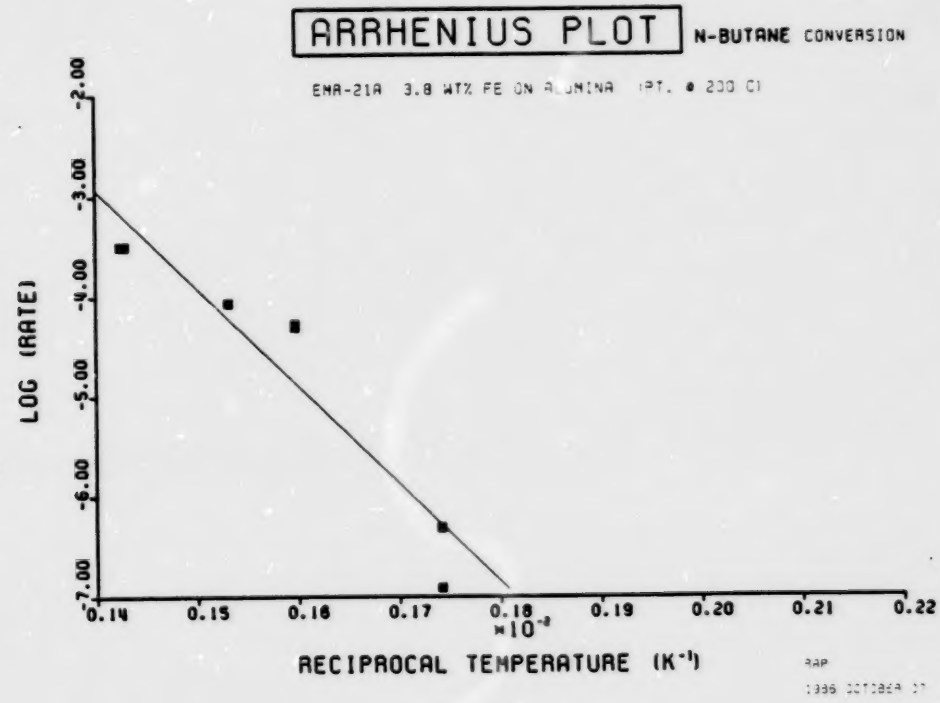

Figure 7-8 Continued

SAMPLE: EMR-21b 3.8 wt% Fe on Alumina (pt. 3 600 C)
MASS: 1651 g

DATE: 1986 October 02
EXPERIMENTER: RAP

REACTANTS: n-Butane 8.0 cm3/min
Hydrogen 30.0 cm3/min
Argon 30.0 cm3/min

GC COLUMN: Porasil-C
CARRIER GAS: Nitrogen
COLUMN TEMP: 60.0 C

PRESSURE: 310.3 kPa

SPECIES IDENTIFICATION

A. methane
B. ethane/ethylene
C. propane
D. propylene
E. iso-butane
F. n-butane
G. iso-butene
H. trans-2-butene
I. cis-2-butene

REACTION RATES (mol/h g)

TEMP (°C)	SPECIES A	B	C	D	E	F	G	H	I	TOTAL CONVERSION
25	5.481 -7	.000 0	.000 0	.000 0	.000 0	-1.370 -7	.000 0	.000 0	.000 0	.0000
25	1.057 -6	.000 0	.000 0	.000 0	.000 0	-2.643 -7	.000 0	.000 0	.000 0	.0000
25	8.560 -7	.000 0	.000 0	.000 0	.000 0	-2.140 -7	.000 0	.000 0	.000 0	.0000
100	.000 0	.000 0	.000 0	.000 0	4.592 -8	-4.592 -8	.000 0	.000 0	.000 0	.0000
200	.000 0	.000 0	.000 0	.000 0	1.570 -7	-1.570 -7	.000 0	.000 0	.000 0	.0000
300	4.520 -7	.000 0	.000 0	.000 0	8.060 -8	-2.903 -5	.000 0	2.884 -5	.000 0	.0014
300	4.119 -7	.000 0	.000 0	.000 0	.000 0	-5.000 -5	.000 0	2.573 -5	2.417 -5	.0007
375	1.316 -5	6.301 -7	5.144 -7	.000 0	3.905 -7	-1.609 -3	3.534 -4	7.394 -4	5.122 -4	.0425
425	5.363 -6	4.150 -7	2.792 -7	2.115 -6	7.340 -7	-6.814 -3	1.613 -3	2.954 -3	2.243 -3	.0453
500	1.097 -5	8.358 -6	4.857 -6	4.838 -5	8.976 -6	-3.590 -2	9.735 -3	1.451 -2	1.159 -2	.5023

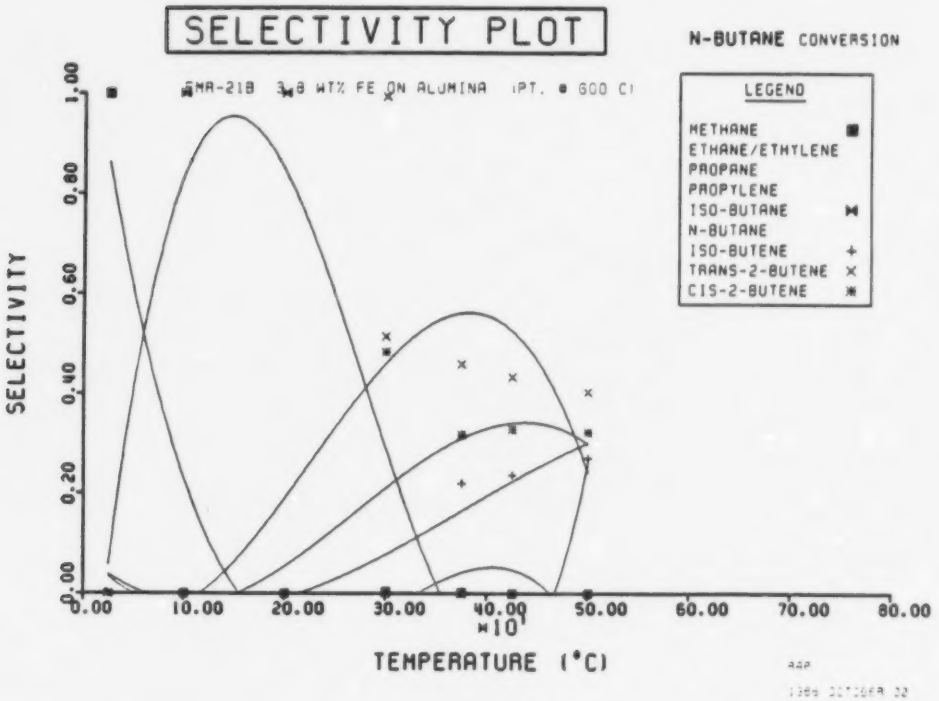

Figure 7-9 n-Butane Conversion Catalysis Results for Sample EMR-21b

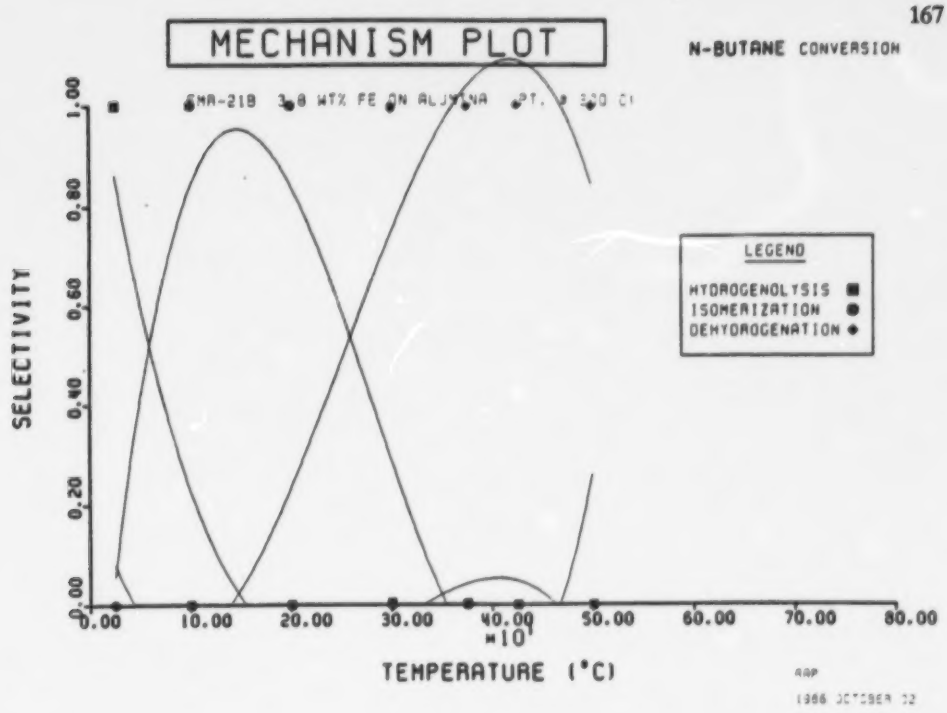

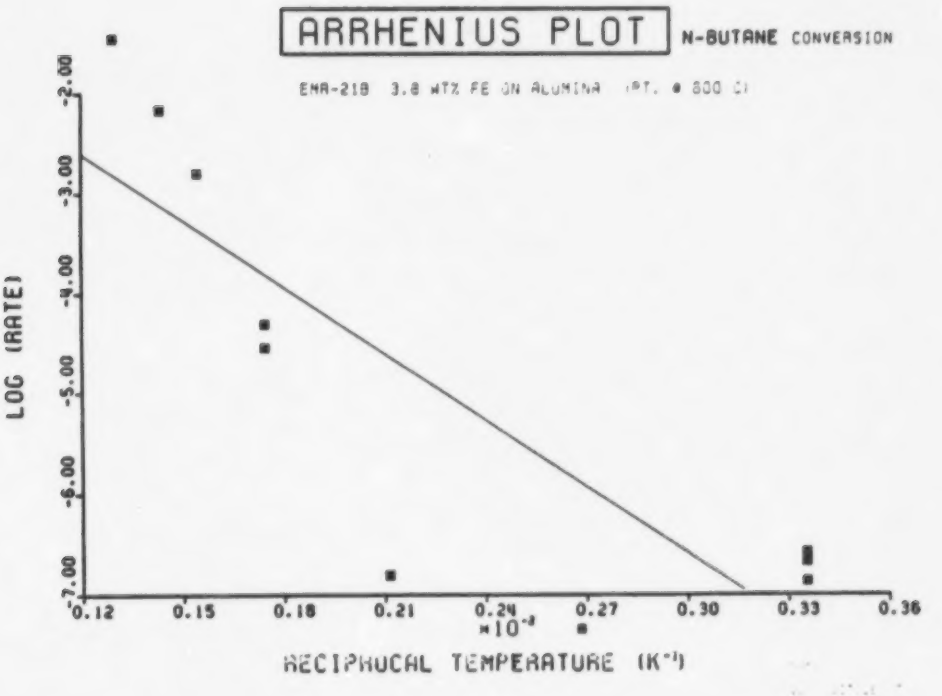

Figure 7-9 Continued

SAMPLE	EMR-11 b	EMR-11 a	EMR-21 a	EMR-21 b
Metal Loading	3.5 wt%	3.5 wt%	3.8 wt%	3.8 wt%
Support Material	SiO_2/Al_2O_3	SiO_2/Al_2O_3	Al_2O_3	$Al2O_3$
Pretreatment Temperature	450°C	250°C	200°C	600°C
Activity at 25°C	Yes	Trace	No	Trace Methane
Alkane Production	Less Than Olefins	Dominant 200-400oC	1/10 Olefin Rate	Much Less Than Olefins
Propane	Major Alkane	Trace	Trace	Very Little; Only above 350°C
Ethane	Half Propane Rate Below 100°C	About 10x Propane Rate	Trace	Same as Propane
Methane	Trace Near 375°C	Much More Than Ethane	Modest; Similar to Olefin Rate	About 10x Propane Rate
Isomerization	Similar to Propane Rate	Trace Only	Trace Only	Slow above 350°C; Trace Below
Dehydrogenation	About 10x Overall Alkane Rate	10x Alkane Rate Above 400°C	Active at High Temperatures	Very Active Above 300°C
Propylene	Not Detected	Only Above 400°C	1/10 Rate of Other Olefins	1/1000 Rate of Other Olefins
1-Butene	Never	Never	Never	Never
iso-Butene	Not Observed in Middle Temperature Range	Very Little Observed Below 400°C	Very Little Observed Below 400°C	Only Observed at Temperatures Above 375°C
trans-2-Butene	High Temperature Only; Major Product	Major Product Above 400°C	Major Product Above 300°C	Major Product Above 300°C
cis-2-Butene	Not Observed	Substantial Above 400°C	Substantial Above 300°C	Substantial Above 300°C
iso:trans:cis Ratio (approximate)	1:2:0	1:2:1	1:3:2	1:3:2
Colour Change of Sample	Gray to White	Gray to White	No Change	Gray to Black

Table 7-2 Catalytic Characteristics of MVS-Generated Supported Iron Samples

7.3.1 MVS Generated Fe Catalyst on Silica/Alumina Support

A series of n-butane conversion experiments was conducted using a 3.5 wt% Fe catalyst (EMR-11b). The support material was 6% silica/ 94% alumina (SMR-6) in powder form, and vacuum pretreated at 450°C. The loading conditions were chosen in order to facilitate the stabilization of at least some low valent Fe in the final catalyst material. The high pretreatment temperature yields a lower surface hydroxyl concentration on the support before metal impregnation, hence leading to oxidation of fewer zerovalent Fe organometallic precursor molecules and/or the final Fe agglomerates. Furthermore, it has been reported in the literature, that for both Fe[33] and Ni[13,34], a certain fixed quantity of metal precursor will become oxidized, while the remainder will not. For this reason, higher total metal loadings would also be expected to give rise to the presence of some low (or likely zero) valent surface entities.

An inspection of the virgin catalyst material handled anaerobically, and one exposed to atmospheric air, indicated marked differences in colour. The anaerobic material was fairly dark gray, while the air-exposed material was orange; these are the familiar appearances for Fe(0) or Fe(II), and Fe(III) respectively.

The catalyst pretreatment used before the butane conversion runs, followed the usual temperature program. However, for the reductive step, the hydrogen concentration in the gas stream was about 60% instead of the usual 20%. As with all previous pretreatments, the maximum temperature was 310°C. The experiment on sample EMR-4 (low loading Fe on alumina) was repeated using the higher hydrogen concentration in the pretreatment step. As in the first experiment on this sample, no activity whatsoever was observed.

Butane conversion data were collected over a temperature range beginning at room temperature (25°C), and extending above 400°C. Perhaps the most remarkable observation was the catalytic activity measured at room temperature. Even the most active of the catalysts previously examined in the present research did not show detectable product levels below 175°C. In general, the activity was seen as a pulse having maximum initial conversion, followed by exponential decay (for all product substances concerned). The characteristics of the activity decay is discussed in greater detail later in this section, however, it is noteworthy that this was not an exceptionally fast decline of activity. In three hours of steady state reaction, the loss was less than one order of magnitude.

The observed product distribution indicated that the hydrogenolysis, isomerization and dehydrogenation mechanisms were all active at room temperature. The most significant of these was

dehydrogenation, having a selectivity consistently above 80% for 25 and 50°C. Somewhat surprisingly, the only dehydrogenation product was isobutene. Between 100 and 300°C, only isomerization and hydrogenolysis (producing isobutane and the alkanes respectively) were found to have about 50% selectivities. In mild contrast to the previously discussed EMR-3b and EMR-5 Ru/Fe bimetallic samples, isomerization was not the major of these two. It is however noteworthy that for both of the bimetallic samples examined, as well as the present sample, these two reactions have selectivities which are reasonably close to each other. With respect to Figure 7-6, it may actually not be true that the dehydrogenation rate was identically zero between 100 and 300°C. This results from the fact that the sensitivity for detection of butenes was very low relative to that for the lighter products. Although there must have occurred at least some minimum in the selectivity curve for dehydrogenation (betwen the maxima at 25 and 400°C), this *valley* could be much shallower than that depicted. Detection of isobutene becomes difficult at reaction rate levels for which the corresponding selectivity would still be roughly 50%.

In the present, pure Fe sample, the overall rate of reaction was comparable with that of the Fe rich EMR-5 bimetallic sample at 200°C. However, for the present sample, the rate remained virtually invariant between this temperature and about 360°C, whereas in the bimetallic case a substantial temperature dependence was observed. With respect to the Ru rich bimetallic sample, the rate was found to be comparable at 300°C, but again without any similarity in the temperature dependence of the observations.

In the high temperature range (360 - 420°C), the results were somewhat more like those of the two bimetallic samples. Beginning at about 350°C, the selectivities for hydrogenolysis and isomerization fell off quite sharply (with increasing temperature) as dehydrogenation products appeared. Whereas for the bimetallics, the distribution was 2:1:1 for the trans, cis and iso-butenes respectively, for the present sample, only the trans and iso products were observed. These were produced with a selectivity ratio of approximately 1:1.

In the high temperature limit of these experiments, the present sample had an overall activity which was more than an order of magnitude lower than that of the bimetallic samples. This could possibly be interpreted as an indication of far fewer catalyst sites per unit catalyst mass. If indeed low valent Fe is the active phase, it would be reasonable to suggest that in a 3.5 wt% sample, much of the Fe may still be in oxidized form. A further experiment could involve examination of a yet more heavily loaded and/or dehydroxylated Fe sample. As shown in the Arrhenius plot, there was essentially no temperature dependence of the reaction rate in the high temperature range. This observation has been attributed to diffusion controlled kinetics in the previous samples. However, the levelling off in the previous samples

occurred at an absolute rate of reaction more than ten times greater than in the present case. It should be borne in mind at this point, that the present support is not the same as in the catalysts previously examined; the diffusion and thermal properties could therefore be sufficiently different to account for some differences in the onset of transport inclusions. However, since the surface areas and thermal conductivities are known to be roughly similar, it is difficult thus to explain a tenfold difference in limiting reaction rate. It was furthermore observed that temperature invariance occurred in the 200 to 300°C range, at an overall rate considerably lower than that observed near 400°C. A different explanation would be required in any case, for this plateau.

One very remarkable feature of the hydrogenolysis reaction was observed throughout the entire temperature range: the absence of methane in the product stream. This is made perhaps more remarkable in view of the fact that the major hydrogenolysis product was propane, not ethane. It may be speculated that on this catalyst (especially when one considers the importance of dehydrogenation in this system), the breaking of C-C bonds in the butane reactant gives at least one unsaturated surface intermediate. It is certainly a further possibility that both fragments (containing one and three carbon atoms respectively) may be hydrogen deficient. The larger of these, as well as ethane precursors may be easily hydrogenated off the catalyst surface, while methyl, carbene etc. intermediates may not. It has been well established[45] that Fe surfaces used in such systems as CO hydrogenation, can be quickly and easily deactivated by the buildup of similar fragment species, as well as graphitic species. The buildup of irreversibly bound hydrocarbon and carbon fragments could also provide a good explanation for the observed activity decay.

It has been suggested also, that some of the surface intermediates may desorb by first migrating together to form ethane or propane precursors (for which the final step before desorption would likely be hydrogenation). Based on statistical information, this seems not to be the case, since such a mechanism would be expected to yield much greater quantities of ethane. In fact, no ethane production was observed at temperatures greater than 100°C. Further evidence against the concept of ethane production via fragment migration is that if such a phenomena were the true path, a different temperature dependence would be expected. Since migration rates are known to increase with increasing temperature, so too would the ethane production rate. Also, if the deactivation process did involve a time-dependent buildup of single-carbon fragments, and ethane was produced through the coupling of these, then the rate of production would be expected to increase with elapsed time (coincidentally with the change in surface concentration of the fragments).

At 360 and 390°C, there were very small quantities of methane observed. In work with previous samples at these temperatures, (although hydrogenolysis was certainly not the major reaction path) the

greatest selectivity among hydrogenolytes was for methane followed by ethane. Whether the production of methane would show positive temperature dependence here cannot be determined, since the hydrogenolysis reaction is virtually completely overshadowed by dehydrogenation.

In order to examine the possibility of surface buildup of carbonaceous fragments more closely, the hydrogen pretreatment procedure was repeated. During the treatment, the reactor effluent was sampled. Unsaturated species are known[46] to be easily removed under the conditions described previously, while graphitic poisoning would require considerably higher temperatures (ca. 550°C) to be reversed. There was no observed removal of hydrocarbons from the surface when the sample was heated to 310°C in an atmosphere of pure argon (although a trace of n-butane was detected, this was attributed to a small leakage of reactant through the feed line control valve). As predicted however, the introduction of H_2 in the pretreatment-gas stream yielded methane in the effluent stream. The pretreatment was continued with frequent sampling, until methane was no longer detected. The total elapsed time was approximately 2.0 h. During this time, the total quantity of methane produced was considerably smaller than the quantity of propane produced during the previous set of experimental runs. If the assumption were made that each molecule of propane produced required that a single-carbon entity be left behind on the catalyst surface, then a mass balance on the above results would suggest that most of the carbonaceous deposits were not hydrogenated off (and may therefore be graphitic in nature).

A second series of n-butane conversion runs was conducted using a 3.5 wt% Fe catalyst, which was identical to that discussed above except for the support pretreatment temperature. The sample EMR-11a was pretreated at 250°C (the above sample EMR-11b was pretreated at 450°C). Results for these experiments are presented in Figure 7-7. As before, the usual hydrogen treatment of the sample before reaction was carried out; again, a 50% hydrogen in argon stream was used at a maximum temperature of 310°C.

The first part of this experiment was an isothermal transient run, conducted in the same manner as for the EMR-11b sample. As with the first catalyst sample, some activity was observed at room temperature, however the overall rates of reaction were about two orders of magnitude lower. For this reason, an attempt to examine the transient behaviour of catalyst activity would be essentially futile. The distribution of reaction products was quite similar for both samples. In all cases methane was not detected, but ethane and propane were. The isomerization reaction was also observed in both samples.

The second part of the experiment involved the usual examination of butane conversion up to 450°C. In contrast to the EMR-11b sample, methane was detected in the product stream; in fact, it was

throughout the experiment, the major hydrogenolysis product. The rate of isomerization was very low over the entire range of temperatures studied. As with the previous sample, isobutene was the only dehydrogenation product detected at temperatures up to 400°C. Above this however, the trans and cis isomers were also produced along with propylene. The relative proportions of the butenes (above 400°C) was generally near 1:1:1, although the trans isomer was the major of these by a slight margin. The rate of production of propylene was about an order of magnitude lower than that of the butenes, but interestingly the rate of production of propane was considerably less than this.

7.3.2 MVS Generated Fe Catalyst on Alumina

A highly loaded iron sample (3.8 wt%) on alumina was produced using a vacuum pretreatment temperature of 200°C. Results for this catalyst (EMR-21a) are presented in Figure 7-8.

Unlike the highly loaded Fe samples produced on the silica/alumina support, there was no activity observed at room temperature. In fact, activity was first observed when the temperature reached values above 300°C. The activation energy seems quite high; thus for temperatures near 400°C, the catalyst could be said to be comparably active (with respect to the other samples).

As is typical for Fe catalysts, the major products were the butenes, and in the present case, propylene production was also relatively important. Among the butenes produced using this catalyst, there were roughly equal amounts of the cis and trans isomers, and about half that quantity of isobutene in the effluent. The distribution of hydrogenolysis products showed predominantly methane at the temperatures of interest, with a much lower rate of ethane production, and barely measurable rates of propane production. The overall rate of isomerization was also rather low (being comparable to the total hydrogenolysis rate).

Another sample (EMR-21b) was produced on the alumina support pretreated at 600°C. Results for n-butane conversion on that sample are presented in Figure 7-9.

In contrast to the previous alumina supported sample (EMR-11a), there were trace levels of activity measured at room temperature. These only represented however, methane production. For the SMR-6 supported samples which showed activity at room temperature, the major products were olefinic. There were also trace levels of isomerization product detected between room temperature and about 300°C, however in marked similarity to the other alumina supported sample, significant activity was only measured above 300°C.

In the higher temperature range, the results were very similar for the two EMR-21 samples. The major reaction products were the butenes although propylene was also produced in significant proportions. Among these, there were roughly similar production rates for the cis and trans isomers (though slightly greater trans production). Somewhat less isobutene was produced, while the production of propylene was first detected at 425°C (and at about two orders of magnitude slower rate).

Among the hydrogenolysis products, again methane was the one produced at the greatest rate. In the EMR-21b sample however the rate of ethane production was only one order of magnitude slower (rather than about two for the EMR-21a sample); the propane rate was less than that of ethane, but again the difference in the two rates was smaller for the EMR-21b sample.

The reported value for the activation energy is highly affected by the trace results at low temperatures (a discussion of this principle has been given earlier). If these results were neglected, a value much closer to 200 kJ/mol would be determined. This is consistent with all of the dehydrogenation rate data which have been collected in the other experiments. The Arrhenius plot for this sample shows particularly good linearity, and as mentioned above, there is no indication of transport inclusions.

7.4 Mechanistic Interpretation of Results

A possible mechanism has been proposed based on several concepts put forth by Ozin[40] in order to explain the observed distribution of products. This mechanism accounts for the relative proportions of the various dehydrogenation and isomerization products very well, and is also adequate for explaining the observed quantities of hydrogenolysis products and the source of deactivation. It is also consistent with the observed deactivation kinetics, results of the hydrogen regeneration process, and the expected valence state of the Fe particles.

As demonstrated in table 7-2, all but the EMR-11b sample have quite similar properties, while that sample exhibited some unusual features in its distribution of products. Most notable of the differences between EMR-11b and the remaining samples was the absence of methane as the major hydrogenolysis product, and the total absence of the cis isomer of 2-butene.

There were also many similarities among the four samples. In every case, dehydrogenation was considerably more significant than the hydrogenolysis reaction. The relative distribution of the butenes (trans more than cis more than iso, but all fairly close) was quite similar for all (except of course EMR-11b

in which cis was missing). All of the samples except EMR-21a showed measurable activity at room temperature.

Figure 7-10 depicts an entire reaction scheme which can be demonstrated to fit the observed data (at least qualitatively for the present time).

Immediately following the system indicated as #3, there is a branch where two possible submechanisms are shown. One, showing dehydrogenation of the propyl radical continues in systems #5 to #13; the other, in which hydrogenolysis of the radical takes place, is presented from system #14 on. The products methane and cis-2-butene are resultant from the latter mechanism. It is therefore hypothesized that both submechanisms are active in all samples except EMR-11b. In this sample, only the dehydrogenation route has an appreciable rate. This will be rationalized later. The two reaction submechanisms will be discussed separately.

7.4.1 Dehydrogenation Submechanism

The particularly unusual features of this reaction system which must be accounted for in a mechanistic model, include the absence of methane as a hydrogenolysis product, as well as the absence of the cis isomer in the range of butenes detected. Furthermore, the dominance of the reaction path leading to isobutene and isobutane must be considered.

System #1 as indicated in the figure, shows the reactant butane bound to the catalyst surface by all four carbon atoms. This scheme has been cited by Sinfelt[28], as being requisite for cleavage of C-C bonds (as in direct hydrogenolysis). As will be shown, this pattern may well hold for the other two reaction types as well. The predicted distribution of hydrogenolysis products by direct C-C bond scission would be 1:1:1 for propane/ethane/methane (neglecting secondary reactions as would be more likely in the low temperature range). Including the subsequent hydrogenolysis of propane and ethane, the product distribution would then be shifted to methane ethane propane; the trend being made more pronounced with increasing temperature. Such patterns are in fact typical with many systems. One example from the present research would be on the ASC-1 (Ru created by reduction of RuCl3 precursor) catalyst.

The system #2 in Figure 7-10 (indicated as not being a valid pathway in this mechanism) depicts the expected distribution of dehydrogenation products if direct reaction were permitted. This would be a 2:1 mixture of 1-butene and the sterically favoured cis isomer of 2-butene, respectively. By incorporating the assumption that removal of H atoms from the secondary carbon atoms was slightly favoured (based on thermodynamics), the distribution could perhaps be somewhat closer to 1:1. This pathway would not

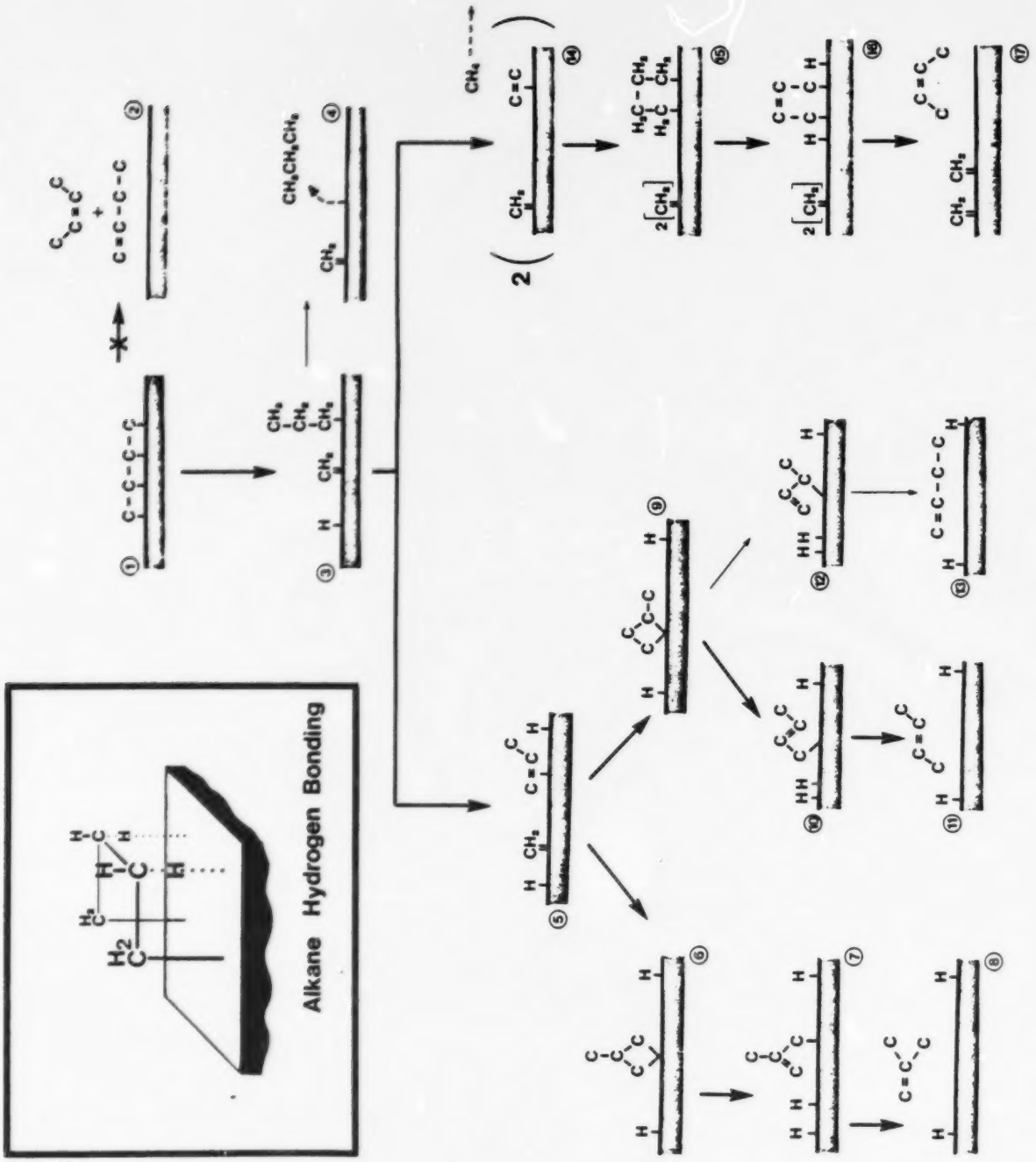

Figure 7-10 Postulated Surface Reaction Mechanism for n-Butane Conversion on MVS Generated Supported Iron Catalysts

explain the production of trans-2-butene (at least not as being significantly more important than that of either the cis isomer or 1-butene); nor would it account for the presence of isobutene.

In the present mechanism, system #3 shows cleavage of the terminal bond with dehydrogenation of the methyl unit, to yield a propyl radical, a carbene and a hydride on the surface. It is reasonable to speculate that further dehydrogenation of the carbene could provide the source of graphitic carbon poisoning discussed in the previous section (although this is certainly not necessary to explain deactivation). It is well established that the metal-carbon double bond in the surface carbene is relatively strong[47], hence removal of methane by direct hydrogenation of the carbene is not observed. It must be pointed out that the absence of methane among hydrogenolysis products is somewhat of an oddity, wherein most catalysts seem to favour direct hydrogenolysis.

During the hydrogen regeneration process, the used catalyst was observed to give off a large, short-lived pulse of propane followed by a more long-lived pulse of methane. This provides good evidence that the surface intermediates are (the weakly bound) propyl radicals and (the more strongly bound) carbenes. Incidentally, propane could also be generated by hydrogenating the η^2-propylene intermediates (as in system #5) from the surface.

The pathway leading to system #4 indicates the proposed source of propane. It has been shown with a small arrow (indicating it as a minor reaction path), however this classification depends on the temperature considered; in the middle range observed, it could perhaps be considered a major path. The bond by which the propyl radical is attached to the surface is less strong than that of the carbene intermediate, therefore propane is easily hydrogenated from the surface. Analogously, this is probably the source of ethane via removal of an ethyl radical produced by terminal bond cleavage of propane (this being of course, a secondary reaction).

A second possible reaction involving the surface propyl radical is depicted in system #5. This involves β-elimination from the propyl radical, to give a propylene intermediate η^2-bonded to the surface Fe atom. In systems #6 and #9, there are depicted two possible reaction paths between the surface carbene and the propylene intermediate. The one leading to system #6 is sterically favoured and is therefore indicated as the major reaction path (however, increasing temperature favours a shift toward production of the asymmetric metallocyclic species).

The proposed metallocyclic nature of the surface intermediates is based on work by Hugues et al.[41] in which similar species were directly observed. This was accomplished in a CO hydrogenation over

an Fe system (as in the Fischer-Tropsch synthesis) and also in ethylene conversion. In both systems, high selectivities for propylene production were explained in terms of the formation of metallocyclobutane surface species from surface carbenes and ethylene. Also discussed, were reactions between surface carbenes and propylene to yield a methyl substituted metallocyclobutane species, which in turn would lead to 1-butene production. The results were explained on the basis of the observed reaction products and by analogy with reactions between olefins and both tantalum-carbene and tungsten-carbene complexes.

The resultant surface species which would be produced via a second β-elimination in the methyl substituted metallocyclobutane complex is shown in system #7. Desorption of this from the surface (leading to system #8) would give rise to the isobutene (and explain its presence as one of the major products among the butenes). Also, if hydrogenation of the intermediate shown in system #7 occurred to an appreciable extent, isobutane would result. From the observed results on this system, hydrogenation of this intermediate seems to become more significant at higher temperatures.

Proceeding from a mechanism involving only C-C bond cleavage and/or adsorption of less than four carbon atoms in butane, it would be difficult to derive a means of producing isobutane, especially one which would account for its dominance.

Because of the asymmetry of the metallocyclic intermediate in system #9, the second β-elimination from this species could be expected to yield two different products, as shown in systems #10 and #12. Again, based on steric considerations, that shown in system #12 would be a minor path relative to that which yields system #10. The intermediates shown in systems #10 and #12 would yield trans-2-butene and 1-butene respectively (or n-butane in both cases if desorption with simultaneous hydrogenation occurred).

7.4.2 Hydrogenolysis Submechanism

A second possible fate of the propyl radical shown in system #3 would be to undergo hydrogenolysis of the terminal carbon. If such a process did occur, it could explain the production of methane by the present set of samples.

The following is proposed as an explanation why this submechanism seems to be significant for all but the EMR-11b sample. First of all, the surface H atoms in the case of Fe catalysts would be expected to be hydride-like, hence nucleophilic. Also, as the partial charge (or average oxidation state) of a small Fe cluster was increased, one would expect the propyl radical to assume an overall nucleophilic character. However, through a charge induction effect, the terminal carbon atom would be made slightly more

electrophilic. Of all the samples in the group, EMR-11b would be most likely (on the basis of the support and calcining conditions) to contain the least oxidized Fe particles, hence diminishing the tendency for terminal hydrogenolysis of the propyl radical. It should be noted that the configuration of the propyl radical as shown in system #7 is somewhat misleading: each of the C-C bonds has some flexibility such that the terminal carbon atom is not necessarily far away from the surface.

In a system in which both submechanisms were active, the relative rate of hydrogen removal of the propyl radicals as propane would be less that if only one submechanism was active (given that both have comparable rates). The selectivity toward product propane would therefore also be lower. Such was indeed observed in the present set of samples.

In the system shown in #14, the resultant two-carbon fragment assumes the configuration of a η^2-ethylene/metal complex. This could then be hydrogenated (though in the present case at a very low rate) to produce ethane. Proceeding to system #15, two of these surface ethylene complexes are shown to react. The first step in such a reaction may involve migration of the ethylenes, either to two adjacent metal atoms, or to a single metal atom. In solution chemistry, bis and tris ethylene - metal complexes of this type have been prepared[48,49]; these are known to cyclize, producing species like that shown in system #15. An alternative structure for the metallocyclic four-carbon intermediate could be drawn by having both ends bound to the same metal atom. The remaining details of this mechanism would be equally valid in either case (actually, the metallocyclic intermediate shown in the earlier part of this mechanism uses the latter structure). Although the literature for homogeneous phase preparations shows a metallocyclopentane-like structure, the metallocyclohexane-like structure was chosen on the basis of a lessened strain on the ring (hence a lower energy for the latter configuration).

A double β-elimination (concerted or sequential) from the metallocycle leads to system #16. Again, the two carbon atoms involved need not be as far from the surface as the figure would seem to indicate. Figure 7-10b (insert) shows a three dimensional view of the proposed intermediate, indicating *soft bonding*[50] of the β hydrogen atoms. These are then easily abstracted. If the resultant metallocycloalkene desorbs (more properly, is hydrogenated off) from the surface, system #17 will result, showing the cis product. This also indicates an additional process in which surface carbene buildup can occur.

An analogous reaction between two propylene surface radicals (such as in system #5) is ruled out on the basis of steric considerations. This is precisely the same argument used to account for the

difference in stability[51] between the tris-ethylene and tris-propylene platinum precursors used in preparing the catalysts discussed in Chapter VIII.

7.5 Summary

Ruthenium catalysts prepared via metal vapour synthesis have appreciable activity for the hydrogenolysis of n-butane. Iron catalysts so prepared show activity only if they have relatively high (about 2 wt%) loading. MVS iron samples acted primarily as dehydrogenation catalysts.

In bimetallic preparations which incorporated both of these metals, both dehydrogenation and hydrogenolysis were observed at significant rates. Evidence suggests that the Ru stabilizes lower valence states of Fe (whereas oxidized iron does not show catalytic activity).

Unimetallic Fe catalysts showed the greatest activity when the support material from which they were produced was most dehydroxylated. The present results are in agreement with related literature which speculates that surface OH groups completely oxidize the initial quantities of Fe impregnated, and that any excess Fe will be stabilized in less oxidized states.

A mechanism has been proposed in order to explain the distribution of products for the set of Fe catalysts. Key features of this mechanism include various C-C bond scission processes, as well as dehydrogenation/ rehydrogenation steps and the formation of different metallocyclic surface intermediates. The mechanism agrees qualitatively with the product distribution and also with the observed deactivation behaviour.

CHAPTER VIII

Catalysis on the Nickel, Platinum and Nickel/Platinum Bimetallic MVS Materials

As with the previously discussed iron/ruthenium system, the probe reaction used to help characterize the nickel/platinum system was the conversion of n-butane. The experimental conditions were essentially the same as before: reductive pretreatment followed by reaction at various temperatures covering the same range. The molar ratios of the reactant gases were also unchanged from the previous set of experiments.

8.1 Unimetallic Platinum Samples

8.1.1 Platinum on Silica Materials

In the first set of results, the series of platinum/silica MVS materials, in which the carrier pretreatment temperature (hence initial surface OH concentration) was varied, was subjected to reaction conditions. The results for these materials were analyzed using the same computer program as was used to analyze the Fe/Ru data; one example is presented in Figure 8-1, since, not surprisingly, there were no remarkable differences in behaviour between any of these samples.

The pattern of selectivities showed that at the low temperature range (below about 225°C), hydrogenolysis was the major reaction path; at the intermediate temperatures (reaching a maximum very close to 300°C), the major product was observed to be that of the isomerization reaction; and above 375°C, the dehydrogenation reaction became the dominant path. Perhaps the only difference with respect to the various pretreatment temperatures, was that the 200°C sample showed somewhat less prominence of the isomerization reaction. Although its selectivity did reach a maximum at 300°C, the value was only 40%, whereas for the 600 and 800°C pretreated materials, the respective maxima reached about 80% at that temperature.

SAMPLE: EMR-20a 2.2 wt% Pt on Silica (Pt. @ 200 C) DATE: 1987 June 10-15
MASS: 0838 g EXPERIMENTER: Prokopowicz

REACTANTS: n-Butane 2.0 cm3/min GC COLUMN: Poraeil-C
Hydrogen 10.0 cm3/min CARRIER GAS: Nitrogen
Argon 10.0 cm3/min COLUMN TEMP: 60.0 C PRESSURE: 196.5 kPa

SPECIES IDENTIFICATION

A. Methane
B. Ethane/Ethylene
C. Propane/ene
D. Iso-Butane
E. n-Butane
F. Iso-Butene
G. trans-2-Butene
H. cis-2-Butene
I. Pentanes/enes

REACTION RATES (mol/h g)

TEMP (C)	SPECIES A	B	C	D	E	F	G	H	I	TOTAL CONVERSION
100.	1.988 -7	7.550 -8	5.149 -8	.000 0	-1.241 -7	.000 0	.000 0	.000 0	.000 0	.0000
300.	3.251 -4	2.071 -4	9.805 -5	1.902 -4	-6.486 -4	.000 0	.000 0	.000 0	.000 0	.0038
150.	3.573 -7	4.942 -8	.000 0	.000 0	-8.901 -8	.000 0	.000 0	.000 0	.000 0	.0000
200.	3.839 -7	3.679 -7	3.110 -7	.000 0	-9.132 -7	.000 0	.000 0	.000 0	.000 0	.0000
250.	3.162 -3	6.950 -4	1.476 -4	3.229 -4	-1.283 -3	3.171 -5	.000 0	2.986 -5	2.548 -6	.0252
250.	3.926 -5	2.355 -5	1.406 -5	9.047 -6	-3.068 -5	.000 0	.000 0	.000 0	.000 0	.0008
350.	3.388 -3	7.146 -4	1.417 -4	1.961 -4	-1.319 -3	3.656 -5	.000 0	3.614 -5	1.872 -6	.0259
350.	2.640 -3	6.211 -4	8.593 -5	7.113 -5	-1.117 -3	2.583 -5	.000 0	.000 0	.000 0	.0219
400.	2.263 -3	6.997 -4	1.649 -4	2.209 -4	-1.283 -3	.000 0	.000 0	1.199 -4	6.067 -6	.0252
430.	1.538 -3	3.008 -4	1.367 -4	1.530 -4	-1.426 -3	3.660 -4	.000 0	3.617 -4	7.939 -6	.0280

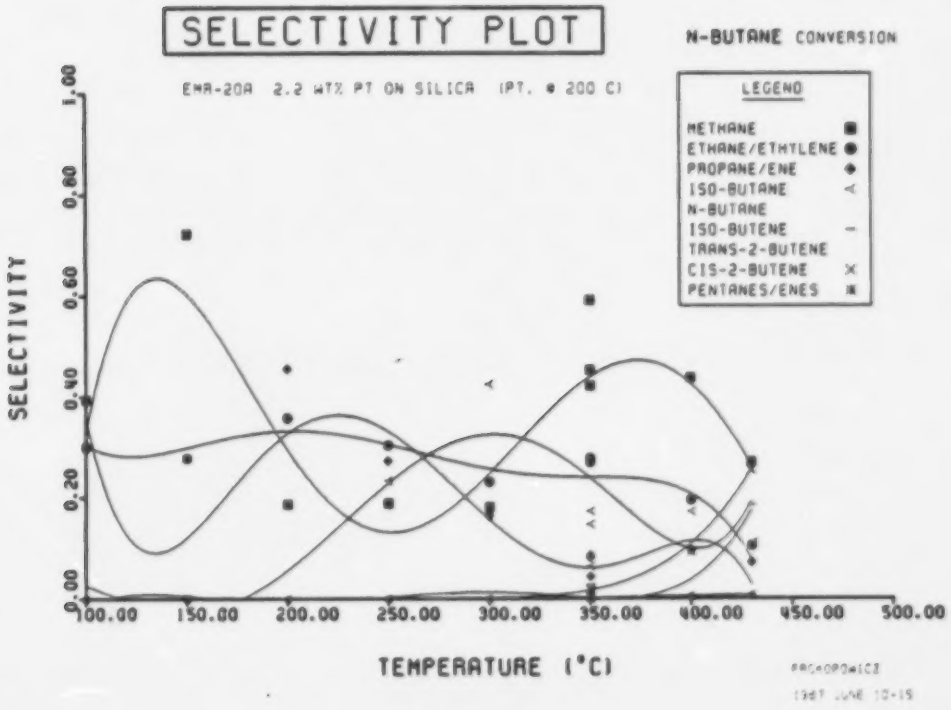

Figure 8-1 n-Butane Conversion Catalysis Results for Sample EMR-20

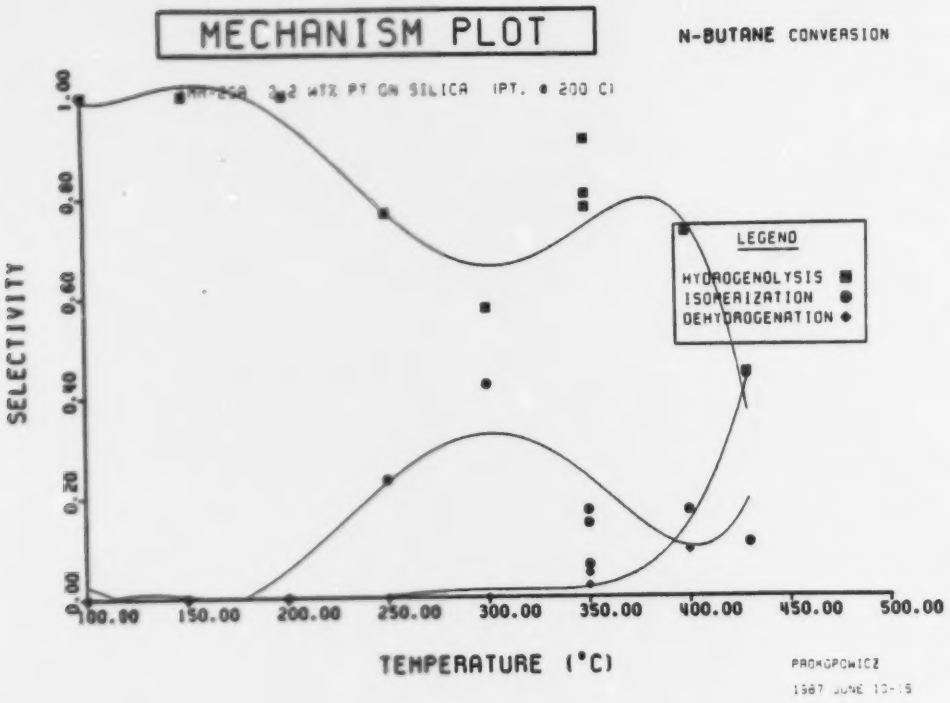

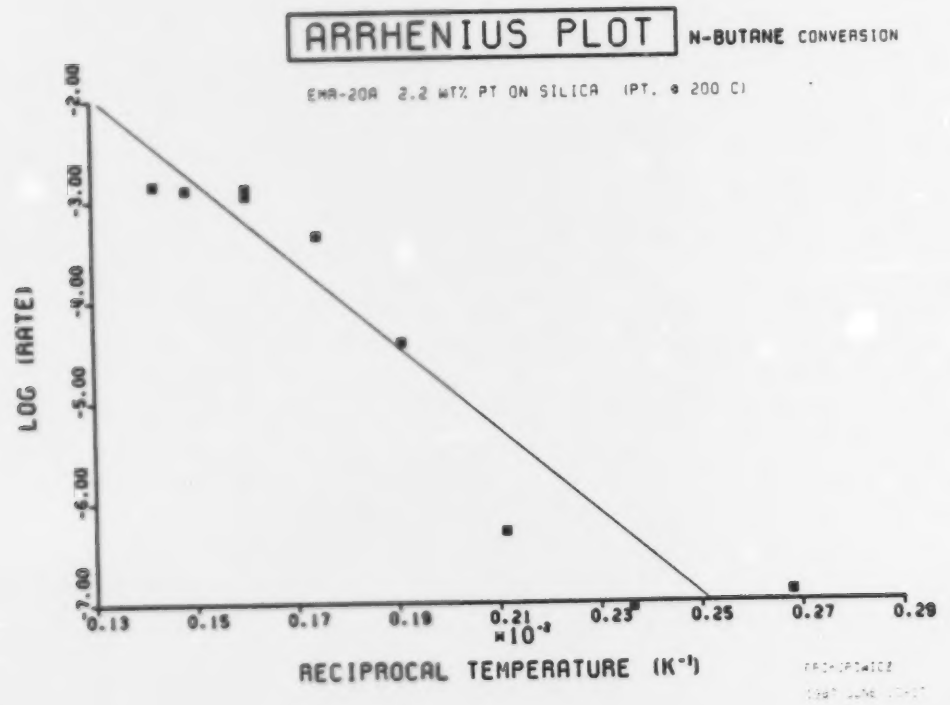

Figure 8-1 Continued

The distribution of reaction products within the hydrogenolysis class showed a similar pattern with respect to support pretreatment temperature. The relative proportions of methane, ethane and propane were generally invariant except for the sample pretreated at 200°C (which showed modest differences when compared to the remaining samples). It was generally true for these materials, that cleavage of the terminal C-C bond was preferred. Thus, methane and propane selectivities were higher than that toward ethane. The sample pretreated at 200°C however, did produce relatively more ethane. At the very low reaction temperatures (less than about 250°C), it sometimes occurred that the propane selectivity appeared to be zero at 200°C then suddenly jumped to the value which was appropriate (in terms of the methane selectivity) at 225°C. This was due to a lack of instrumental sensitivity for the detection of propane at the lowest temperatures (hence overall reaction rates). As the experiment approached the higher temperatures, the ethane and methane selectivities increased. As had been observed in the Fe/Ru system, such could be attributed to secondary reactions in which propane and ethane can further hydrogenolyze during the residence in the reactor.

Within the dehydrogenation class, the product distribution was:

$$\text{trans} > \text{cis} \approx \text{iso}$$

and was invariant even for the low temperature pretreated sample. It is interesting that the small differences in selectivities between samples whose supports were pretreated at different temperatures appeared only with respect to the hydrogenolysis reaction path, and not the dehydrogenation path. Furthermore, measurements by such techniques as XPS spectroscopy, and CTEM particle size distribution determinations did not reveal any differences which could be correlated with the catalysis observations. Of course, electronic differences corresponding to only a few tenths of a formal valence number, while being difficult to measure via XPS, may well have been sufficient to produce noticeable differences in catalytic behaviour.

8.1.2 European Standard Platinum Catalyst

As a control experiment, a sample of the European standard Pt/SiO_2 catalyst was also run under identical conditions. For this sample, the same qualitative pattern of selectivities was also observed. This points to an independence of the catalytic selectivity with respect to particle size in the 1.2 to 2.0 nm range.

It may be speculated that for the conversion of larger hydrocarbons, this need not be the case. According to Martin[21], the hydrogenolysis reaction for a four-carbon reactant requires an ensemble of about 16 adjacent metal atoms; for an eight-carbon species, this value would be much larger, such that there would be a considerable difference in the number of reactive ensembles between metal cluster materials whose average particle sizes were 1.2 and 2.0 nm. In future experiments, in which larger hydrocarbons would most likely be used, one might therefore expect that the pattern of selectivities would not be so similar for MVS platinum materials and conventional supported Pt materials like EUROPLAT. It should be mentioned that the selectivity pattern over the EUROPLAT sample was virtually identical to that over the two MVS samples whose supports were pretreated at the higher temperatures. The same modest discrepancies as which were observed between the Pt/SiO_2 MVS materials, were also manifest in the difference between EUROPLAT and the 200°C pretreated MVS sample.

8.1.3 Platinum on Alumina Materials

The two MVS-generated Pt/Al_2O_3 materials synthesized, using support pretreatment temperatures of 200 and 600°C were subjected to n-butane conversion testing, under the same experimental procedure as all of the above work.

Unlike the silica-supported platinum materials, the support pretreatment temperature did not have a significant effect on the selectivity pattern over the 200 to 600°C range. Again, the general pattern (by reaction class) indicated hydrogenolysis to be the major path at low temperatures, and isomerization to dominate in the intermediate temperature range. The isomerization actually experienced its onset about 50 C° earlier than in the case of the silica supported materials. The one striking difference between the silica and alumina materials, in terms of general selectivity patterns, was the absence of dehydrogenation dominance at the high temperature end of the scale. This is most likely the result of a slightly later onset of this reaction path. Even with the other samples thus far examined, it was only observed to start at 375 or 400°C. For this reason, a further experiment is suggested, in which a reaction temperature of at least 440°C would be examined.

Within the hydrogenolysis reaction class, there was also a great similarity between the silica and alumina supported materials. As before, cleavage of the terminal C-C bond in n-butane was preferred, as indicated by the highest selectivity being observed for propane (essentially throughout the entire temperature range). Since considerably less methane seemed to be produced, it must be assumed that either methane builds up on the surface or, more likely, is removed from the system by further reaction. It is probably not unreasonable to speculate that one-carbon surface fragments may be involved in the

mechanism which leads to the production of isobutane. The maximum selectivity with respect to ethane production was about 10%.

8.1.4 Summary of Platinum Results

As might be expected for platinum, in terms of its difficulty of being oxidized, there was no strong support effect seen by comparing silica and alumina. What differences appear, seem to affect the temperature at which certain reaction classes begin to exercise their dominance in the selectivity profile. As for differences arising from changing the surface hydroxyl concentrations of the initial support material, there was only modest evidence which related to the hydrogenolysis reaction alone.

8.2 Unimetallic Nickel Samples

8.2.1 Nickel on Silica Materials

In the same type of experiment as for the Pt/SiO_2 samples, three Ni/SiO_2 MVS materials were also examined. As with the platinum group, each comprising a total of four samples, data were available for only three samples due to a failure of one reactor in each run. An example of the results over one of the Ni/SiO_2 samples is presented in Figure 8-2.

Once again, there were no striking differences in the pattern of selectivities over the range of support pretreatment temperatures. In the case of unimetallic nickel samples, the important reaction path was hydrogenolysis throughout the entire temperature span, although small amounts of dehydrogenation and isomerization products were also detected (ca. 5% in both cases). This is in agreement with literature results[22] for conventionally produced Ni/SiO_2 catalysts. The selectivities for hydrogenolysis, isomerization and dehydrogenation were consistent over the entire temperature range. Thus, all three reaction classes demonstrated the same apparent activation energy. Earlier, it was observed for the Fe/Ru system, for example, that the dehydrogenation reaction had an activation energy about 150 kcal/mol greater than that of the hydrogenolysis reaction. There is a note of caution warranted here: the above conclusion may be stated without considering data above 325°C and is therefore valid; above that temperature the reaction rate can be seen[a] to be diffusion controlled (under those circumstances it would not be surprising to

---

a this is readily observed by examining the zero slope in the Arrhenius plots in the region corresponding to temperatures above 300°C.

SAMPLE: EMR-19 2.0 wt% Ni on Silica (Ptd @ 725 C)
MASS: 2700 g
DATE: 1987 0714 0813
EXPERIMENTER: Prakopowicz
REACTANTS: n-Butane 6.1 cm3/min
Hydrogen 10.0 cm3/min
Argon 10.0 cm3/min
CARRIER GAS: Nitrogen
VOLUME TEMP: 60.0 C
PRESSURE: 101.0 kPa

SPECIES IDENTIFICATION

A. methane
B. ethane/ethylene
C. propane
D. propylene
E. iso-butane
F. n-butane
G. iso-butene
H. trans-2-butene
I. cis-2-butene

REACTOR DATA (Wt B 1)

TEMP (C)	SPECIES A	B	C	D	E	F	G	H	I	TOTAL CONVERSION
200	1.017 -6	5.891 -8	1.075 -6	4.164 -7	000 0	-1.402 -6	000 0	000 0	000 0	.0001
250	1.684 -4	1.750 -5	1.224 -4	2.526 -6	1.182 -5	-1.772 -4	000 0	2.084 -5	000 0	.0111
300	9.937 -4	1.958 -4	4.921 -5	000 0	3.086 -6	-3.886 -4	000 0	2.268 -6	000 0	.1142
225	1.004 -6	7.494 -8	6.653 -7	2.769 -7	000 0	-9.951 -7	000 0	000 0	000 0	.0001
250	4.923 -5	5.018 -6	4.079 -5	000 0	5.170 -6	-5.572 -5	000 0	5.143 -8	000 0	.0057
300	9.596 -4	2.281 -4	8.813 -5	000 0	6.695 -6	-4.284 -4	000 0	5.580 -6	000 0	.1287
325	8.938 -4	1.743 -4	8.740 -5	000 0	2.354 -5	-4.362 -4	000 0	2.896 -5	1.011 -5	.0672
350	8.717 -4	1.807 -4	7.102 -5	1.731 -6	2.114 -5	-4.197 -4	000 0	2.425 -5	1.598 -5	.0604
375	8.311 -4	1.153 -4	4.735 -5	3.914 -6	1.669 -5	-4.062 -4	000 0	6.660 -5	3.278 -5	.0650
400	9.349 -4	5.256 -5	2.380 -5	4.345 -6	8.148 -6	-3.985 -4	000 0	8.731 -5	4.196 -5	.0249

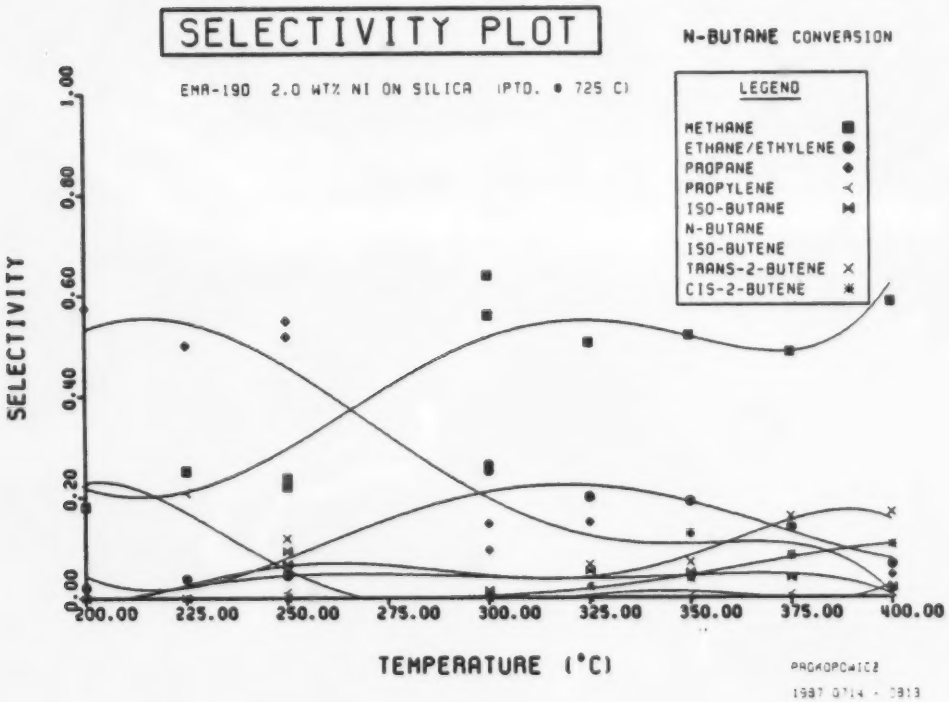

Figure 8-2 n-Butane Conversion Catalysis Results for Sample EMR-19

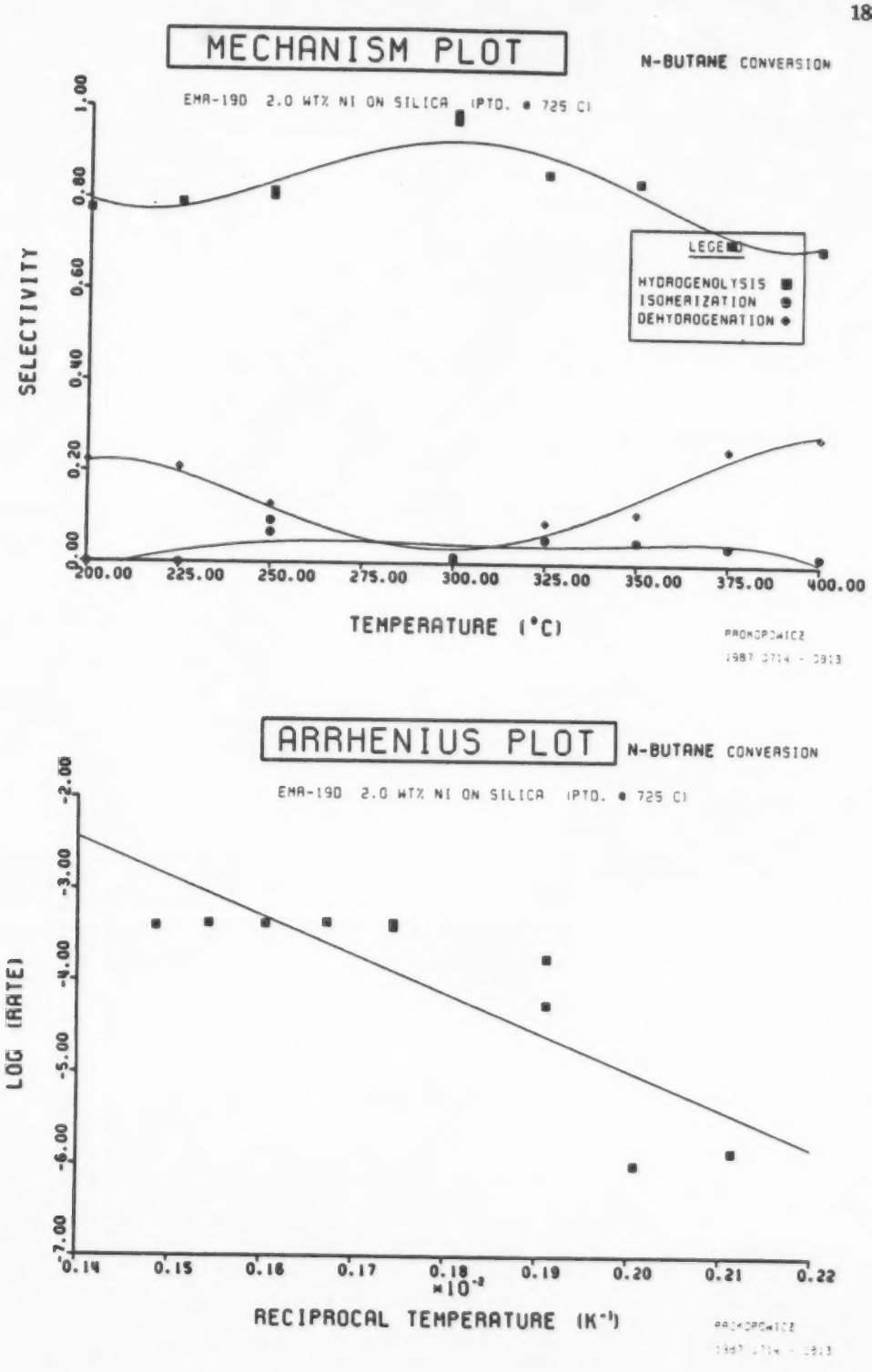

Figure 8-2 Continued

observe the same *apparent* activation energy for most reactions, since all such values would be constrained by the rate limiting process). In all of the nickel samples, the overall activity was much greater than that of the corresponding platinum samples.

Among the hydrogenolysis products, the major one was methane, except at temperatures below 250°C or so, at which propane and methane were both produced in significant yields. There was an increase in the relative amount of ethane produced with respect to increasing reaction temperature. As was observed over platinum materials, the hydrogenolytic bond cleavage seems to favour the terminal position. It is reasonable that the increase in ethane selectivity was again indicative of the increasing rate of secondary reactions at higher temperatures. The pattern, suggestive that ethane comes from the terminal hydrogenolysis of propane, was most clearly illustrated for the samples whose supports were pretreated at 200 and 725°C (although it was observed as well on the 600°C pretreated material).

The pattern of selectivities within the dehydrogenation class was typical of the platinum materials, in terms of the relative amounts of trans-2-butene and cis-2-butene; however, the iso-butene product was not detected. The most likely explanation for this, was that the amount of isobutene generated was just below the detection threshold of the gas chromatograph (even the amounts of the other two isomers were quite small). It could also be speculated that the low relative rate of isobutane production was associated with the lack of significant production of isobutene. This would obviously imply a mechanism in which isobutane was produced and then subsequently dehydrogenated.

8.2.2 Nickel on Alumina Materials

As was carried out with the platinum MVS materials, only two alumina supported specimens were synthesized. These corresponded to support pretreatment temperatures of 200 and 800°C.

Similarly to what was observed for the silica supported samples, these were hydrogenolysis catalysts over the entire experimental range of temperatures. The ratio of hydrogenolysis selectivity to that of the other two reaction classes combined was about 95 %. For the silica supported materials, the same ratio was about 85 % (actually varying between 80 and 90 %). In consideration of the greater ease of oxidation of nickel (relative to that of platinum) it might be expected that support differences (particularly in the relative acid strengths of SiO_2 and Al_2O_3) would produce more marked differences in catalytic behaviour. This is perhaps the case, since changing from silica to alumina brought about a halving of the relative isomerization + dehydrogenation rate. Furthermore, the observed order of selectivities on silica supported materials: Dehydrogenation Isomerization became reversed on alumina supported materials.

In the hydrogenolysis products, the cleavage of terminal C-C bonds was once again favored. As with virtually all of the MVS materials discussed, higher temperatures seem to permit secondary reactions; here again the property of terminal hydrogenolysis preference directed these reactions as well.

Evidence suggests that the distribution of dehydrogenation products was the normally observed, trans > cis ≈ iso pattern. This was of course, somewhat difficult to conclude confidently because of the low overall dehydrogenation selectivities on these samples.

8.3 Bimetallic Nickel/Platinum Materials

8.3.1 General Results

The bimetallic MVS nickel/platinum specimens which have been synthesized in the presently reported research were all impregnated onto alumina. This was done partly to accommodate the requirements of some of the other characterization techniques (particularly FMR and EPR spectroscopies). A completion of the study of this system should involve synthesis of some silica supported bimetallics as well. For each of the MVS syntheses, two levels of support pretreatment (200 and 600°C) were used; a total of five separate MVS reactions produced samples having various Pt/Ni atomic ratios. The total metal loading in all of these was kept the same as much as possible, and was also the same as that of the corresponding unimetallic preparations.

Comparison of the bimetallics showed, first of all, that in terms of catalytic results there was no difference between materials whose supports were pretreated at 200°C and those pretreated at 600°C. This was entirely expected because of the similar behaviour of both alumina-supported unimetallics. Qualitatively, the hydrogenolysis and isomerization reactions appeared to decrease and increase respectively, in a smooth fashion as the fraction of platinum increases. The dehydrogenation reaction however, which was not a major path on either unimetallic, reached remarkably high selectivities in the middle composition range. This is elaborated upon in the following section. It appears that the addition of small amounts (the first 16%) of platinum to nickel materials produced a more substantial difference in catalytic results than addition of the first 25% of nickel to unimetallic platinum.

The selectivity patterns within the alkane product group were not unusual. Like all of the materials in this series, there was a pronounced tendency for terminal bond cleavage of the n-butane reactant, as well as a trend toward secondary reactions at higher temperatures. At higher values of the

Pt fraction, the dominance of propane as the major alkane did not yield to methane (and secondarily produced ethane); this was most likely related to the overall drop in significance of hydrogenolysis.

In the case of the dehydrogenation products, the internal selectivity pattern was usual, although it was only on the bimetallics of composition near 50 atomic% where the overall dehydrogenation selectivity was relatively high.

8.3.2 Selectivity as a Function of Atomic Composition

Probably the most effective way of representing a comparison between both of the unimetallic catalysts, and the various compositionally intermediate bimetallics, is to plot the isothermal selectivity versus fraction of platinum. The choice of reaction temperature is arbitrary to a certain extent, however the value of 300°C was deemed most appropriate for two reasons. First, the overall reaction rates at temperatures much below this value are low, hence experimental uncertainty is greater; furthermore, the nickel and (to a lesser extent) the nickel-rich bimetallic data suffer the problem of transport interference in the true reaction rates, as previously discussed. Another reason for avoiding the choice of higher temperatures is the possible complication due to the selectivity patterns being determined by secondary reactions. Figure 8-3 shows the results, wherein the three reaction classes are plotted against the platinum atomic fraction. In addition to the various bimetallic MVS materials represented in the figure, results from a control experiment are included. This was a physical mixture of unimetallic nickel and unimetallic platinum MVS materials, combined in proportions such that the atomic ratio was 1:1 (0.5 fraction platinum).

The data in this figure present direct evidence of the cooperative or interactive effect of the two metals in the bimetallic preparations, which in turn implies that each of the supported particles does in fact contain both metals. If the situation were that the support surfaces contained intimately dispersed, but separate and non-interacting unimetallic particles, then one would expect that the selectivity patterns for any given composition would be determined simply by the weighted average of the constituent unimetallic selectivities. Graphically, this would mean that the curves in Figure 8-3 would be straight lines connecting the (pure Ni and pure Pt) endpoints. If one inspects the three points which represent the physical mixture, as in the control experiment, this is seen to be exactly the case. In the bimetallic material data, there is a significant departure from these lines. Such is certainly most obvious for the dehydrogenation reaction, whose selectivity on either unimetallic sample is 3 to 4%, yet whose selectivity on the 1:1 bimetallic sample reached a value of 40%. The curvature for the two other reactions, though not so dramatic, is statistically significant. In some discussions, it has been suggested that the curvature could be attributed to experimental error. This is not reasonable however: noting that the level of experimental

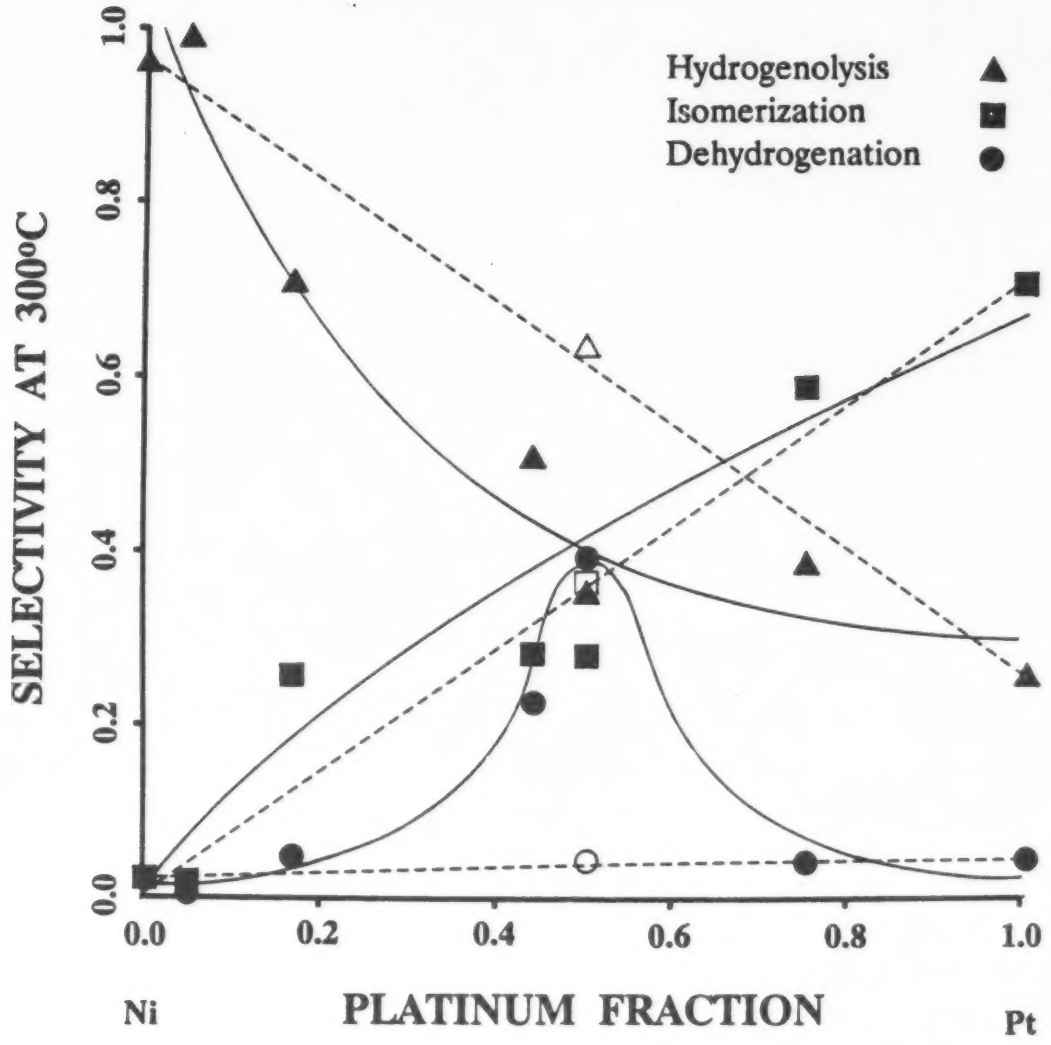

Filled Symbols Represent Bimetallic MVS Data

Opened Symbols Represent Physical Mixture of Unimetallic MVS Materials

Figure 8-3 Selectivities at 300°C for n-Butane Conversion over MVS-Generated Pt/Ni (Al_2O_3) Particles

error with respect to selectivity values at this temperature is approximately 10%, it would be further required that such error cause a random distribution of data points both above and below the expected (based on non-interaction of the two metals) line.

The results may be considered qualitatively, in terms of a speculative structure of the bimetallic particles (in the Section 8.5, this will be expanded in a more quantitative manner). If one invokes the concept of structure sensitivity[21] for the hydrogenolysis and isomerization (but not the dehydrogenation) reactions, then it would be expected that the reaction rates would be decreased for these, over bimetallic catalysts. This would be caused by a decrease in the relative number of large surface ensembles of either pure metal in the bimetallic case, as compared with their unimetallic counterparts.

8.4 Static MVS Generated Platinum Materials

Catalysis testing was carried out on the three Pt/Al_2O_3 Static-MVS samples discussed in Chapters II and III. Because of the independence of catalytic results with respect to support pretreatment temperature in previous experiments with platinum particles on alumina, these initial tests were carried out on only one member of each group.

The reader will probably recall the CTEM particle size distribution results discussed in Chapter III, in which the $Pt(N_2)_3$ precursor yielded a virgin supported particle material having a much larger average particle size than that yielded by either the $Pt(CO)_4$ or $Pt(C_2H_4)_3$ precursors. It turned out however, that after heating to about 300°C, in a reducing atmosphere, the average particle sizes of these three materials reached essentially the same value. This was carried out before catalysis results were obtained. It is therefore not surprising that the results of catalytic testing on these materials were so similar for the carbonyl and tris-dinitrogen precursor generated materials. Likewise, the $Pt(C_2H_4)_3$ generated static MVS material showed results quite similar to those of the corresponding Solution Phase MVS material. Catalytic results for the $Pt(N_2)_3$ Static Phase MVS material are presented in Figure 8-4.

A comparison between the static MVS generated and solution phase MVS generated platinum clusters revealed a very striking dissimilarity for materials generated from precursors other than the tris ethylene species. While both groups of materials demonstrated a dominance of the hydrogenolysis reaction at the low end of the temperature range, the high temperature results showed only dehydrogenation in the static MVS samples. In contrast, the solution phase MVS materials showed no dehydrogenation in that range, and instead revealed almost complete dominance of the isomerization reaction. Actually,

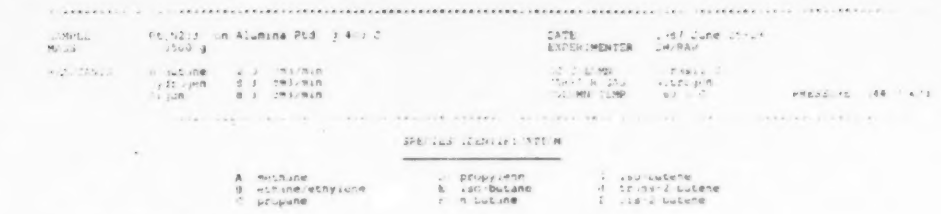

SPECIES IDENTIFICATION

A methane
B ethane/ethylene
C propane
D propylene
E iso-butane
F n-butane
G iso-butene
H trans-2-butene
I cis-2-butene

TEMP (°C)	SPECIES									TOTAL CONVERSION
	A	B	C	D	E	F	G	H	I	
200	1.936 -7	300 3	300 0	300 3	300 0	-4.981 -8	300 0	300 3	300 3	[illegible]
250	2.442 -7	300 0	300 3	300 3	300 0	-6.124 -8	300 0	300 0	300 0	[illegible]
300	2.163 -7	300 0	300 3	300 3	300 0	-1.324 -8	300 0	6.494 -5	6.448 -5	[illegible]
325	1.476 -7	300 0	300 -3	300 0	300 0	-2.322 -8	300 3	1.350 -8	9.715 -6	[illegible]
350	1.564 -7	300 3	300 0	300 3	300 0	-5.727 -8	1.191 -8	2.585 -8	1.451 -8	[illegible]
375	1.658 -7	1.083 -7	3.927 -8	300 0	300 0	-1.478 -3	2.356 -8	5.388 -8	3.652 -8	[illegible]
400	1.559 -7	1.585 -7	1.218 -7	1.135 -6	300 0	-1.527 -3	3.650 -8	8.715 -8	5.195 -8	[illegible]

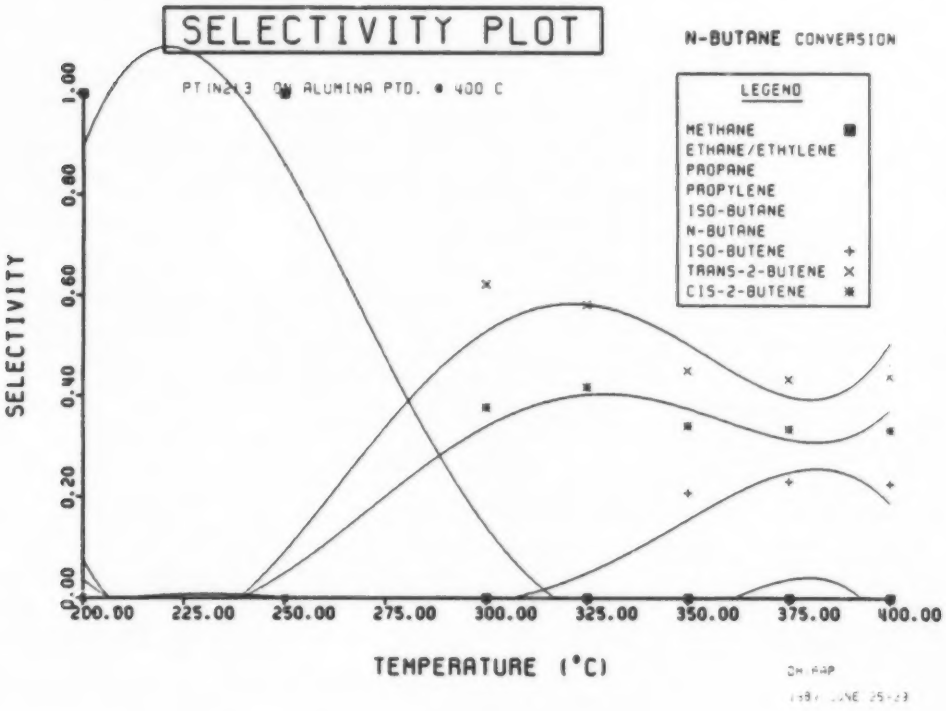

Figure 8-4 n-Butane Conversion Catalysis Results for a Static MVS Sample Produced from $Pt(N_2)_3$

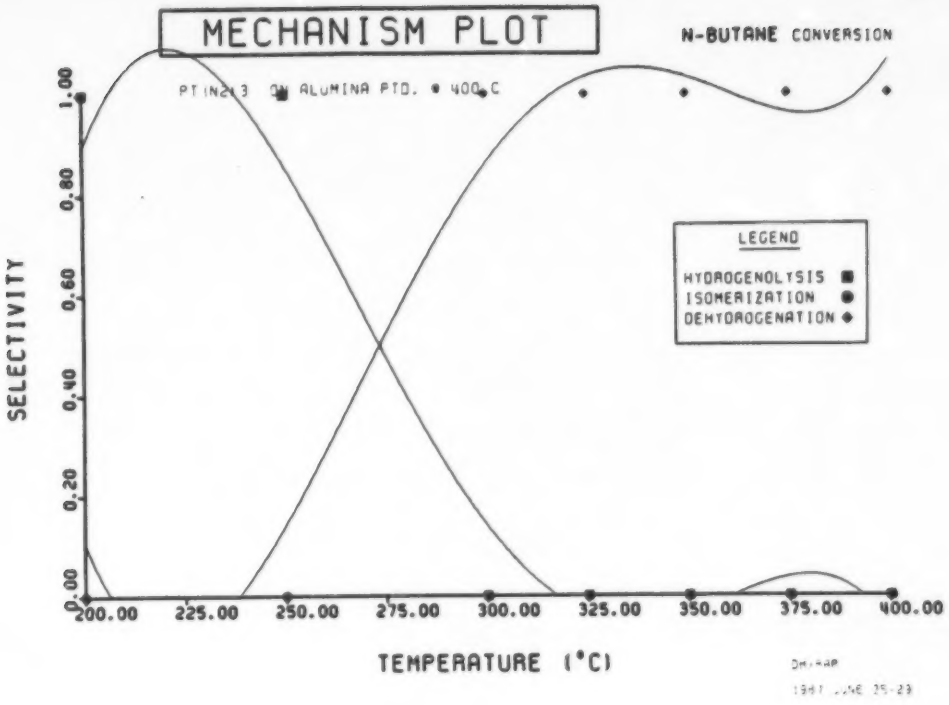

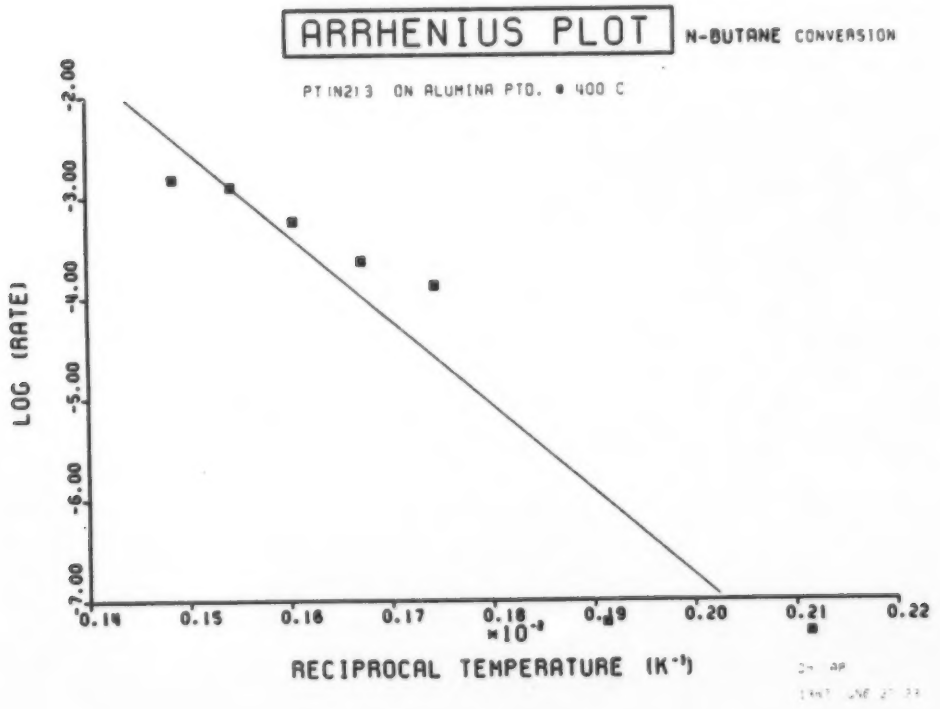

Figure 8-4 Continued

one might even question whether hydrogenolysis dominates (in the static MVS samples) even at the low temperatures: it is true that the detection sensitivity for butenes is such that, just below the threshold, their (undetected) concentration would still correspond to a significant selectivity level.

One of the catergoric differences between the static and solution-phase classes of these MVS materials, which is often discussed, is the relative amounts of carbonaceous fragments left on the surface after the impregnation with precursor and subsequent reaction. The solution phase materials are expected to have far greater quantities of this type of surface contamination, both arising from the organic metal-solvating ligands and from possible adsorption and/or reaction of the organic solvent. Certainly the static material produced from $Pt(N_2)_3$ cannot contain carbon, and spectroscopic examination (using XPS) of the other two materials has also shown a lack of observable surface C deposits. Unfortunately, it is difficult if not impossible to relate this difference to the observed catalytic behavioral differences.

As will be discussed in greater detail in the next section of this chapter, it is commonly held that the hydrogenolysis and isomerization reactions require a substantial group of surface metal atoms as a catalytic site, whereas the dehydrogenation reaction is believed to proceed through reactant adsorption on a single metal atom. In order to be consistent with this postulate, it would be required that the presence of surface carbon contamination cause an increase in the number of *ensembles* or groups of atoms (which would catalyze the isomerization reaction) relative to the total number of catalytically active single surface atoms (which are thought to catalyze dehydrogenation). Such an explanation seems therefore highly unlikely.

Perhaps it is not useful to look strictly at the differences in final chemical composition, in order to explain the catalytic differences. Another difference between static and solution MVS is more apparent in the impregnation reaction. In the static case, the contact temperature was much lower (hence the viscosity of the precursor was higher) than in the Solution Phase MVS case. At this point, the role of ligands, fragments etc. may also be considered in the agglomeration process which created the surface-bound metal clusters.

It is easy to imagine, under the highly disparate conditions under which the precursor/surface reaction took place in the two classes of system, that the final metal particles may have had different packing structures (even though the sizes were the same). Such differences could be much more easily used to rationalize the catalytic behaviour.

Just to illustrate the point by means of a speculative example, it may be supposed that the Solution Phase MVS syntheses led to a hexagonal close-packed structure. Supposing further that the static synthesis produced a more loosely configured array of surface particles (for simplicity of argument, say having a cubic close-packed structure), one could propose the following. It must of course be assumed that the structures would be stable up to the maximum reaction temperature.

On the h.c.p. surface, a butane reactant molecule might adsorb onto four adjacent atoms[a]. It can be shown that if the butane molecule is either in its cis or trans configuration, the four carbon atoms would match up with four h.c.p. platinum atoms. If a reactant molecule were also to adsorb onto four adjacent platinum atoms in a c.c.p. array, it would first have to assume a highly (energetically) unfavoured structure. Thus the number of catalytically active ensembles in the latter case could be extremely small. Obviously, the number of single metal atoms would be much more similar in both cases.

This would explain the dramatic increase in dehydrogenation selectivity over the static MVS samples. If one examines the overall rates of reaction, the model is further substantiated. In the static case, the rate is between one and two orders of magnitude less, exactly the expected result owing to suppression of two highly active reaction paths.

Direct measurement of the packing structures for these materials could be obtained in principle, by application of the technique[27] of Extended X-ray Absorption Fine Structure (EXAFS) Spectroscopy.

In metallurgical studies, it has commonly been found that various solid metal phases, having different packing structures can be stabilized by either slowly or very rapidly cooling molten samples. Slower cooling tends to favour highly ordered and more closely packed phases, whereas rapid cooling produces looser, less ordered (or even amorphous) packings.

The support contact reaction in MVS synthesis may possibly be thought of in this manner: the sudden contact between the precursor solution and the support material is analogous to a (more or less) catastrophic cooling of a liquid phase. Obviously, the transition is chemical in nature rather than purely

---

a even so, it might exclude other adsorbates from adsorbing nearby, hence giving rise to an effective ensemble size greater than four. Such is consistent with the pertinent literature on alkane hydrogenolysis.

physical, however the principles of kinetics apply in both cases. Since the tris-ethylene precursor is stable to considerably higher temperatures than the other Solution Phase MVS precursors, one might envisage a lesser driving force for its decomposition and the subsequent surface attachment of its Pt atoms. If such a feature led to slower agglomeration kinetics, then more ordered particles would be expected than for the carbonyl or dinitrogen precursor. At some future time, it may also be useful to determine the effect of viscosity of the medium during the contact reaction (recalling that there is a wide range of temperatures employed, depending on the type of MVS synthesis used).

8.5 Bimetallic Surface Model

A model is proposed in order to account for the observed catalytic data. Through an examination of the assumptions required to make the model achieve quantitative agreement with the results, one can derive a description of the bimetallic surfaces themselves. Although no model ever gives a unique, unequivocal explanation for observed phenomena, it can be shown that the present model is reasonable, is in agreement with results obtained using several other characterization techniques, and is consistent with most of the ideas in the current literature (each of which is based on many experimental systems and relies on the application of various analytical methods).

The general formulation of the model began with the assumption that the carrier supported metal particles were truly bimetallic. Such a notion is well borne out by the STEM-EDAX results which gave strong evidence that both metals were always associated with a single particle. It was next assumed that for at least one of the possible reaction classes (i.e., hydrogenolysis, isomerization and dehydrogenation), a catalytic reaction site must consist of more than a single surface metal atom. This idea is commonly discussed in many places in the literature[16,21,26] and is referred to as an *ensemble* catalyst site. It is commonly agreed that of the three reaction paths mentioned above, dehydrogenation requires a single surface metal atom, while the other two reactions require larger ensembles. Thus, one refers to dehydrogenation as being structure insensitive; hydrogenolysis and isomerization are structure sensitive reactions. Clearly, the incorporation of two metals into a particle will bring about a reduction in the number of ensembles of atoms of each metal; the more intimately mixed these metals are, the greater will be the degree of ensemble reduction relative to that which would be found in the unimetallic analog of the particle in question. For the following discussion and formulation of the model, the term *ensemble attenuation* is defined as the factor by which the total number of ensembles of n atoms of a particular metal is decreased (in the bimetallic system) relative to the number of ensembles of the same size (n atoms) which would exist if the second metal were not present. For example, if ensembles of four nickel atoms

are considered and it turns out that in a 50 at% bimetallic sample, the attenuation factor is 1/16, this means that there are only one sixteenth as many groups of four adjacent nickel atoms in the bimetallic material as there would be in a unimetallic nickel sample having the same total number of atoms and the same spatial structure. It is obvious that in any model of this type, the overall fraction of the two metals will affect the degree of ensemble attenuation (with respect to both of the metals) but also, this parameter will be affected by the degree of short-range order or structural arrangement of the atoms within each particle. The more disordered each particle is, the greater will be the degree of ensemble attenuation of metal A with increasing incorporation of metal B. Furthermore, the attenuation factor will be greater as the ensemble size for which the factor is defined is allowed to increase.

8.5.1 Neighbour Independent Occupation Model

It was pointed out earlier that analysis of individual metal clusters on the support surface showed that the compositions of such had a certain variability. On the average, the composition was quite close to that of the bulk, but particle to particle differences were manifest. In order to consider this apparent property of the MVS materials, a first approximation of the arrangement of atoms within a bimetallic particle could be formulated by assuming that every such atom was randomly placed in its ultimate position with uniform probability. An alternative, and perhaps more clear way of making this same statement, is to say that for any position in any metal cluster, the probability of occupation by metal A is proportional to the bulk fraction of metal A in the sample. In this picture therefore, a large sample containing a statistically significant number of atoms must necessarily have the correct bulk composition. This description of the structure of a bimetallic system does not allow for any preference of atoms of one kind to be associated with like atoms; occupation of any site within the model surface is completely independent of the occupation of every other surface site.

As developed so far, the model could actually be applied without using a computer (and random number generator) to generate and then analyze segments of model surface. This was not done, since, as will be shown in the section immediately following this, a degree of versatility in using the model would be lost. In a somewhat more sophisticated variation of the model, the assumption of minimum short range order (which results from assuming completely independent placement of every atom in the model system) will be abandoned.

For the first order model, in which the occupation of each surface site was independent of the occupation of neighboring sites, the attenuation factor with respect to either metal can easily be shown to be equal to the fraction of that metal in the bulk sample raised to the exponent n (where n is the size of the ensemble). As an example, if $n = 4$ atom ensembles are being considered for a 50 atomic % Pt/Ni

sample, then the attenuation factor for nickel is $(0.5)^4$ which is 1/16. It is also obvious that in the present form of the model, it would make no difference what shape the ensembles took. This above calculation is valid regardless of the relative position of the four atoms in the ensemble. In other variations of the model, in which the occupation of certain surface sites did affect the occupation probability of nearby sites, there would be a shape effect, in which ensembles of various patterns would be attenuated by differing degrees, depending on the direction in which occupation of grouped positions by like atoms was favoured.

The actual calculation carried out by the computer in representing the first approximation model was as follows: The number of atoms in the model surface was decided. Although this was purely arbitrary, the number was required to be large enough so that the bulk composition would approach the value defined by the probability of occupation of surface sites. If for example, the probability that a given atom be platinum were set to a value of 0.2 (hence, by definition that of Ni would be 0.8), and at least several hundred thousand atoms were used (necessarily comprising a few hundred individual clusters), one would always observe the calculated bulk composition of the model surface to be extremely close to 20% platinum.

Before the assignment of identity to each atom in the system, the spatial arrangement of the particles was first defined. Again somewhat arbitrarily, the surface atoms were assumed to have a hexagonal close-packed structure. Since prior experimental work had produced some knowledge of the particle size distribution, the computer program was written with the capability of representing the correct P.S.D. in the bimetallic model. This was done by converting the CTEM size histograms to number of clusters versus nuclearity. That is, the P.S.D. in the model is stated as: n_1 clusters of size y_1, n_2 clusters of size y_2, and so on, throughout the range extending from the minimum to the maximum number of atoms in any cluster. The relationship between measured diameter in the CTEM micrographs and the number of surface atoms in a particle has been worked out by Martin[21] for cubo-octahedra (which have the correct two-dimensional packing arrangement on their surfaces and which are observed to exist for both free and supported clusters of these types of metals). It should also be pointed out here that the atoms were assumed spherical and the diameter of Ni atoms was used to relate the CTEM results to nuclearity values. Although the diameter of Ni is slightly different from that of Pt, this has been neglected for simplicity. The implicit assumption in the bimetallic model therefore, is that platinum atoms fit into the spaces in a nickel lattice without significantly disrupting either the size or structure of the supported particles. Numerically, the relationship was developed using values of m, the number of atoms along one edge of the cubo-octahedron. The total number of atoms N_t is given by:

$$N_t = 1 + a(m-1) + b(m-1)^2 + c(m-1)^3 \qquad [8.1]$$

where $a = 11/3$, $b = 5$ and $c = 10/3$; the number of surface atoms N_s is further given by:

$$N_s = 12 + 10m\,(m-2) \qquad [8.2]$$

Complete cubo-octahedra occur for integral values of m (i.e., m = 2,3,4,...). In the case of incomplete cubo-octahedra, one would approximate using the next larger complete model, since these are less closely packed and would appear larger due to the limited resolution of the CTEM microscope. Under the previously discussed assumption that surface site occupation is independent of neighbouring site occupation, it can be shown that the results will not be particle size dependent; the computer program's capability of including the particle size distribution in the model was again supplied for versatility, so that variations to the model could be attempted. In other possible models, certain aspects of the results would be dependent on the particle size distribution.

The next step in the model formulation was to define the surface site occupation. As previously stated, this was accomplished on an atom-by-atom basis. However, the program used a particular filling order, so that the close packed configuration was realized. Figure 8-5 shows both the convention for naming the surface coordinate positions and the filling order of these.

At that point in the calculation, the nature of the system had been defined. The remainder of the calculation focused on analyzing it. The following method was used to *count* the number of complete ensembles of metal A and metal B in each particle in the model surface.

First of all, any pattern of four surface positions can be expressed as a 2 x 3 matrix. In this vectorial convention, there are three pairs of surface-position coordinates which represent the second, third and fourth atoms in the pattern, given that the first atom has coordinates (i,j). As an example of this, the following matrix represents one of the linear surface configurations:

$$\begin{bmatrix} 1 & 0 \\ 2 & 0 \\ 3 & 0 \end{bmatrix}$$

This means that the coordinates of the four surface positions in this configuration are (i, j), (i + 1, j), (i + 2, j) and (i + 3, j). All of the possible patterns for the four-atom-ensemble model are presented in Figure 8-6. There are either three or six rotations for each of the pattern types: linear, cyclo, cis, trans, etc. (depending on their respective symmetries). Each pattern type and rotation was represented by a different matrix. The counting algorithm proceeded by examining the four positions defined by each matrix using

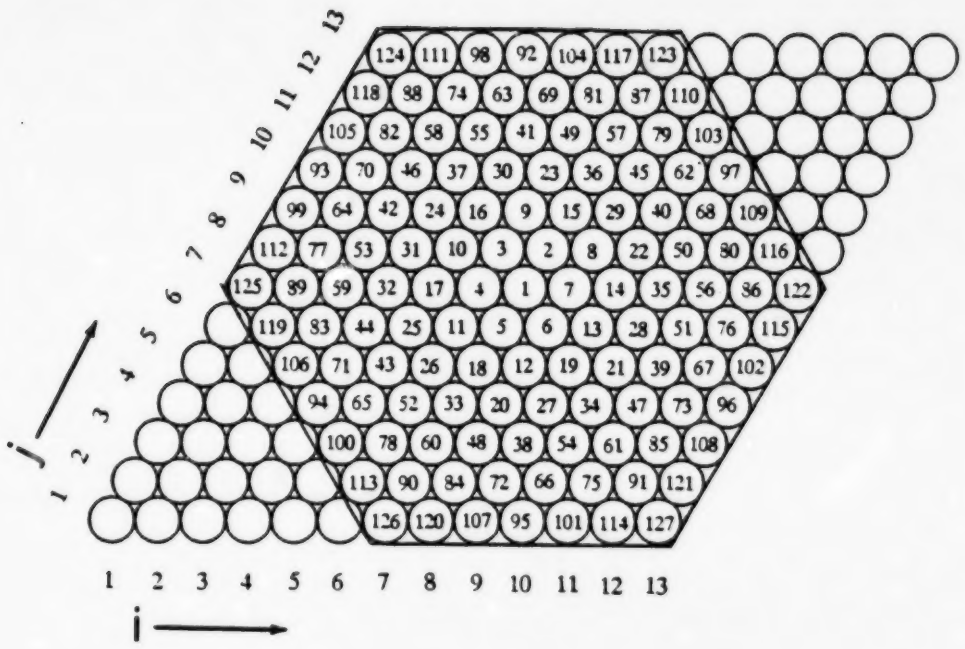

Figure 8-5 The Packing Structure, Coordinate System and Filling Order Conventions for the NIO Bimetallic Surface Model

every first-atom position (i,j), for which all four surface positions were occupied by metal atoms. Whenever it turned out that all four metal atoms were either metal A or metal B, then an appropriate counter index was incremented. There was also a counter which registered the total number of four occupied positions having any combination of the two metals (this was used to represent the total number of ensembles). The counting procedure was applied to all of the particles in the model. At the end of the counting, the program determined the ratios of pure metal A and pure metal B ensembles to the total number of ensembles. It also had the capability of doing this for each of the six pattern types separately. Thus, a weighting factor can be assigned to each of the configurations. This allows the model to discriminate between catalytic site shapes which would be likely or unlikely candidates for reactant conversion.

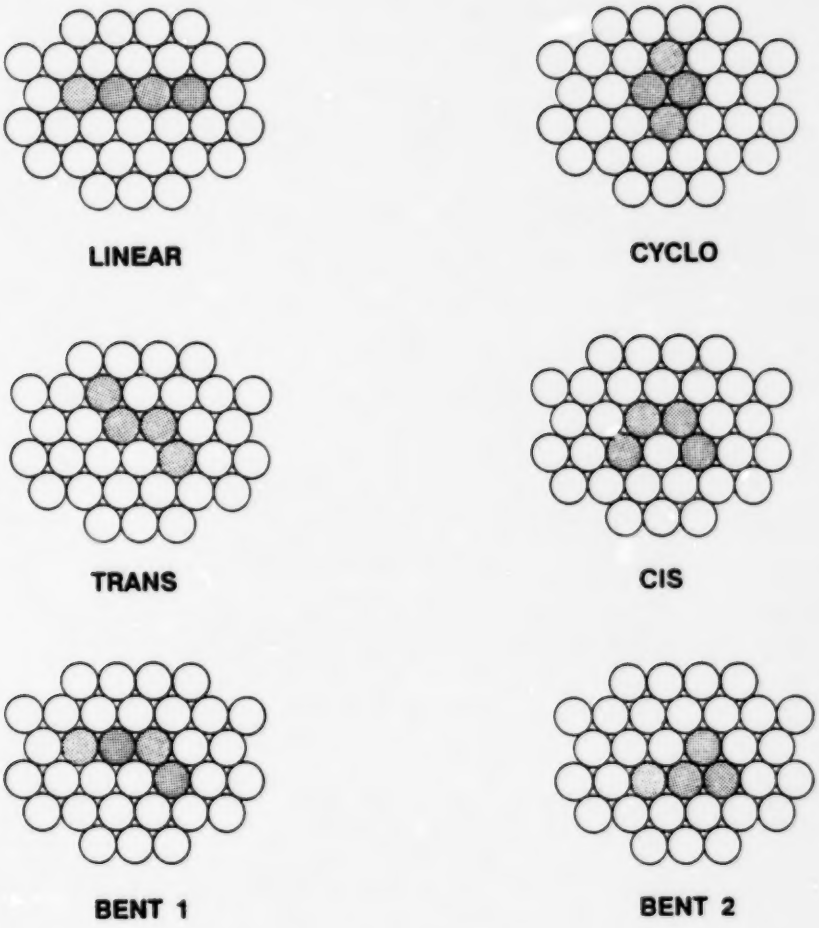

Figure 8-6 Possible Configurations for Four-Atom Ensembles in the NIO Bimetallic Surface Model

Ultimately, the reaction rates (for the model) were calculated. For the structure sensitive reactions, the rates were given by the ratio of metal A sites in the bimetallic sample to that of unimetallic metal A, times the reaction rate over pure metal A, plus the corresponding metal B attenuation factor, times the reaction rate over pure metal B. In the butane conversion reaction system, the attenuation of the two structure sensitive reaction paths automatically led to the augmentation of the selectivity value for the third, since by definition, the selectivities for the three reactions total unity.

The entire calculation described above was carried out for a series of bimetallic compositions ranging between pure metal A and pure metal B.

Results for the model in which it was assumed that the occupation of surface sites is neighbour-independent, are shown along with the actual experimental data in Figure 8-7. Although a first inspection of the model-generated curves may appear to show a rather poor fit, the qualitative pattern does agree with the experimental data. The hydrogenolysis and isomerization reactions show the expected attenuation in their selectivities (reaching a maximum for the 50 % Pt surface) and the dehydrogenation selectivity is correspondingly augmented. The magnitude of these trends for the present model shows an overestimate of the desired behaviour however, requiring some form of modification of the model beyond its present from. Obviously, one way of approaching a better fit to the observed data would be to decrease the ensemble size. This was the chosen method however, since it would conflict with the literature work which in fact supports ensemble sizes even larger than four[21]. Furthermore, another more reasonable way exists in which to predict a less drastic degree of ensemble attenuation.

8.5.2 Variable Short-Range Order Model

A relatively simple modification to the neighbour-independent occupation (NIO) model led to the variable short-range order model (VSRO). In this adaptation, the algorithms which introduce the particle size distribution, choose metal identity based on the required bulk composition of the bimetallic (model) sample and which search for ensembles of four like atoms on the surface remain unchanged. Also, the same filling order of coordinate positions on the particle map is used. The difference is that instead of being filled atom by atom, the computer program fills the map in groups of like atoms.

Results from two runs of the VSRO model are depicted in Figure 8-8. In the upper portion of the figure, calculations were carried out using patches of ten atoms, and in the lower portion, a size of twenty five was used. At approximately this value, an optimal fit of the observed results was realized. The ensemble sizes in this case were kept at a value of four for both the hydrogenolysis and isomerization reactions.

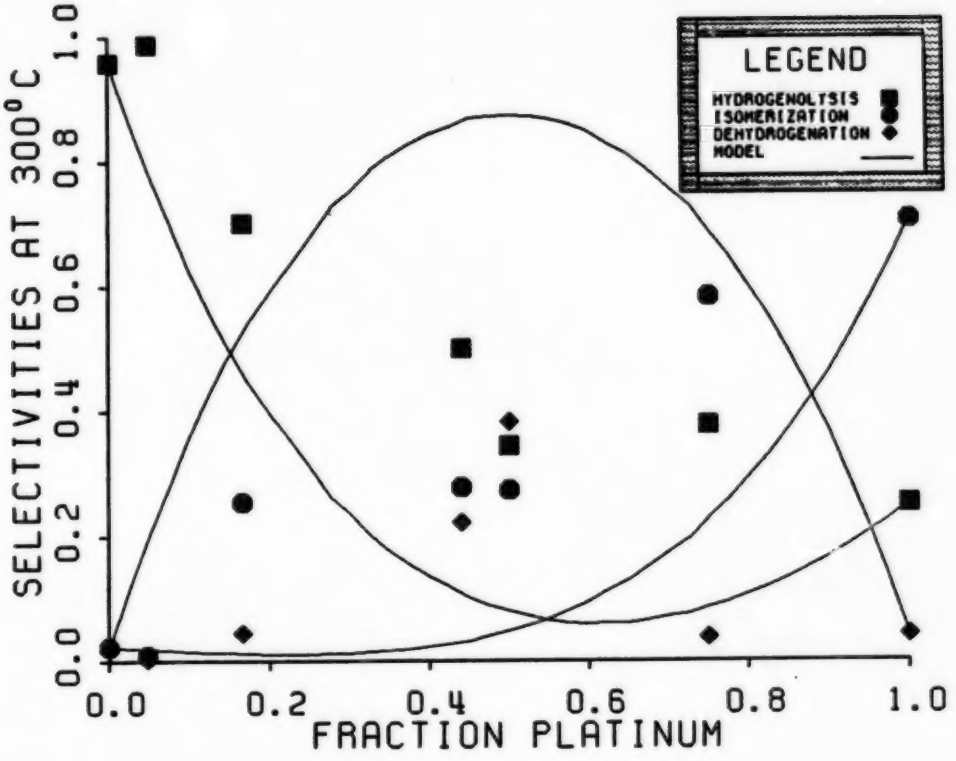

Figure 8-7 Results from the NIO Bimetallic Surface Model

8.5.3 Fully Segregated Particle Model

At this point, it may be argued that the arbitrary choice of four atoms as the ensemble size is not entirely reasonable. Current thinking in the catalytic literature suggests[17] that the value is acceptable for the isomerization path, but that for hydrogenolysis, a value of between twelve and sixteen should be used. Applying this change alone to generate a third model would have the effect of increasing the predicted dehydrogenation selectivity very profoundly, ultimately yielding predicted selectivity patterns much like those of the NIO model. This could be counterbalanced however, by increasing the degree of segregation of the two metals. Thus the approach taken in implementing a third model, was to make the assumption that the bimetallic particles were fully segregated, and vary the ensemble sizes until a fit of the observed data was achieved.

The results of this final model are depicted in Figure 8-9, and yielded values of four and sixteen for the isomerization and hydrogenolysis ensemble sizes respectively. As stated in Section 8.5.1, the calculations implicitly involved the known particle size distributions of these materials; in this final model, such remained the case.

At first inspection, it may seem that fully segregated particles should not have fewer multi-atom ensembles than the corresponding unimetallics. It must be kept in mind however, that both the unimetallics and bimetallics had the same particle size distributions. Therefore a *two phase*, 1.3 nm bimetallic particle may be thought of as a pair of 0.6 nm unimetallic particles in contact with each other (hence appearing in a CTEM image as a 1.3 nm entity). In this size range, it can be easily demonstrated that there would be a considerable difference in the number of large ensembles on the surface of a 1.3 nm particle as compared with a 0.6 nm particle.

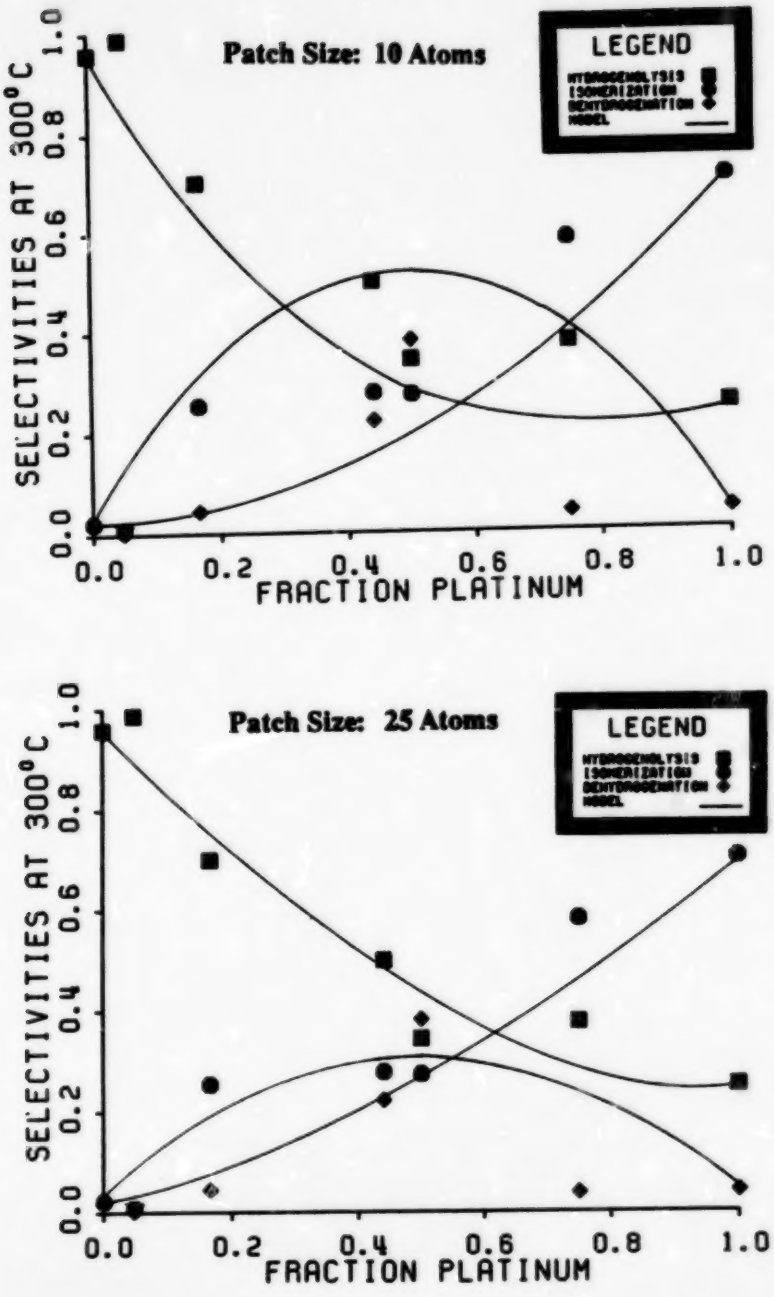

Figure 8-8 Results from the VSRO Bimetallic Surface Model

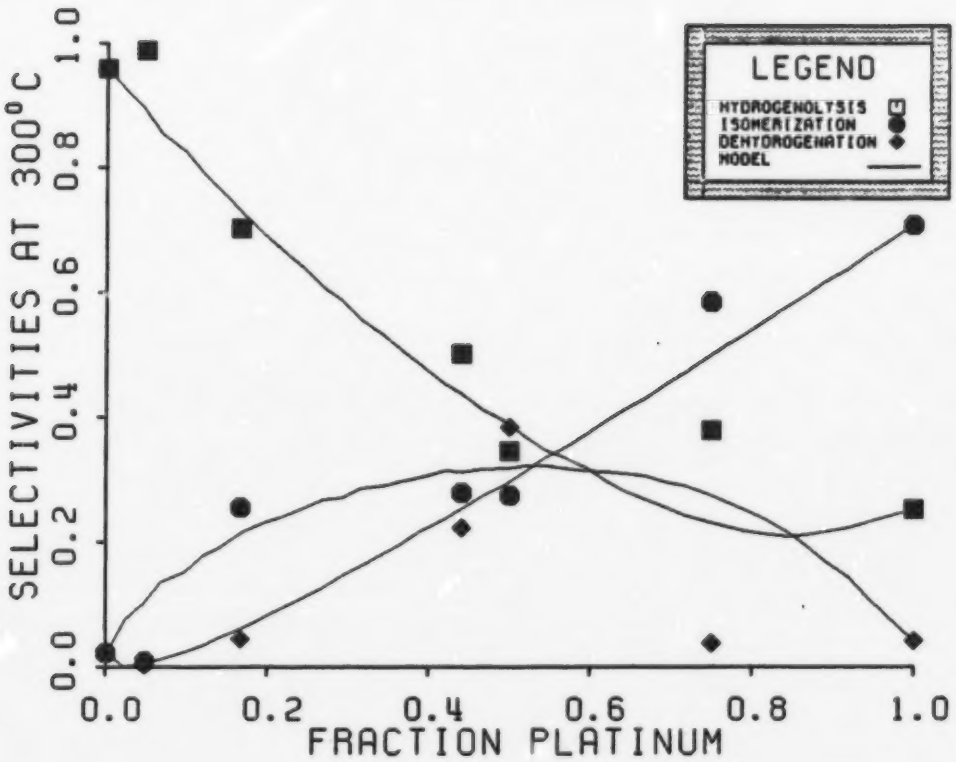

Figure 8-9 Results from the Fully Segregated Bimetallic Surface Model

CHAPTER IX

Examination of MVS Materials by Extended X-ray Absorption Fine Structure Spectroscopy

9.1 Introduction and Analytical Capabilities

The phenomenon of Extended X-ray Absorption Fine Structure has been observed by Kronig et al.[101,102] as early as 1931, and has been recognized to occur for most elements in the gas (except monatomic), liquid and both crystalline and amorphous solid phases. The development of a comprehensive theoretical treatment of EXAFS was carried out by Stern[103,104], in which the full potential of the technique for revealing structural details of various samples was realized.

X-ray absorption spectra are characterized by edges rather than peaks: the sudden increase in absorption coefficient corresponds to a minimum energy threshold required before the x-ray photons can cause ejection of a particular core level electron from atoms of interest in a sample. Photons having slightly greater energies than this threshold value may also be absorbed (through the simultaneous excitation of other electrons in the photoionized atom, by causing Auger and higher order processes, inelastic losses and so on).

The EXAFS signal is seen on the high-energy side of x-ray absorption edges, and commonly extends from about 30 to 1500 eV beyond the threshold of the edge. The typical appearance of the signal is that of a highly damped oscillatory fluctuation in the absorption coefficient versus energy plot. It results from the backscattering of the ejected photoelectrons by other atoms in the near environment of the absorber. Through an analysis of the EXAFS signal therefore, the spatial arrangement of the atoms in the vicinity of an x-ray absorber can be elucidated. Various electronic and temperature dependent (vibrational disorder for example) features of the system are also manifest in the information contained within the EXAFS signal.

Since EXAFS spectroscopy involves x-ray transmission measurements, it is not a surface technique *per se*. There are two situations however, in which it becomes so. Since an EXAFS signal experiment probes the environment of interest, the technique would be surface sensitive in cases where that element was strictly found, or enriched in surface regions. Most catalytic materials are designed to have just this kind of situation. Alternatively, the x-ray absorption coefficient, along with its EXAFS information, may sometimes be determined from a measurement of Auger photoemissions in the sample of interest. Since the Auger electrons have escape depths which are normally on the order of 2 nm for dense solids (including supported catalyst materials), this related technique called SEXAFS (i.e. Surface EXAFS) is exclusively surface sensitive.

One of the most important advantages in EXAFS is its ability to reveal structural information in non-crystalline samples. Of these, supported metal cluster materials represent a major field of interest; related crystallographic techniques such as x-ray and low energy electron diffraction cannot be applied to such systems. The kind of structural information which can be obtained through the use of EXAFS analysis, includes the number and type of neighboring atoms (about the absorber), and the interatomic distances involved. For such determinations, one typically[126] achieves accuracies of 0.001 to 0.003 nm. Of further advantage, is that this information can be obtained for particular coordination shells around the central absorber (although there is, naturally a decrease in sensitivity upon examining progressively larger shells). In addition, EXAFS can yield measurements of the R.M.S. displacements of these bonds with respect to their equilibrium distances, as well as the degree of static disorder in such systems. In some materials which are analyzed, it is possible to extract measurements of the angles between certain selected chemical bonds. This affords again, accuracies within the same range as those obtained in crystallographic measurements, yet is applicable to non-crystalline systems as well.

9.2 Theory of EXAFS

In order to derive the structural information which is available from an x-ray absorption measurement, there are three stages in the manipulation of data and subsequent calculation. In the first, the EXAFS signal must be extracted from the overall absorption spectrum. This procedure involves

baseline correction, normalization of the signal relative to the absorption edge, and in some cases the removal of instrumental artifacts[a]. In the second stage, the Fourier transform of the raw EXAFS oscillation is calculated. This has the effect of representing the EXAFS data as a plot of the transform magnitude versus radial distance from the absorber, in which various peaks corresponding to scattering entities are visible. The third stage in the calculations involves *Fourier filtering*, or isolation of the part of the EXAFS information which represents only the first coordination shell. The data are then back transformed so that a theoretical scattering equation can be fit. Contained within the equation, are all of the structural parameters of interest.

9.2.1 Isolation of the EXAFS Signal from X-ray Absorption Data

In order to extract the EXAFS signal (i.e., that which contains a description of only the environment of the absorber), the recorded absorption coefficient is normalized through application of the following:

$$\chi(E) = \frac{\mu(E) - \mu_o(E)}{\mu_o(E)} \qquad [9.1]$$

where $\chi(E)$ is the oscillatory EXAFS signal $\mu(E)$ is the measured absorption coefficient and $\mu_o(E)$ is the absorption coefficient for the absorber in the free-atom state. Although $\mu_o(E)$ may be obtained through measurements for many systems, it is also routinely calculated using semi-empirical techniques as described by Lytle et al.[109] and Via et al.[110]. Graphically, this transformation yields the appearance of a damped (toward higher energies) oscillation along a flat baseline.

In order to relate the EXAFS data to the theoretical equation containing structural parameters, the above is expressed in wavevector space. The relationship between kinetic energy E and wavevector k is given by:

$$k = \sqrt{\frac{8\pi^2 m}{h^2}(E-E_o)} \qquad [9.2]$$

---

a these usually appear as sharp discontinuities in the plot of absorption coefficient versus energy, and are caused by such phenomena as (for example) the passage of harmonics of the radiation wavelength at which the absorption is being scanned, through the monochromator

where m is the mass of an electron, h is Planck's constant, and E_o is the threshold energy of the electronic shell in the atom from which the photoelectron was ejected following absorption of the x-ray photon. The EXAFS phenomenon in most systems is adequately described in terms of single electron / single scattering theory. The first and most general treatment of EXAFS theory, by Sayers, Stern and Lytle[109] regarded the neighboring atoms as point scattering sources. Other theories have been employed[111,112,113], in which more detailed scattering potentials are involved.

9.2.2 Theoretical Scattering Function for K and L_I Edges

The most straightforward treatment of the scattered photoelectron wave can be applied to K and L_I absorption edges (arising from 1s and 2s initial states respectively). Because of the spherical symmetry of these initial states, the form of the scattered wave equation displays only radial and not angular terms. In k-space, the EXAFS function may be represented by the following, where it is expressed as the sum of all waves scattered by N_j neighboring atoms (here, the subscript i denotes the central absorber, and j denotes the scatterers) and F_j is the backscattering amplitude from each neighbor.

$$\chi(k) = \sum_j N_j \, S_i(k) \, F_j(k) \, \exp\left(-2\sigma_j^2 k^2\right) \, \exp\left(\frac{-2r_j}{\lambda_j(k)}\right) \, \frac{\sin(2kr_j + \phi_{ij}(k))}{kr_j^2} \qquad [9.3]$$

The above function can be seen as having two parts. The sine term, with its $\frac{1}{kr^2}$ dependence is representative of spherical wave scattering. In this term, the total phase shift is given by $\phi_{ij}(k)$, however this may be broken down into a component corresponding to the central atom (which is multiplied by a factor of two to account for the fact that the central phase shift is experienced twice in backscattering, once outgoing and once incoming). The second part of the function contains several amplitude attenuation factors. The S_i function accounts for losses due to excitation processes of the absorber, such as shakeup and shakeoff[a]. Similarly, the exponential term containing $\exp\left(\frac{-2r_j}{\lambda_j(k)}\right)$ accounts for inelastic losses due both to the neighboring atoms and the medium. λ_j is the electron mean free path. The other exponential term contains a Debye-Waller factor.

---

a these are respectively, processes in which outer electrons in the absorber are either promoted to bound excited states or unbound states

The term containing the Debye-Waller factor accounts for losses as a result of thermal vibrations and static (i.e. structural) disorder of the system. Experimentally, it is sought as one of the parameters which can be obtained through curve fitting. Its determination provides yet more information about the system being analyzed; in particular, the root mean square bond displacement for the ij pairs, as well as the degree of bond polarization.

9.2.3 Theoretical Scattering Function for L_{II} and L_{III} Edges

If one examines the EXAFS literature, it can be readily seen that L_{II} and L_{III} x-ray absorption edges are commonly used. This is usually the case when either another element in the sample interferes with the K or L_I edges, or these occur at energies which are out of range of the instrument (this is usually constrained by the monochromator design).

The L_{II} and L_{III} edges correspond to initial states having p symmetry. According to the selection rules which govern the x-ray absorption process, the final state can be either of s or d symmetry. Furthermore, the sinusoidal part of the scattered wavefunction will have angular dependence. The expression for the EXAFS function in this case is:

$$\chi(k) = \sum_j S_i(k)\, N_j \frac{|f_j(\pi,k)|\exp(-2\sigma_j^2 k^2)}{k r_j^{\,2}} \exp\left(\frac{-2r_j}{\lambda_j(k)}\right) \cdot$$

$$\left[\frac{1}{2}\left(1 + 3\cos\Theta_j\right) M_{21}^2 \sin(2kr_j + 2\delta'_2(k) + \theta_j(k)) + \frac{1}{2} M_{01}^2 \sin(2kr_j + 2\delta'_0(k) + \theta_j(k))\right.$$

$$\left. + M_{01}M_{21}(1 - 3\cos^2\Theta)\, \sin(2kr_j + \delta'_0 + \delta'_2 + \theta_j(k))\right] \left[M_{21}^2 + \frac{1}{2} M_{01}^2\right]^{-1} \qquad [9.4]$$

The various amplitude attenuation factors are the same as those used in equation [9.3] (with the exception of the π factor in the backscattering amplitude term).

The angular part of the function contains three terms. These correspond to a final state having s-symmetry, d-symmetry and a cross term which involves s outgoing and d incoming waves (and vice versa). The M coefficients are the dipole matrix elements for the transitions involved. In EXAFS, the dipole approximation is used almost universally; Lee and Pendry[112] show that it is valid as long as the wavelength of the x-ray photons exceeds that of the initial state orbital. The phase shifts in [9.4] have been expressed

in terms of the scattering at the central atom (twice) and each neighbor (once). For the central atom phase shift terms, the subscripts 0 and 2 indicate the angular momentum of the final states (s and d respectively).

Although equation [9.4] may seem unmanageable in terms of its application to experiment, Teo and Lee[114] have proposed some practical simplifications. These researchers have made determinations of the ratio M_{21}/M_{01} for several elements (for example, Ti, W and Zn), and found this to have an almost energy-invariant value of about 5. As a direct result of this, one can easily show that the $l = 0$ contribution is less important by a factor of approximately 50, hence rendering its effect nearly unobservable. It is therefore possible to analyze EXAFS from these edges, by employing a slightly modified K-edge expression, in which $2\,\delta_2'$ is used as the appropriate central atom phase shift.

9.2.4 Application of the Theoretical Equations in Curve Fitting Data

As previously stated, experimental data must be Fourier transformed as part of the procedure which allows curve fitting, in order that only one coordination shell be involved. This is done according to:

$$\rho_n(r) = \frac{1}{(2\pi)^{1/2}} \int_{k_{min}}^{k_{max}} w(k)\, k^n\, \chi(k)\, e^{2ikr}\, dk \qquad [9.5]$$

It is readily obvious that experimental curve has been multiplied by two correction factors in the above. The k^n factor arises from a product of the $1/k$ dependence of the scattered wavefunction (which appears explicitly in equation [9.3]), and the implicit $1/k^2$ dependence [a] of the backscattering amplitude factor F_j. Therefore $n = 3$ is most usually employed, although $n = 1$ and less commonly $n = 2$ are sometimes chosen[115]. By applying this correction, the severe damping of the EXAFS signal with increasing k is removed. This weighting of the data provides unbiased fitting of the data with respect to the theoretical equation, over the entire range of radial distance which is of interest to the data analysis. The $w(k)$ factor is a window or *apodization* function. It is used to select part of the observed EXAFS function; this has the physical significance of removing all contributions to the signal which do not come from scattering in the coordination shell to which the theoretical equation corresponds. Shells other than the first are rarely of

---

a this comes from the Born approximation at high values of k, wherein the scattering amplitude has (approximately) such dependence

interest. Furthermore the theoretical scattering equations involving multiple shells are considerably more complicated.

A plot of the Fourier transform demonstrates a series of peaks located at radial distance positions. The intensity of these peaks is related to the number of scatterers at such distances, however the exact position of the peaks in the plot is not equal to the true interatomic distances between the absorber and the neighbors. This is a result of the phase shift in the scattered waves; the size of such shifts is typically observed to be on the order of 0.01 nm or so.

The operation of taking the inverse Fourier transform (IFT) of the filtered data is accomplished according to:

$$\chi(k) = -\int_0^\infty \frac{g(r)}{kr^2} \sin(2kr + \phi(k))\, dr \qquad [9.6]$$

in which the notation $g(r)$ has been used to replace $\rho_n(r)$ in [9.6], indicating the applied corrections.

The experimental data are finally fit to the theoretical equation using an iterative least-squares approach. In so doing, the error of fit is minimized with respect to all of the structural parameters appearing in the theoretical EXAFS equation.

9.3 Experimental Details

9.3.1 Sample Preparation and Data Collection

The unimetallic nickel, platinum and bimetallic nickel/platinum samples, subjected to analysis by EXAFS were all treated carefully in order to ensure that they represented the exact materials which were used in the catalysis experiments. Since earlier experience had shown that sample handling, even in a well maintained dry-box, could result in unacceptable levels of contamination (particularly by adsorption of oxygen), a special reactor/EXAFS cell was designed. This is shown in Figure 9-1. The main feature of

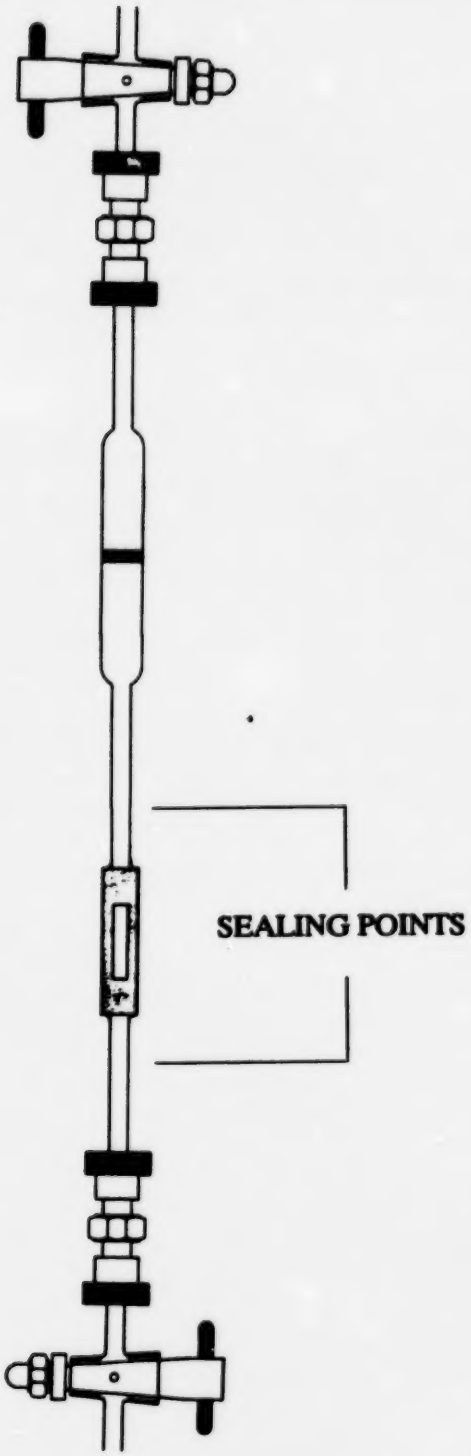

Figure 9-1 Pretreatment Reactor / EXAFS Cell Used for Rigorously Anaerobic Sample Handling

this design was the ability to perform the reductive pretreatment [a] of the MVS materials, then move the resulting sample into the EXAFS cell section, and seal off the glass tubing at the points marked in the figure. A stream of rigorously clean helium was prepared using Supelco™ water/oxygen traps, capable of reducing both concentrations to levels below 1 ppm. After inverting the reactor/cell assembly, and allowing the sample powder to settle into the cell section, the stream of helium was used to pack the sample efficiently against the fritted disk epoxied into the end of the cell farthest from the reactor section. Quantities initially loaded into the apparatus were calculated such that the cell would be completely filled after sealing. The cell sealing was accomplished under an atmosphere of helium, by using liquid nitrogen to cool the reactor section, thus reducing the internal pressure sufficiently.

The EXAFS cell body was constructed of aluminum, and attached to the glass tubing by high vacuum epoxy resin. The opening used for X-ray transmission through the sample measured 0.4 by 2.0 cm, with an optical path length of 1.0 cm. The windows were constructed of a 25μ thick film of Kapton™ which was also sealed using high vacuum epoxy. After several hours of storage, the windows curve slightly inward due to the diffusion of helium from the inside of the sealed cells. This served as a means of ensuring the absence of leaks which would result in sample contamination.

The X-ray absorption data were collected by direct ratioing of the intensities of the monochromatized radiation before and after the sample. These were obtained with the sample at a temperature of 100 K, using X-ray radiation from a 2.5 GeV synchrotron storage ring (Brookhaven National Laboratory, Upton N.Y.) at currents ranging from 65 to about 100 mA. A Si(220) channel-cut crystal monochromator was used to collect X-ray absorption spectra at the nickel K (8.333 keV) and platinum L_{III} (11.56 keV) edges. In order to exclude higher energy harmonics of the principal radiation frequency, a piezoelectric crystal was used to detune the Si crystal by 50% of the maximum incident intensity. Also, the energy resolution was defined through the use of a 2.0 mm slit positioned before the monochromator along the synchrotron beamline.

X-ray intensity measurements were made in a conventional transmission arrangement, using a pair of GSK Scientific™ ionization chamber detectors. The incident intensity monitor was operated with a path length of 10.0 cm through 20.26 kPa of argon; the post-sample detector had a path length of 30.0

---

a this was carried out using exactly the same gas concentrations, flowrates, temperature and reaction time as in the catalysis experiments.

cm through 91.17 kPa of argon. The detector output signal was collected using a CAMAC™ data acquisition and control system.

9.3.2 Calculations

Specific details of the extraction of the normalized EXAFS oscillations from the raw x-ray absorption data are presented by Sayers and Bunker[117]. To accomplish this, a linear pre-edge baseline was extrapolated over the entire spectral range containing EXAFS information, and the technique[117] of step normalization was used. The Fourier transform and transform *filtering* methods were carried out in a standard fashion as described in reference 117, and section 9.2.4. Quantitative results were obtained by fitting a theoretical model of the appropriate EXAFS function to isolated data which corresponded to *first shell only* scattering, through the use of a nonlinear least squares algorithm. The phase shift and amplitude correction data which were required in the above calculation, were obtained empirically from a Pt foil and diluted[a] NiO standard.

9.4 EXAFS Results

9.4.1 Pt L_{III} Edge EXAFS for Unimetallic Pt and Bimetallic Ni/Pt Samples

The materials synthesized in the presently reported research, which were chosen for analysis by EXAFS include: EMR-23 (a unimetallic sample, produced by solution phase MVS); EMR-27 (a bimetallic Pt/Ni sample, also produced by SPMVS); and a sample marked "DH-002", which was produced in the static reactor using the $Pt(N_2)_3$ precursor. The raw EXAFS data, after ratioing against the height of the absorption threshold (i.e., normalized) are presented in Figure 9-2, for the above samples. In Figure 9-3, the *k*-weighted Fourier transform amplitude for the unimetallic and bimetallic MVS samples (excluding the static reactor material) are illustrated. Data from the platinum reference sample was used to perform phase shift and amplitude correction on the spectra recorded for the MVS samples.

After extracting the contribution to the total EXAFS which resulted from only the first coordination shell about the platinum, the data were fit to a theoretical model in order to extract structural parameters. These are listed in Table 9-1, and include average coordination numbers, bond lengths and Debye-Waller factors for the two samples.

---

a using Al_2O_3, and in proportions such that the Ni content was equal to 3 wt%.

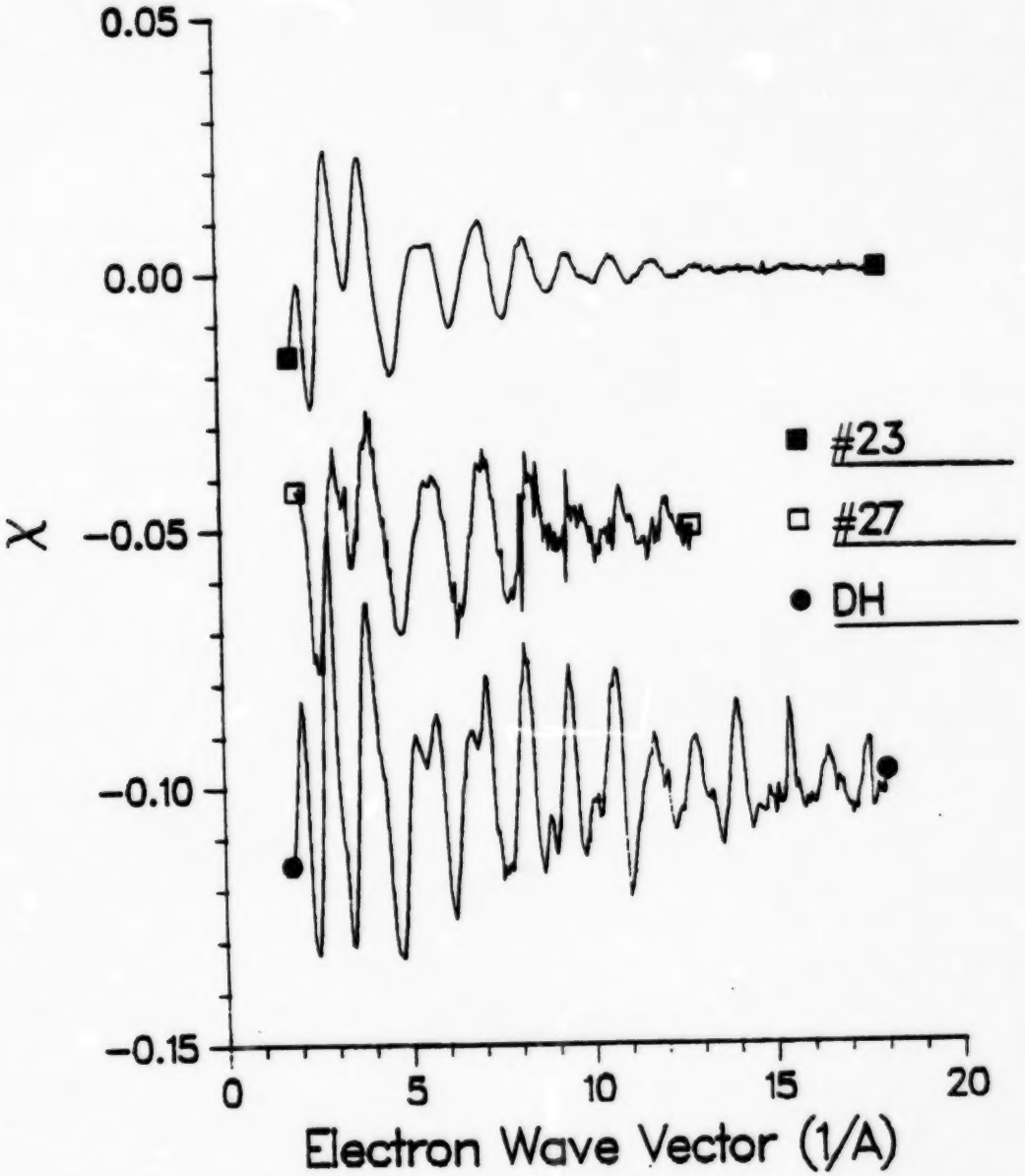

Figure 9-2 Normalized Pt-L_{III} EXAFS Data Measured at 100 K

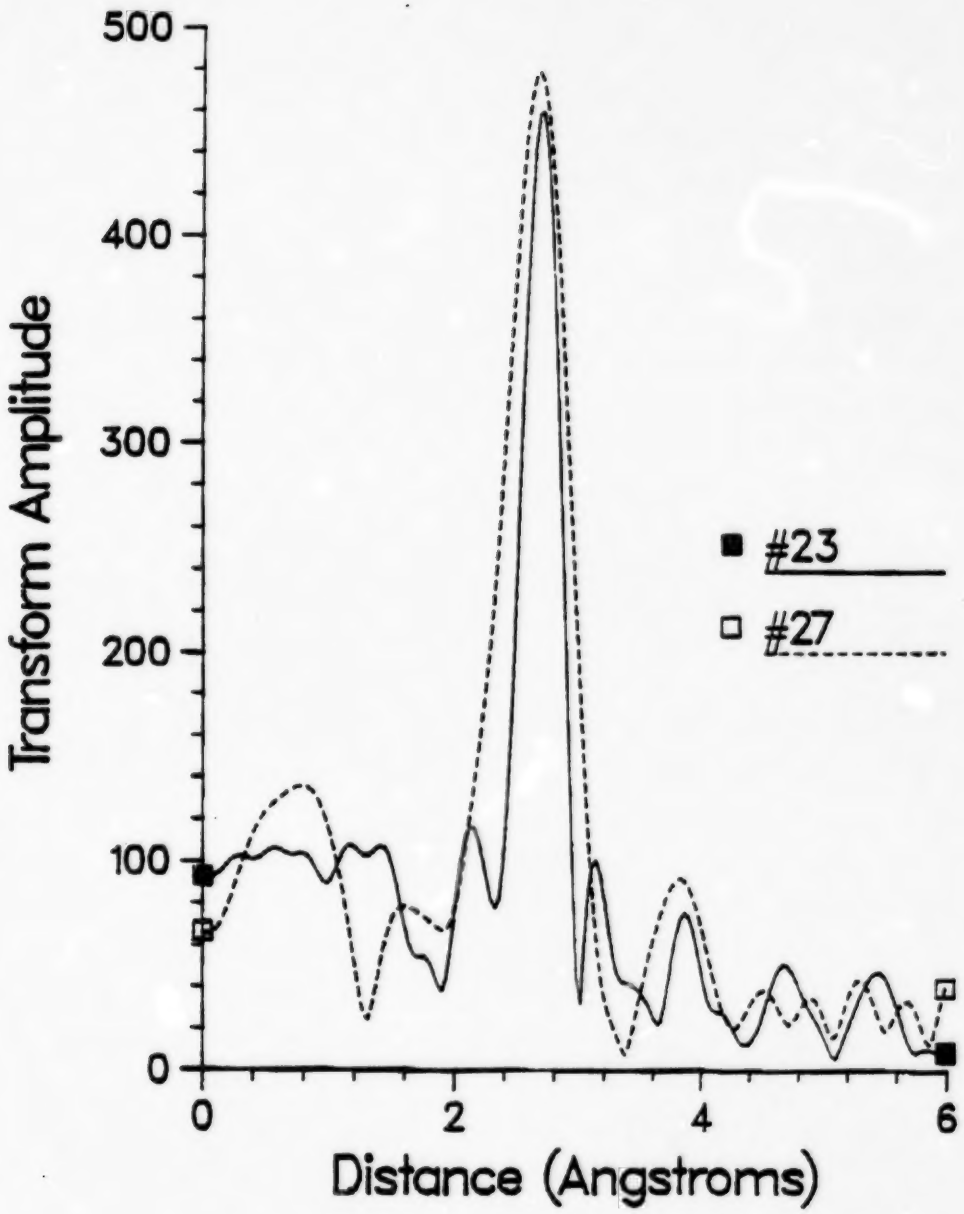

Figure 9-3 Fourier Transform Amplitude of the Pt-L_{III} EXAFS Data Measured at 100 K

9.4.2 Nickel K Edge EXAFS for Unimetallic Ni, Bimetallic Ni/Pt Samples

The normalized EXAFS signal taken at the Nickel K edge is presented in Figure 9-4 for both the unimetallic sample (EMR-22) and the Ni/Pt bimetallic (EMR-27), as well as a NiO standard sample (the rock salt form, diluted with Al_2O_3). As in the case of the platinum samples, the *k*-weighted Fourier transform of the EXAFS χ function was calculated for each sample, and is plotted in Figure 9-5. The structural parameters corresponding to the nickel-containing phases of the supported particles are also given in Table 9-1.

SAMPLE	COORDINATING ATOM	COORDINATION NUMBER	BOND LENGTH (Å)	DEBYE-WALLER FACTOR ($\times 10^{-3}$)
PLATINUM L_{III} EDGE				
EMR-23	Pt	7.4	2.725	5.80
EMR-27	Pt	7.5	2.715	3.78
NICKEL K EDGE				
EMR-22	O	6.6	2.072	1.92
EMR-27	O	6.0	2.059	2.74

Table 9-1 Structural Parameters of MVS Materials Determined by EXAFS Analysis

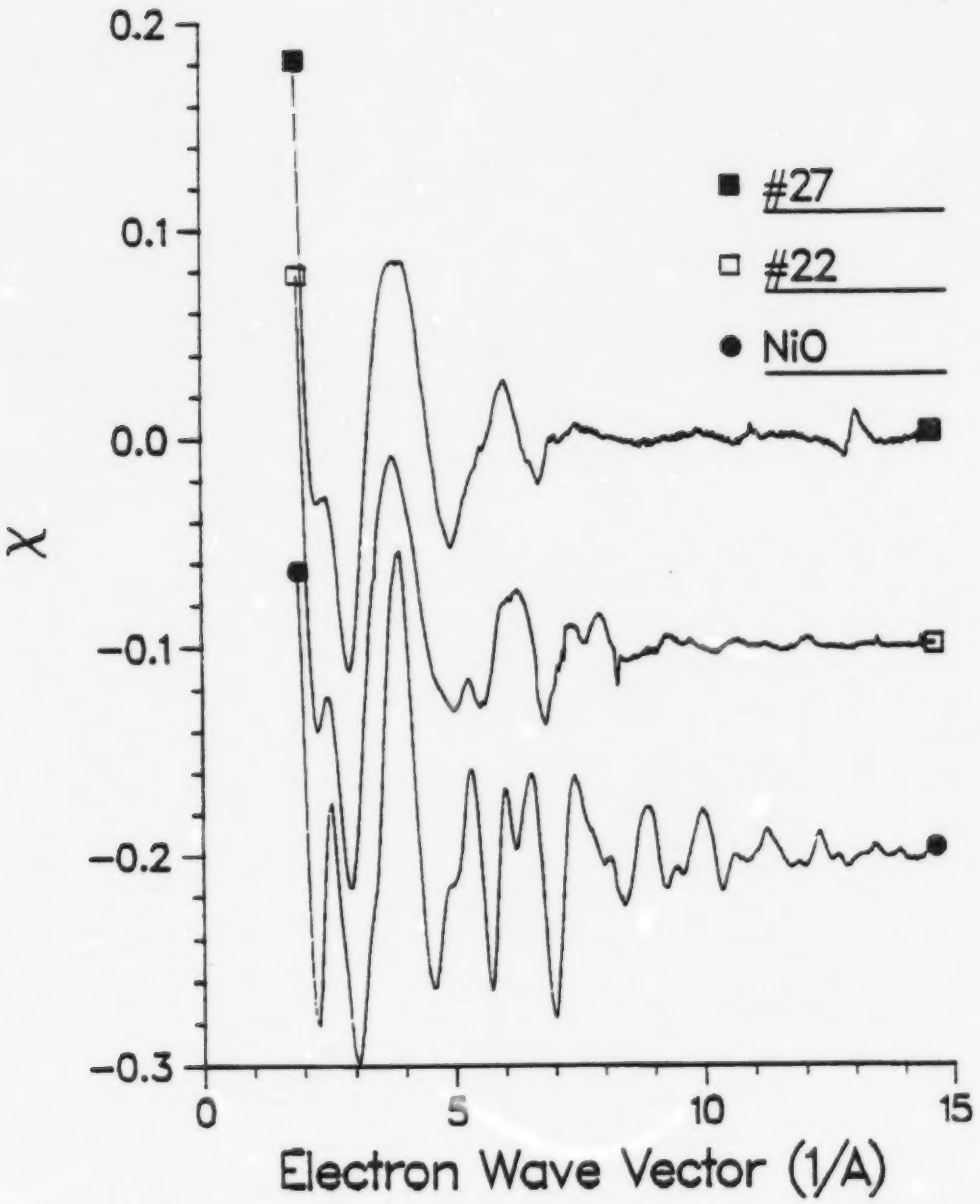

Figure 9-4 Normalized Ni-K EXAFS Data Measured at 100 K

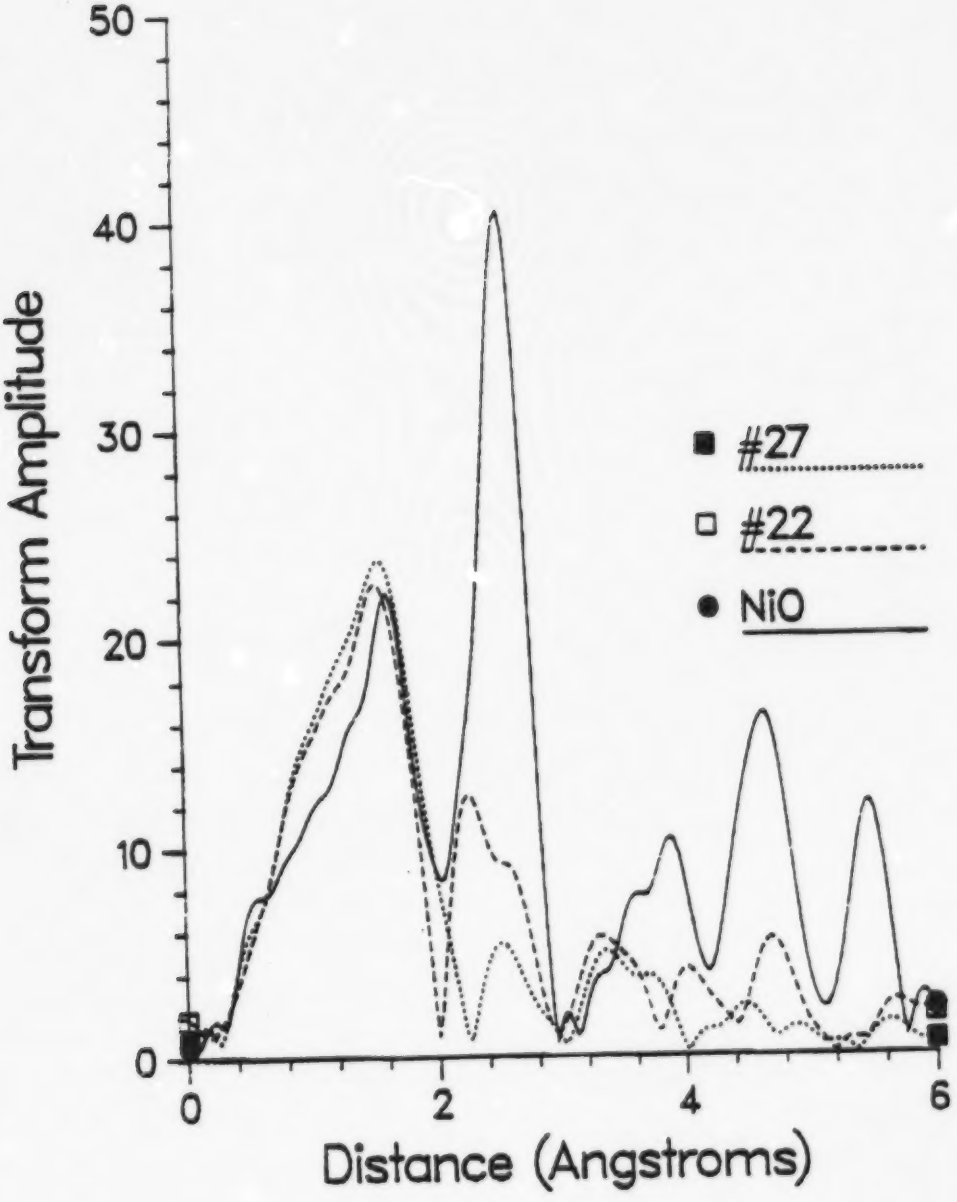

Figure 9-5 Fourier Transform Amplitude of the Ni-K EXAFS Data Measured at 100 K

9.5 Discussion of EXAFS Results

9.5.1 Examination of the Platinum L_{III} Edge

The normalized EXAFS oscillations for both of the solution phase MVS-generated samples display behaviour which is typical[110,118-122] for supported, small particle platinum catalysts. This is characterized by a strong signal arising from backscattering due to other platinum atoms in the first coordination shell of the average platinum atom. There are also some weak interferences, appearing as higher frequency oscillations superimposed on the main EXAFS function. These can be attributed to a contribution by backscattering from higher coordination shells. The low amplitude of these higher shell signals is indicative of the fact that only very few of the particles were actually large enough to have a second shell. This result is consistent with the CTEM results presented in Chapter III, which indicated particle size distributions having very few particles larger than 2 nm. Thus, an estimate of the average particle size of the MVS clusters made from EXAFS measurements would be consistent with the previously obtained value of about 1.2 to 1.5 nm.

In the case of the static reactor generated sample produced from the $Pt(N_2)_3$ precursor, the interferences can be seen to have a larger amplitude. Furthermore, the amplitude of the major oscillation extends to a considerably higher value of k. These two observations are consistent with a greater degree of agglomeration of these particles. Experience with larger particle supported Pt materials proves that observed EXAFS signals lose their sensitivity to particle size at values above approximately 4 nm. An estimate of the average particle size for the DH-002 sample would be at about that value.

The Pt-L_{III} EXAFS signal for the bimetallic sample contained a lower signal-to-noise ratio than in the case of the unimetallic sample. Such observation is not attributable to differences in the amount of platinum present, but rather to x-ray absorption by the nickel which was also present in the sample. In the region above the Pt-L_{III} edge, the absorption coefficient for nickel[124] is similar to that for platinum. Therefore, the relative absorption by Pt was reduced by about half, and consequently the spectral data were collected over a narrower range of energies. Despite the reduced data quality for the bimetallic sample, its characteristics were, in the qualitative sense, very much like those of the unimetallic platinum materials.

The values for the various structural parameters listed in Table 9-1 also demonstrate that both the unimetallic and bimetallic MVS materials have characteristics quite similar to previously studied Pt catalysts[123]. Among these are bond lengths shorter than those observed for bulk platinum, and coordina-

tion numbers of about 7.5 for Pt particles in the 1.2 to 1.5 nm range. This is again, in very good agreement with the results of the CTEM studies reported earlier.

The values of the Debye-Waller parameter for the two MVS samples indicate a slightly greater degree of order in the bimetallic case. This is the reason why the weak contributions due to second shell scattering have a somewhat greater amplitude (for the latter). It must be noted that both the particle size distribution and the degree of order will affect this amplitude. Thus, there is no evidence that the bimetallic particles are larger than the unimetallic ones.

As was alluded to above, the Fourier transforms shown in Figure 9-3 required phase shift and amplitude correction for Pt-Pt scattering, using data from the standard reference sample. Without such correction, broad features displaying multiple maxima would have resulted, due to the complicated[124] amplitude and phase functions for platinum. This procedure yielded sharp, symmetric peaks located at the correct Pt-Pt bond distance (essentially the same for both samples). An additional benefit provided by this, was the possibility of revealing subtle additional coordinations. An example relevant to the presently described materials would be an additional contribution arising from a small amount of Pt-Ni coordination. Such was not however observed.

The difference in breadth of the two principal peaks (for EMR-23 and EMR-27) is a direct result of difference in energy range spanned by the two datasets. As more oscillations are included, better definition of this peak is expected to result. The broader peak in the bimetallic case means neither that this sample contained more platinum, nor that the scattering environment of the platinum atoms contained nickel.

9.5.2 Examination of the Nickel K Edge

The normalized nickel K edge EXAFS signals, shown in Figure 9-4, are characteristic of backscattering by a low atomic number entity in the first coordination shell of the average nickel atom. No means is available whereby one might differentiate between carbon and oxygen as this entity, however the former is less likely than the latter. This is made clear by the close agreement with data for the NiO standard.

As in the platinum case, the reference sample's EXAFS data showed a strong contribution by second and higher order coordination shells, whereas for MVS samples, the contribution was very weak. In the bimetallic sample, in fact, the higher contributions were virtually unobserved. This indicates that the unimetallic nickel particles and the nickel-containing part of the bimetallic particles may be thought

of as extremely small NiO crystallites. It is not surprising that the bimetallic sample appears to have a significantly smaller average particle size. The reader may recall that the unimetallic and bimetallic particles both had essentially identical sizes; the nickel *half* of the (0.5 atomic fraction) bimetallic would therefore be smaller.

Examination of Figure 9-5, showing the *k*-weighted Fourier transform amplitude, reveals almost perfect replication of the broad Ni-O scattering feature (located below 0.2 nm) between the MVS samples and the NiO standard material. In agreement with the platinum results for the bimetallic sample, there is no evidence of any contribution to the nickel results by platinum in its environment. If such had occurred, a marked decrease in the Ni-O amplitude would have been expected.

The particular phase of NiO which was chosen as the standard reference sample had a rock salt (NaCl) structure wherein the Ni-O coordination number was six. As shown in Table 9-1, the values estimated from the EXAFS data are in adequate agreement with this, as well as with bond lengths[125]. Because of the close agreement between the structural parameters for the MVS materials and the NiO, it may be stated that virtually all of the nickel atoms are fully coordinated by six oxygen atoms, rather than platinum or other nickel atoms. This has demonstrated that under the pretreatment conditions used (25% H_2 at 300°C), none of the nickel was reduced to the zerovalent state. Furthermore, based on the *rigorously* oxygen-free sample handling, it must be concluded that the oxygen in the NiO phase was abstracted from the alumina surface during the impregnation step in the synthesis. In chapter IV, it was noted that nickel XPS data showed no measurable difference in the oxidation state between virgin MVS materials and those which had been reduced.

The small deviation from the expected coordination number of 6, in the unimetallic sample, is attributed to a minor interference between the first Ni-Ni shell and the Ni-O shell in the reference data.

In the case of metal oxides, small particles typically have metal ions which are completely coordinated by the appropriate number of oxygen atoms. Thus, estimates of their particle sizes cannot be accomplished in the same way as in the case of noble metals for example, where the coordination number is related to the particle size. However, for the MVS materials discussed here, the extremely weak contributions by shells larger than the first imply that the previously stated size distribution estimates are correct.

9.6 Summary of the EXAFS Study

All of the information obtained by EXAFS analysis of the x-ray absorption data is in agreement with the particle size distribution measurements made throughout the presently reported research project. It also agrees with the information regarding the oxidation states of both nickel and platinum in MVS materials (treated for use as catalysts); platinum remains zerovalent, but even with rigorous oxygen exclusion and hydrogen reduction at 300°C, the Al_2O_3 support causes the $Ni(C_2H_4)_3$ precursor to yield fully oxidized nickel upon its decomposition and anchoring to the surface.

By examining both the Ni-K and Pt-L_{III} absorption edges in the bimetallic sample, it was observed that neither metal had any effect on the immediate environment of the other. This provides strong evidence that the assumption of completely segregated or *two-phase* bimetallic particles, used in the model discussed in Chapter VIII is absolutely sound.

These bimetallic particles may best be described as a platinum phase, structurally similar to other supported platinum catalyst materials of the same size regime, in intimate proximity to a nickel(II) oxide microcrystallite. The latter would be expected to be about the size of a single unit cell of NiO, for most particles in the sample. A model of this idealized bimetallic particle is depicted in Figure 9-6.

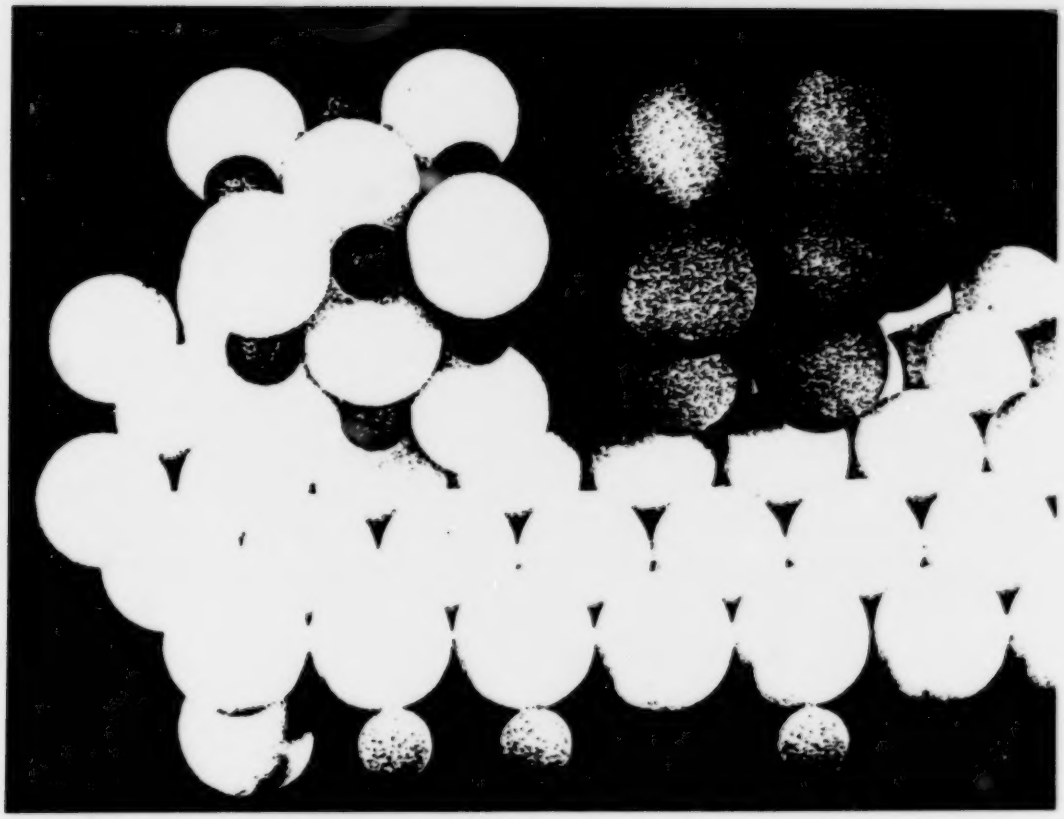

Figure 9-6 A Structural Detail Model of the MVS-Generated Bimetallic Ni/Pt Particle

CHAPTER X

Conclusions and Recommendations

10.1 Conclusions

- The technique of Metal Vapour Synthesis has been used to synthesize many samples containing ultra-small particles of unimetallic iron, ruthenium and bimetallic iron/ruthenium, as well as unimetallic nickel, platinum and bimetallic nickel/platinum, anchored to high surface area oxide supports. These support materials include silica, alumina and a mixed alumina/silica (94% Al_2O_3 - 6% SiO_2). The iron/ruthenium group of samples were produced through the intermediacy of bis-toluene metal(0) organometallic compounds, while the nickel/platinum system utilized tris-ethylene metal(0) precursors.

- The application of both Conventional and Scanning Transmission Electron Microscopy (CTEM and STEM) yielded estimates of the average particle sizes, and the particle size distributions of a large and representative group of MVS samples (from both the Fe/Ru and Ni/Pt preparations). In all cases, the particle sizes were extremely small compared to conventional, highly dispersed, oxide supported catalysts which involve any combinations of these four metals. None of the virgin MVS materials demonstrated average particle sizes greater than 1.0 nm; in fact, all were considerably less than this value, and in several (virgin) samples, particles were not observable at all.

- The average particle sizes of samples which had been hydrogen reduced at 300°C was between 1.0 and 1.6 nm for all of the samples examined. This conclusion was supported by other characterization techniques used throughout the research, including the EPR/FMR magnetic probes, analyses using chemisorption, and also EXAFS.

- Use of the MVS samples as catalysts, employing reducing atmospheres and temperatures up to 430°C, produced no further increase in average particle sizes. This observation is a demonstration of excellent resistance to sintering possessed by MVS materials, as compared with conventional supported catalysts produced by other means.

- Sintering in the case of high-temperature treatments in oxygen was limited to producing average particle sizes not in excess of 2.0 nm, for nickel and platinum containing specimens (the oxidation of Fe/Ru materials was not examined).

- The EDAX technique demonstrated that for both the Fe/Ru and Ni/Pt systems, MVS (yielding the aforementioned organometallic precursors) produced *truly bimetallic* supported particles. There exists good evidence that this capability is derived from the similarities in the decomposition temperatures of such precursor compounds. In order to arrive at the conclusion about truly bimetallic particles, it was necessary to perform EDAX analyses of *individual* particles, requiring a spatial resolution of 1.0 x 1.0 nm.

- The use of XPS allowed an examination of many of the electronic properties of the particles. From this, evidence was obtained that Pt remained zerovalent while the Ni in the particles was in an oxidized form. In bimetallic particles containing both elements, there was no indication of charge transfer between them. Evidence was gathered however, that the mechanism by which the particles were attached to the support surface involved metal-to-surface charge transfer.

- Application of XPS to the Fe/Ru bimetallic system demonstrated that in this latter case, there was metal-to-metal charge transfer. In particular, the presence of ruthenium allowed the iron to be present in a slightly less oxidized form.

- The chemisorption of hydrogen, oxygen and especially carbon monoxide (the latter being examined by FTIR) were used to confirm the extremely small particle sizes of many Ni, Pt and Ni/Pt samples. Two size-dependent phenomena, namely enthalpy of chemisorption and the coverage dependent shift in the carbonyl stretching frequency were explored, and compared with those exhibited by other supported particle systems of various size regimes.

- The EPR/FMR study, applied to a subset of the samples involved in this research, led to conclusions that species such as Ni^{+1} and Ni^{+2} were created by reaction of the zerovalent precursors with surface hydroxyl (Brønsted acid) groups on the supports. These served as nucleating centres for migrating precursor entities which ultimately incorporated into the supported particles.

- The catalytic results (using the conversion of n-butane in hydrogen as a probe reaction) for the bimetallic samples showed behaviour quite different from either of the two corresponding unimetallics. In particular, the Ni/Pt bimetallics showed a marked increase in dehydrogenation selectivity relative to the unimetallics. This is rationalized on the basis that the bimetallic particles differed geometrically from their unimetallic counterparts in such a way that there were fewer large ensembles of atoms (these are considered necessary to catalyze the hydrogenolysis and isomerization reactions). A computer model of the surface structure gave excellent agreement with the catalytic results. This model proposed a highly segregated structure (for the bimetallic particles) and catalytic sites comprised of 16, 4 and 1 atoms for the hydrogenolysis, isomerization and dehydrogenation reactions respectively. Surface reaction mechanisms and intermediates consistent with these ideas have been postulated.

- The catalysis results for Fe, Ru and Fe/Ru also demonstrated a *bimetallic effect*. Unimetallic Ru MVS materials acted as hydrogenolysis catalysts, while the unimetallic Fe samples showed no catalytic activity whatsoever unless very high total loadings of metal were employed. In the case of the corresponding Fe/Ru bimetallic material, substantial dehydrogenation activity was observed; this has been attributed to Fe in an oxidation state lower than +3. It is believed that for heavily loaded unimetallic Fe materials, such exists due to the limited number of surface OH groups (having a limited capacity for oxidizing the $Fe(toluene)_2$ precursors). In bimetallic Fe/Ru materials, the ruthenium can stabilize less oxidized iron, even when large amounts of iron are not supplied.

- Finally, application of the EXAFS technique verified the *assumption* of the segregated structure possessed by the Ni/Pt bimetallic particles, while agreeing with the size estimates and oxidation state information provided by the various other techniques, and revealing some details of how the atoms were arranged within the unimetallic and bimetallic particles.

- The platinum atoms were observed to have other platinum atoms in their vicinity, and to have an average coordination number close to 7.4 (which is typical for small platinum clusters having sizes of about 1 nm). The nickel part of the *two phase* bimetallic particles may be adequately described as ultra-microcrystalline NiO, probably containing a single unit cell per particle. This is consistent with the form having a rock salt structure (Ni-O coordination number 6).

10.2 Recommendations

- The technique of Metal Vapour synthesis should be extended to produce (and later characterize) iron, ruthenium, nickel and platinum containing materials using other support materials such as silicas and aluminas with different surface areas and initial OH concentrations, carbon and magnesia. Also, these same metals should be incorporated into supported particle preparations through the use of various other organometallic precursors.

- Other metals, both in unimetallic form and in various combinations should be used to produce MVS materials.

- Further characterization of the presently synthesized MVS materials should be accomplished using the technique of Mössbauer spectroscopy. This could be used to gain further knowledge about the structural and oxidation state properties of Fe and Fe/Ru particles, as could the technique of EXAFS which has not as of yet been applied to the Fe/Ru MVS system.

- A recommended area of theoretical work involves computer modelling of the vibrational behaviour (particularly in terms of surface coverage dependence for isotopic mixtures) of CO. This would proceed from an approach which has been discussed in the literature, and includes the various appropriate adsorbate interactions (eg. vibrational, through-metal coupling), but with the added feature that these would be angle dependent. Such would allow a realistic representation of the present particle sizes, which have been seen to affect the results in a profound way.

- A more extensive collection of EPR/FMR data, than that reported here has been obtained. At the present time a large number of calculations and compilations of results have yet to be performed. Part of this should involve the analysis of individual FMR spectra, in order to assemble the thermomagnetic curves. The fitting procedure used to simulate these would yield a third particle size distribution measurement. The magnetic resonance investigations have not yet been extended to the bimetallic preparations; such work is also recommended. Also, the platinum and platinum containing bimetallic samples are expected to give rise to observable conduction electron spin resonance (CESR) spectra. This technique could also provide valuable geometric, electronic and magnetic structural information about the presently synthesized MVS materials.

- The catalysis results reported here for the Ni/Pt system and the associated bimetallic surface model should be improved through the collection of more data. This should involve both the repetition of catalysis runs already carried out and the examination of other bimetallic composition ratios (which would require the synthesis of new samples). If such were accomplished, a more quantitative approach to the modelling would be possible.

- Catalytic reactions other than n-butane conversion should be examined as a means of further characterizing all of the MVS materials discussed here. An interesting reaction could be carried out using ethylcyclohexane as a reactant. This would be expected to undergo each of the previously observed reactions (i.e., hydrogenolysis isomerization and dehydrogenation), as well as the additionally possible aromatization reaction.

REFERENCES

1. Andrews,M.P., "*Apparatus and Techniques for Using Metal Atoms and Molecular High Temperature Species in New Materials Synthesis*", 1987.

2. Andrews,M.P., Francis,C.G., Huber,H.X., Molnar,K., Ozin,G.A., Inorg.Chem., *in press.*

3. Green,M.L.H., J.Organomet.Chem., **200**, 119 (1980).

4. Whyte,T.E.Jr., Dalla Betta,R.A., Derouane,E.G., Baker,R.T.K., Eds., Catalytic Materials: Relationship between Structure and Reactivity, ACS Symp.Ser. 248, June 1983 pp. 3-19.

5. Fischer,K., Jonas,K., Wilke,G., Angew.Chem.Int.Ed.Engl., 12, 565 (1973); Green,M., Howard,J.A., Spencer,J.L., Stone,F.G.A., J.Chem.Soc.Chem.Comm., 1975, 3.

6. Nazar,L., Ph.D. Thesis, University of Toronto, 1986 (and references cited therein).

7. Choplin,A., Huang,A., Theolier,A., Gallezot,P., Basset,J.M., J.Amer.Chem.Soc., **108**, 4224 (1986).

8. Delannay,F., Ed., The Characterization of Heterogeneous Catalysts, Marcel Dekker Inc., New York, 1984 (and references cited therein).

9. Gallezot,P., Leclercq,C., "*Caracterisation des Catalyseurs par Microscopie Electronique, Conventionelle et Analytique, a Haute Resolution*", 1986.

10. Sindorf,D.W., Maciel,G.A., J.Phys.Chem., **87**, 5516 (1983).

11. Matyi,R.J., Schwartz,L.H., Butt,J.B., Catal.Rev.Sci.Eng., **29**, 41 (1987).

12. Ichikawa,M., Fukushima,T., Yokoyama,T., Kosugi,N., Kuroda,H., J.Phys.Chem., **90**, 1222 (1986).

13. Bonneviot,L., Che,M., Olivier,D., Martin,G.A., Freund,E., J.Phys.Chem., **90**, 2112 (1986).

14. Tonkyn,R., Weisshar,J.C., J.Phys.Chem., **90**, 2305 (1986).

15. Tzou,M.S., Teo,B.K., Sachtler,W.M.H., Langmuir, 2, 773 (1986).

16. Wojciechowski,B.W., Corma,A., Catalytic Cracking, Chemical Industries Series, Vol. 25, Marcel Dekker Inc., New York, 1986.

17. Dorling,T.A., Lynch,B.W.J., Moss,R.L., J.Catal., 20, 190 (1971).

18. Gallezot,P., *Unpublished Work*, 1985.

19. Rooksby,N., X-ray Identification and Crystal Structure of Clay Minerals, London, 1951 p.254.

20. Wynblatt,P., Gjostein,N.A., Prog.Solid State Chem., 1975.

21. Martin,G.A., Catal.Rev.Sci.Eng., 30(4), 519 (1988).

22. Taylor,W.F., Yates,D.J.C., Sinfelt,J.H., J.Catal., 4, 374 (1965).

23. Haddleton,D., *Unpublished Internal Report*, 1987 p.14.

24. Huber,H.X., Haddleton,D., *Unpublished Work*, 1987.

25. Kundig,E.P., Moskovits,M., Ozin,G.A., J.Mol.Struct., 14, 137 (1972).

26. Sinfelt,J.H., Bimetallic Catalysts: Discoveries, Concepts and Applications, John Wiley & Sons Publ. Co., New York, 1983.

27. Teo,B.K., EXAFS: Basic Principles and Data Analysis, Springer-Verlag, Berlin, 1986.

28. Sinfelt,J.H., Bimetallic Catalysts: Discoveries, Concepts and Applications, John Wiley & Sons Publ. Co., New York, 1983. pp. 52-59.

29. Klabunde,K.J., Imizu,Y., Chem.Ind., 22, 225 (1985).

30. Kitajima,N., Kono,A., Ueda,W., Moro-oka,Y., Ikawa,T., J.Chem.Soc.Chem.Comm., 1986, 674.

31. Chow,M., Park,S.H., Sachtler,W.M.H., Appl.Catal., 19(2), [illegible] (1985).

32. Whyte,T.E.Jr., Catal.Rev., 8(11), 117 (1973).

33. Boudart,M., Delbouille,A., Dumesic,J.A., Khammouma,S., Topsoe,H., J.Catal., 37, 486 (1975).

34. Bonneviot,L., Olivier,D., Che,M., J.Chem.Soc.Chem.Comm., 1982, 952.

35. Ozin,G.A., Andrews,M.P., U.S. Pat. 4,569,924, 1986.

36. Engstrom,J.R., Goodman,D.W., J.Amer.Chem.Soc., 108(15), 4653 (1986).

37. Godber,J., Ozin,G.A., *Unpublished Work*, 1985.

38. Sinfelt,J.H., Bimetallic Catalysts: Discoveries, Concepts and Applications, John Wiley & Sons Publ. Co., New York, 1983. p.17.

39. Hudgins,R.R., "*The Problem of Avoiding Transport Interference*", 8th. Canadian Symposium on Catalysis, Waterloo, Ontario, May, 1982.

40. Ozin,G.A., *Unpublished Work*, August 1986.

41. Hugues,F., Besson,B., Basset,J.M., J.Chem.Soc.Chem.Comm., 1980, 719.

42. Dalla Betta,R.A., Cusumano,J.A., Sinfelt,J.H., J.Catal., 19, 343 (1980).

43. Bolivar,C., Charcosset,W.G., Frety,R., Tournayan,L., Betizeau,C., Leclerq,G., Maurel,M., J.Catal., 45, 179 (1980).

44. Snedecor,G.W., Cochran,W.G., Statistical Methods, 7th.Ed., Iowa State Press, Ames, Iowa, 1980.

45. Somorjai,G.A., Ed., Chemistry in Two Dimensions: Surfaces, Cornell University Press, London, 1981 pp. 381-406.

46. Adesina,A.A., Hudgins,R.R., Silveston,P.L., *Unpublished Work*, University of Waterloo, Waterloo, 1984.

47. Haiduk,I., Zuckerman,J.J., Basic Organometallic Chemistry, Walter de Gruyter, Berlin, 1985 pp.18-19.

48. Grubbs,R.H., Migashita,A., J.Amer.Chem.Soc., 100, 1300 (1978).

49. Fischer,K., Jonas,K., Wilke,G., Angew.Chem.Int.Ed.Engl., **12**, 629 (1973).

50. Demuth,J.E., Ibach,H., Lehwald,S., Phys.Rev.Lett., **40**, 1044 (1978).

51. Godber,J., Huber,H.X., Prokopowicz,R.A., Ozin,G.A., *Unpublished Work*, 1985.

52. Eischens,R.P., Francis,S.A., Pliskin,W.A., J.Phys.Chem., **60**, 194 (1956).

53. Severson,M.W., Tornquist,W.J., Overend,J., J.Phys.Chem., **88**, 469 (1984).

54. Severson,M.W., Russell,A., Campbell,D., Russell,J.W., Langmuir, **3**, 202 (1987).

55. Moskovits,M., Hulse,J., Surf.Sci., **78**, 397 (1978).

56. Crossley,A., Krug,D.A., Surf.Sci., **68**, 528 (1977); and Surf.Sci., **95**, 131 (1980).

57. Hammaker,R.M., Francis,S.A., Eischens,R.P., Spectrochim.Acta., **21**, 1295 (1965).

58. Dignam,M.J., Moskovits,M., J.Chem.Soc.Farad.II., **69**, 56 (1973).

59. Somorjai,G.A., Chemistry in Two Dimensions: Surfaces, Cornell University Press, Ithaca, New York, 1981 pp. 283-330.

60. Shigeishi,R.A., King,D.A., Surf.Sci., **75**, L397 (1978).

61. Chou,P., Vannice,M.A., J.Catal., **104**, 17 (1987); Vannice,M.A., Hasselbring,L.C., Sen,B., J.Catal., **97**, 66 (1986); Sen,B., Ph.D. Thesis, Pennsylvania State University, 1987.

62. Moskovits,M., Ozin,G.A., J.Mol.Struct., **32**, 71 (1976); Moskovits,M., Ozin,G.A., Cryochemistry, John Wiley & Sons Publ. Co., Toronto, 1976.

63. Buckingham,A.D., Proc.Roy.Soc.(London), **A248**, 169 (1958).

64. Shigeishi,R.A., King,D.A., Surf.Sci., **58**, 379 (1976).

65. M^{c}Intosh,D.F., Michaelin,K.H., Can.J.Spectr., **24**, 1 (1979) and references cited therein.

66. Reference 8, pp. 225-298.

67. Briggs,D., Seah,M.P., Eds., Practical Surface Analysis by Auger and X-ray Photoelectron Spectroscopy, John Wiley & Sons Publ. Co., New York, 1983.

68. Swift,P., Surf.Interfac.Anal., 4, 47 (1982).

69. DeJong,K.P., Geus,J.W., Joziasse,J., J.Catal., 65, 437 (1977).

70. McIntyre,N.S., Rummery,T.E., Cook,M.G., Owen,D., J.Electrochem.Soc., 123, 1165 (1976).

71. Bouwman,R., Biloen,P., J.Catal., 48, 209 (1977).

72. Matienzo,L.J., Swartz,W.E., Grim,S.O., Inorg.Nucl.Chem.Lett., 8, 1085 (1972).

73. Bard,A.J., Parsons,R., Jordan,J., Eds., Standard Potentials in Aqueous Solution, Marcel Dekker Inc., New York, 1985.

74. Abragham,A., Bleany,B., Electron Paramagnetic Resonance of Transition Metal Ions, Oxford University Press, London, 1970.

75. Weltner,W.Jr., Magnetic Atoms and Molecules, Scientific and Academic Editors, New York, 1983.

76. Kittel,C., Introduction to Solid State Physics, John Wiley & Sons Publ. Co., Toronto, 1976.

77. Schmidt,F., Stapel,U., Walther,H., Ber.Bunsenges.Phys.Chem., 88, 310 (1984).

78. He,M.Y., Xiong,G., Toscano,P.J., Burwell,R,L.Jr., Marks,T,J., J.Amer.Chem.Soc., 107, 641 (1985).

79. Sindorf,D.W., Maciel,G.E., J.Amer.Chem.Soc., 105(6), 1487 (1983); Bronnimann,C.E., Chuang,I.S., Hawkins,B.L., Maciel,G.E., J.Amer.Chem.Soc., 109(5), 1562 (1987).

80. Knözinger,J., Catal.Rev.Sci.Eng., 17, 31 (1978).

81. Peri,J.B., J.Phys.Chem., 69, 211 (1965); J.Phys.Chem., 69, 220 (1965); J.Phys.Chem., 64, 1526 (1960).

82. Burwell,R., J.Catal., 63, 463 (1980); J.Coll.Interfac.Sci., 75, 95 (1980).

83. Thomas,J., Angew.Chem.Int.Ed.Engl., 22, 614 (1983).

84. Michalik,J., Narayana,M., Kevan,L., J.Phys.Chem., 88, 5236 (1984).

101. Kronig,R. de L., Z.Physik., 70, 317 (1931).

102. Kronig,R. de L., Z.Physik., 75, 468 (1932); Z.physik., 76 (1932).

103. Stern,E.A., Sayers,D.E., Lytle,F.W., Phys.Rev.B, 11, 4836 (1975).

104. Stern,E.A., Sayers,D.E., Dash,J.G., Shechter,H., Bunker,B., Phys.Rev.Lett., 38, 767 (1977).

105. Teo,B.K., EXAFS: Basic Principles and Data Analysis, Springer-Verlag, Berlin, 1986, p.23.

106. Lee,P.A., EXAFS Spectroscopy: Techniques and Applications, Teo,B.K., Joy,D.C., Eds., Plenum Press, New York, 1981.

107. Winnick,H., Doniach,S., Synchrotron Radiation Research, Plenum Press, New York, 1980.

108. Kincaid,B.M., Eisenberger,P., Phys.Rev.Lett.B., 34, 1361 (1975).

109. Lytle,F.W., Sayers,D., Stern,E., Phys.Rev., B11, 4825 (1975).

110. Via,G.H., Sinfelt,J.H., Lytle,F.W., J.Chem.Phys., 71, 690 (1979).

111. Ashley,C.A., Doniach,S., Phys.Rev.B., 11, 1279 (1975).

112. Lee,P.A., Pendry,J.B., Phys.Rev.B, 11, 2795 (1975).

113. Grosso,G., Pastori,P.G., J.Phys.C, 13, L919 (1980).

114. Teo,B.K., Lee,P.A., J.Amer.Chem.Soc., 101, 2815 (1979).

115. Reference 26, pp. 53-130.

116. Reference 105, pg. 196.

117. Sayers,D.E., Bunker,B.A., in X-ray Absorption: *Principles, Applications, Techniques of EXAFS, SEXAFS and XANES*, Chemical Analysis Series, Vol. 92, Koningsberger,D.C., Prins,R., Eds., John Wiley & Sons Publ. Co., New York, 1988; p. 211.

118. Robota,H.J., Cohn,M.J., Ringwelski,A.Z., Eades,R.A., Mat.Res.Soc.Symp.Proc., 111, 201 (1988).

119. Kip,B.J., Duivenvoorden,F.B.M., Koningsberger,D.C., Prins,R., J.Catal., 105, 26 (1987).

120. Koningsberger,D.C., Sayers,D.E., Solid State Ionics, 16, 23 (1985).

121. Lytle,F.W., Greegor,R.B., Marques,E.G., Sandstrom,D.R., Via,G.H., Sinfelt,J.H., J.Catal., 95, 546 (1985).

122. Moraweck,B., Renouprez,A.J., Surf.Sci., 106, 35 (1981).

123. Van Zon,J.B.A.D., Koningsberger,D.C., Van't Blik,H.F.J., Sayers,D.E., J.Chem.Phys., 82, 5742 (1985).

124. Prokopowicz,R.A., Huber,H.X., Robota,H.J., Ozin,G.A., *manuscript in preparation*, 1989.

125. Donnay,J.D.H., Ed., Crystal Data: Determinative Tables, 2nd. Ed., Amer.Cryst.Assoc., Washington D.C., 1963.

126. Sayers,D.E., Bunker,B.A., in X-ray Absorption: *Principles, Applications, Techniques of EXAFS, SEXAFS and XANES*, Chemical Analysis Series, Vol. 92, Koningsberger,D.C., Prins,R., Eds., John Wiley & Sons Publ. Co., New York, 1988.

Summary

Liquid phase (rotary reactor) and cocondensation phase (rotary and static reactor) metal vapour syntheses (MVS) have been used to produce extremely small particles of Fe, Ru and Fe/Ru, as well as Ni, Pt and Ni/Pt on SiO_2 and Al_2O_3, through the intermediacy of labile bis-toluene and tris-ethylene metal(0) precursors. The Fe/Ru system was first investigated, mainly to gain experience with the synthesis and characterization techniques; the Ni/Pt system has been much more thoroughly investigated. It was the purpose of this research to explore the many fascinating properties of these materials using such techniques as: high resolution (1.0 x 1.0 nm) Scanning Transmission Electron Microscopy combined with Energy Dispersive X-ray elemental Analysis (STEM-EDAX), Conventional Transmission Electron Microscopy (CTEM), X-ray Photoelectron Spectroscopy (XPS), Electron Paramagnetic Resonance and Ferromagnetic Resonance (EPR/FMR) spectroscopies, Chemisorption and Fourier Transform Infrared (FTIR) spectroscopy, Ultraviolet/Visible (UV-Vis) spectroscopy, Catalysis and Extended X-ray Absorption Finestructure Spectroscopy (EXAFS).

The microscopy work has revealed that all of the supported particles have extremely small sizes (about 1.0 nm on the average) and narrow size distributions about the mean value. Such ultra small particles were observed to have excellent resistance to sintering under a variety of conditions. The EDAX technique, with which large numbers of individual particles were analyzed, proved that the synthesis had yielded truly *bimetallic* particles.

The use of XPS allowed an examination of many of the electronic properties of the particles. From this, evidence was obtained that Pt remains zerovalent while the Ni in the particles is in an oxidized form. In bimetallic particles containing both elements, there was no indication of charge transfer between them. Evidence was gathered however, that the mechanism by which the particles are attached to the support surface involves metal-to-surface charge transfer.

Chemisorption of hydrogen, oxygen and especially CO (the latter being examined by FTIR) were used to confirm the extremely small particle sizes. Two size-dependent phenomena, namely enthalpy of chemisorption and the coverage dependent shift in the carbonyl stretching frequency were explored, and compared with those exhibited by other supported particle systems of various size regimes.

The EPR/FMR study, applied to a subset of the samples involved in this research, led to conclusions that species such as Ni^{+1} and Ni^{+2} are created by reaction of the zerovalent precursors with surface hydroxyl (Brønsted acid) groups on the supports. These serve as nucleating centres for migrating precursor entities which ultimately incorporate into the supported particles.

The catalytic results (using the conversion of n-butane in hydrogen as a probe reaction) for the bimetallic samples show behaviour quite different from either of the two corresponding unimetallics. In particular, the bimetallics showed a marked increase in dehydrogenation selectivity relative to the unimetallics. This is rationalized on the basis that the bimetallic particles differ geometrically from their unimetallic counterparts in such a way that there are fewer large ensembles of atoms (these are considered necessary to catalyze the hydrogenolysis and isomerization reactions). A computer model of the surface structure gave excellent agreement with the catalytic results. This model proposed a highly segregated structure (for the bimetallic particles) and catalytic sites comprised of 16, 4 and 1 atoms for the hydrogenolysis, isomerization and dehydrogenation reactions respectively. Surface reaction mechanisms and intermediates consistent with these ideas have been postulated.

Finally, application of the EXAFS technique verified this assumption of segregated bimetallic particles, while agreeing with the size estimates and oxidation state information provided by the various other techniques, and revealing some details of how the atoms are arranged within the uni- and bimetallic particles

Recommended further work includes the examination of two or more different probe reactions, including that of ethylcyclohexane conversion (wherein ring-opening and aromatization would be additionally possible reaction paths).